



HAL
open science

New initiating systems for radical and cationic photopolymerization under visible light irradiation and their 3D and 4D applications

Hong Chen

► **To cite this version:**

Hong Chen. New initiating systems for radical and cationic photopolymerization under visible light irradiation and their 3D and 4D applications. *Polymers*. Université de Haute Alsace - Mulhouse, 2022. English. NNT : 2022MULH5626 . tel-03948689

HAL Id: tel-03948689

<https://theses.hal.science/tel-03948689v1>

Submitted on 20 Jan 2023

HAL is a multi-disciplinary open access archive for the deposit and dissemination of scientific research documents, whether they are published or not. The documents may come from teaching and research institutions in France or abroad, or from public or private research centers.

L'archive ouverte pluridisciplinaire **HAL**, est destinée au dépôt et à la diffusion de documents scientifiques de niveau recherche, publiés ou non, émanant des établissements d'enseignement et de recherche français ou étrangers, des laboratoires publics ou privés.

THÈSE

Présentée et soutenue le **12th Juillet 2022** par :

HONG CHEN

Pour l'obtention du titre de Docteur en Chimie des Matériaux de :

L'UNIVERSITÉ DE HAUTE ALSACE

**New initiating systems for radical and cationic
photopolymerization under visible light irradiation and their 3D
and 4D applications**

Members du Jury

Pr. Odile Fichet	Université de Cergy-Pontoise	Rapporteuse
Dr. Erwan Nicol	Université Le Mans	Rapporteur
Pr. Angélique Simon Masseron	Université de Haute-Alsace	Examinatrice
Dr. Pu Xiao	Australian National University	Invité
Pr. Jacques Lalevée	Université de Haute-Alsace	Directeur de thèse

Abstract

Even though photopolymerization technology has been successfully applied to coatings, adhesives, 3D printing and many other fields in the past decades since the scientific and technological development, photopolymerization processes under mild conditions (e.g.; low light intensity and visible light sources) are still the focus of research in this technology. The greatest challenges are the design and synthesis of high-performance photoinitiators (PIs) / photoinitiating systems (PISs) that can work effectively under more moderate conditions such as low light intensity and visible light sources. The main aim of this Ph.D. project is to develop novel efficient visible light sensitive and/or water-soluble PIs/PISs and then prepare polymers/hydrogels by 3D printing technology and study their 4D applications. In this Ph.D. thesis, we have carried out research in three main directions, firstly, we designed and synthesized a series of dyes with chalcone as the central structure, which exhibit excellent absorption properties in the near UV/visible region and are used as highly efficient UV-visible PIs. Based on above researches, we further developed more efficient visible PIs with the introduction of metal salt ions. These PIs combined with co-initiators as a visible light initiating system that could initiate deep-curing of the monomers and meanwhile reduce the metal salt ions into metal particles to prepare polymers with uniform distribution of metal nanoparticles. Finally, we prepared a series of water-soluble PIs, which exhibited the advantages of higher water solubility and sensitive to visible light sources than the commercially available water-soluble PIs. Moreover, it can also reduce silver cations (Ag^+) to silver nanoparticles (AgNPs) to prepare the antibacterial hydrogels. All these three types of PIs are visible light sensitive and can be used to produce 3D polymers or hydrogels by 3D printing technology, among which water-soluble PIs are compatible with high water solubility and compatibility with visible low-power light sources. The newly developed highly efficient visible light sensitive PISs provide a wider range of applications which responded the demand for light-cured products (hydrogels or polymers) and met the needs of 3D printing technology.

This work was funded by the China Scholarship Council (CSC:201906280059).

and many of the new proposed photoinitiators were synthesized by our partner Dr. Frédéric Dumur from the Aix-Marseille Université.

CONTENTS

ABSTRACT	I
CONTENTS	III
Part I. Context and Bibliography	1
1. General Introduction	1
2. Photopolymerization Technology	4
3. 3D Printing Technology	8
3.1 Method	9
3.2 Materials	10
3.3 Applications	13
3.3.1 <i>Medical materials</i>	14
3.3.2 <i>Aerospace</i>	15
3.3.3 <i>Transportation</i>	16
3.3.4 <i>Industrial equipment and consumers/electronics</i>	16
4. 3D Printing via Photopolymerization	18
4.1 Method	18
4.1.1 <i>Stereolithography (SLA)</i>	18
4.1.2 <i>Digital light processing (DLP)</i>	19
4.1.3 <i>Continuous digital light processing/continuous liquid interface production (CDLP/CLIP)</i>	19
4.1.4 <i>Photopolymer jetting (Polyjet)</i>	20
4.2 Light sources	21
4.3 Photoinitiators / Photoiniting systems (PIs/PISs)	22
4.3.1 <i>Visible light-sensitive PIs for 3D printing</i>	23
4.3.1.1 <i>Dyes-based PIs for 3D printing</i>	24
4.3.1.2 <i>Organometallic PIs for 3D printing</i>	27
4.3.1.3 <i>Modification of UV PIs</i>	28
4.3.2 <i>Water soluble PIs for 3D printing</i>	29
4.4 Monomers/oligomers and related applications	33
4.1.1 <i>Monomers/Oligomers for photopolymerization based 3D printing of composite materials</i>	34
4.1.2 <i>Monomers/Oligomers for photopolymerization based 3D printing of shape memory polymers (4D printing)</i>	37
5. Conclusion	41
References	42

Part II. Free Radical Photopolymerization of Chalcones Based Three-Component Photoinitiating Systems and Their Applications in 3D Printing	53
1. Introduction	53
2. Experimental Section	55
2.1 Materials	55
2.2 Photopolymerization reactions monitored by real time fourier transformed infrared spectroscopy (RT-FTIR)	56
2.3 UV-visible absorption spectroscopy	56
2.4 Fluorescence and cyclic voltammetry experiments	56
2.5 Electron spin resonance-spin trapping (ESR-ST) experiments	57
2.6 3D printing experiments	57
2.7 Swelling experiments	57
2.8 4D printing experiments	58
2.9 Molecular modeling	58
References.....	58
Chapter 1. Photoinitiators Derived From Natural Product Scaffolds: Mono-Chalcones In Three-Component Photoinitiating Systems And Their Applications In 3D Printing	61
1. Photoinitiation Ability of the Chalcones Contained Three-Component Systems	62
2. 3D Applications	64
2.1 Direct laser write experiments by using chalcones based three-component PISs	65
2.2 The swelling kinetics of obtained PEG-polymers	66
3. Proposed Chemical Mechanisms	67
3.1 Light absorption properties of the chalcones in acetonitrile	67
3.2 Steady state photolysis of chalcones 4, 9, 10 and 12	69
3.3 Fluorescence quenching and ESR experiments to study electron transfer reaction for chalcones	73
4. Conclusion	77
References	78
Chapter 2. Novel D-π-A and A-π-D-π-A Three-Component Photoinitiating Systems Based on Carbazole/Triphenylamino based Chalcones and Application in 3D and 4D Printing	79
1. Synthesis of Chalcones 1-10	80
2. Photoinitiation Ability of the Chalcones based PISs	81
3. Proposed Chemical Mechanisms	84

3.1 UV-visible absorption properties of the chalcones in acetonitrile	84
3.2 Steady state photolysis of chalcones	86
3.3 Fluorescence quenching experiments and cyclic voltammetry to study electron transfer reaction in chalcone based systems	89
3.4 ESR experiments: free radicals generated in chalcone based systems	92
4. 3D and 4D applications	94
4.1 3D printing experiments based on the two-component PISs	94
4.2 The swelling of PEG-polymer initiated by chalcone/Iod	95
4.3 Reversible deformation: the shape memory of 4D behavior of PEG-polymer via swelling and dehydration induced actuation	96
5. Conclusion	98
Annex	99
References	101
Part III. Preparation of Composites Containing AgNPs Using Newly Developed Dyes-Based Photoinitiator and Their 3D/4D Applications	103
1. Introduction	103
2. Experimental Section	104
2.1 Materials	104
2.2 Free radical photopolymerization (FRP) and cationic photopolymerization (CP) initiated by dye/Iod/amine based-PISs	105
2.3 Involved chemical mechanism	105
2.3.1 <i>UV-vis absorption properties of dyes and their steady-state photolysis process with Iod/amine</i>	<i>105</i>
2.3.2 <i>Fluorescence experiments of the dyes</i>	<i>106</i>
2.3.3 <i>Electron spin resonance (ESR) spin trapping (ESR-ST) experiments and the redox potentials of dyes</i>	<i>106</i>
2.4 Preparation of the silver nanoparticles (AgNPs)	106
2.4.1 <i>Preparation of AgNPs in DMF</i>	<i>106</i>
2.4.2 <i>Preparation of AgNPs within polymers through in-situ photopolymerization processes</i>	<i>107</i>
2.5 Characterization of polymers	107
2.5.1 <i>TEM and SEM of AgNPs</i>	<i>107</i>
2.5.2 <i>Dynamic time sweep rheology</i>	<i>107</i>
2.5.3 <i>Tensile strength of polymers</i>	<i>107</i>
2.6 Applications in 3D and 4D printing	108
2.6.1 <i>Direct laser write experiments to prepare the single and IPN polymers with/without AgNPs</i>	<i>108</i>

2.6.2 Swelling experiments of the obtained polymers	108
2.6.3 Shape-memory effects of single and IPN polymers with/without AgNPs (4D behavior)	108
2.7 Antibacterial effect of IPN containing/without AgNPs	109
References	109
Chapter 1. In Situ Generation of Ag Nanoparticles During Photopolymerization by Using Newly Developed Dyes-Based Three-Component Photoinitiating Systems and The Related 3D Printing Applications and Their Shape Change Behavior	112
1. UV-Visible Absorption Properties of the Different Chalcones in Acetonitrile	113
2. Photopolymerization Kinetics	114
2.1 Free radical polymerization (FRP) kinetics of PEG-DA	114
2.2 Cationic polymerization (CP) kinetics of EPOX	117
2.3 Free radical polymerization (FRP) initiated by Dyes 3 and 5-based two-component PISs or only dyes as the PIs	118
3. Proposed Chemical Mechanisms	119
3.1 Steady state photolysis	119
3.2 Fluorescence quenching experiments	121
3.3 ESR experiments	124
4. The Generations of AgNPs in DMF Solution and PEG-Polymers	124
5. The Influence of AgNPs on the Physical Properties of PEG-Polymers	125
5.1 3D direct laser write experiments	126
5.2 Water swelling of PEG-polymers containing/without AgNPs	126
5.3 The reversible shape-memory effect of PEG-polymer containing/without AgNPs	127
6. Conclusion	129
Annex	131
References	135
Chapter 2. Interpenetrating Polymer Network Hydrogels Using Natural Based Dyes Initiating Systems: Antibacterial Activity and 3D/4D Performance	137
1. Photoinitiation Ability of the Proposed Dyes-Based PISs Upon Visible Light	138
1.1 Free radical polymerization (FRP) of PEG-DA	138
1.2 Cationic polymerization (CP) of EPOX	139
1.3 The fabrication of IPN polymers through different ratios of PEG-DA and EPOX	140
2. The Involved Chemical Mechanisms	141
2.1 UV-visible absorption properties of the proposed dyes	141

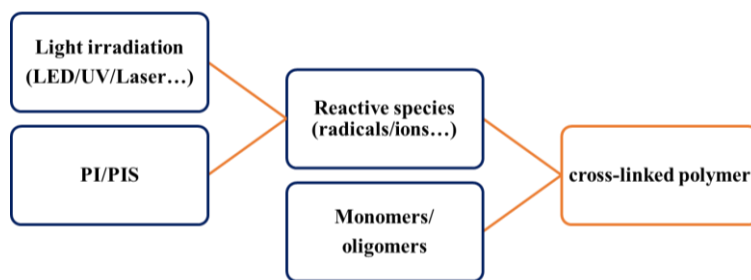
2.2 Steady state photolysis	143
2.3 Fluorescence quenching experiments	144
2.4 Feasibility of the interactions between dyes and Iod/amines	147
2.5 ESR-spin trapping experiments for dye 5 with Iod/EDB system	148
3. AgNPs Generated in DMF Solution and IPN-Polymers	149
4. Characterization of IPN Polymers	152
5. Applications in 3D and 4D Printing	153
5.1 3D laser write experiments based on the dye 5-based three-component PIS	153
5.2 Swelling of PEG-DA-, EPOX-, IPN- and AgNP containing IPN- polymers	154
5.3 The reversible deformation effect of PEG-DA-, IPN- and AgNP containing IPN- polymer	156
6. Antibacterial Effect of IPN Containing/Without AgNPs	157
7. Conclusion	159
Annex	161
References	169
Part IV. Water-Soluble/Visible-Light-Sensitive Naphthalimide Derivative Based Photoinitiating Systems: 3D Printing of Antibacterial hydrogels	173
1. Introduction	173
2. Materials and Methods	175
2.1 Chemical compounds	175
2.2 Water solubility of proposed naphthalimide derivatives	176
2.3 Involved chemical mechanisms	176
2.4 Photopolymerization experiments	177
2.4.1 <i>UV-Vis absorption properties of the selected dyes and their photolysis process and fluorescence quenching process with Iod and amine</i>	<i>177</i>
2.4.2 <i>Electron spin resonance (ESR) spin trapping experiments (ESR-ST) and the free energy changes of dyes with Iod/amine</i>	<i>177</i>
2.5 Dynamic time sweep rheology and tensile strength of the manufactured hydrogel	177
2.6 Preparation of silver nanoparticles (AgNPs)	178
2.6.1 <i>Preparation of AgNPs in DMF/ water using the proposed water-soluble PIS</i>	<i>178</i>
2.6.2 <i>Preparation of AgNPs in hydrogels</i>	<i>178</i>
2.7 Applications in 3D and 4D printing	178
2.7.1 <i>Direct laser write experiments to prepare hydrogels</i>	<i>178</i>

2.7.2 Swelling experiments of the obtained hydrogels	178
2.8 Antibacterial effect of of hydrogels with different content of AgNPs	179
3. Results and Discussion	179
3.1 Water solubility of proposed naphthalimide-derivatives	179
3.2 Photopolymerization efficiency of the proposed water-soluble dyes based PIS	180
3.3 Investigation of the involved chemical mechanisms	182
3.4 Preparation of silver nanoparticles (AgNPs)	188
3.5 Mechanical properties of obtained hydrogels	189
3.6 Applications in 3D and 4D printing	191
3.7 Antibacterial activity of hydrogels with different content of AgNPs	193
4. Conclusion	194
Annex	195
References	199
Part V. Conclusions and Perspectives	203
1. Conclusions	203
2. Perspectives	204

Part I. Context and Bibliography

1. General Introduction.

Since 1915, when Ostromislensky started to study the photopolymerization process (as shown in **Scheme I-1**, [1]), this technology has attracted a lot of attentions in academic research and polymer industrial production, therefore it has been rapidly developed and widely used in various fields, ranging from individualized commercial products (e.g. jewelry [2] and electronic components [3,4]), dental and food industries, to emerging fields such as drug delivery [5], surgical medical devices [6], and biomaterials and tissue engineering [7]. 3D printing, also known as rapid prototyping (RP) or solid-freeform (SFF), is an additive manufacturing (AM) technology that is used to fabricate a variety of structures and complex geometries from three-dimensional (3D) model data [8-10]. Combining 3D printing technology with photopolymerization technology, the developed photopolymerization based 3D printer is not only efficient and energy saving, but also has the advantages of high precision and personalized customization of 3D printing, bringing significant benefits for people's production and daily lives. Since the introduction of the first commercial photopolymerization based 3D printer (SLA 250) in 1988 [11], the technology has gradually developed and commercialized, reaching a commercial value of more than \$10 billion. Despite the fact that 3D printing *via* photopolymerization has made major advances in industrial production [12-14], the printing process *via* photopolymerization under milder conditions (e.g., low light intensity, visible light source, room temperature, etc.) remains a hotspot. It's more beneficial to printing with living cells, providing an excellent method for resolving a variety of medical issues that still exist today. The most challenging aspect of this technology is designing and synthesizing high-performance photoinitiators/photoinitiating systems (PIs/PISs) that can operate efficiently in milder environments.



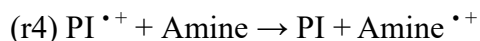
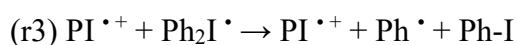
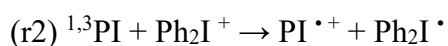
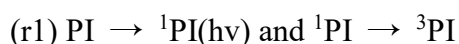
Scheme I-1. Schematic representation of the photopolymerization process.

Furthermore, the intensity of light source and the wavelength of irradiation are additional parameters that influence the efficiency of the polymerization process [15]. The “PIS” is clarified as a group of interacting or interrelated entities that includes PIs, co-initiators and additives (e.g. iodonium salt, amine, N-vinylcarbazole, silane, etc.), where the choice of PIs is critical in initiating the polymerization process as it directly controls the reaction rate. Nevertheless, due to their relatively good solubility and photo-reactivity in curable resins, iodonium salts are commonly utilized as common components of PIS for photopolymerization. Furthermore, amines also play an important role in photopolymerization as electron donors due to their great electron donating ability to boost the photoinitiation efficiency of PISs. Besides, visible light sources, such as LEDs, are appealing candidates for many applications due to their cheaper cost, low energy consumption, and ability to provide manipulators with safe operating conditions [16].

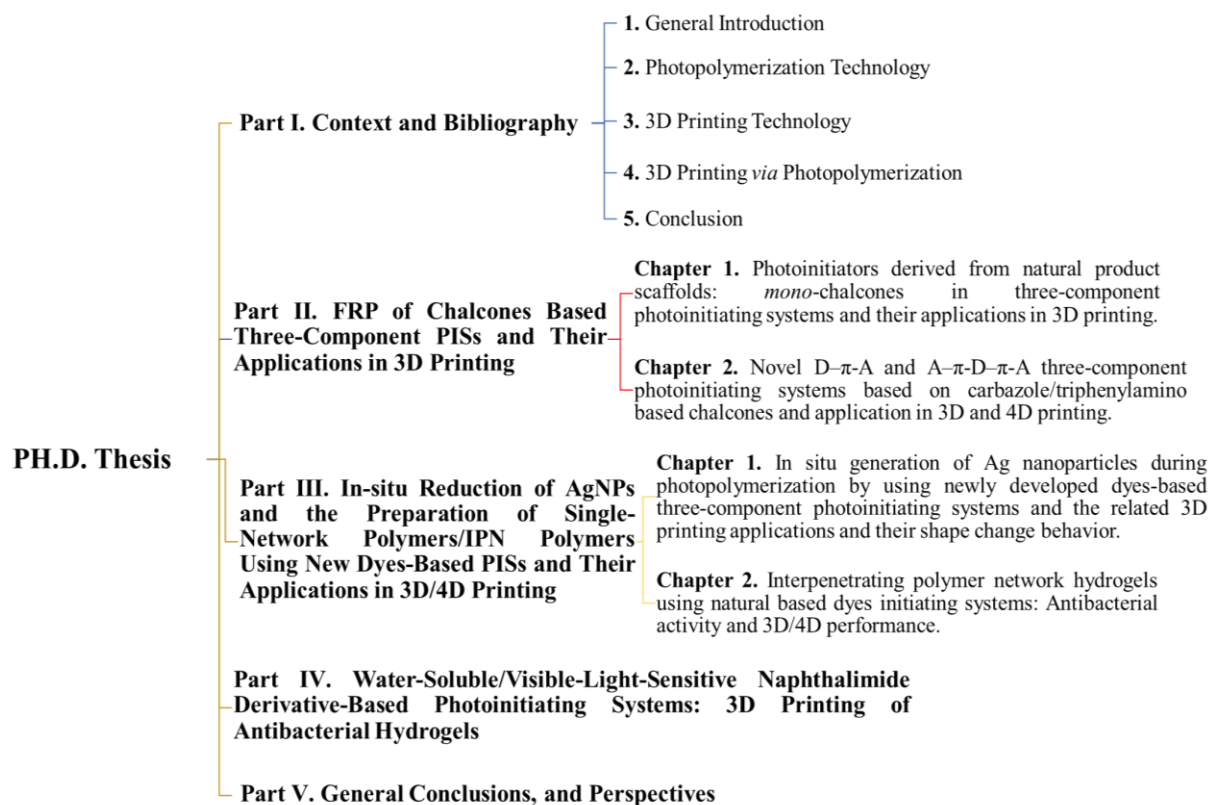
Parallel to the photoinitiation ability, another active research field is the shape memory effect of polymers. Thanks to their flexibility, biocompatibility and unlimited chemical modification possibilities, shape memory polymer (SMP) materials have clearly proven to be excellent alternatives for metal materials [17]. The shape-memory effect is not dependent on a specific material property of the single polymers; rather, it is the consequence of a subtle interplay between the polymer structure and morphology, as well as the applied processing and programming technologies. The programming and shape restoration process is shown in the following steps: First, the polymer is typically processed to obtain its permanent shape; then, the polymer is deformed and fixed the intended temporary shape under external stimuli (the process is called programming);

finally, withdrawing the stimulus used before or applying another stimulus will induce the shape-memory effect, allowing the recovery of the stored temporary shape can be observed [18]. The introduction of metal ions into the photopolymerization process is a third popular research area, where the morphology of metal nanoparticles (MNP) and the properties of nanocomposites can be adjusted to meet the needs of various applications ranging from imaging [19], radiation curing [20] and optical technologies to (bio)medicine [21], microelectronics [22] and materials science by coordinating the control of kinetics of two simultaneous processes, in situ photoreduction and photopolymerization process.

In this PH.D. thesis, combining several of the above topics (the synergistic progression of photoreduction and photopolymerization, synthesis of composite materials, and 4D printing shape-memory effect), several dye-based PIs with strong absorption properties in the visible region were prepared. When combined with iodonium salt (Iod) and amines (EDB/TEA/L-Arg), a highly efficient three-component PIS that is suitable for visible light and exhibits high polymerization efficiency was prepared. The interaction of PI and additives in PIS initiates the polymerization reaction via oxidation–reduction mechanisms (presented in reactions (r1)-(r5)), resulting in reactive radicals and cations under light irradiation [23,24].



The proposed PISs will greatly facilitate the contribution of photopolymerization to contemporary industrial processes like 3D printing technology. Furthermore, the antibacterial properties of the produced composite hydrogels including metal nanoparticles should assist to expand the applications of photopolymerization in biomedicine (regenerative medicine, photocurable dental composites, drug delivery, tissue engineering, etc.). The main contents of this thesis were indicated in **Scheme I-2:**



Scheme I-2. The plan of the thesis.

This work was funded by the China Scholarship Council (CSC:201906280059). and many of the new proposed photoinitiators was synthesized by our partner Dr. Frédéric Dumur from the Aix-Marseille Université.

2. Photopolymerization Technology.

The term photopolymerization (also known as photocuring technology) refers to the process of photoinitiated chain polymerization [25-28]. In a more general sense, it refers to the polymerization of monomers directly stimulated by light, as well as the polymerization caused by photosensitizers and PIs, which is also known as photosensitive polymerization. The technology, which utilizes electromagnetic radiation (or light) as an energy source for polymerize functional monomers, oligomers and polymers, serves as the foundation for important commercial processes with broad applicability, such as photoimaging and ultraviolet (UV) curing of coatings [2] and inks [3] etc. Photopolymerization was first observed in 1845, when Blyth and Hoffmann got a transparent glass-like product by exposing styrene monomer to sunshine [29].

Berthelot and Gaudecheon were the first to polymerize ethylene into a solid using UV radiation rather than sunlight [30]. Following that, Ostromislenshi began to investigate the phenomena of photopolymerization, demonstrating the chain reaction nature of vinyl polymerization and the high productivity of photopolymerization for the first time in 1912 [1]. In the 1960~1980s, photopolymerization was really introduced as a new type of green environmental protection technique. When compared to traditional thermal polymerization, photopolymerization has the advantages of environmental friendliness, no solvent volatilization, high productivity, wide adaptability, cheap cost, low energy consumption, and so on; consequently, it has become a research hot spot for polymeric materials.

The monomer constitutes a large portion of the photopolymerization system, which primarily refers to the incorporation of active functional groups or oligomers. It's mainly divided into three categories: polymers with unsaturated groups (acrylates, unsaturated polyesters, unsaturated polyvinyl alcohol derivatives, unsaturated polyamides and epoxy resins); compounds containing thiols and olefins (primarily for polymerization reactions) [31]; and saturated polymers, like halogenated polymers [32], sulfur-containing polymers [33] and some dyes. The selection of monomer is directly connected to the applications of the fabricated objects. It is mainly used to adjust the viscosity of the photosensitive formulations, but it also affects the polymerization rate of the entire photosensitive system as well as the physical and chemical characteristics of the polymer formed after deep-curing. In response to the requirements of green chemistry, the following principles should be followed when selecting monomers: a) low viscosity; b) fast curing; c) no organic solvents; d) can be cured at room temperature or low temperature; e) inexpensive and widely available.

PI/PIS is a key point of the photopolymerization system, although their proportion is small, generally in the 0.1 wt%-5 wt%, it plays a critical role in its photopolymerization speed. A PI is a substance that can absorb radiation energy, undergo photochemical modifications following excitation, and generate reactive intermediates (free radicals or cations) capable of initiating polymerization [8]. After

absorbing the energy of light radiation, the PIs rapidly transition from the molecular ground state (S_0) to the excited singlet state (S_1) through the π - π^* or n - π^* transition. The excited singlet state is extremely unstable and has a limited lifetime, it may either revert to the ground state by fluorescence emission (f) or relaxation (ic), or it can reach the excited triplet state (T_1) via inter-system crossing (isc). Through phosphorescence (phos) and intersystem crossing, molecules in the triplet state can then return to the ground state. After undergoing monomolecular or bimolecular chemical action, molecules in the excited state (singlet or triplet state) produce active fragments that can initiate chain polymerization, such as free radicals, cations, etc.; with the characteristics of condensation polymerization, also known as Photo-condensation. Figure I-1 depicts the photoinitiation process of PI schematically [34]. The PI must be chosen in accordance with the following criteria: a) has an appropriate absorption spectrum (matching the light source) and extinction coefficient; b) has a high quantum efficiency; c) has some thermal stability; d) is miscible with the reaction system; e) is non-toxic, odorless and does not yellow the reaction product

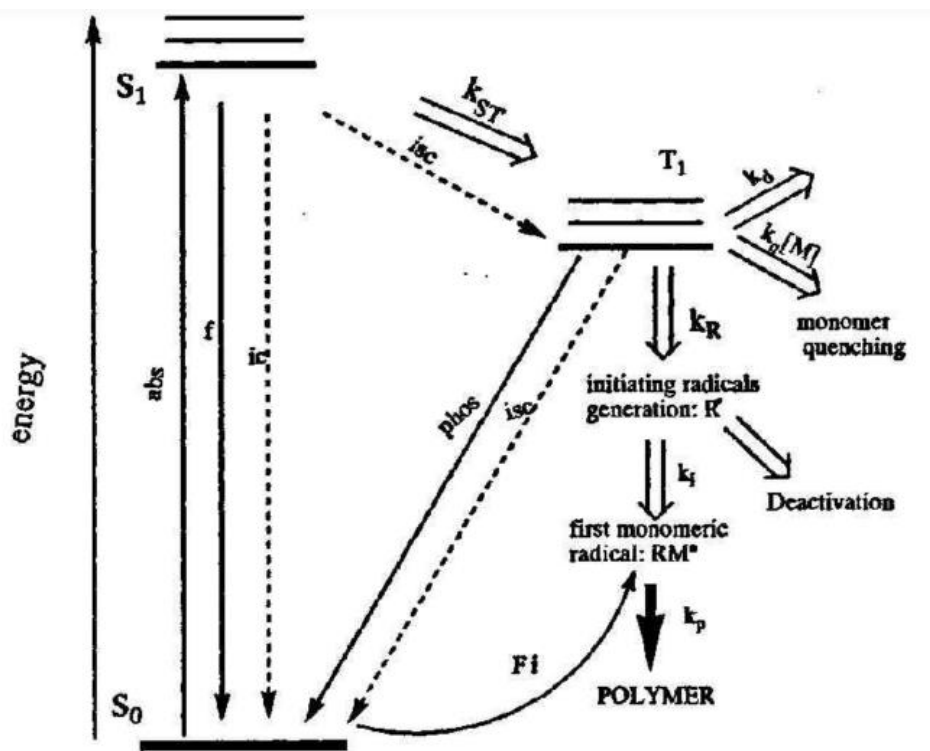
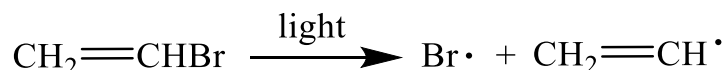


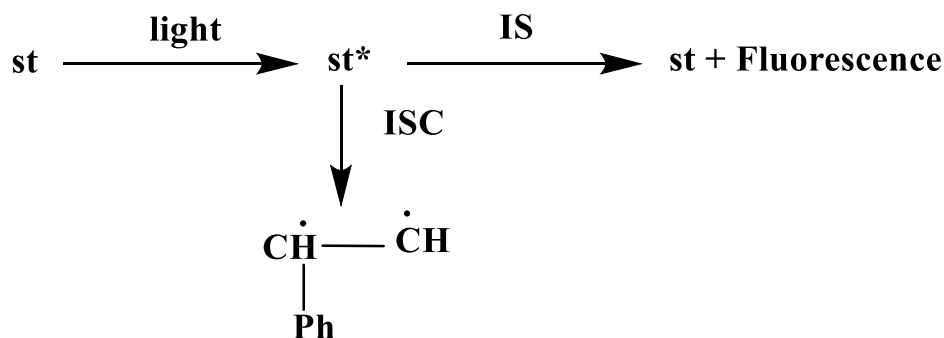
Figure I-1. The photoinitiation process of PI/PIS [34].

Based on the involved mechanism, photopolymerization can be divided into chain process polymerization reactions and non-chain process polymerization reactions. The basic mechanism of photopolymerization in the chain process is free radical polymerization (FRP), and there are different ways of photoinitiated FRP.

1) Polymerization is initiated by the reactive species generated by direct excitation of monomers or polymer molecules comprising chromophore- or carbonyl-containing polymer molecules by light. For example, Ostromislensky [1] produced poly(bromovinyls) in this manner and demonstrated that the efficiency of the photopolymerization process was significantly larger than that of an ordinary photochemical reaction.



2) photoactive molecules (PIs/photosensitizers) initiate photopolymerization, and the reactive center created by the cleavage of photoactive molecules or transfer energy to a monomer or to other molecules capable of generating substances that initiate photopolymerization. In this way, Blyth and Hoffmann created a transparent glass-like product out of styrene [15].



3) photo-excited complex molecules [mainly charge transfer complexes (CTC) generated by electron donor-acceptor interactions, which can greatly lower the energy required for charge separation] [35]. Polymerization is initiated by active species such as free radicals and ions produced by the dissociation of excited molecular complexes.



Kaya et al. synthesized and characterized a novel dual-chromophore sulfonium

salt PI with thioxanthone and benzoyl group, namely 2-isopropylthioxanthium benzoyl hexafluoroantimonate (ITXPhenS), which can form charge transfer complexes (CTCs) with the electron donor N, N-dimethylaniline (DMA) that exhibited absorption properties in the visible light range [36]. Furthermore, the CTC was shown to be capable of initiating radical and cationic polymerization of different monomers under visible and natural light. The hypothesized process involves the formation of radicals and ionic species within the CTC by hetero- and/or homo-cleavage of IXPhenS, followed by electron transfer events. Radical PIs are also well established see Section 4.3 below.

Non-chain photopolymerization is mostly a partial polymerization process that is sluggish and inefficient for quick photocuring systems. A photosensitizer with a molecular structure that comprise olefins, α , β -unsaturated ketones, α , β -unsaturated esters, diazoketides, azides, carbonyl azides, sulfone azides and diazo salts of the eight categories must be included in the non-chain photopolymerization system [27]. The photo crosslinking reaction has a long shelf life and particular photochemical criteria, such as excellent resolution, good dimensional stability, and strong resistance to etching performance of photoresists.

3. 3D Printing Technology.

3D printing technology is essentially a digital emerging manufacturing technology that is based on a three-dimensional computer design model. Using a software layered discrete and computer numerical control (CNC) molding system, metal powder [37], ceramic powder [38], plastic resin [39], cellular tissue [40] and other special materials were deposited and bonded layer-by-layer by using laser beams, hot melt nozzles and other methods and then superimposed to manufacture a solid product. As the machining process of this technology does not require molds, theoretically it is possible to manufacture components with approximately infinitely complex shapes. More importantly, 3D printing also liberates individuals from the limits of traditional processing methods, allowing them to create more novel, useful, and optimized products, bringing about advances in medical [41], consumer goods [42], and industrial [43]

aerospace [44], automotive [45], mold [46], and other industries. Aside from eliminating the time-consuming engineering of traditional processes that require multiple processing procedures, 3D printing technology also has high reproducibility and controllability, rapid manufacturing, personalized product line, easy modification of products at the design level, no space limitation, and convenient cost-effective manufacturing. It has altered the traditional assembly line manufacturing paradigm, reduced companies' need on manpower and production space, and had a significant and far-reaching impact on product processing methods.

3.1 Method.

prototypes for 3D printing may be traced back to the introduction of inkjet printers in 1976, but it wasn't until Charles Hull applied optical technology to rapid prototyping in 1984 that the curtain was formally raised on 3D printing [11]. After decades, 3D printing technology has continued to develop and improve, relying on top technologies in multidisciplinary fields such as information technology, precision mechanics, and materials science, and various applications in different industries have evolved to become one of the hottest frontier technologies today. Fused deposition modeling (FDM) is the most prevalent method of 3D printing that uses mostly polymer filaments (FDM). Furthermore, additive manufacturing of powders via selective laser sintering (SLS), selective laser melting (SLM), or liquid binding in three-dimensional printing (3DP), as well as inkjet printing (polyjet or multijet printing), contour crafting, stereolithography (SLA), direct energy deposition (DED), and laminated object manufacturing (LOM), are the primary methods of AM (see [Figure I-2](#), [9]). In the creation of composite items, each approach has advantages and limitations. The selection of manufacturing process is determined by the beginning material, the processing speed and resolution requirements, the final product cost and performance criteria (summarized in [Table I-1](#), see Page 17).

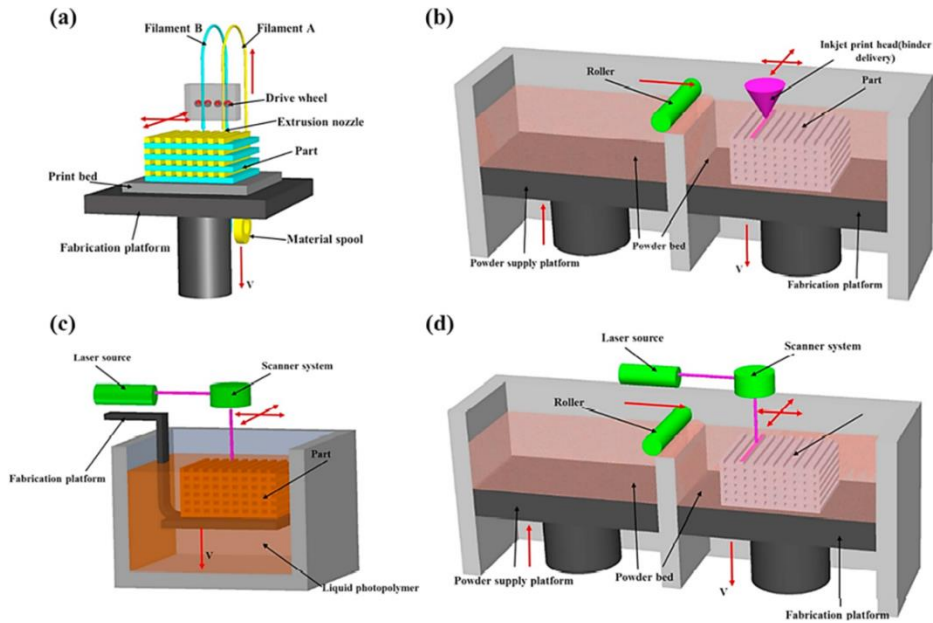


Figure I-2. Schematic diagrams of four primary methods of additive manufacturing: (a) fused deposition modeling; (b) inkjet printing; (c) stereolithography; and (d) powder bed fusion [9].

3.2 Materials.

The properties of 3D printable material, which is an important foundation of this technology, greatly influence the overall performance of the generated objects. So far, a variety of 3D printable materials have been established, including polymers, metals, ceramic materials, and so on [37-40]. According to a recent Wohlers analysis (Wohlers report 2021, [47]), the materials market for additive manufacturing will expand from \$1.916 billion in 2019 to \$2.105 billion in 2020. **Figure I-3** depicts the global 3D printing materials market structure.

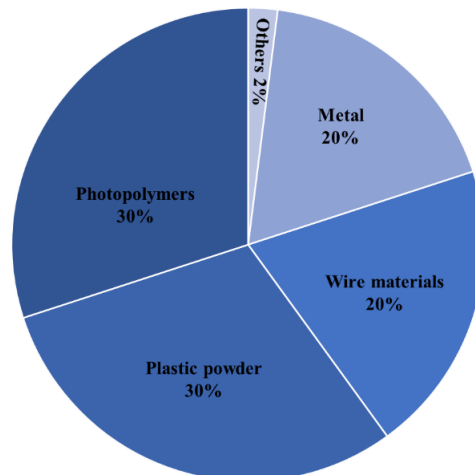


Figure I-3. The global 3D printing materials market structure [47].

Polymers are the most often utilized materials in the 3D printing industry due to their versatility and ease of usage in various 3D printing technique. Polymers for AM can be available in the form of thermoplastic filaments, reactive monomers, resin, or powder, with the most common types being photosensitive resins, thermoplastics, and hydrogels. Photosensitive resin, which is suitable for photocuring (SLA), was one of the first materials used in 3D printing. When exposed to a specific light source, polymerization processes can occur, resulting in curing. It has found widespread application in electronics production, holograms, adhesives, printing, medical, and other sectors [41-46]. One of the most frequent 3D printing materials is thermoplastic polymers. Such polymers have excellent processing qualities in general, and their mechanical properties, dimensional stability, etc. can be effectively improved after modification [48,49]. The term “Hydrogel” refers to a three-dimensional (3D) network structure formed by cross-linking hydrophilic polymer chains embedded in a water-rich environment, with broadly tunable physical and chemical properties [50]. It’s an ideal material for tissue engineering and has great potential in this field. The hydrogel formed by 3D printing technology can achieve not only intricate shapes, but also complex holes and even gradient structures, giving 3D printed hydrogels features not attainable through standard production processes. There are currently few commercially accessible hydrogel printing materials, and the majority of them are still in the laboratory development stage.

Metal additive manufacturing has shown promising growth prospects in recent years. Metal powder is the most widely used material and may be utilized in a range of 3D printing methods, including SLM, EBM, etc [37]. Concerning on the type of metal materials, it can be divided into iron-based alloys, titanium and titanium-based alloys, nickel-based alloys, cobalt-chromium alloys, aluminum alloys, copper alloys and precious metals [51]. Iron-based alloys were the first and most thoroughly explored class of 3D printing metal materials, and they are especially well suited for mold fabrication due to their low cost, high hardness, good toughness, and machinability [52].

Titanium and titanium alloys are ideal materials for medical instruments, chemical equipment, aerospace and sports equipment due to their remarkable high specific strength, good heat resistance, corrosion resistance, and biocompatibility [53]. Nickel-based alloys and Cobalt-based alloys are the high-temperature alloys, which widely applied in aerospace, petrochemical, marine, energy and other areas [54]. Aluminum alloys have a low specific gravity, excellent corrosion resistance, great fatigue resistance, and high specific strength and stiffness, making them an excellent lightweight material. Copper alloy has good thermal conductivity and can be used in the manufacture of mold inserts or rocket engine combustion chamber. Magnesium alloy is currently the lightest metal in practical applications, with good biocompatibility and degradability. Its Young's modulus is the closest to that of human bone and it can be used as a lightweight or implant materials. Precious metals such as gold, silver, platinum, and others are generally used to customize luxury items such as jewelry, and their applications are very limited.

Ceramic materials are among the oldest materials used by humans, still considered "new" in the field of 3D printing. This is due to the fact that most ceramic materials have a high or no melting point (e.g., SiC, Si₃N₄, [38, 55]), making them difficult to shape directly with external energy fields, and most of them require reprocessing after shaping (drying, sintering, etc.) to obtain the final product, limiting the promotion of 3D printing with ceramic material. It does, however, offer the advantages of high hardness, high temperature resistance, and stable physical and chemical properties that polymers and metal materials do not have, giving it a wide range of applications in aerospace, electronics, automotive, energy, biomedical, and other industries. Advanced ceramics are a class of high-performance ceramics that uses high-purity raw ingredients and can manipulate the chemical ratios and organizational structure intentionally.

The evolution of 3D printing materials has progressed from polymer materials, metal materials to ceramic materials. At present, new materials are still emerging in each field, reflecting the vitality of 3D printing technology. Despite the fact that the present category of 3D printing materials has covered the majority of the material

systems, the materials that can be successfully applied to 3D printing are merely a drop in the ocean when compared to the vast material system that exists today. In order to keep up with the future development trend of 3D printing structure and function integration, it is required to constantly innovate in 3D printing new materials, 3D printing new technologies, and 3D printing new equipment.

3.3 Applications.

3D printing is regarded as one of the key technologies driving a new round of technological revolution and economic change, with promising future prospects. Since the 1980s, the global additive manufacturing industry has grown to tens of billions of dollars, covering architecture, engineering construction (AEC), industrial design, automotive, aerospace, military, engineering, oral and pharmaceutical industry, biotechnology (human organ transplantation), fashion, footwear, jewelry, glasses, educational affairs, geographic information systems, diet and many other fields (according to Wohlers report 2021, [47]). **Figure I-4** is a compilation of the major applications about 3D printing according to the Wohlers Report 2019 [56].

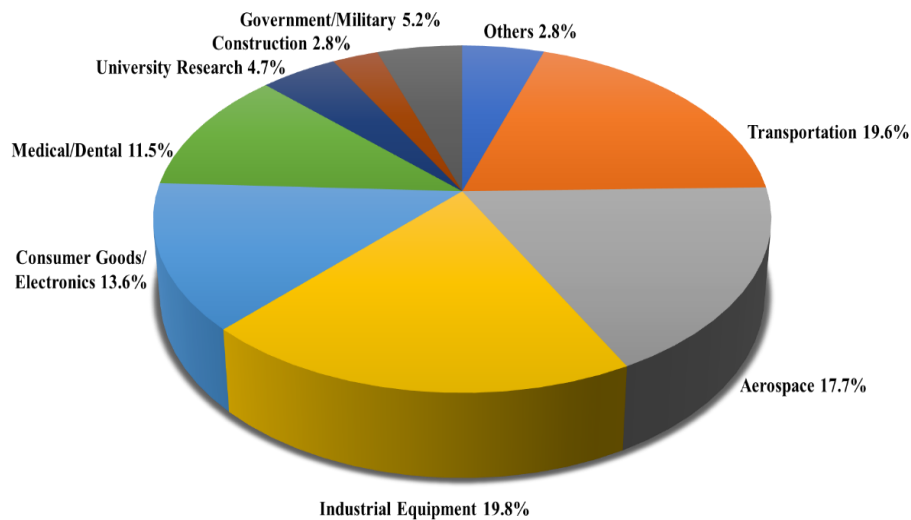


Figure I-4. The major applications of 3D printing from Wohlers Report 2019 [56].

As can be seen from the figure, the main applications of industrial-grade 3D printing in the world are concentrated in five major fields: transportation, aerospace, industrial equipment, consumers and electronics, and medical.

3.3.1 Medical materials.

Additive manufacturing technologies have been widely applied to medical materials, especially in the fields of tissue engineering, medical models, medical devices and pharmaceutical formulations (summarized in **Figure I-5**) [41]. The huge market for 3D printed medical and chemical applications is illuminated by a diversity of printing technologies and products. Tissue engineering using 3D printing is focused on two components, functional biomaterials for tissue implantation and tissue models for disease research. Furthermore, 3D printed tissue models play an important role in disease mechanism research, pharmacological testing of new drugs, preclinical therapy effectiveness, and anatomical investigations of complicated organs. For example, Organogenesis Inc (one of the world's most prominent suppliers of FDA-approved 3D printed medical devices) introduced GINTUITM, a tissue engineering product for oral soft tissue repair and regeneration in 2012 [57]. his colleagues used the PJP 3D printing technique to create artificial skin [58] that can considerably improve wound skin recovery. Wallacea et al. [59] used peptide-modified junctional cold gel mixed with brain cells as a bioprinting ink to print 3D brain models to help scientists better understand brain structure, advancing the study of neurological brain illnesses such as Alzheimer's and Parkinson's. Li et al. developed a 3D biological model of human lung cancer A549 cells on a framework made of serine protein and chitosan [60]. VanKoevering et al. demonstrated the first application of 3D printing in the treatment of difficult fetal craniofacial abnormalities and perinatal management.

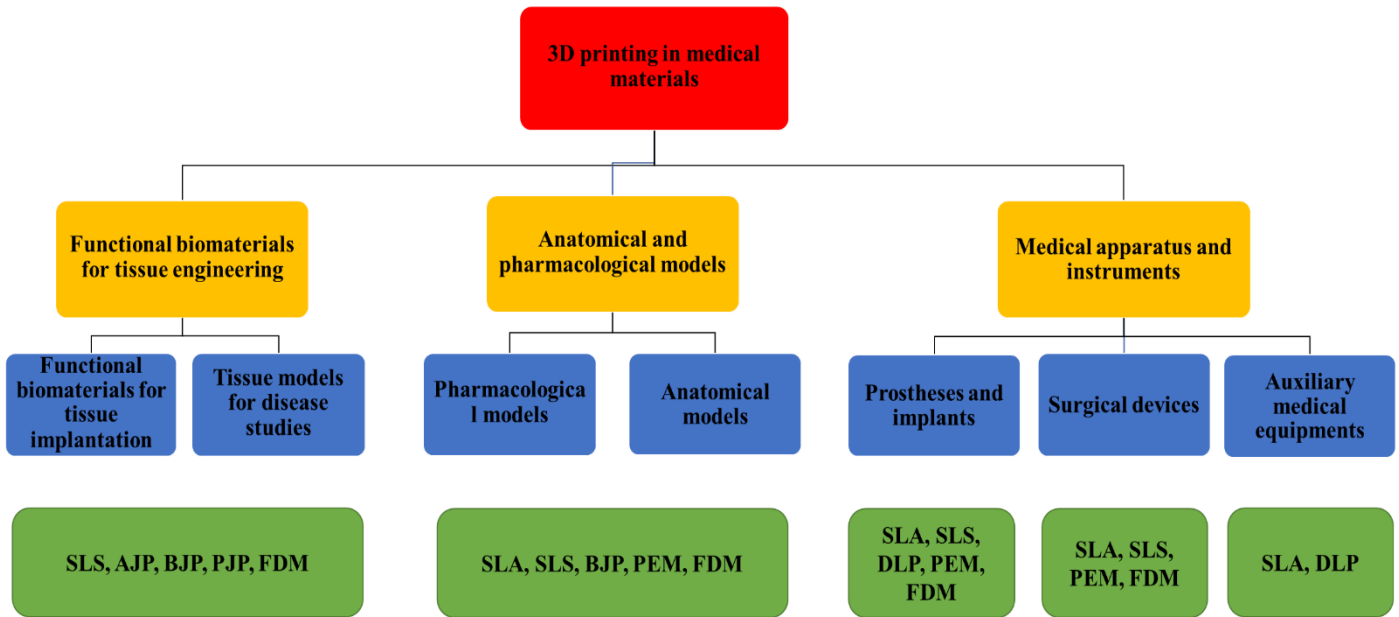


Figure I-5. The applications of 3D printing technology in medical materials [57].

3.3.2 Aerospace.

AM has had a tremendous impact on the aerospace sector since it offers numerous opportunities in terms of design, materials, and manufacturing methods. Functional items can be built in near-net shape in a short amount of time using AM, resulting in increased reliability and lower costs [44]. Furthermore, because AM allows for the creation of grid-structured components, it can lower the weight of the aircraft, improving fuel efficiency. Engineers can construct more complicated rocket propulsion systems for space applications that can carry larger payloads and even print parts for future space flights. The T25 sensor housing (Figure I-6a) from General Electric (GE) is one of the first 3D printed parts to be FAA-certified for installation on a commercial GE Leap jet engine [62]. "GKN Aerospace" developed the first advanced "Ariane 6 Nozzle (SWAN)" for the "Vulcan 2.1" engine (Figure I-6b) produced by "Airbus Safran Launchers" [63]. Arconic manufactures titanium fuselage and engine pylon components for the Airbus A350 XWB and A320 test versions, as well as NASA's SLS/Orion spacecraft vents [64].

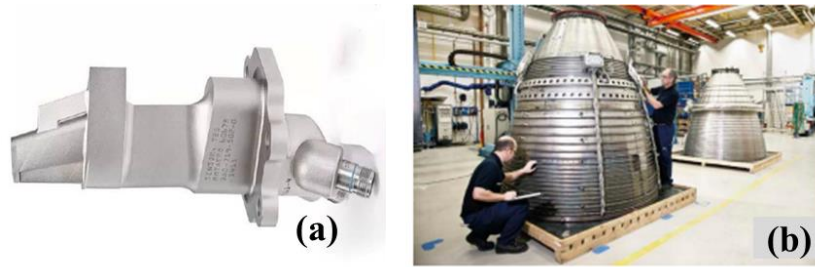


Figure I-6. The 3D printed (a) T25 sensor housing [62] (b) In the foreground, Vulcain 2 demonstration nozzle with more than 50 kg of DED material [63].

3.3.3 Transportation.

In this field, there are more market-oriented enterprises. In addition to being interested in the advantages of 3D printing manufacturing technology, they are also apprehensive about the expense. As a result, the use of 3D printing for exploration and development in the field of transportation is more than feasible. Of course, batch applications are affected by 3D printing's own cost and batch capacity limits. For example, the world's first 3D-printed miniature reinforced concrete pedestrian bridge (12 meters long, 1.75 meters wide, Martin 2017, [Figure I-7a](#), [65]) has been constructed in Madrid's Castilla-La Mancha City Park. The “Urbee”, jointly manufactured by the American engineering firm Kor Ecologic and Stratasys (producer of the 3D printer Stratasys), is the world's first car to utilize 3D printing technology (bodies and windows are 3D printed, as seen in [Figure I-7b](#), [66]).

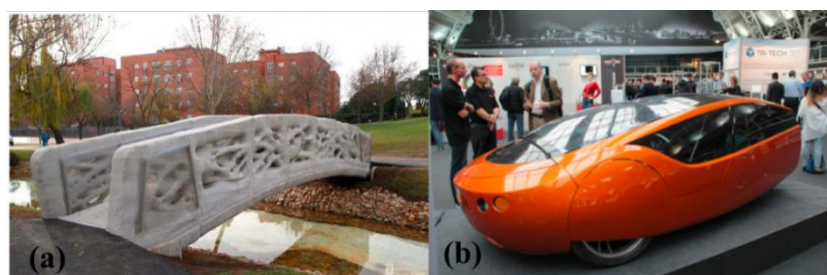


Figure I-7. The photos of (a) 3D-printed miniature reinforced concrete pedestrian bridge [65]; (b) the world's first car to use 3D printing technology – “Urbee” [66].

3.3.4 Industrial equipment and consumers/electronics.

In the field of industrial equipment, the core printing of injection molds, as well as the manufacture of parts on some non-standard equipment, and the application of auxiliary tooling in production lines, are frequently seen. In the sphere of consumer

goods, the customization potential of 3D printing are increasingly being exploited to give items more personalized features in order to attract different groups of people [42].

Printer Type	Methods	Materials	Applications	Benefits	Drawbacks	Reference
Extrusion	Fused Deposition Modeling (FDM) or Fused Filament Fabrication (FFF)	Continues filaments of termoplastics polymers; Continues reinforced polymers	Rapid prototyping, Toys, Advanced composite fibre-parts	Low cost, High speed, Simplicity	Weak mechanical properties, Limited (only thermo-plastics) materials, Layer-by-layer finish	[67]
	Automatic Grouting Ceramic Materials	Metal alloys, Cermets, Metal matrix composites, Ceramic matrix composites	Structural materials, Electronic materials, Photonic crystals, Biological materials.	Low cost, Environmentally friendly, Structural complexity	High material requirements (high solids content), Complicated process	[68]
Metal Wire Type	Electron Beam Free Forming Fabrication (EBF3)	Almost all metal alloys	Aerospace, Repair, Retrofitting, Cladding	Automatic forming and welding, Easy to operate, Shape controllable	High cost, Limited materials	[69]
Granular	Direct Metal Laser Sintering (DMLS)	Almost all metal alloys	Aerospace, Automotive, Medical individual parts manufacturing, Small injection molds and inserts	High precision, Very few molding restrictions, Small batches, Personalized complex Parts for processing	The overall technical difficulty is relatively high, Expensive, Limited applications,	[70]
	Electron Beam Melting (EBM)	Almost all metal alloys including titanium alloys	Electronics, Rapid Prototyping, Rapid Manufacturing, Tooling, Biomedical	High speed, High strength, Shape complexity	High cost, Produces X-rays	[71]
	Selective Laser Melting (SLM) / Selective Laser Sintering (SLS)	Titanium alloys, Cobalt chromium alloys, Stainless steel, Thermoplastics, Metal powders, Ceramic powders	Biomedical, Electronics, Aerospace, Lightweight structures, Heat exchangers	Fine resolution, High quality	Slow printing, Expensive, High porosity in the binder	[72]
	Selective thermal sintering (SHS)	Thermoplastic powder	Biomedical, Heat exchangers	Fine resolution, High quality	Slow printing, Expensive, High porosity in the binder	[73]
Powder Inkjet Needle Type	Gypsum 3D Printing (PP)	Gypsum	Biomedical, Building	Fast forming speed, Personalized design, Full-color printing	Limited materials, Low accuracy, Low surface quality	[74]
Laminated	Laminated Object Manufacturing (LOM)	Paper, Metal -filled tapes, Polymer composites, Ceramics, Metal rolls	Paper manufacturing, Foundry industries, Electronics, Smart structures	Reduced tooling and manufacturing time, A vast range of materials, Excellent for Manufacturing of large structures	Low surface quality and dimensional accuracy, Limitation in manufacturing of complex shapes	[75]
Photopolymerizable	Stereolithography (SLA)	A resin with photo-active monomers (Epoxy Resin, Acrylic)	Biomaterials, Prototyping	Fine resolution, High quality	Limited materials, Slow printing, Expensive	[76,77]
	Digital Light Processing (DLP)	A resin with photo-active monomers	Biomaterials, Prototyping	High precision, Fast speed, High quality, Great resolution	Need a support structures, Inferior physical properties, Low work temperature	[76,78]
	Continuous digital light processing/ continuous liquid interface production (CDLP/CLIP)	A resin with photo-active monomers	Biomaterials, Prototyping	High precision, Fast speed, Excellent resolution, High quality	Limited materials, Expensive	[76,79]
	Photopolymer jetting (Polyjet)	A resin with photo-active monomers	Biomaterials, Prototyping	High printing quality and precision, fast printing speed, wide use.	Requires support structure, relatively high cost of consumables, low strength of molded parts.	[80]

Table I-1. A summary of main materials, main applications, benefits and limitations of the primary technologies for additive manufacturing.

4. 3D Printing *via* Photopolymerization.

Photo-curing was the first 3D printing technology (1984), and it is also the most advanced 3D printing method today. The basic principle of this technology is to use the additive molding of materials to divide the shape of a 3D target object into several planar layers and scan the liquid photosensitive resin with a beam of a specific wavelength (depending on the PISs) so that each layer of the liquid photosensitive resin is deep-cured, while the area not exposed to light beam remains liquid state. Each layer is stacked to form the desired target items, and the material utilization rate can be achieved to 100% [76]. The photopolymerization-based 3D printing technique demonstrated the benefits of both the photopolymerization process and 3D printing technology. Moreover, this technology also offers spatial and temporal controllability, which opens up more possibilities and potential for its development and applications. The fabrication speed is still an issue that can be resolved by developing an efficient initiating system.

4.1 Method.

3D printing via photopolymerization includes four technological routes [76]: the first is stereolithography (SLA), which uses a laser as the light source; the second is the development of digital light processing (DLP) technology based on digital projector; the third is continuous digital light processing/continuous liquid interface production (CDLP/CLIP) technology induced by light emitting diodes (LEDs) and oxygen; and fourth, one of the most advanced technologies, photopolymer jetting (Polyjet).

4.1.1 Stereolithography (SLA).

SLA is the first marketed 3D printing method, and it primarily employs UV laser beams to cure liquid photosensitive resins quickly. In 1988, "3D System" marketed the world's first SLA 3D printer, the SLA 250, which was based on the idea of SLA molding technology. [Figure I-8a](#) [76] depicts a typical SLA printer and its components. The tank

is first filled with liquid photosensitive resin, and then the worktable is immersed in the resin. The focused laser beam scans the required path under computer control, curing the resin in the scanned area to produce a two-dimensional (2D) resin sheet; finally, the worktable is raised and lowered in the Oz direction, and the 3D model is cured and superimposed layer by layer until the 3D model is complete. The accuracy of SLA is proportional to the diameter of the laser beam at the curing point, i.e. the spot size. With the advantages of fast processing speed, high accuracy, good surface quality, and mature technology, SLA is widely used in aerospace, automotive, consumer goods, electrical appliances, and medical fields for design concepts, single-piece small batch precision casting, and product models and molds.

4.1.2 Digital light processing (DLP).

DLP is a rapid prototyping technology that differs from SLA notably in the curing method, which substitutes a digital light projector for the mirror that reflects the laser source. DLP first digitally processes the image signal, and then projects the light to cure the liquid polymer layer by layer until the final model is completed. In comparison to SLA technology's point-to-line and then line-to-surface forming processes, DLP forms layer by layer, allowing it to print quicker than SLA printers. The accuracy of a DLP printer is primarily determined by the projector's resolution. **Figure I-8b** [76] depicts a typical DLP machine and its components.

4.1.3 Continuous digital light processing/continuous liquid interface production (CDLP/CLIP).

CDLP/CLIP technology is an advancement of DLP technology [76]. Unlike SLA and DLP technologies, CDLP/CLIP uses digital projection with specific LED and an oxygen-permeable window (similar to contact lenses). This oxygen-permeable window forms a “dead zone” as thin as 10 μm , allowing liquid resin to flow between the printed component interface and the window. Within the “dead zone”, oxygen inhibits resin from deep-curing near the window, allowing a continuous flow of liquid beneath the printed object. Above the “dead zone”, polymerization is initiated by the LED. This uncured resin flow improves the printed part's resolution and lowers the likelihood of

print failure owing to peeling pressures. The components of a typical CDLP/CLIP machine. A typical CDLP/CLIP machine and its components are shown in [Figure I-8c](#) below.

4.1.4 Photopolymer jetting (Polyjet).

Polyjet, one of the most advanced technologies in 3D printing technology, is similarly based on the principle of curing photosensitive polymers upon irradiation with UV light. The photopolymer material is injected onto the platform layer by layer through a nozzle during the printing process, and each layer is immediately deep-cured under UV irradiation, yielding a fully cured 3D object by printing and stacking layer by layer [80]. Polyjet, as a material-jet 3D printing technology, can handle higher viscosity photosensitive polymers, and its precision is mostly determined by the size of its nozzle. More crucially, by adding a print head, multi-material printing can be easily conducted, enabling it to be utilized to print more integrated sensors and actuators with components composed of different photosensitive polymers. PolyJet technology is also a powerful AM method that produces smooth, exact prototypes, parts and tools (a typical Polyjet machine and its components are seen in [Figure I-8d](#) below.). Layer resolutions of up to 16 μm and accuracies of up to 0.1 mm enable the fabrication of thin-walled and complicated geometries from a diverse variety of materials.

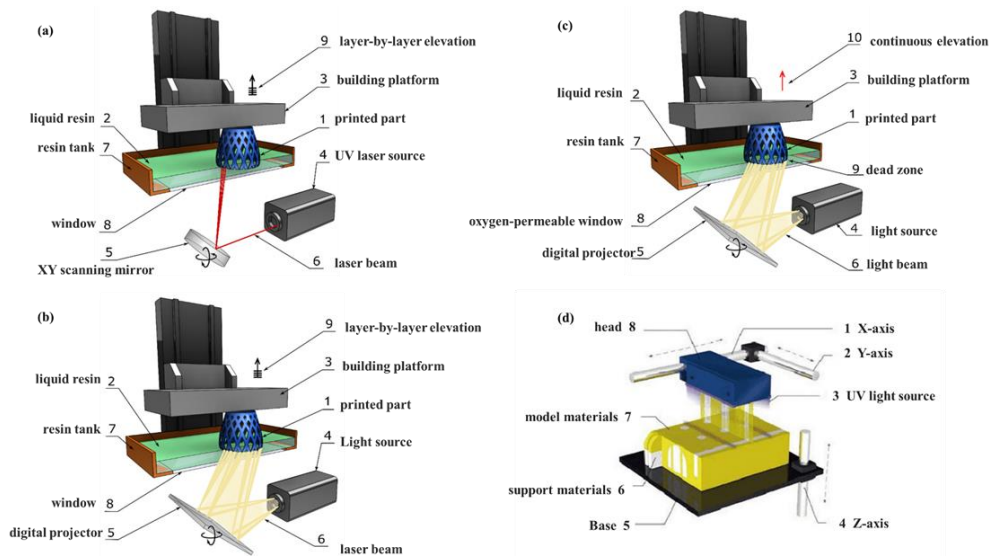


Figure I-8. Components of a typical (a) SLA machine; (b) DLP machine; (c) CDLP/CLIP machine [76]; (d) Polyjet machine [80].

4.2 Light sources.

Continuous lamps (xenon, mercury arc, Xe-Hg, doped mercury, microwave), pulsed light sources, laser sources (e.g. laser diode arrays), etc. are commonly employed in photochemistry. Furthermore, sunshine is regarded as an enthralling light source, and domestic lamps may be appropriate for specific purposes under gentle irradiation setting. LED is a relatively new light source; following decades of rapid growth, it was successfully popularized in the late twentieth century. Commercially available LEDs have a nominal intensity of about 10-100 mW/cm² and a luminous effectiveness of roughly 60 lm/W LEDs can create light more efficiently and precisely in the emitted wavelength range without requiring expensive or specialist equipment. Moreover, many inherent advantages such as low energy consumption, no ozone release, low heat, low price, less maintenance, long life, low operating temperature, etc.; making it an ideal choice for photopolymerization (see [Figure I-9](#), [14, 81]). Compared to other types of light sources, LEDs have a narrow emission range, typically 20-30 nm in spectral line width, leading in a conspicuous absorption spectrum for PI. As a result, LEDs are currently the most appealing choices for green 3D printing via photopolymerization.

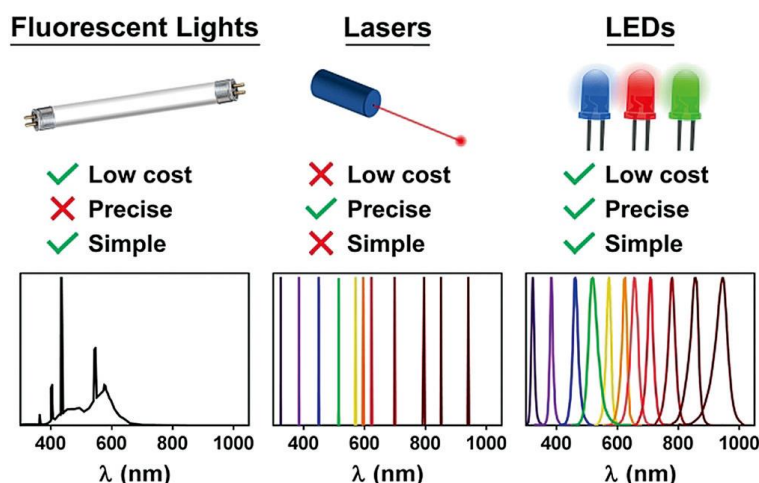


Figure I-9. Light sources used for photochemistry [81].

4.3 Photoinitiators / Photoinitiation systems (PIs/PISs).

The PI is mainly responsible for converting photolytic energy into active substances during photopolymerization based AM, and the generated active substances initiate deep-curing of monomers/oligomers. Since the PIs directly dictates the speed

of photocuring process and also affects the physical and mechanical properties of the printed item, it plays a key role in the entire photopolymerization based AM process. PIs are classified into three categories based on the sort of active material formed: free radical PIs, cationic PIs, and anionic PIs. In comparison to cationic and anionic PIs, free radical PIs have the benefits of rapid initiation, a large diversity, and low cost, making them the most extensively utilized kind in photopolymerization-based 3D printing. The mechanism by which PIs create free radicals vary depending on their structure and can be classified into two types, cleavage type (Type I) and hydrogen capture type (Type II), based on the distinct mechanisms of free radical generation.

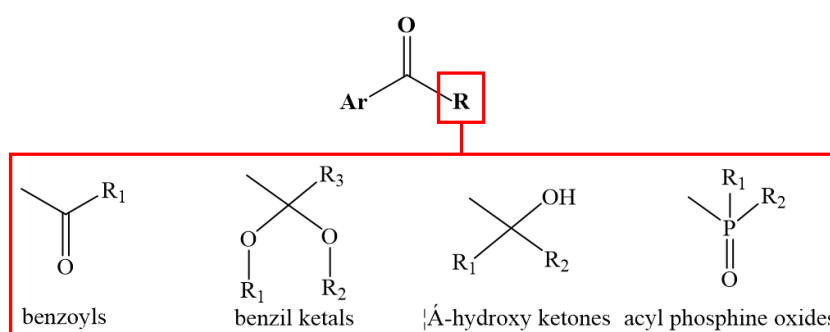
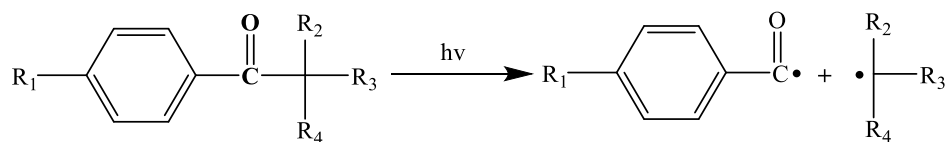


Figure I-10. Chemical structures of partially cleavable PIs [82].

The majority of cleavage PIs contain aromatic alkyl ketone structures, such as benzoyl and its derivatives, acyl phosphine oxides, α -hydroxy ketones and their derivatives, etc. (as shown in the [Figure I-10](#), [82]). After absorbing light energy, there is a transition from the ground state to the excited singlet state, followed by a transition to the excited triplet state (T1) via inter-system crossing (isc). The molecules in the excited state undergo homogenous cleavage of chemical bonds to form active free radicals, hence initiating polymerization reaction of unsaturated groups in monomers/prepolymers. The cleavage mechanism is shown as below.:



Hydrogen abstraction PIs (Type II) cannot generate reactive radicals on its alone and must be combined with other co-initiators to form a multi-component PIS. Such initiators are generally aromatic ketone compounds, with co-initiators primarily

consisting of tertiary amines, silanes, etc. Some of the hydrogen abstraction PIs are depicted in **Figure I-11**.

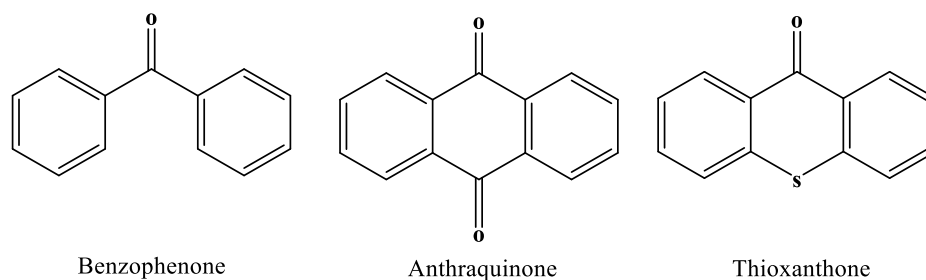


Figure I-11. Chemical structures of partially hydrogen abstraction PIs [82].

As shown in **Figure I-12**, the two-component PIS of benzophenone and triethylamine are used as an example to illustrate the mechanism of generating active radicals: after being irradiated by a specific wavelength of light source, the benzophenone transitions from the ground state to the excited state and interacts with the lone pair electrons of the N on triethylamine to transfer electrons from the amine to the benzophenone to form an excited complex, and then the proton at the α -position of N is transferred to generate two free radicals [83].

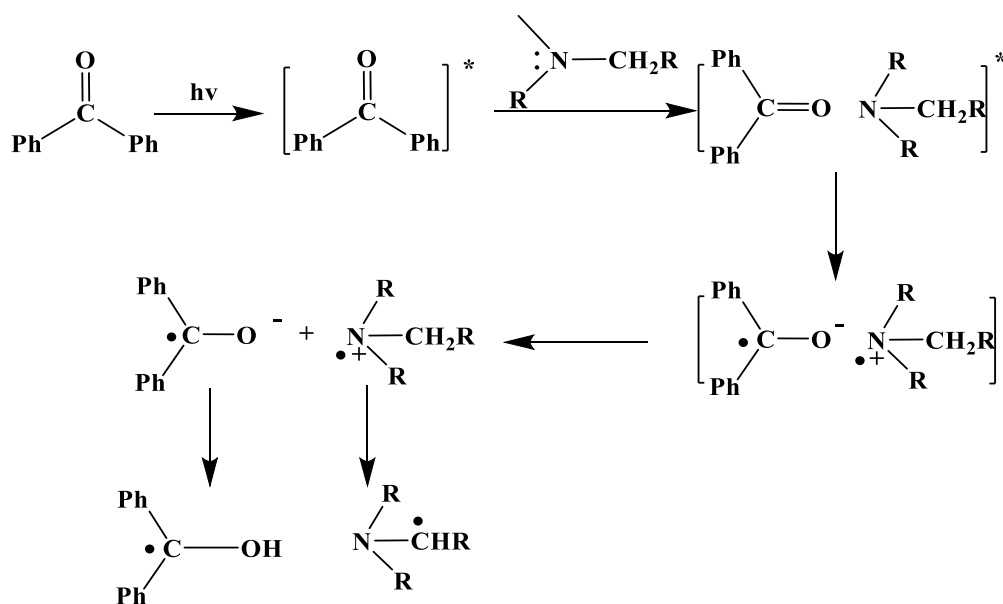


Figure I-12. The mechanism of the two-component PIS of benzophenone and tertiary amine to generate active radicals [83].

4.3.1 Visible light-sensitive PIs for 3D printing.

Polymerization under visible light irradiation has attracted the curiosity of many

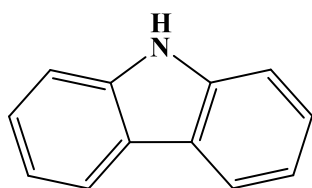
researchers in recent years [84,85]. The use of visible light with wavelengths higher than 400 nm avoids the constraints imposed by high-energy UV irradiation and lowers the risk of skin and eye damage. With the rapid development of light-emitting diodes (LEDs), visible light LED is more environmentally friendly, emits less ozone, has low thermal impacts, and has a longer lifetime than UV light. Furthermore, the wavelength of UV radiation is short, and the depth it can penetrate is limited, making deep curing difficult. As the wavelength of the light source increases, the penetration depth is greater, and the curing of thick filled materials becomes more favorable. Moreover, light with longer wavelengths is also more-friendly to living cells and is better suited for biomedical applications and dentistry, etc [85]. Improving the absorption of PIs in the visible region or red-shifting their absorption bands is mainly accomplished by enlarging the conjugated structure within the molecule or introducing push-pull electron groups. Due to the low photon energy of visible light, the energy provided by it is difficult to achieve the homogeneous cleavage of chemical bonds, therefore this direction concentrates primarily on the development of hydrogen abstraction PIs, particularly multi-component PIS, and there are few reports on cleavage PIs.

4.3.1.1 Dyes-based PIs for 3D printing.

Carbazole is a polycyclic aromatic hydrocarbon that is made up of a nitrogen-containing five-membered heterocyclic ring fused with a benzene ring on each side, as indicated in Table I-2. Due to the involvement of the N atom in the five-membered ring, carbazole possesses an excellent rigid planar structure with electron-rich characteristics, extending the electron ionization range from a single benzene ring to the entire rigid plane. This allows the carbazole to be linked to the electron-pulling structure, resulting in a "push-pull" dye with increased absorption in the visible region. Hu and co-workers synthesized a series of symmetric bifunctional PIs (Table I-2, [86]), each of which contained an oxime ester moiety as a potential starting functional group and a conjugated carbazole as a chromophore. The conjugated carbazole-based oxime esters exhibited a broad absorbance band from 250 to 400 nm, as well as noteworthy photobleaching properties during photolysis. With the irradiation of LED@405 nm, the

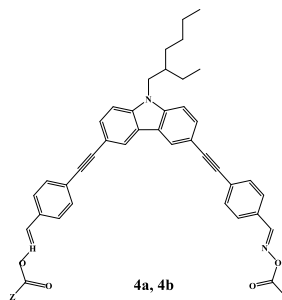
initiation efficiency of the novel PI was comparable to that of the commercial visible light PI TPO. A vertical resolution of 50 μm was achieved when adopting oxime esters as PIs in the DLP 3D printing process to fabricate precision objects. The A- π -D- π -A core structure endows the oxime ester enough two-photon cross-section (102-136 GM) to build intricate 3D microstructures with nanoscale spatial resolution utilizing two-photon 3D printing techniques. In addition, the thermal stability of PI (>160 $^{\circ}\text{C}$) is sufficient for daily storage. Qiu et al [87] developed a visible light sensitive PI DCCA with an oxime acrylate structure (see [Table I-2](#)). Its maximum linear absorption was appeared in the visible region (400-480 nm), which has a good overlap with the emission spectrum of conventional blue light sources and may efficiency initiate acrylate polymerization with the irradiation of LED@450 nm. Printing 3D items with complex geometric elements with great resolution and precision demonstrates the applicability of DCCA in 3D printing. Furthermore, Liu et al. [88] from our group conducted a study in this area and generated eight new carbazole derivatives by introducing different substituents (benzoyl, acetyl, styryl) on the carbazole scaffold (see [Table I-2](#)). Interestingly, the benzoyl substituent attached to the carbazole group can form the benzophenone moiety, constituting a one-component Type II benzophenone-carbazole PI. The synergistic interaction of the benzophenone moiety and the amine in the carbazole moiety can generate free radical, which can initiate the FRP of acrylates (one-component Type II PI behavior). Furthermore, quick polymerization rates and high functional conversion of acrylates were observed when amines and/or iodonium salts were added to the system. In addition, the benzophenone-carbazole PI demonstrated good cationic photopolymerization (CP) efficiency upon expose to LED@405 nm in the presence of iodonium salts. In the presence of both Iod and amines, 3D patterns were successfully obtained by direct laser write experiments using this proposed benzophenone-carbazole PI.

Photoinitiators	Absorption wavelength (nm)	Photoinitiators	Absorption wavelength (nm)
-----------------	----------------------------	-----------------	----------------------------



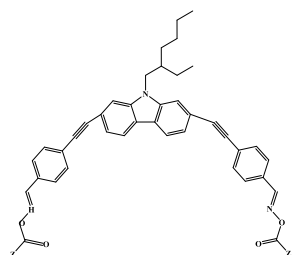
Carbazole

[86]



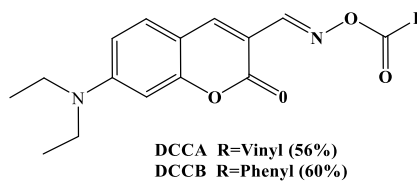
4a, 4b

250~500
[86]



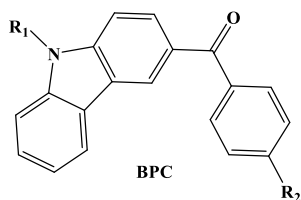
4c, 4d

250~500
[86]



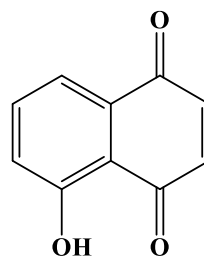
DCCA R=Vinyl (56%)
DCCB R=Phenyl (60%)

250~500
[87]



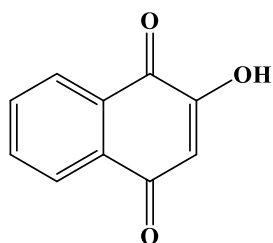
BPC

310~400
[88]



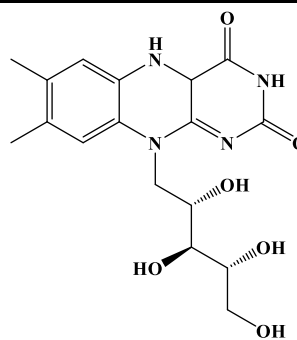
5HNQ

250~500
[89]



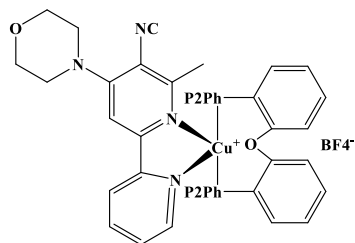
2HNQ

300~430
[89]



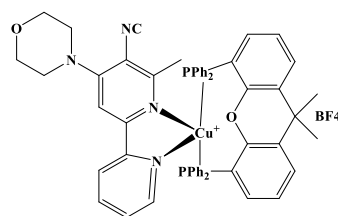
MWCNTs

300~430
[90]



Cu 1

370-510
[93]



Cu 2

370-510
[93]

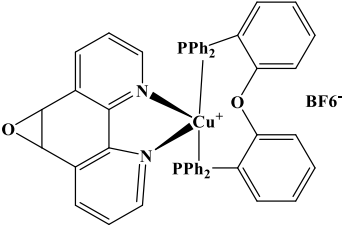
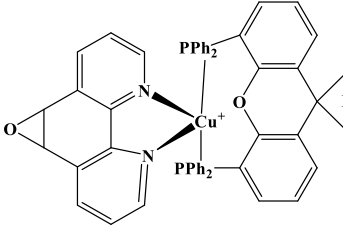
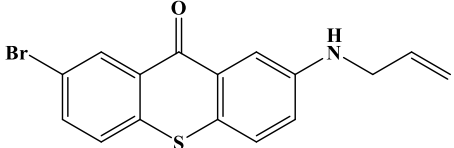
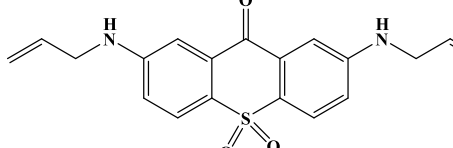
 <p>Cu 3</p>	350-480 [93]	 <p>Cu 4</p>	300-430 [93]
 <p>TX 1</p>	350~500 [94]	 <p>TX 2</p>	350~530 [94]

Table I-2. The Developed visible-light-sensitive PIs for 3D printing.

Recently, two naphthoquinone derivatives have emerged as effective visible light sensitive PIs (see [Table I-2](#), [89]). Specifically, two naphthoquinone derivatives, namely 5-hydroxy-1,4-naphthoquinone (5HNQ) and 2-hydroxy-1,4-naphthoquinone (2HNQ), were combined with different additives such as diphenyl iodonium hexafluorophosphate (Iod), N-vinylcarbazole (NVK), benzoyl bromide (R-Br), N-phenylglycine (NPG), and ethyl 4-dimethylaminobenzoate (EDB) as PIS for the FRP of trimethylolpropane triacrylate (TMPTA) and the CP of triethylene glycol divinyl ether (DVE-3). Since, the maximum absorption of 5HNQ appeared in the visible region (blue light), it has the potential to perform under blue LED light irradiation, and the 5HNQ/Iod/EDB based three-component PIS can be used to print a triglyceride diacrylate/trimethylolpropane triacrylate mixture under air using a ProJet printer.

Moreover, Gallastegui et al. [90] presented a novel visible light sensitive PIS for FRP of acrylic monomers based on riboflavin (Rf), triethanolamine, and multiwalled carbon nanobutes (MWCNTs) (see [Table I-2](#)). The new PIS can manufacture 3D printed items based on conductive polyacrylamide/CNT nanocomposites in minutes using a LCD 3D printer, paving the possibility for conductive nanocomposites to be 3D printed in new ways.

4.3.1.2 Organometallic PIs for 3D printing.

Although PIs with organic structures are commonly used in industrial photocuring

applications, organometallic PIs (photoredox catalysts) have been widely utilized in laboratory investigation. These metal complexes exhibit good photochemical properties, such as strong visible light absorption, relatively long-lived excited states, and appropriate redox potentials [91]. These compounds can act as photo-redox catalysts (*via* oxidation or reduction cycles) [15, 23, 92] to generate active substances that drive various photopolymerization systems such as photo-initiated atom transfer-radical polymerization (ATRP), photo-induced RAFT, and others. The use of photo-redox catalysts has also been explored in 3D photocuring applications. Borjigin et al. [93] synthesized four copper complexes (Cu1, Cu2, Cu3, and Cu4, see [Table I-2](#)) as three-component PISs with iodonium salts and amines for the rapid and effective initiation of FRP of TMPTA and CP of EPOX monomers upon irradiation with LED@405 nm. Finally, Cu1/Iod/EDB based three-component PIS were used to prepared a smooth and regular 3D objects of interpenetrating polymer networks (IPNs) from a mixture of these two monomers by direct laser write experiments.

4.3.1.3 Modification of UV PIs.

Aside from the previously mentioned development of new dye-based and metal complex-based visible light sensitive PI, another strategy is to modify commercial UV sensitive PI to increase their absorption in the visible range or red-shift their absorption band. For example, Breloy et al. [94] modified thioxanthone, thioxanthone, which was originally utilized as a near-UV PI, to produce monoamine or diamine-substituted thioxanthone derivatives, as displayed in [Table I-2](#), TX₁ and TX₂. The presence of amine groups enables TX₁₋₂ to initiate FRP by intermolecular electron/proton transfer under visible light and can also act as an electron donor to iengage with (MePh)₂I⁺, or the electron donor interacts with MDEA, resulting in increased initiation efficiency. In addition, these thioxanthone derivatives can also be used in the thiol-ene click reaction. Furthermore, the IPN derived from TX₂ can sustain the multiplication of living cells, showing that TX₂ is practically non-biotoxic, making it attractive for use in food packaging and biomedical coatings.

4.3.2 Water soluble PIs for 3D printing.

Water is used as a diluent for photopolymerization systems as it is colorless, tasteless, non-toxic, non-irritating, almost costless, non-flammable, and non-explosive, and it eliminates the problem of volatile compound emissions associated with the use of reactive monomers or organic solvents as diluents. With the improvement of national requirements for environmental protection, the attention of water-based photopolymerization technology has gradually increased, and the application fields have been extended to food packaging and biomedical fields [41,95]. Additionally, aqueous photopolymerization systems contain less oxygen concentration than oil-based photopolymerization systems, reducing the inhibitory effect of oxygen on FRP [96]. Consequently, the design and synthesis of aqueous PIs has emerged as a new frontier in PIs research.

2-Hydroxy-1-[4-(2-hydroxyethoxy) phenyl]-2-methyl-1-propanone (I2959, **Figure I-13**) is a well-known biocompatible water-soluble PI. It has little toxicity and frequently utilized in the manufacture of biomaterials [97]. Later, lithium phenyl-2,4,6-trimethylbenzoylphosphonate (LAP, **Figure I-13**) was presented as a water-soluble PI with around a 10-fold improvement in solubility over I2959, which has good biocompatibility and high reaction performance [98]. Recently, TPO (see in **Figure I-13**), an efficient commercial PI for non-aqueous systems, was reported to be converted into water-dispersible nanoparticles, enabling rapid 3D printing of complex hydrogels. Specifically, n-butyl acetate, SDS (as a surfactant), isopropanol (as a co-solvent), and PVP (as a crystallization inhibitor) were mixed to create an organic phase, in which TPO was dissolved, resulting in an oil-in-water microemulsion containing TPO. The microemulsions were then spray dried to form water-dispersible TPO nanoparticles, which were very efficient for the photopolymerization of acrylamide/ethoxylated trimethylolpropane triacrylate aqueous formulations (38.5 wt% acrylamide and 8.9 wt% ethoxylated trimethylolpropane triacrylate) and enabled the printing of stable wood pile structured hydrogels using a Freeform Plus 3D printer [99]. **However, the I2959 and TPO mentioned above are only suitable for UV light sources and are slightly harmful to living cells, restricting their utility in biological applications involving living cells.**

Only the LAP is sensitive to visible light that also exhibited excellent water solubility.

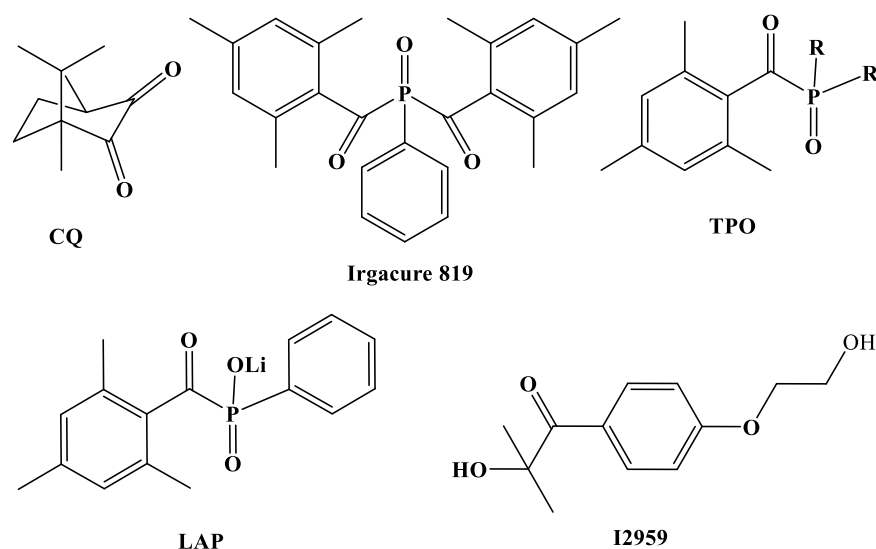


Figure I-13. Commercial visible-light-sensitive PI and water-soluble PI for 3D printing [97-99].

Recently, Wang et al. [78] proposed a facile but adaptable approach for preparing highly water-soluble and biocompatible PIs for 3D printing of high-resolution hydrogel structures using digital light processing (DLP). A simple and efficient one-pot approach was used to synthesis metallo-phenyl (2,4,6-trimethylbenzoyl) hypophosphonate (M-TMPP)-based PI with great water solubility (up to 50 g/L) and outstanding biocompatibility, matching the conditions for biomedical applications (see [Figure I-14a](#)). Furthermore, they used M-TMPP for 3D printing to produce 3D forms with high water content (80 wt%), high resolution ($\sim 7 \mu\text{m}$), high deformability (over 80% compression), and complex geometry. Due to their quick mechanical response and good stability under cyclic stress, printed hydrogel structures have a lot of potential in flexible electronic sensors.

Le et al. [100] synthesized a novel type I diphenyl-phosphine oxide PI containing a 2,6-dimethyl-4-dimethylaminobenzoyl group (see [Figure I-14b](#)). The presence of tertiary amino groups at the para-position of the benzoyl group increases absorption in the visible range and is easily converted to water-soluble derivatives after subsequent protonation or quaternization process. A water-soluble mono-acylphosphine oxide molecule with the quaternary ammonium group $\text{N}(\text{CH}_3)^3\text{OTf}^-$ is formed via

quaternization with methyl trifluoromethanesulfonate (MeOTf). This PI has high water solubility, high stability, near-UV range absorbance, low cytotoxicity, efficient α -cleavage, and its polymerization rate equivalent to the conventional water-soluble mono-acylphosphine oxide TPO-Li. This novel PI can be used to prepare hydrogels and aqueous polymer dispersions for 3D printing.

In addition, Risangud et al. [101] utilized a poly (ethylene glycol)-block-poly(ϵ -caprolactone) (PEG114-b-PCLx) copolymer to increase the water solubility of 2,4,6-trimethylbenzoyl-diphenylphosphine oxide (TPO). Polymerization of the PEG114-b-PCLx copolymer began with traditional ring-opening polymerization. Subsequently, TPO-encapsulated nanoparticles (TPO@PEG114-b-PCLx) were prepared using nanoprecipitation and dehydrated via lyophilization. The hydrodynamic average size of the resultant nanoparticles ranged from 190 to 360 nm when the molecular weight of PEG114-b-PCLx and the ratio of TPO: PEG114-b-PCLx were varied, and the TPO encapsulation efficiency was approximately 21-35%. Following that, DLP 3D printing of a mixture of poly(ethylene glycol dimethacrylate) (PEGDMA) and methacrylate-functionalized dextran (Dex-MA) produced hydrogels that were not cytotoxic to chondrocytes and fibroblasts.

Two-photon polymerization of 3D hydrogel constructs is frequently employed in biological tissue engineering. To improve the biocompatibility of the hydrogel structure, Gao et al. [102] prepared a novel ionic carbazole water-soluble PI to achieve the preparation of aqueous 3D hydrogel structures. Through host-guest interactions, 3, 6-bis [2-(1-methyl-pyridinium) vinyl]-9-methyl-carbazole diiodide (BMVMC) and cucurbit uril (CB7) have been employed to build superior water solubility complexes (see [Figure I-14c](#)). The binding ratio of CB7/BMVMC is 1:1, and the two-photon absorption (TPA) cross-section of the complex is increased to 2500 GM compared to 750 GM of the BMVMC molecule. Then, the CB7/ BMVMC complex was used as the PI and PEG-DA as the monomer to obtain an aqueous photoresist with a low laser threshold of 3.7 mW and a high resolution of 180 nm. Benefiting from the fluorescent properties of the CB7/ BMVMC complex, confocal fluorescence images were obtained

without the help of any fluorescent probes. Subsequently, a 3D-engineered hydrogel scaffold microstructure was fabricated by two-photon polymerization technique, and the good biocompatibility of BMVMC-CB7 complex and the as-prepared photoresist was demonstrated by culturing the structure with living L929 cells, which is expected to be further applied in tissue engineering.

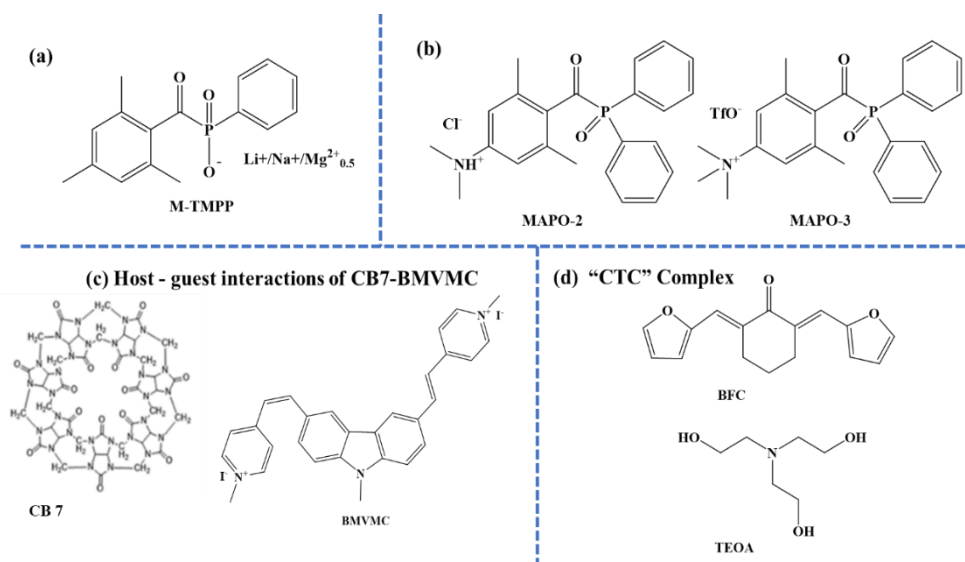


Figure I-14. The Developed water-soluble PIs for 3D printing. (a) molecular structure of M-TMPP [78]; (b) the chemical structure of MAPO-2 and MAPO-3 [100]; (c) molecular structure of CB7 and BMVMC [102]; (d) the chemical structure of BFC and TEOA [103].

In addition, Li et al. [103] devised a method to convert water-insoluble PIs into water-soluble PIs. The water-insoluble PI (*2E,6E*)-2,6-bis(furan-2-ylmethylidene)cyclohexan-1-one (BFC) (electron receptor) and the water-soluble co-initiator triethanolamine (TEOA) (electron donor) were simply mixed to form the [BFC-TEOA] electron transfer complexes (CTCs). Based on the strong CTC effect, [BFC-TEOA] CTC not only has increased absorption in the visible region, but it also exhibited enhanced water solubility. Photopolymerization kinetics indicated that [BFC-TEOA] CTC at a concentration of 2 wt% can rapidly and efficiently initiate the polymerization of aqueous monomer AM in water (see [Figure I-14d](#)).

4.4 Monomers/oligomers and related applications.

Monomers and oligomers can be photopolymerized during 3D printing in the presence of an appropriate PI, which plays a decisive role on the characteristics of the resulting 3D object. More crucially, the physicochemical properties of 3D objects are inextricably linked to their applications. Photosensitive resins are the most common monomers/oligomers used in 3D printing via photopolymerization. Since (meth)acrylate-based resins are compatible with different types of commercially available 3D printers as well as custom 3D printers, multifunctional (meth)acrylates resin is used in the majority of commercial photosensitive formulations. As shown in **Figure I-15**, the most common (meth)acrylate monomers/oligomers used in 3D printing are PEGDA, diurethanedimethacrylate (UDMA), triethylene glycol dimethacrylate (TEGDMA), bisphenol a-glycidyl methacrylate (*Bis*-GMA), trimethylolpropane triacrylate (TTA) and bisphenol a ethoxylate diacrylate (*Bis*- EDA) [104-106].

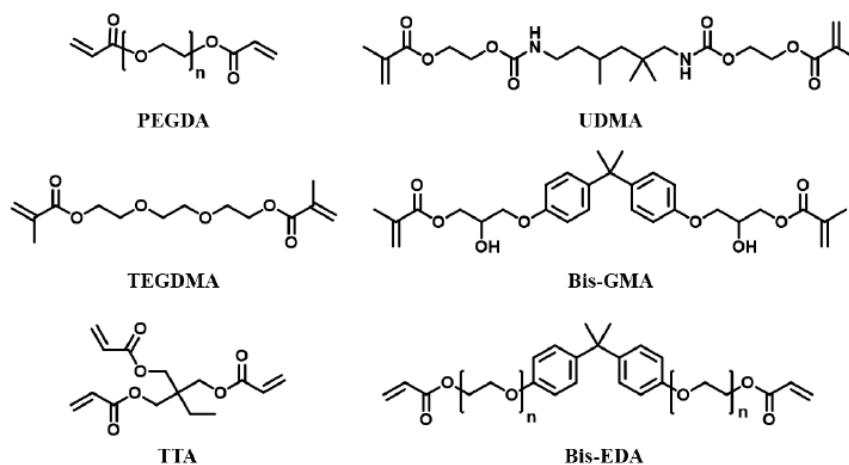


Figure I-15. Examples of meth(acrylate) monomer/oligomer typically used in 3D photopolymerization [104-106].

However, not all commercial monomers/oligomers are available for specific applications where the properties of 3D printed items cannot be achieved using commercial resins. Therefore, new monomers/oligomers need to be designed and developed for 3D printing of materials with the desired properties. Currently, the properties of any single material are insufficient to meet the requirements of complicated applications (such as tissue engineering). As a result, the investigation of producing novel monomers/oligomers, combining the properties of a single material

and complementing their separate strengths and weaknesses to build a composite polymer with more appropriate functionalities, has become a popular topic. Novel monomers/oligomers created for 3D printing via photopolymerization and their applications are explained in greater detail below.

4.4.1 Monomers/Oligomers for photopolymerization based 3D printing of composite materials.

In order to meet the required mechanical and functional properties of the material for various applications, we often combine multiple materials, one method is to cross-link multiple photosensitive resins to form composite materials or even interpenetrating network polymers, while another is to directly add fibers, particles or nanomaterials into photosensitive resins to enhance functionalize their properties.

Particles/fillers, such as ceramic particles, glass particles, etc. are widely applied to improve the characteristics of polymers due to their low cost and ease of mixing with monomers/resins (see [Section 3.2](#) above). Different properties can be improved with various kinds of particles, like adding aluminum oxide (Al_2O_3) to adjust dielectric permittivity or ceramic to enhance tensile, compressive modulus and linear shrinkage. In other recent works, Zhang et al. [107] added more than 75 wt% zeolite particles to the photosensitive resin trimethylolpropane triacrylate (TMPTA) to obtain composites with good mechanical properties and low shrinkage by using direct laser write technique. Compared with pure zeolite powder, the N_2 adsorption properties were only slightly decreased. Glass particles were combined to photosensitive resins by Felzmann et al. to create cellular bio-glasses for bone repair [108]. Ventura et al. [109] used mask-image-projection-based stereolithography to print silicon nitride ceramic objects. However, the addition of fillers will impact the photosensitive resin's light scattering; the larger the particle content, the stronger the light scattering will be, reducing the formulation's depth of cure. Therefore, a promising method is to fuse the precursor polymer of particles such as ceramics with the photosensitive resin and then printed using SLA/DLP. As shown in [Figure I-16a](#), Eckel et al. [110] fabricated SiOC ceramic objects with complex geometries using SLA technology, such as using thiol/vinyl

containing siloxane monomers. The addition of particles also aids in the resolution of volume shrinkage problem caused by the decrease in intermolecular distances caused by interactions of van der Waals forces and covalent bonds following the reaction of the resin to form a cross-linked network during 3D printing by photopolymerization.

The trend of replacing traditional materials (aluminum, wood, and steel) with fiber-reinforced polymer composites continues to offer impetus for the development of innovative technologies to lower prices while improving functionality and quality. Glass and carbon fibers are typically short fibers that are often utilized in 3D printing as reinforcing elements to improve the mechanical properties of composites. Numerous studies have shown that these reinforcing components randomly dispersed in the resin can improve the mechanical properties of the material. Furthermore, better directional mechanical properties for objects with specialized load-bearing applications can be achieved by controlling these reinforcements in the resin matrix. For example, Asif et al. [111] proposed a new photopolymerization-based 3D printing method that employs the acoustic radiation force of an ultrasonic standing wave to organize carbon fibers in a photocurable resin, causing them to follow the standing waves (see [Figure I-16b](#)). After the node layout and printing, the final object's stretch resistance is greatly increased.

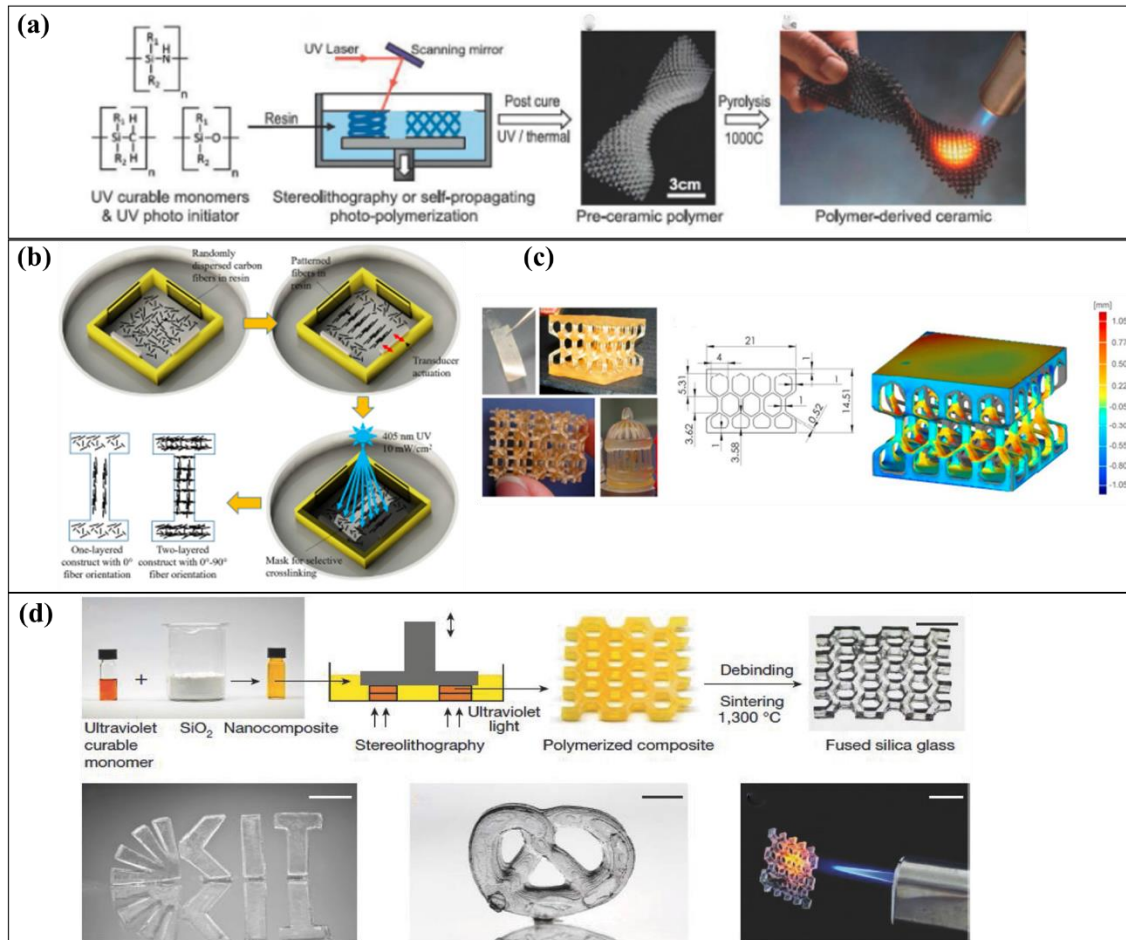


Figure I-16. (a) Additive manufacturing of polymer-derived ceramics [110]; (b) Illustration of alignment of fibers using ultrasonic actuation and curing of resin in the shape of dog bone specimen using a UV light source [111]; (c) 3D printed PEG-based hybrid nanocomposites obtained by Sol-Gel technique [112]; (d) 3D printing of fused silica glass [113].

In order to improve the strength of 3D printed polymer materials, nanomaterials (e.g. cellulose nanocrystals) are frequently employed as reinforcements and mixed with polymer materials to prepare high-strength and multifunctional 3D printed nanocomposites. As illustrated in **Figure I-16c**, Chiappone et al. [112] employed DLP to print a complex multilayer architecture using a mixed formulation of 3-(trimethoxymethylsilyl) propyl methacrylate (MEMO), tetraethyl orthosilicate (TEOS) and PEGDA (Mw=600 g/mol) in the presence of a PI (Irgacure 819). The 3D printed items were then exposed to acidic vapor, which caused a sol-gel reaction of the metal-alkoxysilanes contained in the polymer network to form inorganic nanoparticles in situ

(as seen in **Figure I-16d**). Surprisingly, the formation of the inorganic phase enhanced the T_g, Young's modulus, and surface hardness. Similarly, Kotz et al. [113] used SLA to print photosensitive monomers distributed with silica nanoparticles. **Figure I-16d** shows a structure made of pure fused silica glass after the final sintering of the 3D printed "green body" at 1300 °C. In addition, the mechanical characteristics or functionalization of the material can be modulated by in situ generation of nanoparticles (metal nanoparticles, hydrogel nanoparticles, etc.) during the 3D printing process. Sharma et al. [77] used SLA technique to create a berberine (BBR)-loaded hydrogel nanoparticles consisting of PEGDA as a monomer and poly (ethylene oxide) (PEO) as a swelling aid, wrapped in photopolymerizable monolith vats for drug delivery applications.

4.4.2 Monomers/Oligomers for photopolymerization based 3D printing of shape memory polymers (4D printing).

The construction of 4D printed structures is one of the most widely described uses for photopolymerized materials. When compared to regular 3D printing, 4D printing technology refers to a revolutionary additive manufacturing process with an additional time dimension. SMP materials are stimuli-responsive materials, which have the capability of changing their shapes in response to an external stimulus such as heat [114], light [115], water [116,117], electric field [118] or magnetic field [119], etc. 4D printing technology can be achieved by applying shape memory polymer (SMP) in 3D printing technology. Indeed, 4D printing combines the benefits of both 3D printing and SMPs. Complex SMP structures may be created and built in a relatively short period of time, which is useful when creating specialized tools for biomedical devices, aerospace engineering, soft robotics, etc. Indeed, 4D printing combines the benefits of both 3D printing and SMPs.

Shape memory epoxy resins with better durability and good shape memory qualities may be printed by changing the crosslinking density, which is a commonly used thermosetting resin for cationic photopolymerization. For example, Yu et al. [114] applied an acrylate-epoxy hybrid photopolymer to successfully print a 3D structure that

automatically restored its original shape after hand bending in an 85 °C hot water bath (as illustrated in [Figure I-17a](#)). Moreover, as the temperature rises, the time required decreases. In addition, the fabricated 3D structure has good thermal stability as well as mechanical properties like high strength and good toughness. Azo polymers are well known molecular photo-switches, and their photoisomerization process may be a potential mechanism for a variety of phototropic effects, including mechanical photoactivation. Roppolo et al. [115] used photocurable polymer formulations containing azobenzene compounds to accomplish precision DLP 3D printing of cross-linked matrices. The Young's modulus of the 3D printed structures changed after laser irradiation, resulting in softening or hardening dependent on the T_g of the polymeric matrix and the operational temperature. The proposed device could have many interesting applications in different contexts, such as: a light-activated mechanical damper.

Hydrogel is one of the most effective materials for responding to changes in water content, and their ability to swell in the presence of water can be precisely regulated, allowing for 4D printing. For example, Zhao et al. [116] created a bilayer water-responsive structure with hydrophilic PEGDA as the swelling moiety and hydrophobic PEGDA as the rigid moiety, resulting in directional bending in water. Both materials are photocurable, therefore they can be easily patterned into complex shapes (such as the floral structures illustrated in [Figure I-17b](#)) using DLP. Additionally, when the cured hydrogel is immersed in ethanol, the uncured monomer in the less irradiated portion diffuses out and leaving loose holes in the network. After drying, a process known as desolvation occurs, which can reverse this process and result in a reversible shape change. For example, Han et al. [117] presented a miniaturized needle with bioinspired backward-facing curved barbs (200 μm broad) for enhanced tissue adhesion, which was created using a digital light processing 3D printing technology. Desolvation-induced deformation was used to construct the backward-facing barb on the MN by utilizing the crosslink density gradient in the photocurable polymer. Biomimetic MNs with improved tissue adhesion enable more steady and robust performance for drug

administration, biofluid collection, and biosensing.

Electrochemical actuation can also be directly induced by an electric field. In contrast to water and heat reactions, electrical stimulation can accurately and quickly vary amplitude, phase, and frequency for immediate and reversible responses [118]. Polymers and gels capable of converting electrical energy into mechanical energy include conductive polymers, liquid crystal elastomers, and carbon nanotubes (CNTs). Among them, electroactive hydrogels (EAH) are extensively utilized to prepare 3D printing of photopolymerization-based actuators due to their biomimetic features and processability. For example, Lyu et al. [118] devised a fast multi-material projection micro-stereolithography technology that uses dynamic fluid control of multiple liquid photopolymers within an integrated fluid cell. **Figure I-17c** depicts a bilayer hydrogel bundle made up of hydrogels with varying swelling properties under an electric field. Various types and degrees of bending deformation can also be created by mixing the applied stimuli simultaneously.

Another stimulus that enables remote actuation and wireless control of devices is a magnetic field. Magnetic actuators for 3D printing via photopolymerization are commonly manufactured by including magnetic fillers into flexible photocurable resins or loading magnetic particles onto printed structures via a surface functionalization technique. Under the influence of magnetic forces, actuation such as torque, deformation, shrinkage, extension, and bending can occur. As illustrated in **Figure I-17d**, Zhu et al. [119] demonstrated unique DLP-based 3D printing process termed micro continuous optical printing (COP) and constructed a hydrogel-based free-swimming microfish structure (height ~30 μm , length ~120 μm). By replacing the solution, Pt nanoparticles were loaded into the fish tail for propulsion, and Fe_3O_4 nanoparticles were placed into the fish head for orientation. Time-lapse photographs of microfish movement in 15% H_2O_2 vividly show the microfish's remote guidance capacity by rotating a nearby magnet.

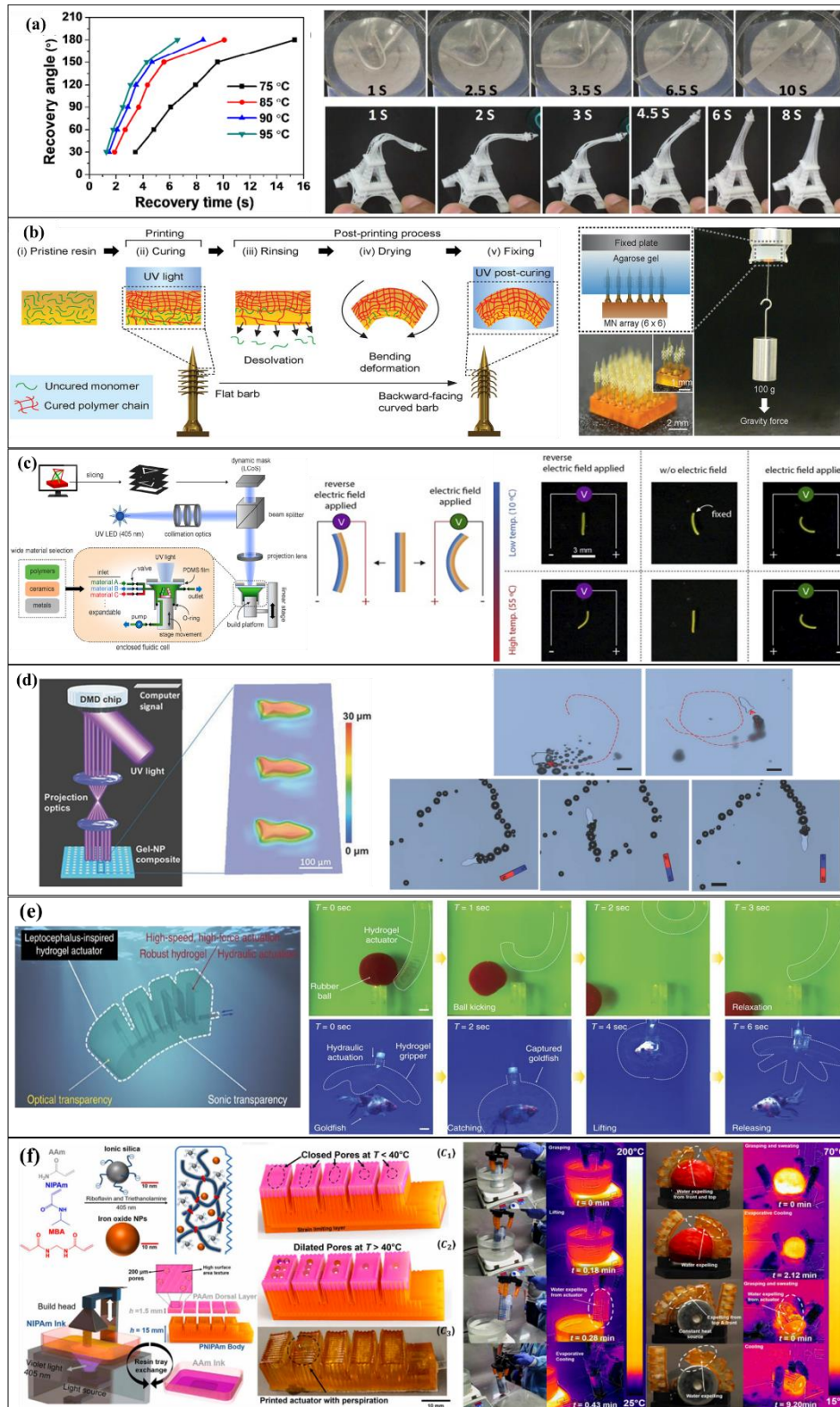


Figure I-17. 3D printing *via* photopolymerization for shape memory polymers. (a) Fold-deploy test results for printed samples with time in water bath at different temperatures [114]; (b) The process to program deformation of horizontally printed barbs into the backward-facing shape (left), and the strong tissue adhesion ability of the

microneedle array[117]; (c) Bilayer hydrogel beam printed by the electroactive hydrogels (left), and its various modes and degrees of bending deformation (right) [118]; (d) The microfish with Fe₃O₄ and Pt nanoparticles printed via μ COP method (top), and its moving ability driven by a rotating magnet (bottom) [119]; (e) The powerful optical and sonic transparent hydrogel actuators and their ability to camouflage [120]; (f) Material design, SLA printing system, and the porous actuator (left), and its cooling ability during grasping objects with different heat capacities [121].

Pneumatic or hydraulic actuation is accomplished by the dynamic reconfiguration of the gas or liquid within a chamber comprised of highly malleable materials. These actuators enable fast response, compliance at low temperatures, and generation of powerful forces in the presence of an external pump or compressor. Yuk et al. [120] developed a biomimetic hydrogel-based actuator, seen in Figure 17e, that can be hydraulically actuated in water with high speed and force while also providing optical and acoustic concealment. Swimming, kicking, and even catching live goldfish were all possible with the actuator. Mishra et al. [121] demonstrated a soft hydraulic "smart" hand capable of temperature regulation via autonomous localized sweating through micropores. As shown in Figure I-17f, a customized multi-material SLA system was used to print dynamic pores whose size changes with temperature on the finger. The pNIPAM and PAAm were chosen to form the body and fingers of the actuator, respectively. Due of the differing temperature sensitivities of the two composites, the PAAm layer expands at high temperatures ($T > 30\text{ }^{\circ}\text{C}$), increasing the diameter of pore and causing the pressurized fluid to "sweat" out of the actuator. These two gripping and cooling item tests demonstrate the gripper's compliance and cooling capacity for various objects with varying heat capacities.

5. Conclusion.

Commercial PI and monomers/oligomers for 3D printing still have huge limitations, and numerous studies have reported that a variety of visible light sensitive and water-soluble PIs/PISs, as well as some novel materials, are suitable for photopolymerization-based 3D printing in the last few years (2018-2022). Specifically,

fewer water-soluble PIs and a variety of dye-based or macromolecular visible light sensitive PIs have been developed for applications in 3D printing biological materials or aerospace materials. In addition, novel monomers/oligomers can impart specific properties of 3D printed objects (such as toughness, stiffness, and shape memory properties, etc.). Despite great advances in this field, enormous challenges and opportunities also remain. As a result, the development of biocompatible, water-soluble, visible-light-sensitive, high-performance, and stable PIs to boost 3D printing speed remains a popular research area. Furthermore, there are huge opportunities in developing monomers/oligomers and polymers with specific properties (e.g. high reactivity, fluorescence, electrical conductivity, tunable mechanical properties, stimuli-responsive properties, degradability, etc.) for their applications. In addition, the exploration of photocurable biocompatible synthetic and natural polymers for 3D/4D bioprinting is advantageous to the advancement of humans' medical and health fields.

References:

1. Crivello, J. V.; Reichmanis, E. Photopolymer materials and processes for advanced technologies. *Chemistry of Materials* **2013**, *26*(1), 533-548.
2. Zhu, X.; Lu, G.; Nie, J. 3D Printing with Light: Photopolymerization and its application in 3D printing of customized objects. Eds: Xiao, P.; Zhang, J. De Gruyter, **2021**, 1-203.
3. Zhao, W.; Wang, Z.; Zhang, J.; Wang, X.; Xu, Y.; Ding, N.; Peng, Z. Vat photopolymerization 3D printing of advanced soft sensors and actuators: from architecture to function. *Advanced Materials Technologies* **2021**, *6*(8), 2001218-2001249.
4. Dickey, M. D.; Burns, R. L.; Kim, E. K.; Johnson, S. C.; Stacey, N. A.; Willson, C. G. Study of the kinetics of step and flash imprint lithography photopolymerization. *AIChE Journal* **2005**, *51*(9), 2547-2555.
5. Xu, X.; Awad, A.; Robles-Martinez, P.; Gaisford, S.; Goyanes, A.; Basit, A. W. Vat photopolymerization 3D printing for advanced drug delivery and medical device applications. *Journal of Controlled Release* **2021**, *329*, 743-757.
6. Baroli, B. Photopolymerization of biomaterials: issues and potentialities in drug delivery, tissue engineering, and cell encapsulation applications. *Journal of Chemical Technology & Biotechnology: International Research in Process*,

- Environmental & Clean Technology* **2006**, *81(4)*, 491-499.
7. Nguyen, K. T.; West, J. L. Photopolymerizable hydrogels for tissue engineering applications. *Biomaterials* **2002**, *23(22)*, 4307-4314.
 8. Zhang, F.; Zhu, L.; Li, Z.; Wang, S.; Shi, J.; Tang, W.; Li, N.; Yang, J. The recent development of vat photopolymerization: A review. *Additive Manufacturing* **2021**, *48*, 102423-102443.
 9. Wang, X.; Jiang, M.; Zhou, Z.; Gou, J.; Hui, D. 3D printing of polymer matrix composites: A review and prospective. *Composites Part B: Engineering* **2017**, *110*, 442-458.
 10. Douglas, K. Bioprinting: to make ourselves anew. *Oxford University Press* **2021**.
 11. Wohlers, T.; Gornet, T. History of additive manufacturing. *Wohlers report* **2014**, *24(2014)*, 1-118.
 12. Li, J.; Li, S.; Li, Y.; Li, R.; Nie, J.; Zhu, X. In situ monitoring of photopolymerization by photoinitiator with luminescence characteristics. *Journal of Photochemistry and Photobiology A: Chemistry* **2020**, *389*, 112225-112232.
 13. Fouassier, J. P.; Morlet-Savary, F.; Yamashita, K.; Imahashi, S. The role of the dye/iron arene complex/amine system as a photoinitiator for photopolymerization reactions. *Polymer* **1997**, *38(6)*, 1415-1421.
 14. Kim, W. S.; Houbertz, R.; Lee, T. H.; Bae, B. S. Effect of photoinitiator on photopolymerization of inorganic-organic hybrid polymers (ORMOCER®). *Journal of Polymer Science Part B: Polymer Physics* **2004**, *42(10)*, 1979-1986.
 15. Lalevée, J.; Blanchard, N.; Tehfe, M. A.; Peter, M.; Morlet-Savary, F.; Gigmes, D.; Fouassier, J. P. Efficient dual radical/cationic photoinitiator under visible light: a new concept. *Polymer Chemistry* **2011**, *2(9)*, 1986-1991.
 16. Corrigan, N.; Yeow, J.; Judzewitsch, P.; Xu, J.; Boyer, C. Seeing the light: advancing materials chemistry through photopolymerization. *Angewandte Chemie International Edition* **2019**, *58(16)*, 5170-5189.
 17. Schwartz, J. J.; Porcincula, D. H.; Cook, C. C.; Fong, E. J.; Shusteff, M. Volumetric additive manufacturing of shape memory polymers. *Polymer Chemistry* **2022**, *13(13)*, 1813-1817.
 18. Lendlein, A.; & Kelch, S. Shape-memory polymers. *Angewandte Chemie International Edition* **2002**, *41(12)*, 2034-2057.
 19. Ganster, B.; Fischer, U.K.; Moszner, N.; Liska, R. New photocleavable structures: Acylgermane-based photoinitiator for visible light curing. *Macromolecular rapid communications* **2008**, *29(1)*, 57-62.
 20. Gibson, I.; Rosen, D. W.; Stucker, B. Photopolymerization processes. Additive Manufacturing Technologies. Springer, Boston, MA **2010**, 78-119.

21. Bao, Y.; Paunović, N.; Leroux, J. C. Challenges and opportunities in 3D printing of biodegradable medical devices by emerging photopolymerization techniques. *Advanced Functional Materials* **2022**, *32*, 2109864-2109874.
22. Baikerikar, K. K.; Scranton, A. B. Photopolymerizable liquid encapsulants for microelectronic devices. *Polymer* **2001**, *42*(2), 431-441.
23. Labana, S. S. Photopolymerization. *Journal of Macromolecular Science, Part C: Polymer Reviews* **1974**, *11*(2), 299-319.
24. Kim, J. K.; Basavaraja, C.; Yamaguchi, T.; Huh, D. S. Preparation and characterization of smart hydrogel nanocomposites sensitive to oxidation–reduction. *Polymer Bulletin* **2012**, *70*(1), 207-220.
25. Kaur, M.; Srivastava, A. K. Photopolymerization: a review. *Journal of Macromolecular Science, Part C: Polymer Reviews* **2002**, *42*(4), 481-512.
26. Petko, F.; Galek, M.; Hola, E.; Popielarz, R.; Ortyl, J. One-component cationic photoinitiators from tunable benzylidene scaffolds for 3D printing applications. *Macromolecules* **2021**, *54*(15), 7070-7087.
27. Lalevee, J.; Fouassier, J. P. Photopolymerisation initiating systems. The Royal Society of Chemistry, London **2018**, 1-586.
28. Fouassier, J. P.; Lalevee, J. Photoinitiators for polymer synthesis: scope, reactivity, and efficiency. Wiley-VCH. Verlag. GmbH. & Co. KGaA: Weinheim, Germany; **2012**, 1-475.
29. Blyth, J.; Hoffmann, A. W. Ueber das styrol und einige seiner zersetzungsprodouce. *Justus Liebigs Annalen der Chemie* **1845**, *53*(3), 289-329.
30. Oster, G.; Yang, N. L. Photopolymerization of vinyl monomers. *Chemical Reviews* **1968**, *68*(2), 125-151.
31. Machado, T. O.; Sayer, C.; Araujo, P. H. H. Thiol-ene polymerisation: A promising technique to obtain novel biomaterials. *European Polymer Journal* **2017**, *86*, 200-215.
32. Knežević, A.; Tarle, Z.; Meniga, A.; Šutalo, J.; Pichler, G.; & Ristić, M. Photopolymerization of composite resins with plasma light. *Journal of Oral Rehabilitation* **2002**, *29*(8), 782-786.
33. Wang, H.; Wei, J.; Jiang, X.; Yin, J. Highly efficient sulfur-containing polymeric photoinitiators bearing side-chain benzophenone and coinitiator amine for photopolymerization. *Journal of Photochemistry and Photobiology A: Chemistry* **2007**, *186*(1), 106-114.
34. Li, M. Q.; Qiu, W. W.; Hu, P.; Zhu, J. Z.; Liu, R.; Li, Z. Q. Synthesis and structure-activity relationship of coumarin-based oxime-esters as two-photon photoinitiators. *Imaging Science and Photochemistry* **2019**, *37*(5), 415-427.

35. Shakya, S.; Khan, I. M. Charge transfer complexes: Emerging and promising colorimetric real-time chemosensors for hazardous materials. *Journal of Hazardous Materials* **2021**, *403*, 123537-123600.
36. Kaya, K.; Kreutzer, J.; Yagci, Y. A charge-transfer complex of thioxanthonephenacyl sulfonium salt as a visible-light photoinitiator for free radical and cationic polymerizations. *ChemPhotoChem* **2019**, *3(11)*, 1187-1192.
37. Blanco, I. The use of composite materials in 3D printing. *Journal of Composites Science* **2020**, *4(2)*, 42-64.
38. Chen, Z.; Li, Z.; Li, J.; Liu, C.; Lao, C.; Fu, Y.; Liu, C.; Li, Y.; Wang, P.; He, Y. 3D printing of ceramics: A review. *Journal of the European Ceramic Society* **2019**, *39(4)*, 661-687.
39. Zmarzły, P.; Gogolewski, D.; Koziar, T. Design guidelines for plastic casting using 3D printing. *Journal of Engineered Fibers and Fabrics* **2020**, *15*, 155892502091603-155892502091613.
40. You, S.; Li, J.; Zhu, W.; Yu, C.; Mei, D.; Chen, S. Nanoscale 3D printing of hydrogels for cellular tissue engineering. *Journal of Materials Chemistry B* **2018**, *6(15)*, 2187-2197.
41. Zhou, H.; Bhaduri, S. B. Biomaterials in translational medicine: Chapter 12. 3D printing in the research and development of medical devices. Academic Press. **2019**, 269-289. A Biomaterials Approach Woodhead Publishing Series in Biomaterials.
42. Bogers, M.; Hadar, R.; Bilberg, A. Additive manufacturing for consumer-centric business models: Implications for supply chains in consumer goods manufacturing. *Technological Forecasting and Social Change* **2016**, *102*, 225-239.
43. Attaran, M. The rise of 3-D printing: The advantages of additive manufacturing over traditional manufacturing. *Business Horizons* **2017**, *60(5)*, 677-688.
44. Joshi, S. C.; Sheikh, A. A. 3D printing in aerospace and its long-term sustainability. *Virtual and Physical Prototyping* **2015**, *10(4)*, 175-185.
45. Mishra, S. Application of 3D printing in medicine. *Indian Heart Journal* **2016**, *68(1)*, 108-109.
46. Li, R.; Kim, Y. S.; Tho, H. V.; Yum, Y. J.; Kim, W. J.; Yang, S. Y. Additive manufacturing (AM) of piercing punches by the PBF method of metal 3D printing using mold steel powder materials. *Journal of Mechanical Science and Technology* **2019**, *33(2)*, 809-817.
47. Wohlers, T. T.; Campbell, I.; Diegel, O.; Huff, R.; Kowen, J. Wohlers report 2021: 3D printing and additive manufacturing global state of the industry. Wohlers Associates **2021**.
48. Valino, A. D.; Dizon, J. R. C.; Espera, A. H.; Chen, Q.; Messman, J.; Advincula, R.

- C. Advances in 3D printing of thermoplastic polymer composites and nanocomposites. *Progress in Polymer Science* **2019**, *98*, 101162-101181.
49. Deng, S.; Wu, J.; Dickey, M. D.; Zhao, Q.; Xie, T. Rapid open-air digital light 3D printing of thermoplastic polymer. *Advanced Materials* **2019**, *31(39)*, 1903970-1903977.
50. Zhang, Y. S.; Khademhosseini, A. Advances in engineering hydrogels. *Science* **2017**, *356(6337)*, eaaf3627- eaaf3639.
51. Shahrubudin, N.; Lee, T. C.; Ramlan, R. An overview on 3D printing technology: Technological, materials, and applications. *Procedia Manufacturing* **2019**, *35*, 1286-1296.
52. Chou, D. T.; Wells, D.; Hong, D.; Lee, B.; Kuhn, H.; Kumta, P. N. Novel processing of iron-manganese alloy-based biomaterials by inkjet 3-D printing. *Acta Biomater* **2013**, *9(10)*, 8593-8603.
53. Wen, X.; Gao, S.; Feng, J.; Li, S.; Gao, R.; Zhang, G. Chest-wall reconstruction with a customized titanium-alloy prosthesis fabricated by 3D printing and rapid prototyping. *Journal of Cardiothoracic Surgery* **2018**, *13(1)*, 1-7.
54. Hitzler, L.; Alifui-Segbaya, F.; Williams, P.; Heine, B.; Heitzmann, M.; Hall, W.; Merkel, M.; Öchsner, A. Additive manufacturing of cobalt-based dental alloys: analysis of microstructure and physicomechanical properties. *Advances in Materials Science and Engineering* **2018**, *2018*, 1-12.
55. Chen, Z.; Li, Z.; Li, J.; Liu, C.; Lao, C.; Fu, Y.; Liu, C.; Li, Y.; Wang, P.; He, Y. 3D printing of ceramics: A review. *Journal of the European Ceramic Society* **2019**, *39(4)*, 661-687.
56. Kianian, B. Wohlers report 2019: 3D Printing and additive manufacturing state of the industry, annual worldwide progress report: chapter title: middle east: iran. Wohlers Associates Inc **2019**.
57. Fan, D. Y.; Li, Y.; Wang, X.; Zhu, T. J.; Wang, Q.; Cai, H.; Li, W. S.; Tian, Y.; Liu, Z. J. Progressive 3D printing technology and its application in medical materials. *Frontiers in Pharmacology* **2020**, *11*, 122-134.
58. Ahn, S. H.; Lee, J.; Park, S. A.; Kim, W. D. Three-dimensional bio-printing equipmen hnologies for tissue engineering and regenerative medicine. *Tissue Engineering and Regenerative Medicine* **2016**, *13(6)*, 663-676.
59. Lozano, R.; Stevens, L.; Thompson, B. C.; Gilmore, K. J.; Gorkin, R.; 3rd; Stewart, E. M.; in het Panhuis, M.; Romero-Ortega, M.; Wallace, G. G. 3D printing of layered brain-like structures using peptide modified gellan gum substrates. *Biomaterials* **2015**, *67*, 264-273.

60. Li, J.; Zhou, Y.; Chen, W.; Yuan, Z.; You, B.; Liu, Y.; Yang, S.; Li, F.; Qu, C.; Zhang, X. A novel 3D in vitro tumor model based on silk fibroin/chitosan scaffolds to mimic the tumor microenvironment. *ACS Applied Materials & Interfaces* **2018**, *10(43)*, 36641-36651.
61. VanKoevering, K. K.; Morrison, R. J.; Prabhu, S. P.; Torres, M. F.; Mychaliska, G. B.; Treadwell, M. C.; Hollister, S. J.; Green, G. E. Antenatal three-dimensional printing of aberrant facial anatomy. *Pediatrics* **2015**, *136(5)*, e1382-e1385.
62. GE Reports. The FAA cleared the first 3D printed part to fly commercial jet engine from GE. GE reports **2015**.
63. Additive Manufacturing | GKN technology 2016 | GKN Group. <http://www.gkn.com/en/our-technology/2016/additive-manufacturing> **2017**.
64. Ngo, T. D.; Kashani, A.; Imbalzano, G.; Nguyen, K. T.; Hui, D. Additive manufacturing (3D printing): A review of materials, methods, applications and challenges. *Composites Part B: Engineering* **2018**, *143*, 172-196.
65. Wrld's first 3D printed pedestrian bridge in Madrid. (The Institute for Advanced Architecture of Calalonia designs the first 3D printed bridge in the world. Inst. Adv. Archit Calalonia. <http://iaac.net/institute-advanced-architecture-calalonia-designs-first-3D-printed-bridge-world/>.)
66. Quick, D. The Urbee hybrid: the world's first 3D printed car. **2011**.
67. Shaqour, B.; Abuabiah, M.; Abdel-Fattah, S.; Juaidi, A.; Abdallah, R.; Abuzaina, W.; Cos, P. Gaining a better understanding of the extrusion process in fused filament fabrication 3D printing: A review. *The International Journal of Advanced Manufacturing Technology* **2021**, *114(5)*, 1279-1291.
68. Hua, L.; Bowen, P. Application of ceramic 3D printing technology in modern ceramic manufacturing. In 2021 7th International Symposium on Mechatronics and Industrial Informatics (ISMII) **2021**, 160-163. IEEE.
69. Hafley, R.; Taminger, K.; Bird, R. Electron beam freeform fabrication in the space environment. In *45th AIAA Aerospace Sciences Meeting and Exhibit* **2007**, 1154-1163.
70. Duda, T.; Raghavan, L. V. 3D metal printing technology: the need to re-invent design practice. *Ai & Society* **2018**, *33(2)*, 241-52.
71. Terrazas, C. A.; Gaytan, S. M.; Rodriguez, E.; Espalin, D.; Murr, L. E.; Medina, F.; Wicker, R. B. Multi-material metallic structure fabrication using electron beam melting. *The International Journal of Advanced Manufacturing Technology* **2014**, *71(1)*, 33-45.
72. Padmakumar M. Additive manufacturing of tungsten carbide hardmetal parts by selective laser melting (SLM), selective laser sintering (SLS) and binder jet 3D

- printing (BJ3DP) techniques. *Lasers Manuf Mater Process* 2020, 7, 338-371.
73. Singh, D. D.; Mahender, T.; Reddy, A. R. Powder bed fusion process: A brief review. *Materials Today: Proceedings* 2021, 46, 350-355.
74. Lowmunkong, R.; Sohamura, T.; Suzuki, Y.; Matsuya, S.; Ishikawa, K. Fabrication of freeform bone-filling calcium phosphate ceramics by gypsum 3D printing method. *Journal of Biomedical Materials Research Part B: Applied Biomaterials: An Official Journal of The Society for Biomaterials, The Japanese Society for Biomaterials, and The Australian Society for Biomaterials and the Korean Society for Biomaterials* 2009, 90(2), 531-539.
75. Rossi, S.; Puglisi, A.; Benaglia, M. Additive manufacturing technologies: 3D printing in organic synthesis. *ChemCatChem* 2018, 10(7), 1512-1525.
76. Pagac, M.; Hajnys, J.; Ma, Q. P.; Jancar, L.; Jansa, J.; Stefek, P.; Mesicek, J. A review of vat photopolymerization technology: materials, applications, challenges, and future trends of 3D printing. *Polymers* 2021, 13(4), 598-618.
77. Sharma, P. K.; Choudhury, D.; Yadav, V.; Murty, U. S. N.; Banerjee, S. 3D printing of nanocomposite pills through desktop vat photopolymerization (stereolithography) for drug delivery reasons. *3D Printing in Medicine* 2022, 8(1), 1-10.
78. Wang, H.; Zhang, B.; Zhang, J. H.; Ren, P. Y.; Ge, Q.; Li, P.; Huang, W. General one-pot method for preparing highly water-soluble and biocompatible photoinitiators for digital light processing-based 3D printing of hydrogels. *ACS Applied Materials & Interfaces* 2021, 13(46), 55507-55516.
79. Tumbleston, J. R.; Shirvanyants, D.; Ermoshkin, N.; Januszewicz, R.; Johnson, A. R.; Kelly, D.; DeSimone, J. M. Continuous liquid interface production of 3D objects. *Science* 2015, 347(6228), 1349-1352.
80. Gay, P.; Blanco, D.; Pelayo, F.; Noriega, A.; Fernández, P. Analysis of factors influencing the mechanical properties of flat polyjet manufactured parts. *Procedia Engineering* 2015, 132, 70-77.
81. Dietlin, C.; Schweizer, S.; Xiao, P.; Zhang, J.; Morlet-Savary, F.; Graff, B.; Fouassier, J.-P.; Lalevée, J. Photopolymerization upon LEDs: new photoinitiating systems and strategies. *Polymer Chemistry* 2015, 6(21), 3895-3912.
82. Xiao, P.; Zhang, J.; Dumur, F.; Tehfe, M. A.; Morlet-Savary, F.; Graff, B.; Gigmès, D.; Fouassier, J. P.; Lalevée, J. Visible light sensitive photoinitiating systems: Recent progress in cationic and radical photopolymerization reactions under soft conditions. *Progress in Polymer Science* 2015, 41, 32-66.
83. Carbone, N. D.; Ene, M.; Lancaster, J. R.; Koberstein, J. T. Kinetics and mechanisms of radical-based branching/cross-linking reactions in preformed

- polymers induced by benzophenone and *bis*-benzophenone photoinitiators. *Macromolecules* **2013**, *46*(14), 5434-5444.
84. Fors, B. P.; Hawker, C. J. Control of a living radical polymerization of methacrylates by light. *Angewandte Chemie* **2012**, *124*(35), 8980-8983.
85. Bonardi, A. H.; Dumur, F.; Grant, T. M.; Noirbent, G.; Gigmes, D.; Lessard, B. H.; Fouassier, J. P.; Lalevée, J. High performance near-infrared (NIR) photoinitiating systems operating under low light intensity and in the presence of oxygen. *Macromolecules* **2018**, *51*(4), 1314-1324.
86. Hu, P.; Qiu, W.; Naumov, S.; Scherzer, T.; Hu, Z.; Chen, Q.; Knolle, W.; Li, Z. Conjugated bifunctional carbazole-based oxime esters: efficient and versatile photoinitiators for 3D printing under one- and two-photon excitation. *ChemPhotoChem* **2020**, *4*(3), 224-232.
87. Qiu, W.; Zhu, J.; Dietliker, K.; Li, Z. Polymerizable Oxime Esters: An efficient photoinitiator with low migration ability for 3D printing to fabricate luminescent devices. *ChemPhotoChem* **2020**, *4*(11), 5296-5303.
88. Liu, S. H.; Chen, H.; Zhang, Y. J.; Sun, K.; Xu, Y. Y.; Morlet-Savary, F.; Graff, B.; Noirbent, G.; Pigot, C.; Brunel, D.; Nechab, M.; Gigmes, D.; Xiao, P.; Dumur, F.; Lalevee, J. Monocomponent photoinitiators based on benzophenone-carbazole structure for LED photoinitiating systems and application on 3D printing. *Polymers* **2020**, *12*(6), 1394-1409.
89. Peng, X.; Zhu, D.; Xiao, P. Naphthoquinone derivatives: naturally derived molecules as blue-light-sensitive photoinitiators of photopolymerization. *European Polymer Journal* **2020**, *127*, 109569-109577.
90. Gallastegui, A.; Dominguez-Alfaro, A.; Lezama, L.; Alegret, N.; Prato, M.; Gómez, M. L.; Mecerreyes, D. Fast visible-light photopolymerization in the presence of multiwalled carbon nanotubes: toward 3D printing conducting nanocomposites. *ACS Macro Letters* **2022**, *11*(3), 303-309.
91. Ohtsuki, A.; Goto, A.; Kaji, H. Visible-light-induced reversible complexation mediated living radical polymerization of methacrylates with organic catalysts. *Macromolecules* **2012**, *46*(1), 96-102.
92. Zeitler, K. Photoredox catalysis with visible light. *Angewandte Chemie International Edition* **2009**, *48*(52), 9785-9789.
93. Borjigin, T.; Noirbent, G.; Gigmes, D.; Xiao, P.; Dumur, F.; Lalevée, J. The new LED-Sensitive photoinitiators of Polymerization: Copper complexes in free radical and cationic photoinitiating systems and application in 3D printing. *European Polymer Journal* **2022**, *162*, 110885-110895.

94. Breloy, L.; Losantos, R.; Sampedro, D.; Marazzi, M.; Malval, J. P.; Heo, Y.; Akimoto, J.; Ito, Y.; Brezová, V.; Versace, D. L. Allyl amino-thioxanthone derivatives as highly efficient visible light H-donors and co-polymerizable photoinitiators. *Polymer Chemistry* **2020**, *11*(26), 4297-4312.
95. Benedikt, S.; Wang, J.; Markovic, M.; Moszner, N.; Dietliker, K.; Ovsianikov, A.; Grütmacher, H.; Liska, R. Highly efficient water-soluble visible light photoinitiators. *Journal of Polymer Science Part A: Polymer Chemistry* **2016**, *54*(4), 473-479.
96. Tomal, W.; Ortyl, J. Water-soluble photoinitiators in biomedical applications. *Polymers* **2020**, *12*(5), 1073-1103.
97. Williams, C. G.; Malik, A. N.; Kim, T. K.; Manson, P. N.; Elisseeff, J. H. Variable cytocompatibility of six cell lines with photoinitiators used for polymerizing hydrogels and cell encapsulation. *Biomaterials* **2005**, *26*(11), 1211-1218.
98. Fairbanks, B. D.; Schwartz, M. P.; Bowman, C. N.; Anseth, K. S. Photoinitiated polymerization of PEG-diacrylate with lithium phenyl-2,4,6-trimethylbenzoylphosphinate: polymerization rate and cytocompatibility. *Biomaterials* **2009**, *30*(35), 6702-6707.
99. Pawar, A. A.; Saada, G.; Cooperstein, I.; Larush, L.; Jackman, J. A.; Tabaei, S. R.; Magdassi, S. High-performance 3D printing of hydrogels by water-dispersible photoinitiator nanoparticles. *Science Advances* **2016**, *2*(4), e1501381- e1501389.
100. Le, C. M. Q.; Petitoy, T.; Wu, X.; Spangenberg, A.; Ortyl, J.; Galek, M.; Infante, L.; Thérien-Aubin, H.; Chemtob, A. Water-soluble photoinitiators from dimethylamino-substituted monoacylphosphine oxide for hydrogel and latex preparation. *Macromolecular Chemistry and Physics* **2021**, *222*(19), 2100217-2100227.
101. Risangud, N.; Kunkit, N.; Sungkhaphan, P.; Hankamolsiri, W.; Sornchalerm, L.; Thongkham, S.; Chansaenpak, K. Amphiphilic polymeric photoinitiator composed of PEG-b-PCL diblock copolymer for three-dimensional printing of hydrogels. *European Polymer Journal* **2022**, *168*, 111094-111104.
102. Gao, W.; Chao, H.; Zheng, Y. C.; Zhang, W. C.; Liu, J.; Jin, F.; Dong, X. Z.; Liu, Y. H.; Li, S. J.; Zheng, M. L. Ionic carbazole-based water-soluble two-photon photoinitiator and the fabrication of biocompatible 3D hydrogel scaffold. *ACS Applied Materials & Interfaces* **2021**, *13*(24), 27796-27805.
103. Li, J.; Zhang, X.; Nie, J.; Zhu, X. Visible light and water-soluble photoinitiating system based on the charge transfer complex for free radical photopolymerization. *Journal of Photochemistry and Photobiology A: Chemistry* **2020**, *402*, 112803-112809.

104. Yue, J.; Zhao, P.; Gerasimov, J. Y.; Van de Lagemaat, M.; Grotenhuis, A.; Rustema-Abbing, M.; van der Mei, H. C.; Busscher, H. J.; Herrmann, A.; Ren, Y. 3D-printable antimicrobial composite resins. *Advanced Functional Materials* **2015**, *25*(43), 6756-6767.
105. Bagheri, A.; Jin, J. Photopolymerization in 3D Printing. *ACS Applied Polymer Materials* **2019**, *1*(4), 593-611.
106. Al Mousawi, A.; Garra, P.; Schmitt, M.; Toufaily, J.; Hamieh, T.; Graff, B.; Fouassier, J. P.; Dumur, F.; Lalevée, J. 3-Hydroxyflavone and N-phenylglycine in high performance photoinitiating systems for 3D printing and photocomposites synthesis. *Macromolecules* **2018**, *51*(12), 4633-4641.
107. Zhang, Y. J.; Josien, L.; Salomon, J. P.; Simon-Masseron, A.; Lalevée, J. Photopolymerization of zeolite/polymer-based composites: toward 3D and 4D printing applications. *ACS Applied Polymer Materials* **2020**, *3*(1), 400-409.
108. Felzmann, R.; Gruber, S.; Mitteramskogler, G.; Tesavibul, P.; Boccaccini, A. R.; Liska, R.; Stampfl, J. Lithography-based additive manufacturing of cellular ceramic structures. *Advanced Engineering Materials* **2012**, *14*(12), 1052-1058.
109. Ventura, S.; Narang, S.; Guerit, P.; Liu, S.; Twait, D.; Khandelwal, P.; Fish, R. Freeform fabrication of functional silicon nitride components by direct photo shaping. *MRS Online Proceedings Library (OPL)* **2000**, *625*, 81-89.
110. Eckel, Z. C.; Zhou, C.; Martin, J. H.; Jacobsen, A. J.; Carter, W. B.; Schaedler, T. A. Additive manufacturing of polymer-derived ceramics. *Science* **2016**, *351*(6268), 58-62.
111. Asif, S.; Chansoria, P.; Shirwaiker, R. Ultrasound-assisted *vat* photopolymerization 3D printing of preferentially organized carbon fiber reinforced polymer composites. *Journal of Manufacturing Processes* **2020**, *56*, 1340-1343.
112. Chiappone, A.; Fantino, E.; Roppolo, I.; Lorusso, M.; Manfredi, D.; Fino, P.; Pirri, C. F.; Calignano, F. 3D printed PEG-based hybrid nanocomposites obtained by sol-gel technique. *ACS Applied Materials & Interfaces* **2016**, *8*(8), 5627-5633.
113. Kotz, F.; Arnold, K.; Bauer, W.; Schild, D.; Keller, N.; Sachsenheimer, K.; Nargang, T. M.; Richter, C.; Helmer, D.; Rapp, B. E. Three-dimensional printing of transparent fused silica glass. *Nature* **2017**, *544* (7650), 337-339.
114. Yu, R.; Yang, X.; Zhang, Y.; Zhao, X.; Wu, X.; Zhao, T.; Huang, W. Three-dimensional printing of shape memory composites with epoxy-acrylate hybrid photopolymer. *ACS Applied Materials & Interfaces* **2017**, *9*(2), 1820-1829.
115. Roppolo, I.; Chiappone, A.; Angelini, A.; Stassi, S.; Frascella, F.; Pirri, C. F.; Descrovi, E. 3D printable light-responsive polymers. *Materials Horizons* **2017**, *4*(3), 396-401.

116. Zhao, Z.; Kuang, X.; Yuan, C.; Qi, H. J.; Fang, D. N. Hydrophilic/hydrophobic composite shape-shifting structures. *ACS Applied Materials & Interfaces* **2018**, *10*(23), 19932-19939.
117. Han, D.; Morde, R. S.; Mariani, S.; La Mattina, A. A.; Vignali, E.; Yang, C.; Barillaro, G.; Lee, H. 4D printing of a bioinspired microneedle array with backward-facing barbs for enhanced tissue adhesion. *Advanced Functional Materials* **2020**, *30*(11), 1909197-1909209.
118. Han, D.; Yang, C.; Fang, N. X.; Lee, H. Rapid multi-material 3D printing with projection micro-stereolithography using dynamic fluidic control. *Additive Manufacturing* **2019**, *27*, 606-615.
119. Zhu, W.; Li, J.; Leong, Y. J.; Rozen, I.; Qu, X.; Dong, R.; Wu, Z.; Gao, W.; Chung, P. H.; Wang, J.; Chen, S. 3D-printed artificial microfish. *Advanced materials* **2015**, *27*(30), 4411-4417.
120. Yuk, H.; Lin, S.; Ma, C.; Takaffoli, M.; Fang, N. X.; Zhao, X. Hydraulic hydrogel actuators and robots optically and sonically camouflaged in water. *Nature communications* **2017**, *8*(1), 1-12.
121. Mishra, A. K.; Wallin, T. J.; Pan, W.; Xu, P.; Shepherd, R. F. Autonomic perspiration in 3d-printed hydrogel actuators. *Science Robotics* **2020**, *5*(38), eaaz3918- eaaz3928 .

Part II. Free Radical Photopolymerization of Chalcones Based Three-Component Photoinitiating Systems and Their Applications in 3D Printing

1. Introduction.

Since the early 1970s, the free radical photopolymerization has been extensively studied, as this polymerization technique is likely to provide a useful method for generating polymers suitable for various applications ranging from imaging, radiation curing, and optics technologies to (bio)medicine, microelectronics, and material science, while using a traceless reagent to activate the polymerization process, namely light [1-2]. An efficient photoinitiator (PI), which absorbs a certain wavelength of light to generate an active species (e.g.; cation or free radical), is an essential component in the photopolymerization process [3-4]. Although, several metal complexes or metal based compounds (e.g. ruthenium, copper, iron or iridium complexes) have been introduced into the photoinitiating systems (PISs) in the polymer photochemistry field at room temperature under visible light, acylgermanes (ketones containing germanium) were also proposed as visible light sensitive PIs due to a significant red-shift of the $n-\pi^*$ transition; furthermore, it can produce free radicals upon light irradiation through α -cleavage process to initiate the free radical polymerization (FRP) of (meth)acrylate or the cationic polymerization (CP) of 3,4-epoxycyclohexylmethyl-3',4'-epoxycyclohexane carboxylate (EPOX) in combination with Iod [3]. However, finding a new high-performance PISs in order to make the photopolymerization process more efficient upon irradiation with a visible light source is still one of the crucial aspects for the development of free radical photopolymerization reactions.

Plenty of studies have shown that some natural dyes have a great potential and can be used as non-toxic PIs in the manufacture of biocompatible polymer materials [5-6]. After absorbing the appropriate light, natural dyes were promoted to an excited state, which can then interact with additives through an electron (or energy) transfer reaction

to produce active species (e.g.; a cation or a free radical) capable to initiate a photopolymerization reaction [7-8]. Reactivity between natural dyes and additives is closely related to their photochemical properties. In this context, chalcones are a well-established class of natural compounds present in many plants, which has attracted a widespread attention owing to a variety of physiological activities (e.g.; anti-tumor, anti-inflammatory, anti-bacterial, anti-oxidation, etc.) [9-10]. Notably, chalcones which belong to flavonoids can be found in numerous edible plants such as fruits (tomatoes, apples, citrus), nuts and vegetables (potatoes, shallots, bean sprouts) so that their low environmental impact as well as their low toxicity for humans is thus averred. In addition, due to the highly conjugated nature of the framework structure, chalcones exhibit good optical properties and UV-photosensitivity, which is an ideal class of nonlinear optical materials [11-12].

Even if numerous investigations based on versatile PISs were reported, only very few chalcones have been reported by us to be activated in the visible light range and under low light intensity [11]. In this part, we want to extend this seminal work on the chalcone scaffold but using in-silico molecular design for the proposition and synthesis of new high-performance structures. Indeed, these structures were first in-silico designed thanks to molecular modelling calculations to ensure good light absorption (particularly visible light) and high potential photoreactivity through high excited state energy.

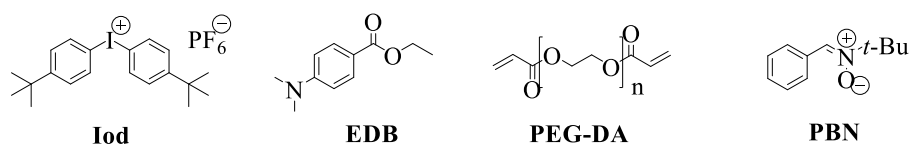
Indeed, the elaboration of novel PISs suitable for irradiation at 405 nm are still actively researched. In order to initiate a free radical photopolymerization, novel PISs comprising a chalcone with an attractive light absorption range as well as a chalcone exhibiting interesting photoinduced electron-transfer properties are proposed through the rational design of the molecular modeling [13-14]. On the basis of theoretical calculations aiming at optimizing the optical properties, the dyes proposed in this work are thus anticipated to exhibit the desirable properties that will allow these dyes to play a key-role in the proposed PISs. To evidence this, their polymerization efficiencies have been examined with benchmark monomers [e.g. PEG-DA] and this is the first time that

such an approach and such a systematic study is carried out on a series of chalcone based PIs.

2. Experimental Section.

2.1 Materials.

The PEG-DA: SR 610 was obtained from Sartomer-Europe and used as the monomer for the free radical photopolymerization. Phenyl-N-tert-butyl nitron (PBN) was purchased from Sigma-Aldrich (St. Louis, MO, USA). Bis-(4-tert-butylphenyl) iodonium hexafluorophosphate (Iod, Speedcure 938) and ethyl 4-dimethylaminobenzoate (amine, Speedcure EDB) were all purchased from Lambson (Lambson Ltd.; Wetherby, UK) and used as co-initiator and electron donor, respectively. Corresponding molecular structures are shown in **Scheme II-1**. All solvents used in this work were of analytical grade and purchased from Sigma-Aldrich (St. Louis, MO, USA).



Scheme II-1. The chemical structure of the iodonium salt (Speedcure 938), amine (Speedcure EDB), PBN and monomers used in this study.

2.2 Photopolymerization reactions monitored by real time Fourier Transformed Infrared Spectroscopy (RT-FTIR).

In order to study the influence of the chalcones/Iod/amine, chalcones/Iod and chalcones/amine combinations as well as chalcones alone on the photopolymerization efficiency, the weight percent of chalcones, iodonium salt and amine were optimized separately and the best conditions were the following ones (chalcones/Iod/amine: 1.5%/1.5%/1.5%, w/w/w in PEG-DA) for our experiments. Photosensitive formulations were polymerized between two polypropylene (PP) films with 1 drop of resin sandwiched between the two films to reduce the O₂ inhibition or into molds (under air) for thick samples. The different samples were polymerized upon irradiation with a LED @405 nm at room temperature. To evidence the crucial role of the chalcone in

these formulations, the Iod/amine (1.5%:1.5%, w/w) based two-compound PIS was used as a blank control. An excellent solubility of all systems was observed in PEG-DA monomers. The decrease of the double bond content of (meth)acrylate functions were continuously monitored by RT-FTIR spectroscopy (JASCO FTIR 4100, Oklahoma City, OK, USA). Evolution of the methacrylate characteristic peaks was followed by FTIR in the near infrared range at $\sim 6160\text{ cm}^{-1}$ for the thick samples (thickness $\sim 1.8\text{ mm}$) and at $\sim 1620\text{ cm}^{-1}$ for the thin films (thickness $\sim 0.1\text{ mm}$). The procedure used to monitor the photopolymerization profiles has been already described in detail in a previous report [15].

2.3 UV-visible absorption spectroscopy.

The UV-visible absorption properties of different chalcones dissolved in acetonitrile at a concentration of $1 \times 10^{-5}\text{ M}$ were studied using JASCO V730 spectrophotometer. Furthermore, photolysis of these PISs was investigated under LED@405 nm where the concentration of chalcones was $5 \times 10^{-5}\text{ M}$, the concentration of iodonium salt (Iod) and amine was 0.01 M.

2.4 Fluorescence and cyclic voltammetry experiments.

Fluorescence properties of the different chalcones dissolved in acetonitrile at a concentration of $1 \times 10^{-5}\text{ M}$ were studied using JASCO FP-6200 spectrofluorimeter. In addition, the fluorescence quenching experiments of the chalcones by Iod or amine were carried out in acetonitrile.

The redox potentials (oxidation potential E_{ox} vs. SCE and reduction potential E_{red} vs. SCE) for the different chalcones were measured in acetonitrile by cyclic voltammetry with tetrabutylammonium hexafluorophosphate (Aldrich) 0.1 M as the supporting electrolyte. A platinum electrode was used as a working electrode and a saturated calomel electrode (SCE) was used as a reference electrode. Moreover, the free energy change $\Delta G_{\text{S1}}^{\text{Iod}}$ or $\Delta G_{\text{S1}}^{\text{EDB}}$ for an electron transfer reaction from the singlet state were calculated from equation 1 or 2 (eq. 1 or 2) where E_{ox} , E_{red} and E_{S1} are the oxidation potential of the electron donor, the reduction potential of the electron acceptor and the excited state energy level (determined from the UV-visible and fluorescence

experiments), respectively. Similarly, the free energy change of the triplet state ΔG_{S1}^{Iod} or ΔG_{S1}^{EDB} was calculated from equations 3 and 4 (eq. 3, eq. 4) where E_{T1} is the triplet state energy level (determined from molecular modeling). The reduction potential of the iodonium salt was -0.7 V and the oxidation potential of EDB was 1.0 V according to literature data [16].

$$\Delta G_{S1}^{Iod} = E_{ox} - (-0.7) - E_{S1} \quad (1)$$

$$\Delta G_{S1}^{EDB} = 1 - E_{red} - E_{S1} \quad (2)$$

$$\Delta G_{T1}^{Iod} = E_{ox} - (-0.7) - E_{T1} \quad (3)$$

$$\Delta G_{T1}^{EDB} = 1 - E_{red} - E_{T1} \quad (4)$$

2.5 Electron spin resonance-spin trapping (ESR-ST) experiments.

The ESR-ST experiments were carried out using an X-band spectrometer (EMX plus, Bruker). LED@405 nm was used as the irradiation source for trapping the production of radicals at room temperature in N₂ saturated tert-butylbenzene solutions and trapped by phenyl-N-tert-butyl nitron (PBN) according to the procedure described in detail. ESR spectra simulations were carried out using WINSIM software [17].

2.6 3D printing experiments.

A computer programmed laser diode @405nm (Thorlabs) with a spot size of about 50 μ m was used as the light source to produce specific three-dimensional patterns from the developed two-component PISs with PEG-DA. Photosensitive formulations were polymerized under air in a homemade glass square tank (2 mm thickness) and the generated patterns were analyzed by a numerical optical microscope (DSX-HRSU from Olympus Corporation, Tokyo, Japan); different laser speeds were investigated.

2.7 Swelling experiments.

The swelling of PEG polymerized by the two-component PISs based on chalcones/Iod (1.5%/1.5%, w/w) were measured by immersing the polymerization products in deionized water at room temperature, and then removing them (n = 4) after 24h, blotting the residual water on the surface of the products quickly with paper. After that, the wet weight of each polymerization product (Wt) was measured and compared

with the initial wet weight (W_0). The swelling ratio (S_r) was defined by equation 5 [18], as follows:

$$S_r (\%) = (W_t - W_0) / W_0 \times 100 \quad (5)$$

2.8 4D printing experiments.

The reversible deformation effect of the PEG based polymers prepared with the two-component PISs based on chalcones/Iod (1.5%/1.5%, w/w) upon irradiation with LED@405nm for 1 min were measured via swelling and dehydration stimuli: first immersing the polymerization products in water at room temperature for 1 min; and then removing them @100 °C for 12 min; finally, removing the products @room temperature [19].

2.9 Molecular modeling.

Molecular orbital calculations were carried out with the Gaussian 03 suite of programs. The electronic absorption spectra for the 10 different carbazole or TPA-based mono-chalcones were calculated with the time-dependent density functional theory at the MPW1PW91/6-31G* on the relaxation geometries calculated at UB3LYP/6-31G* theory level.

Reference:

1. Belfied, K. D.; Crivello, J. V. (Eds.) Photoinitiated polymerization. *ACS Publications: Washington, DC, USA* **2003**.
2. Peng, H.; Bi, S.; Ni, M.; Xie, X.; Liao, Y.; Zhou, X.; Mai, Y. W. Monochromatic visible light “photoinitibitor”: Janus-faced initiation and inhibition for storage of colored 3D images. *Journal of the American Chemical Society* **2014**, *136*(25), 8855-8858.
3. Xiao, P.; Zhang, J.; Dumur, F.; Tehfe, M. A.; Morlet-Savary, F.; Graff, B.; Lalevee, J. Visible light sensitive photoinitiating systems: Recent progress in cationic and radical photopolymerization reactions under soft conditions. *Progress in Polymer Science* **2015**, *41*, 32-66.
4. Fouassier, J. P.; Lalevée, J. Photoinitiators for polymer synthesis-scope, reactivity, and efficiency. *Wiley-VCH Verlag GmbH & Co. KGaA: Weinheim, Germany* **2012**.
5. Zhao, J.; Lalevée, J.; Lu, H.; MacQueen, R.; Kable, S. H.; Schmidt, T. W.; Xiao, P. A new role of curcumin: as a multicolor photoinitiator for polymer fabrication under household UV to red LED bulbs. *Polymer Chemistry* **2015**, *6*(28), 5053-5061.

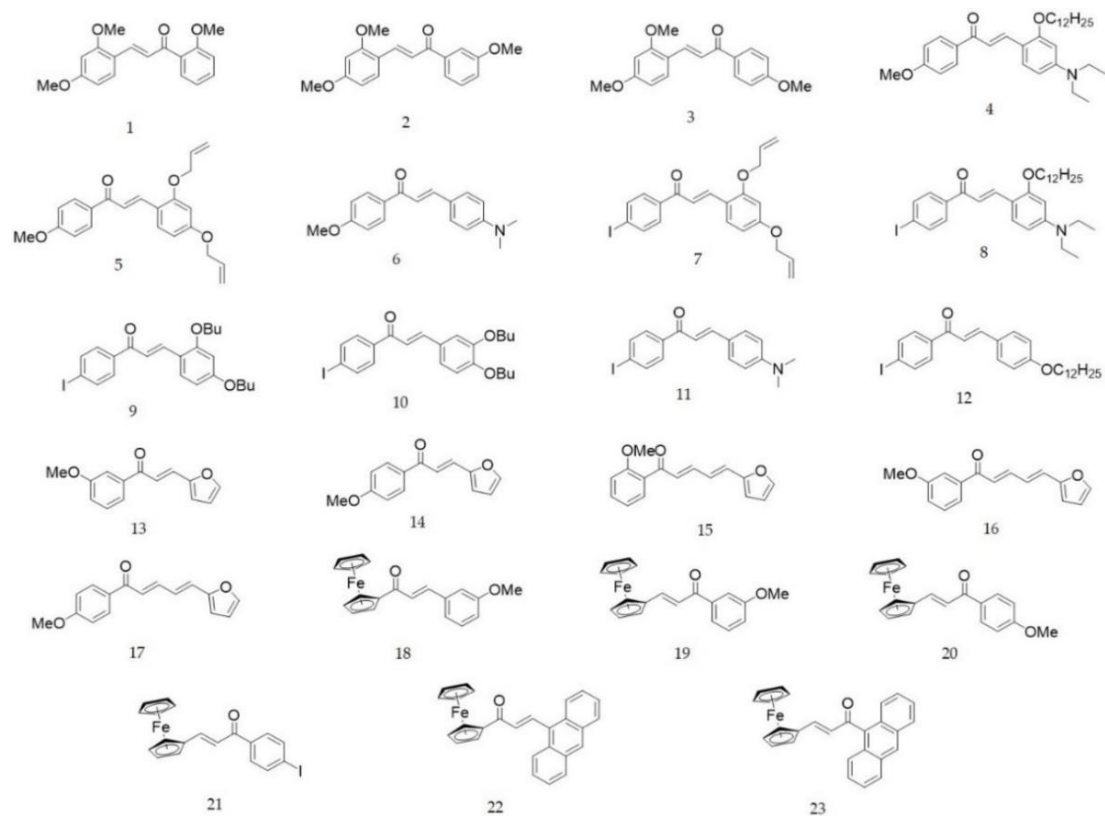
6. Telitel, S.; Schweizer, S.; Morlet-Savary, F.; Graff, B.; Tschamber, T.; Blanchard, N.; Lalevée, J. Soft photopolymerizations initiated by dye-sensitized formation of NHC-boryl radicals under visible light. *Macromolecules* **2013**, *46*(1), 43-48.
7. Radebner, J.; Eibel, A.; Leybold, M.; Gorsche, C.; Schuh, L.; Fischer, R.; Stueger, H. Tetraacylgermanes: highly efficient photoinitiators for visible-light-induced free-radical polymerization. *Angewandte Chemie International Edition* **2017**, *56*(11), 3103-3107.
8. Xiao, P.; Dumur, F.; Graff, B.; Gimes, D.; Fouassier, J. P.; Lalevee, J. Blue light sensitive dyes for various photopolymerization reactions: naphthalimide and naphthalic anhydride derivatives. *Macromolecules* **2014**, *47*(2), 601-608.
9. Rammohan, A.; Reddy, J. S.; Sravya, G.; Rao, C. N.; Zyryanov, G. V. Chalcone synthesis, properties and medicinal applications: a review. *Environmental Chemistry Letters* **2020**, *18*(2), 433-458.
10. Rocha, S.; Ribeiro, D.; Fernandes, E.; Freitas, M. A systematic review on anti-diabetic properties of chalcones. *Current Medicinal Chemistry* **2020**, *27*(14), 2257-2321.
11. Tehfe, M. A.; Dumur, F.; Xiao, P.; Delgove, M.; Graff, B.; Fouassier, J. P.; Lalevée, J. Chalcone derivatives as highly versatile photoinitiators for radical, cationic, thiol-ene and IPN polymerization reactions upon exposure to visible light. *Polymer Chemistry* **2014**, *5*(2), 382-390.
12. Son, K. I.; Kang, S. Y.; Noh, D. Y. Electrochemical and fluorescent properties of ferrocenyl chalcone with N-ethyl carbazole group. *Bulletin of the Korean Chemical Society* **2009**, *30*(2), 513-516.
13. Sun, K.; Xu, Y. Y.; Dumur, F.; Morlet-Savary, F.; Chen, H.; Dietlin, C.; Xiao, P. In silico rational design by molecular modeling of new ketones as photoinitiators in three-component photoinitiating systems: application in 3D printing. *Polymer Chemistry* **2020**, *11*(12), 2230-2242.
14. Zivic, N.; Zhang, J.; Bardelang, D.; Dumur, F.; Xiao, P.; Jet, T.; Lalevée, J. Novel naphthalimide-amine based photoinitiators operating under violet and blue LEDs and usable for various polymerization reactions and synthesis of hydrogels. *Polymer Chemistry* **2016**, *7*(2), 418-429.
15. Lalevée, J.; Blanchard, N.; Tehfe, M. A.; Peter, M.; Morlet-Savary, F.; Gimes, D.; Fouassier, J. P. Efficient dual radical/cationic photoinitiator under visible light: a new concept. *Polymer Chemistry* **2011**, *2*(9), 1986-1991.
16. Zhang, J.; Wang, S.; Lalevée, J.; Morlet-Savary, F.; Lam, E. S. H.; Graff, B.; Xiao, P. 1, 2-Diketones as photoinitiators of both cationic and free-radical photopolymerization under UV (392 nm) or Blue (455 nm) LEDs. *Journal of Polymer Science* **2020**, *58*(6), 792-802.
17. Duling, D. R. Simulation of multiple isotropic spin-trap EPR spectra. *Journal of*

Magnetic Resonance, Series B **1994**, *104(2)*, 105-110.

18. Padmavathi, N. C.; Chatterji, P. R. Structural characteristics and swelling behavior of poly (ethylene glycol) diacrylate hydrogels. *Macromolecules* **1996**, *29(6)*, 1976-1979.
19. Zhang, Z. H.; Corrigan, N.; Bagheri, A.; Jin, J. Y.; Boyer, C. A versatile 3D and 4D printing system through photocontrolled RAFT polymerization. *Angewandte Chemie* **2019**, *131(50)*, 18122-18131.

Chapter 1. Photoinitiators Derived From Natural Product Scaffolds: *Mono-Chalcones In Three-Component Photoinitiating Systems And Their Applications In 3D Printing*

The design and development of high-performance photoinitiating systems applicable to visible light delivered from light-emitting diodes (LEDs) attracts an ever-increasing attention due to their great potential applications in various fields. Chalcones correspond to a well-established class of natural compounds present in many plants. In this context, photoinitiators based on the scaffolds of natural compounds have probably a great potential to open the way for non-toxic photoinitiators in the manufacture of biocompatible polymer materials. In this work, 23 different chalcones selected from in-silico molecular design (i.e. through molecular orbital calculations, the chemical structure are shown in [Scheme II-1.1](#)) are used in conjunction with EDB and Iod to form PISs capable to initiate the polymerization of PEG-DA via an oxidation–reduction reaction mechanism. The formation of hydrogels by photopolymerization of PEG-DA is found very efficient. Remarkably, 10 of the 23 chalcones are completely new and even never synthesized prior to this work (chalcones 4, 5, 7, 8, 9, 10, 12, 15, 16 and 21). By using computational quantum chemistry, fluorescence, steady-state photolysis, and electron spin resonance spin-trapping techniques, the photoinitiation mechanism of three-component PISs based on chalcones/Iod/EDB are clarified. The results demonstrate that several chalcones-based PISs can initiate the free radical photopolymerization. Moreover, the developed chalcone-based three-component systems are applied to generate 3D hydrogel patterns using the 3D laser write technology. This research represents some novel insights into photopolymerization reactions with three-component photoinitiating systems used for 3D printing of hydrogels.



Scheme II-1.1. The chemical structure of the chalcones 1-23 used in this study.

1. Photoinitiation Ability of the Chalcones Contained Three-Component Systems.

The photoinitiation abilities of all the three-component PISs based on chalcones/Iod/amine (1.5%/1.5%/1.5%, w/w/w) were investigated with a PEG-DA. The function conversion vs irradiation time profiles obtained using RT-FTIR are given in the [Figure II-1.1](#) and the final double bond conversions (FCs) of the monomer are summarized in the [Table II-1.1](#). Compared to the blank control which only contains Iod and EDB (1.5%/1.5%, w/w, FC~ 49%), all the three-component systems showed better efficiencies to initiate the polymerization of thin samples in laminate upon irradiation with a LED@405 nm (see [Figure II-1.1](#)). Furthermore, as shown in [Figure II-1.1e](#), chalcone 12 exhibited a higher polymerization efficiency than the Iod/amine blank in thick films, evidencing the crucial role of chalcones on the polymerization initiating ability.

[Figure II-1.1c](#) shows the polymerization profiles of the three-component PISs based on chalcones bearing a furane group (chalcones 13-17). Although the FCs and polymerization rates were good in thin films, no cure in depth was observed in thick

molds with these five chalcones. More interestingly, we observed that some PISs based on the ferrocene-based mono-chalcones (chalcones 18-23) can initiate polymerization in thin films (Figure II-1.1d). This is an interesting result as ferrocene derivatives are mainly used in literature to induce the polymerization of epoxy compounds [1-2]. Methoxy (1-6) or iodine (7-12) based chalcones (Figure II-1.1a and II-1.1b, respectively) show good efficiency with both high polymerization rates and FCs.

By comparing the polymerization efficiencies of the different samples, and more precisely, the final acrylate function conversions and polymerization rates, chalcones 4, 8, 9 and 10 proved to be excellent candidates to promote polymerization processes (e.g.; the FCs of them were 90%, 79%, 85% and 82%, respectively). In addition, chalcone 12 proved to be the best candidate of the series since the polymerization of thick samples was possible with this dye (Figure II-1.1e). Therefore, chalcones 4, 8, 9, 10 and 12 were selected from the series of 23 chalcones as representative structures for more detailed investigations. Nevertheless, these chalcones all showed yellow fluorescence during the polymerization process. After polymerization, except for the polymerized product obtained with the chalcone 12, colors of the polymers obtained with all the other chalcones were deepened [3-4].

Final Acrylate Function Conversions (FCs)							
	chalcone	1	2	3	4	5	6
	FCs (%)	87	81	86	90	71	77
	chalcone	7	8	9	10	11	12
Thin Films	FCs (%)	81	79	85	82	57	58
(~0.1 mm)	chalcone	13	14	15	16	17	18
	FCs (%)	73	74	79	65	69	80
	chalcone	19	20	21	22	23	Blank
	FCs (%)	74	40	75	31	80	49
Thick Films	chalcone	12	Blank				
(~1.8 mm)	FCs (%)	91	89				

Table II-1.1. Summary of the final acrylate function conversions (FCs) at 405 nm for the PEG-DA while using the three-component PISs between chalcones (1.5%, w/w), Iod (1.5%, w/w) and EDB (1.5%, w/w).

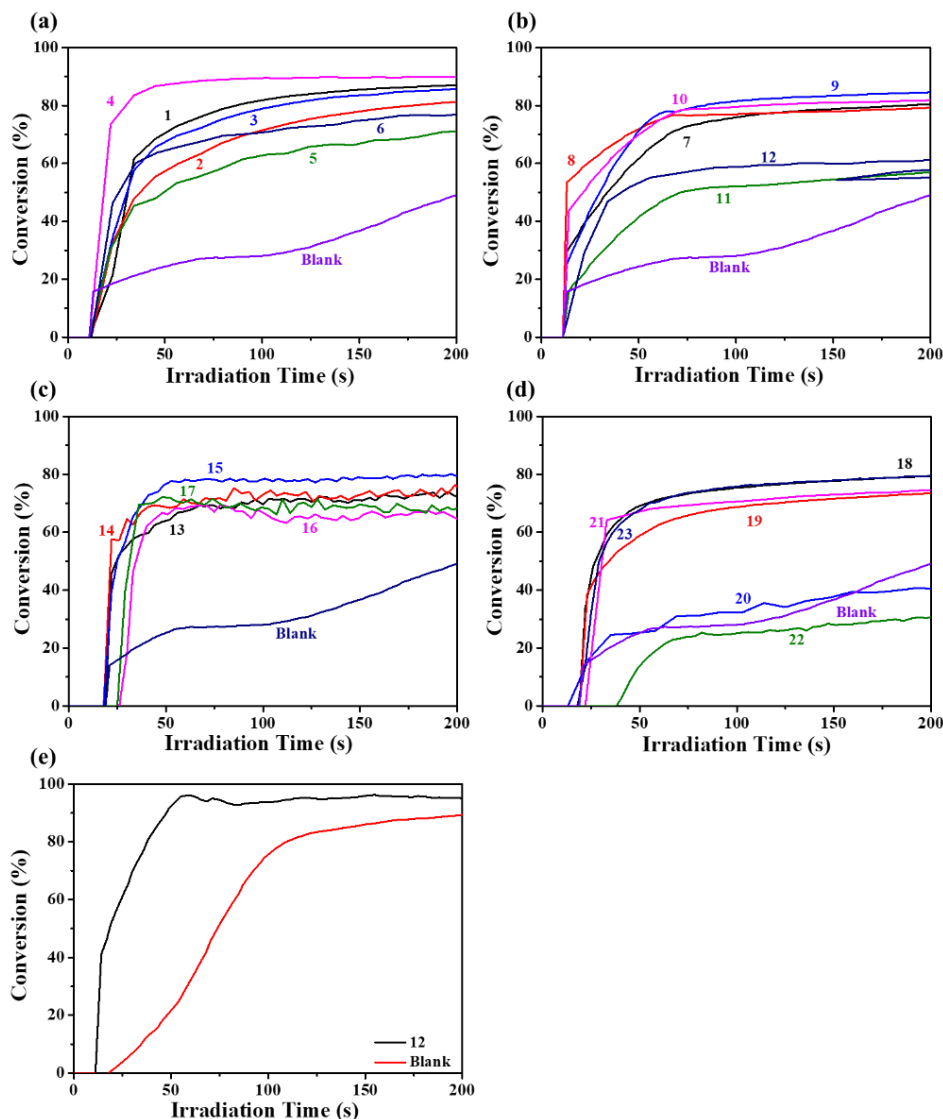


Figure II-1.1. Photopolymerization profiles of PEG-DA (conversions of C=C bonds vs irradiation time) initiated by Iod and EDB upon exposure to a LED@405 nm in laminate, at the same weight ratio chalcones 1-23: Iod: EDB = 1.5%:1.5%:1.5% in PEG-DA, in the presence of (a) methoxy-based chalcones (chalcones 1-6) in thin films; (b) iodine-based chalcones (chalcones 7-12) in thin films; (c) furane-based chalcones (chalcones 13-17) in thin films; (d) ferrocene-based chalcones (chalcones 18-23) in thin films; (e) chalcone 12 in thick molds. The blank control was initiated by Iod/EDB based PISs. The irradiation starts for $t = 15s$.

2. 3D Applications.

2.1 Direct laser write experiments by using chalcones based three-component PIS.

The FRP of PEG-DA could also be confirmed by the application in laser write experiments under air using the three-component PISs based on chalcones/Iod/amine (1.5%/1.5%/1.5%, w/w/w). Tridimensional letter patterns “C H E” were fabricated from PEG-DA initiated by the three-component PISs based on the selected reference chalcones (4, 8, 9, 10 and 12) upon irradiation at 405 nm with a laser. After that, a numerical optical microscope could be used to characterize the 3D patterns. As shown in [Figure II-1.2](#), the chalcone 12-based three-component PIS can easily write stable 3D PEG-based patterns with an excellent spatial resolution under a very short irradiation time due to its high photosensitivity. Contrarily to chalcone 12, chalcones 4, 9, 10 could still induce efficient photopolymerization processes in the irradiated area but required longer irradiation time to produce 3D patterns (always with an excellent spatial resolution). Finally, chalcone 8 proved to be ineffective to form a complete and stable 3D product, irrespective of the irradiation time.

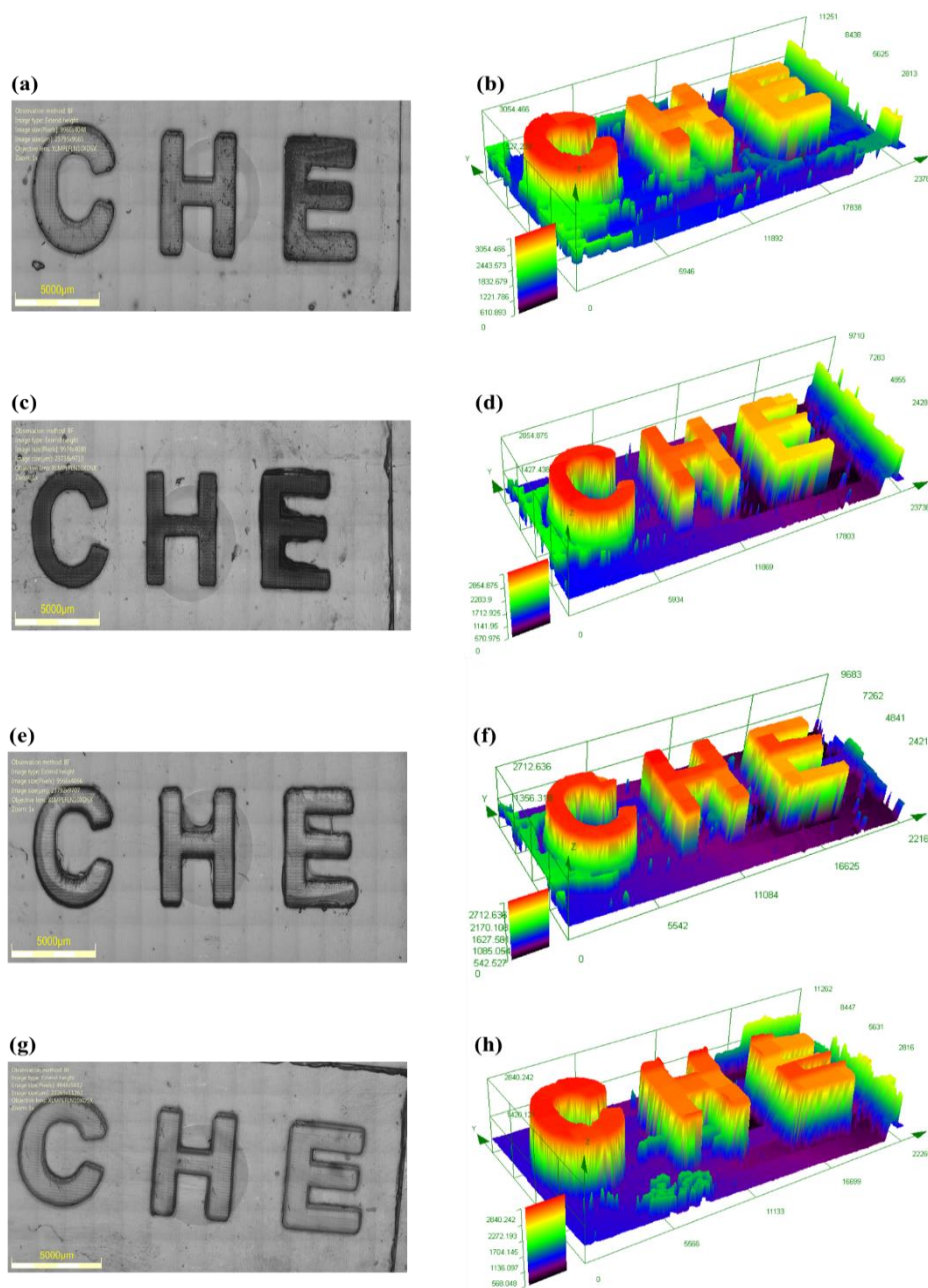


Figure II-1.2. FRP for laser write initiated with chalcones based three-component PISs using PEG-DA as the monomer. Characterization of the 3D patterns by numerical optical microscopy: (left) top surface morphology (right) 3-D overall appearance of color pattern using chalcones/Iod/EDB (1.5%/1.5%/1.5%, w/w/w): (a) (b) chalcone 4; (c) (d) chalcone 9; (e) (f) chalcone 10; (g) (h) chalcone 12.

2.2 The swelling kinetics of obtained PEG-polymers.

The swelling kinetics of the PEG-polymers obtained using the three-component PISs based on the chalcones were investigated by immersing the products in deionized water for 24 h. As shown in the [Figure II-1.3](#), the rate of swelling of the products

gradually increased with time which reached a swelling equilibrium after 5 h. The highest swelling ratio was obtained with chalcone 12 approaching 61%; for products based on the chalcone 4, the swelling ratio was about 55%. However, the swelling ratio for products based on the chalcones 9 and 10 were very low, which just about 5%, this result may be due to the longer irradiation time when prepared the 3D patterns.

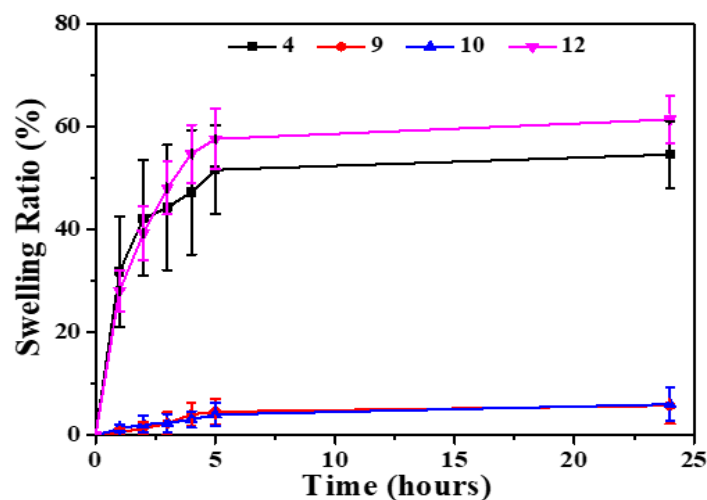


Figure II-1.3. The swelling ratio of PEG-polymer prepared using chalcones 4, 9, 10 and 12 as PIs (with chalcone/Iod/amine: 1.5%/1.5%/1.5%, w/w/w).

3. Proposed Chemical Mechanisms.

According to the results of FRP and 3D patterning experiments, the four selected chalcones (4, 9, 10 and 12) were chosen for the following mechanism studies.

3.1 Light absorption properties of the chalcones in acetonitrile.

The UV-visible absorption spectra of chalcones (chalcones 4, 9, 10 and 12) in acetonitrile are presented in [Figure II-1.4](#), while their absorption maxima (λ_{\max}), extinction coefficients (ϵ_{\max}) at λ_{\max} and at the emission wavelength of the LED@405nm ($\epsilon_{@405\text{nm}}$) are listed in the [Table II-1.2](#). The maximum absorption of chalcones 4, 9, 10 and 12 appeared at 423 nm, 363 nm, 362 nm, and 344 nm, with the relevant extinction coefficients (ϵ_{\max}) of 21 190 $\text{M}^{-1}\text{cm}^{-1}$, 15 770 $\text{M}^{-1}\text{cm}^{-1}$, 18 870 $\text{M}^{-1}\text{cm}^{-1}$ and 16 950 $\text{M}^{-1}\text{cm}^{-1}$, respectively. The results indicate that the introduction of iodine could lead to strongly blue-shift transitions due to a minor resonance, and the lack of electron-donating ability of this group. The optimized geometries as well as the frontier orbitals (highest occupied molecular orbital [HOMO] and lowest unoccupied

molecular orbital [LUMO]) are shown in Table II-1.2. Both the HOMOs and LUMOs were strongly delocalized all over the π -conjugated systems clearly showing the π - π^* transition as being the lowest energy transition [5-6].

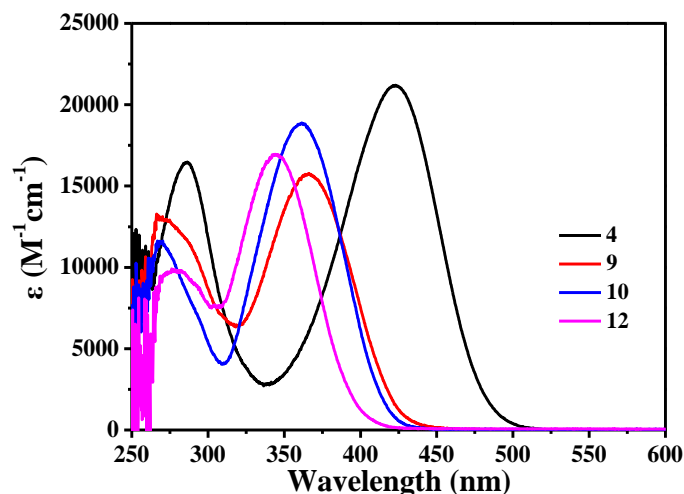


Figure II-1.4. The UV-visible absorption spectra of chalcones 4, 9, 10 and 12 in acetonitrile.

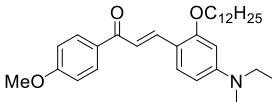
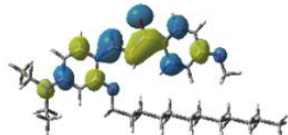
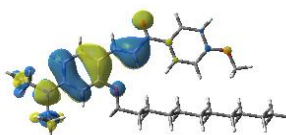
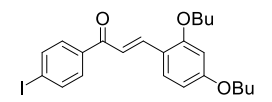
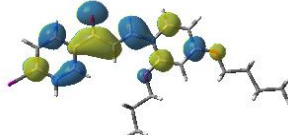
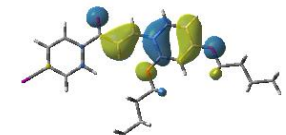
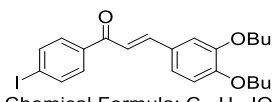
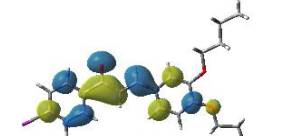
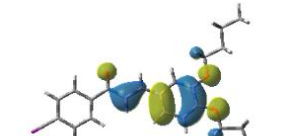
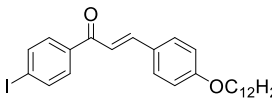
Chalcones	LUMO	HOMO	Absorption properties
 <p>Chemical Formula: $C_{32}H_{47}NO_3$ Molecular Weight: 493.7320</p> <p>chalcone 4</p>			$\lambda_{max} \sim 423 \text{ nm}$ $\epsilon_{max} \sim 21\,190 \text{ M}^{-1}\text{cm}^{-1}$ $\epsilon_{@405\text{nm}} \sim 18\,160 \text{ M}^{-1}\text{cm}^{-1}$
 <p>Chemical Formula: $C_{23}H_{27}IO_3$ Molecular Weight: 478.3705</p> <p>chalcone 9</p>			$\lambda_{max} \sim 363 \text{ nm}$ $\epsilon_{max} \sim 15\,770 \text{ M}^{-1}\text{cm}^{-1}$ $\epsilon_{@405\text{nm}} \sim 5800 \text{ M}^{-1}\text{cm}^{-1}$
 <p>Chemical Formula: $C_{23}H_{27}IO_3$ Molecular Weight: 478.3705</p> <p>chalcone 10</p>			$\lambda_{max} \sim 362 \text{ nm}$ $\epsilon_{max} \sim 18\,870 \text{ M}^{-1}\text{cm}^{-1}$ $\epsilon_{@405\text{nm}} \sim 4330 \text{ M}^{-1}\text{cm}^{-1}$
 <p>Chemical Formula: $C_{27}H_{35}IO_2$ Molecular Weight: 518.4795</p> <p>chalcone 12</p>			$\lambda_{max} \sim 344 \text{ nm}$ $\epsilon_{max} \sim 16\,950 \text{ M}^{-1}\text{cm}^{-1}$ $\epsilon_{@405\text{nm}} \sim 790 \text{ M}^{-1}\text{cm}^{-1}$

Table II-1.2. Contour plots of HOMOs and LUMOs for chalcones 4, 9 and 10 structures optimized at the B3LYP/6-31G* level of theory and their light absorption properties in

acetonitrile: maximum absorption wavelengths λ_{\max} ; extinction coefficients at λ_{\max} (ϵ_{\max}) and extinction coefficients at the emission wavelength of the LED@405 nm ($\epsilon_{@405\text{nm}}$).

3.2 Steady state photolysis of chalcones 4, 9, 10 and 12.

The steady-state photolysis experiments done with the chalcones (e.g.; chalcones 4, 9, 10 and 12) in the presence of the Iod and the amine were carried out in acetonitrile upon irradiation with a LED@405 nm. The effect of the Iod and the amine on the photolysis of the four chalcones are clearly shown in the **Figure II-1.5**. Obvious and significant declines of the UV-visible absorption intensity were observed for the three-component PISs based on the selected chalcones during light irradiation. Photolysis of chalcones 4, 9, 10 (the irradiation time \cong 10 s) were faster than that of the chalcone 12 (the irradiation time \cong 30 s) due to their higher molar extinction coefficients.

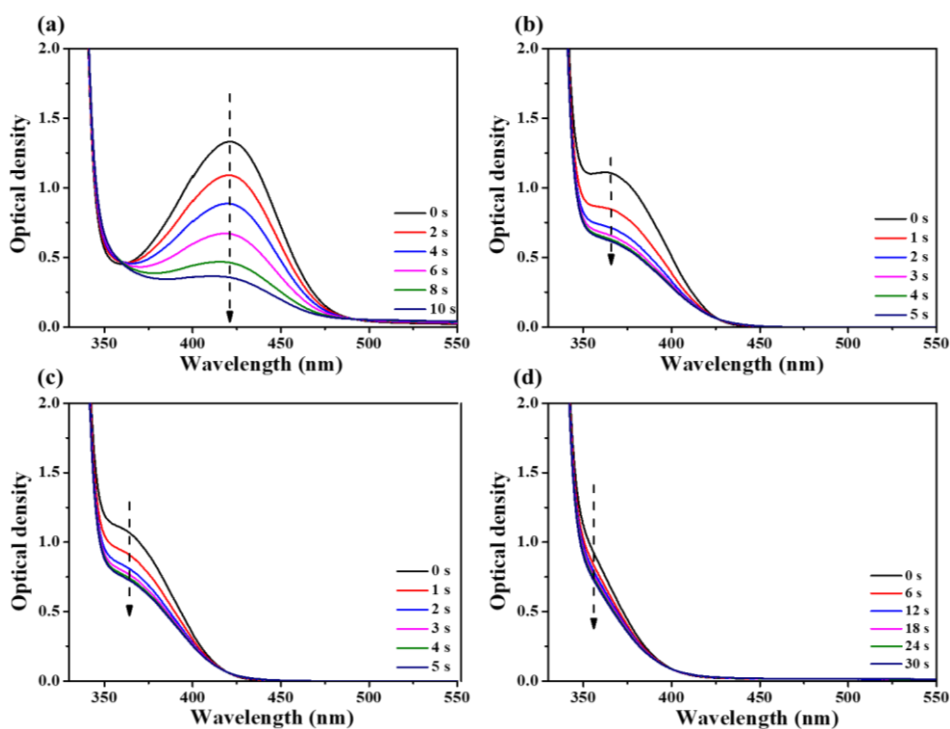


Figure II-1.5. Photolysis of chalcones (5×10^{-5} M) co-initiated with Iod (0.01 M) and EDB (0.01 M) upon exposure to LED@405 nm under air in the solvent of acetonitrile: (a) chalcone 4; (b) chalcone 9; (c) chalcone 10; (d) chalcone 12.

According to the proposed mechanism shown in **Scheme II-1.2**, the reaction process can be divided in two parts: 1) the chalcones combined with the iodonium salt, and 2) the chalcones combined with the aromatic amine. UV-visible absorption spectra

of the photolysis experiments done with the two-component PISs (chalcones/Iod and chalcones/amine) are presented in the [Figure II-1.6](#) and [Figure II-1.7](#), respectively. In the presence of Iod (the same iodonium salt which is used in the three-component PISs), the absorption of the chalcones' characteristic peaks significantly decreased upon light irradiation (see [Figure II-1.6](#)). Similarly, for the chalcones/amine systems (see [Figure II-1.7](#)), significant changes could be detected within a few seconds on the absorption spectra of chalcones 4, 9 and 10 and these significant changes can be assigned to their high molar extinction coefficients at 405 nm (e.g. $\epsilon_{@405} = 18160 \text{ M}^{-1}\text{cm}^{-1}$ for chalcone 4, $\epsilon_{@405} = 5800 \text{ M}^{-1}\text{cm}^{-1}$ for chalcone 9 and $\epsilon_{@405} = 4330 \text{ M}^{-1}\text{cm}^{-1}$ for chalcone 10, respectively; see [Table II-1.2](#)). Conversely, the photolysis process of chalcone 12 was very slow so that no significant change of the absorption under the same irradiation conditions could be observed.

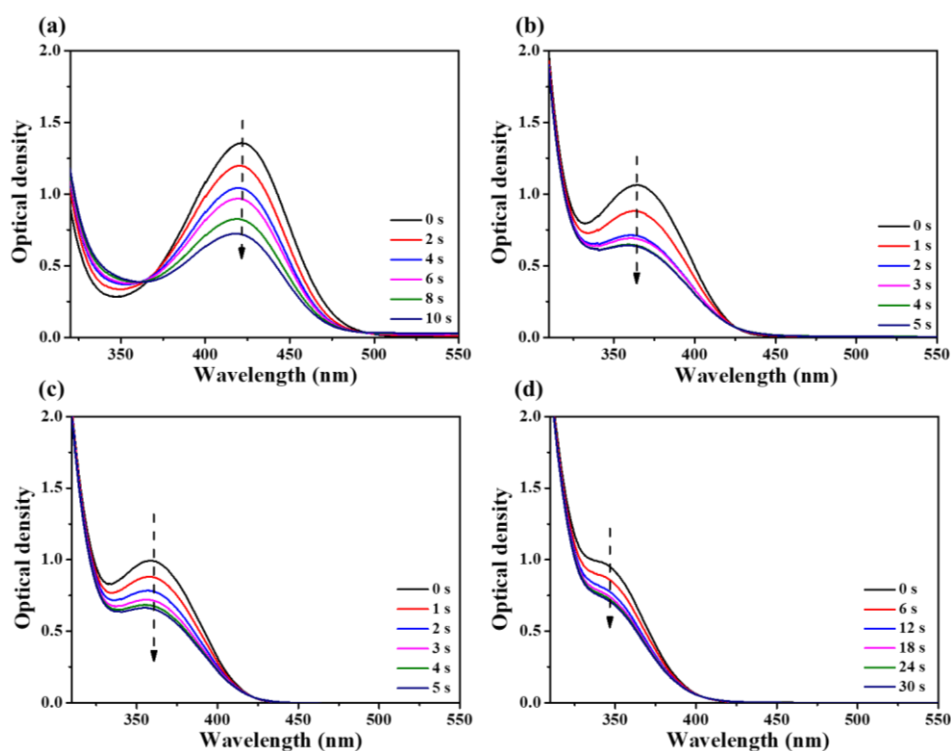


Figure II-1.6. Photolysis of chalcones ($5 \times 10^{-5} \text{ M}$) only in the presence of with Iod (0.01 M) upon exposure to LED@405nm under air in the solvent of acetonitrile: (a) chalcone 4; (b) chalcone 9; (c) chalcone 10; (d) chalcone 12.

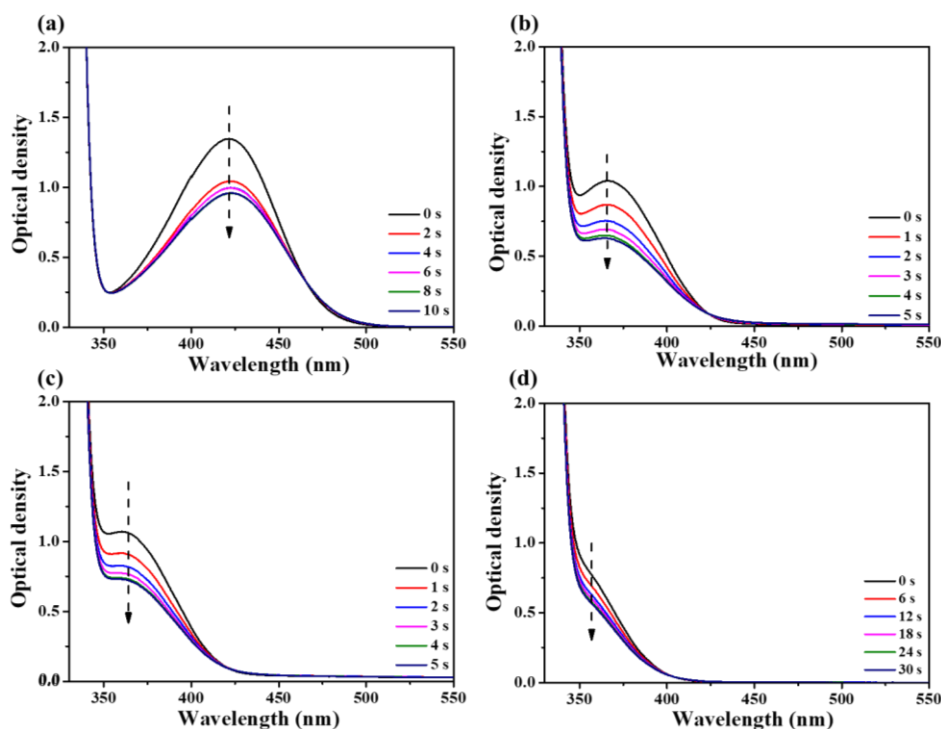


Figure II-1.7. Photolysis of chalcones (5×10^{-5} M) only in the presence of EDB (0.01 M) upon exposure to LED@405nm under air in the solvent of acetonitrile: (a) chalcone 4; (b) chalcone 9; (c) chalcone10; (d) chalcone 12.

According to the UV-visible absorption spectra presented above, we can summarize the consumption of the chalcones *vs.* the irradiation time. Absorption changes detected in their UV-visible absorption spectra were examined both for the three-component PISs (chalcones/Iod/amine) and the two-component ones (chalcones/Iod or chalcones/amine, see [Figure II-1.8](#)). For the three-component systems, we proposed that r1, r2 and r3 occurred. Reactions giving rise to the different radicals generated during photolysis are presented in the [Scheme II-1.2](#). It is obvious from the [Figure II-1.8a](#) that the consumption of chalcone 4 achieved by the three-component PIS (chalcone 4/Iod/amine) was much higher than that observed for the two-component PIS based on chalcone 4/Iod and chalcone 4/amine combinations (e.g. the consumption of chalcone 4 = 71.0% for chalcone 4/Iod/amine *vs* 46.6% for chalcone 4/Iod or 28.7% for chalcone 4/amine) which means that the interaction of three-component PIS based on chalcone 4 was more efficient than the two-component PIS.

As shown in the [Figure II-1.8b-c](#), for the same irradiation time, the consumption profile of chalcones 9 and 10 with the three-component PIS (chalcone 9/Iod/amine and chalcone 10/Iod/amine) were quite close to that reached when using the two-component PISs based on chalcone 9/Iod and chalcone 10/Iod or chalcone 9/amine and chalcone

10/amine combinations (e.g. the consumption of chalcone 9 and 10 reached at 40% - 45% and 30% - 35%, respectively), which indicated that the interactions of the three-component PIS based on chalcones 9 and 10 are on par with those of the two-component PIS.

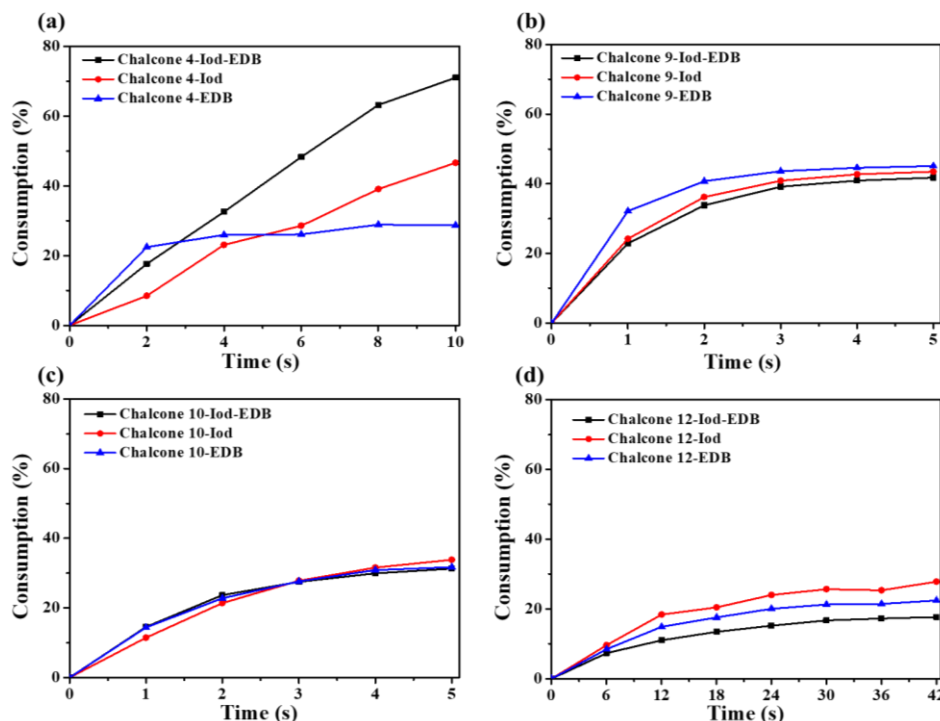
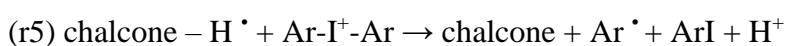
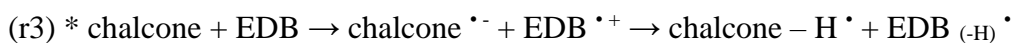
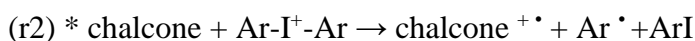
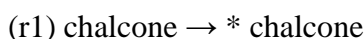


Figure II-1.8. Consumptions of (a) chalcone 4; (b) chalcone 9; (c) chalcone10; (d) chalcone 12 during the photolysis process.

Interestingly, as shown in the [Figure II-1.8d](#), the chalcone 12/Iod combination could achieve the highest consumption of chalcone (~27.7%), while the chalcone 12/Iod/amine three-component system led to the lowest consumption (~17.6%). It is proposed that $\text{EDB}^{\bullet+}$ radical can be formed by electron transfer from EDB, as an N-aromatic electron donor to chalcones (r4), as well as chalcones can be regenerated from chalcone- H^{\bullet} in the presence of iodonium salt (r5), which decelerated the consumption of chalcone 12.



Scheme II-1.2. Proposed photoinitiation mechanisms for the chalcones/Iod/amine redox combination.

3.3 Fluorescence quenching and ESR experiments to study electron transfer reaction for chalcones.

Fluorescence and UV-visible absorption spectra were measured in acetonitrile for chalcones 4, 9, 10 and 12 and the data are presented in the **Figure II-1.9**. Actually, the first singlet excited state energy (E_{S1}) can be determined by the crossing point between the absorption of the UV-*vis* and the fluorescence spectra (e.g. $E_{S1} = 2.62$ V for chalcone 4, 2.98 V for chalcone 9, 2.92 V for chalcone 10 and 3.15 V for chalcone 12; **Table II-1.3**).

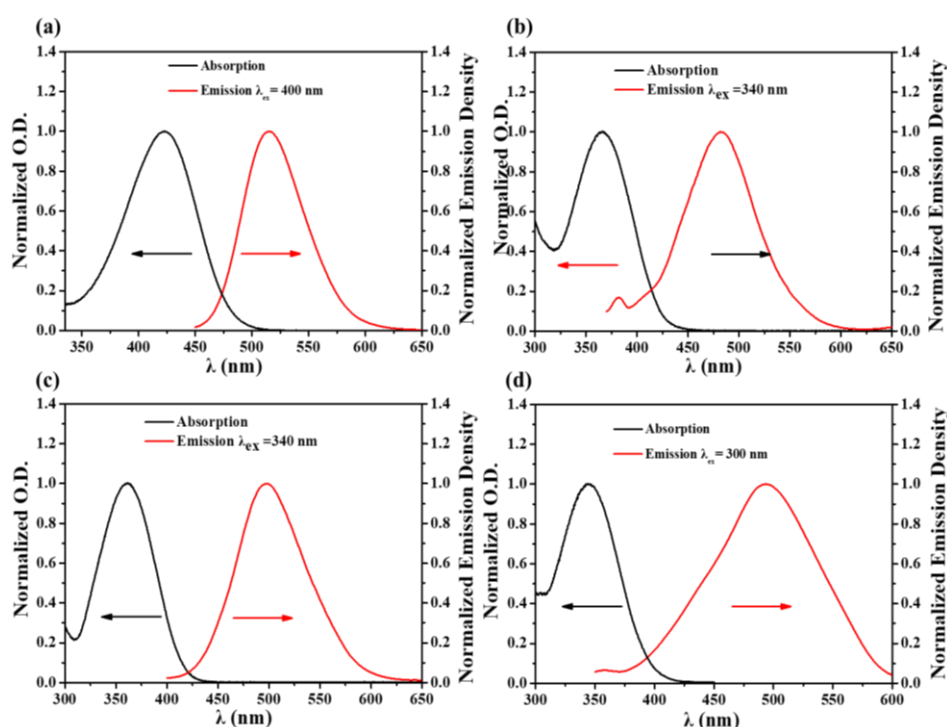


Figure II-1.9. Singlet state energy determination in acetonitrile of (a) chalcone 4; (b) chalcone 9; (c) chalcone 10; (d) chalcone 12.

Fluorescence quenching experiments for chalcones 4, 9, 10 and 12 have been realized in acetonitrile to seek the theoretical feasibility of interactions between chalcone/Iod and chalcone/EDB. The results are presented in **Figure II-1.10**. Fluorescence experiments of chalcone 4 showed a clear decrease of the fluorescence intensity as the quantity of the Iod or the amine increased in the solution, demonstrating that the addition of Iod or amine can interact with the chromophore in the excited singlet state. For chalcones 9 and 10, Iod also acted as a relatively good quencher, but with the amine added, the fluorescence intensity increased. More interestingly, there were no

fluorescence quenching observed for the two-component systems chalcone 12/Iod and chalcone 12/amine and even, an increase of the fluorescence intensity was observed upon addition of Iod or amine, suggesting the formation of a complex. Interaction constant (K_{SV}) is obtained through Stern Volmer plot according to the well-known equation [7-8], then electron transfer quantum yields (Φ_{et}^{Iod} and Φ_{et}^{EDB}) for the according reactions (r6, r7) were calculated from equations 6 and 7 (Table II-1.3).

$$\Phi_{et}^{Iod} = K_{sv}^{Iod} * [Iod] / (1 + K_{sv}^{Iod} * [Iod]) \quad (6)$$

$$\Phi_{et}^{EDB} = K_{sv}^{EDB} * [EDB] / (1 + K_{sv}^{EDB} * [EDB]) \quad (7)$$

	$K_{SV} (M^{-1})$	Φ_{et}^{Iod}	$K_{SV} (M^{-1})$	Φ_{et}^{EDB}	$E_{S1} (V)$
chalcone 4	96.70	0.75	65.47	0.85	2.62
chalcone 9	66.28	0.67			2.98
chalcone 10	103.20	0.76			2.92
chalcone 12					3.15

Table II-1.3. Parameters characterizing the fluorescence properties of chalcones 4, 9, 10 and 12 in acetonitrile: Interaction constant (K_{sv}) between chalcone-Iod and chalcone-EDB systems calculated by Stern–Volmer equation; electron transfer quantum yield (Φ_{et}^{Iod}) of chalcone/Iod interaction and (Φ_{et}^{EDB}) of chalcone/EDB interaction.

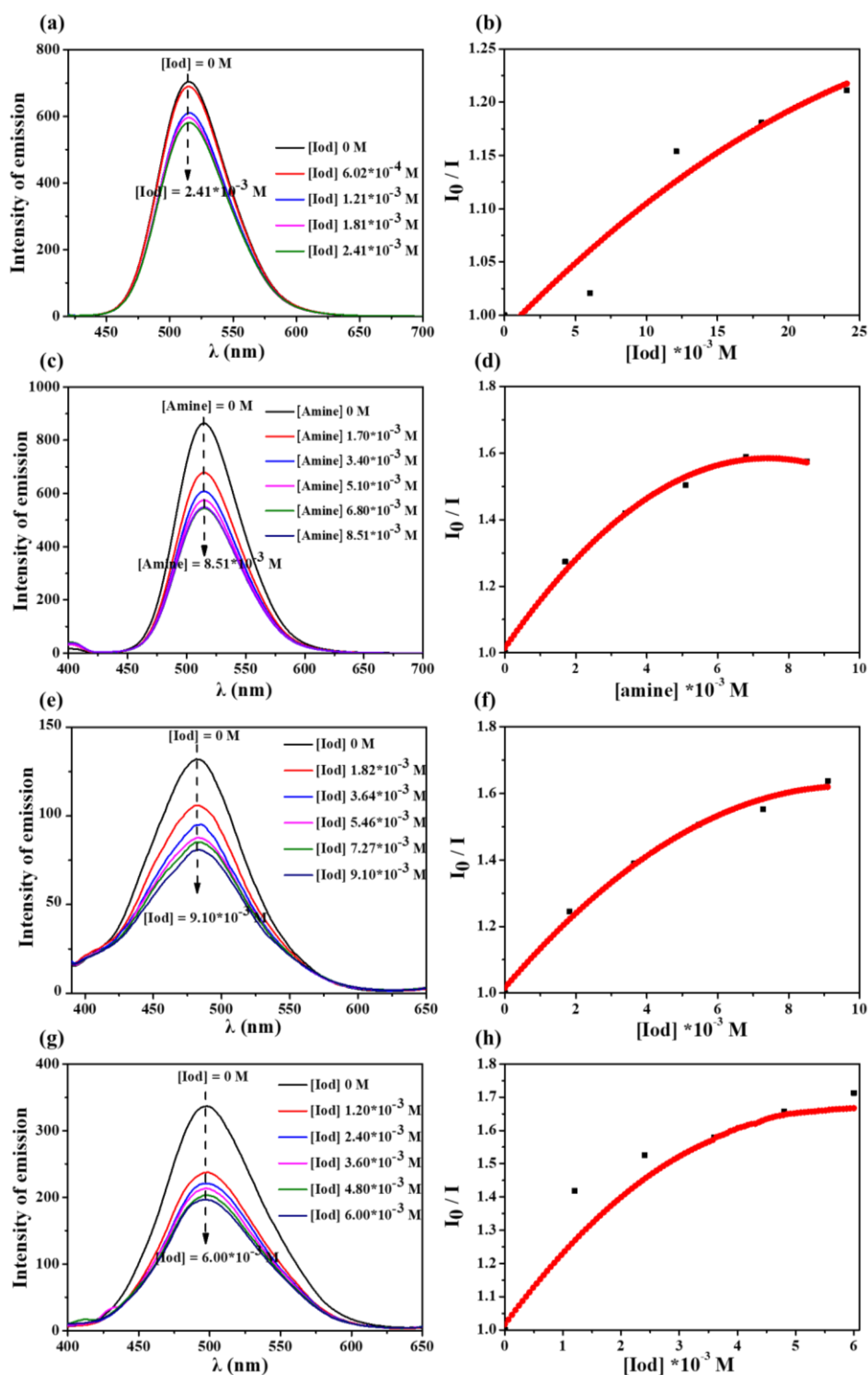


Figure II-1.10. (a) Fluorescence quenching of chalcone 4 by the Iod; (b) Stern–Volmer treatment for the chalcone 4/ Iod fluorescence quenching; (c) Fluorescence quenching of chalcone 4 by EDB; (d) Stern–Volmer treatment for the chalcone 4/EDB fluorescence quenching; (e) Fluorescence quenching of chalcone 9 by Iod; (f) Stern–Volmer treatment for the chalcone 9/ Iod fluorescence quenching; (g) Fluorescence quenching of chalcone 10 by Iod; (h) Stern–Volmer treatment for the

chalcone 10/Iod fluorescence quenching.

Remarkably, very high electron transfer quantum yields (Φ_{et}) are calculated (Table II-1.3) in agreement with efficient r2 and r3 processes. For chalcone 12, the formation of a complex probably governs the reactivity of the system.

To better understand the interactions taking place in the three-component system chalcone/Iod/amine interaction, ESR-spin trapping experiments were carried out on chalcone/Iod, chalcone/amine solutions under N_2 in the presence of N-phenyl tert-butyl nitron (PBN) as the spin trap agent. As shown in the Figure II-1.11, radical adducts were observed: hyperfine coupling constants for nitrogen and hydrogen of $a_N = 14.5$ G and $a_H = 2.2$ G were measured in the chalcone/Iod system; for the chalcone/amine system, the hyperfine coupling constants for nitrogen and hydrogen were characterized by $a_N = 14.4$ G and $a_H = 2.1$ G.

As reported in the literature, the PBN/aryl radical adduct is characterized by $a_N = 14.4$ and $a_H = 2.3$ G [9] which is presently in full agreement with r2 in the present ESR-ST experiments (Figure II-1.11b). Concerning the chalcone/amine system the hyperfine coupling constants given by the simulated spectrum (Figure II-1.11d) evidenced the generation of an aminoalkyl radical (r3) according to experimental data published elsewhere ($a_N = 14.4$ G and $a_H = 2.4$ G, [10]).

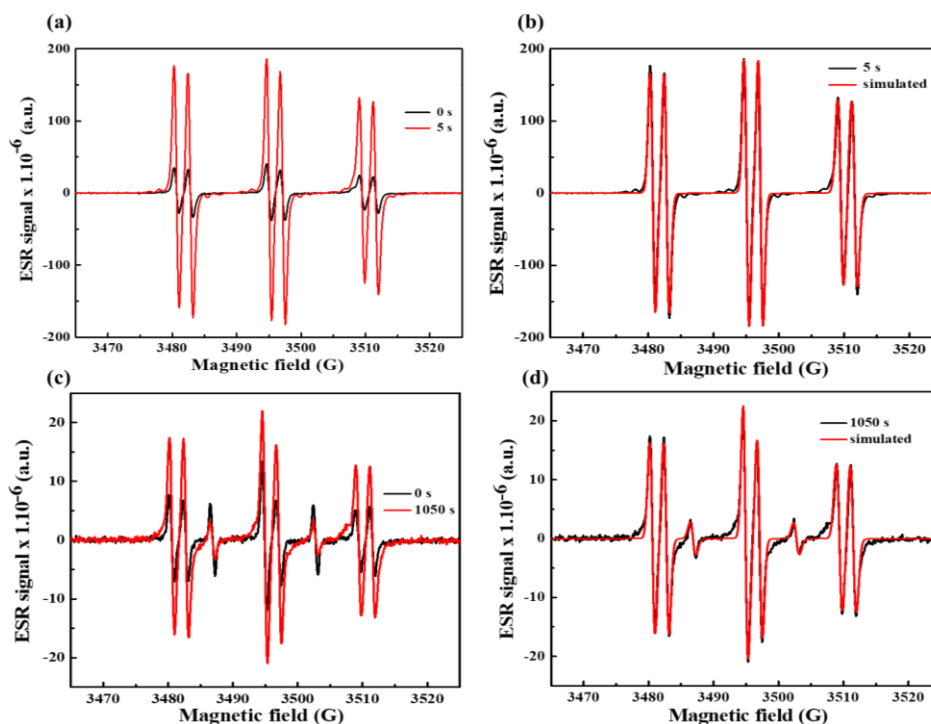


Figure II-1.11. ESR spectra obtained from ESR-spin trapping experiment using PBN = 2 mg/mL (as spin trap agent); EDB = 12.6 mg/mL; Iod = 12.6 mg/mL and chalcone 4 = 0.8 mg/mL in acetonitrile under N₂. (a), chalcone 4/Iod Irradiation time = 5 s (red) and = 0 s (black) spectra; (b) chalcone 4/Iod Irradiation time = 5 s (red) and simulated (black) spectra; (c) chalcone 4/EDB Irradiation time = 1050 s (red) and = 0 s (black) spectra; (d) chalcone 4/EDB Irradiation time = 1050 s (red) and simulated (black) spectra.

4. Conclusions.

In summary, the photoinitiation abilities of a series of three-component systems based on 23 different chalcones have been investigated using low intensity LED@405 nm as the light source. All chalcones exhibited a strong absorption in the visible light range and these structures proved to be very efficient for the free radical polymerization of acrylates under visible LEDs. Remarkably, chalcones 4, 9 and 10 were evaluated as reliable PI to promote efficient kinetics for the polymerization of PEG-DA while using an iodonium salt (Speedcure 938) as the electron-acceptor and EDB as the electron-donor in thin film (thickness ~0.1 mm); in addition, chalcone 12 proved to be the best candidate to promote efficient kinetics for the polymerization of PEG-DA under the same conditions in thick film (thickness ~1.8 mm). Radicals formed by the different PISs have been characterized by Fluorescence quenching and ESR-spin trapping experiments. The high performance of chalcones in radical initiating systems were also shown through the 3D printing resins specially designed with the three-component PISs previously studied. This work not only demonstrated the strong influence of the substitution pattern (*ortho*, *meta*, *para*-positions for the methoxy groups in chalcones 1-3), but also the choice of the different groups used to prepare chalcones (anthracene, ferrocene, alkoxy-substituted aromatic rings). With regards to the dramatic effect of the substitution on the photoinitiation abilities, no clear conclusions can be established at present, the best chalcones 4, 9, 10 and 12 drastically differing in their structures. However, their light absorption properties and their ability to be involved in redox processes (with iodonium or amine) appear as key factor for good reactivity. Other deactivation pathway (back electron transfer reaction) must be also probably taken into account. Conscious of the influence of the substitution pattern as well as the selection of the functional groups used as substituents on chalcones, future prospects will thus

consist in developing more extended families of chalcones to get a deeper insight into the exact role of these two parameters.

References:

1. Corakci, B.; Hacıoğlu, S. O.; Toppare, L.; Bulut, U. Long wavelength photosensitizers in photoinitiated cationic polymerization: The effect of quinoxaline derivatives on photopolymerization. *Polymer* **2013**, *54*(13), 3182-3187.
2. Anderson, J. A.; Hardgrove, E.; Cavitt, T. B.; Reeves, P. C. Photoinitiation of multifunctional acrylates via ferrocene-alkyl chloride charge transfer complexes. *Journal of Coatings Technology and Research* **2007**, *4*(1), 43-49.
3. Kabatc, J. Multicationic monomethine dyes as sensitizers in two-and three-component photoinitiating systems for multiacrylate monomers. *Journal of Photochemistry and Photobiology A: Chemistry* **2010**, *214*(1), 74-85.
4. Tehfe, M. A.; Lalevée, J.; Morlet-Savary, F.; Graff, B.; Blanchard, N.; Fouassier, J. P. Tunable organophotocatalysts for polymerization reactions under visible lights. *Macromolecules* **2012**, *45*(4), 1746-1752.
5. Wakasa, M.; Mochida, K.; Sakaguchi, Y.; Nakamura, J.; Hayashi, H. Fluorescence of silyl and germyl ketones and their primary photochemical processes. *The Journal of Physical Chemistry* **1991**, *95*(6), 2241-2246.
6. Abdallah, M.; Magaldi, D.; Hijazi, A.; Graff, B.; Dumur, F.; Fouassier, J. P.; Lalevée, J. Development of new high-performance visible light photoinitiators based on carbazole scaffold and their applications in 3d printing and photocomposite synthesis. *Journal of Polymer Science Part A: Polymer Chemistry* **2019**, *57*(20), 2081-2092.
7. Rehm, D.; Weller, A. Kinetics of fluorescence quenching by electron and H-atom transfer. *Israel Journal of Chemistry* **1970**, *8*(2), 259-271.
8. Atar, M.; Öngel, B.; Riedasch, H.; Lippold, T.; Neudörfl, J.; Sampedro, D.; Griesbeck, A. G. Intra-and intermolecular fluorescence quenching of alkylthio-substituted phthalimides by photoinduced electron transfer: distance, position and conformational dependence. *ChemPhotoChem* **2020**, *4*(1), 89-97.
9. Tehfe, M. A.; Lalevée, J.; Morlet-Savary, F.; Graff, B.; Blanchard, N.; Fouassier, J. P. Organic photocatalyst for polymerization reactions: 9, 10-bis [(triisopropylsilyl) ethynyl] anthracene. *ACS Macro Letters* **2012**, *1*(1), 198-203.
10. Zhang, J.; Wang, S.; Lalevée, J.; Morlet-Savary, F.; Lam, E. S. H.; Graff, B.; Xiao, P. 1, 2-Diketones as photoinitiators of both cationic and free-radical photopolymerization under UV (392 nm) or Blue (455 nm) LEDs. *Journal of Polymer Science* **2020**, *58*(6), 792-802.

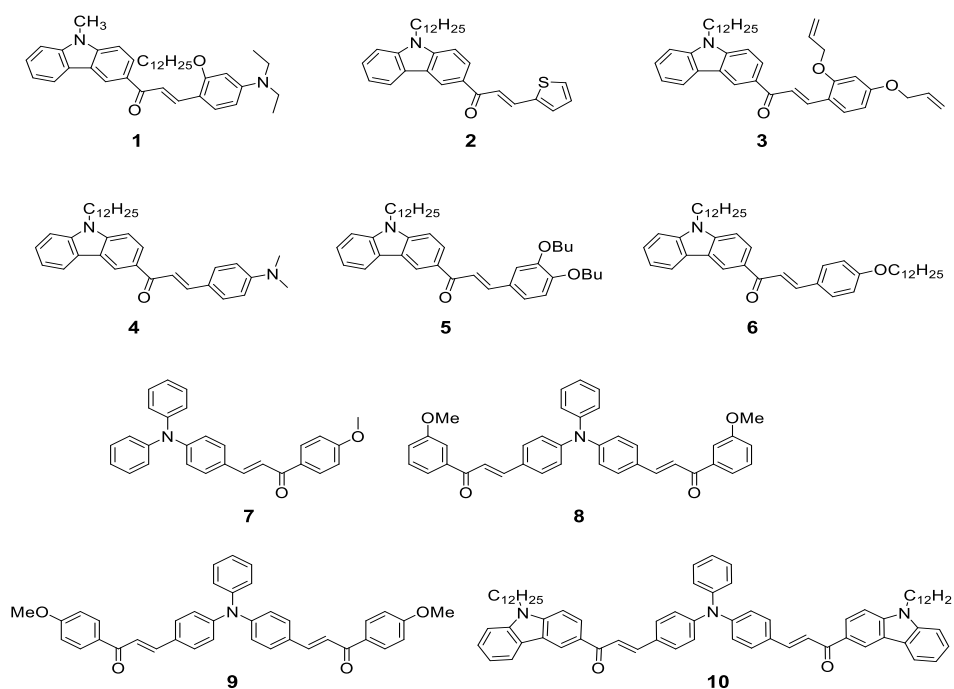
Chapter 2. Novel D- π -A and A- π -D- π -A Three-Component Photoinitiating Systems Based on Carbazole/Triphenylamino based Chalcones and Application in 3D and 4D Printing

In Chapter 1, we have demonstrated that several chalcones combined with an iodonium salt and an amine can act as suitable three-component PISs which present good near UV, visible light absorption properties and high efficiencies for the photopolymerization of acrylates under a LED@405 nm. However, most of the PISs based on chalcone/Iod/amine exhibit less-than-perfect performance upon LED@405 nm irradiation as these compounds have a maximum absorbance below 365 nm where the most common and cost-effective UV/LED lamps irradiate. Hence, in the present study, we wish to improve the absorption properties of chalcones including a red-shifted absorption and high molar extinction coefficients by introducing carbazole or triphenylamine (TPA) groups in the molecular structures [1-2].

Carbazole is an electron donor with a rigid, fully conjugated and planar structure, which has been extensively used in organic electronics due to its facile oxidation and its good hole-transport ability [3-4]. This group has also been extensively used for the design of PIs due to its interesting photophysical properties for radical chemistry [5-6]. Furthermore, triphenylamine (TPA) is one of the most applied electron donors in the design of organic dipolar chromophores and hole-transport materials for organic light-emitting diodes (OLEDs) [7-8]. When introducing a carbazole or TPA group into chalcone to form D- π -A or A- π -D- π -A (where D and A stand for donor and acceptor respectively) structures, an efficient intramolecular charge transfer (ICT) in the excited state can be observed. Considering that carbazoles and triphenylamines are excellent electron donors, the push-pull effect caused by the intramolecular interactions between the donor and the acceptor will lead to a strong charge delocalization all over the molecule, thus inducing the appearance of an intense transition in the visible region [9-10].

In this work, a series of ten chalcones comprising a carbazole unit or a triphenylamine (TPA) group used as the electron donor for chalcones were specifically designed (their chemical structures are shown in [Scheme II-2.1](#)). Remarkably, nine of the proposed chalcones were never reported in literature (never synthesized before).

Only chalcone 7 was reported but only as a precursor for the design of pyrazolines for optical materials [11]. As a result of this strategy, highly conjugated high-molecular-weight PIs were obtained, displaying improved light absorption properties due to their extended poly-aromaticity. These new PIs open new perspectives for the design of novel and efficient PIs. To evidence the interest of these new chalcones, 3D and 4D printing experiments were carried out with PEG-DA photosensitive resin comprising the best PISs investigated. Remarkably, reversible deformation effects on these 3D objects can be stimuli controlled (by hydration or heat) leading to 4D printing applications.



Scheme II-2.1. Chemical structures of chalcones 1-10 examined in this study.

1. Synthesis of Chalcones 1-10.

Chalcones are an important class of natural compounds exhibiting a variety of biological activities [12] so that the access to natural and non-natural structures has been the purpose of numerous researches. Accompanying this need, development of new synthetic methodologies to prepare chalcones has been extensively studied [13]. All chalcones presented in this study have been synthesized by a Claisen-Schmidt reaction between aldehydes **A1-A8** and aromatic ketones **K1-K4** under basic conditions [11]. Thus, by using an aqueous KOH solution and by performing the reactions in ethanol, the different chalcones **1-10** could be prepared with reaction yields ranging from 45% for chalcone 8 and 87% for chalcone 4 (see [Figure II-2.1](#)).

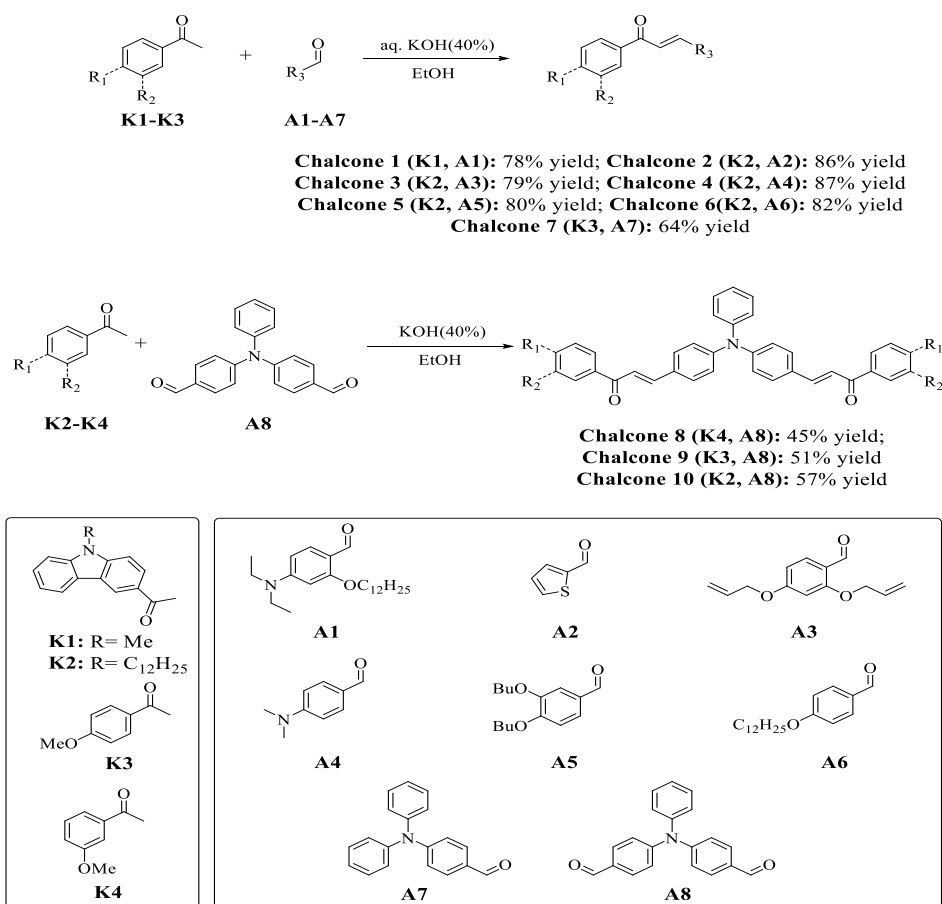


Figure II-2.1. Synthetic routes to chalcones 1-10.

2. Photoinitiation Ability of the Chalcones based PISs.

In order to study the ability of chalcones to act as photoinitiators with additives (Iod and EDB), RT-FTIR technique was used to monitor the associated polymerization profiles upon irradiation with a LED@405 nm. Four different photoinitiating systems were investigated: i) chalcone/Iod/amine (1.5%/1.5%/1.5%, w/w/w) three-component PISs, ii) chalcone / Iod (1.5%/1.5%, w/w) and chalcone/EDB (1.5%/1.5%, w/w) two-component PISs and iii) chalcones alone as PI (1.5% w/w) to initiate the FRP of PEG-DA monomers both in thin films (thickness ~ 0.1 mm) and thick films (thickness ~ 2 mm).

Under the same irradiation conditions, the samples containing only chalcones were not polymerized either in thick molds or thin films. After addition of EDB, the samples could be polymerized between thin films under LED@405nm, while all of them still weren't polymerized in thick molds (see [Figure II-2.2a](#)), which indicates that EDB can improve the polymerization efficiency when combined with chalcones. Furthermore, samples based on the two-component chalcones/Iod PISs and the three-component

chalcones/Iod/amine PISs would be polymerized efficiently both in the thick molds and thin films. In addition, the efficiencies of these two latter systems (chalcone/Iod and chalcone/Iod/EDB) are better than the other two systems (chalcone alone or chalcone/EDB). Typical acrylate function conversions vs irradiation time profiles are shown in [Figure II-2.2](#), and the corresponding final acrylate function conversions (FCs) are outlined in [Table II-2.1](#), respectively.

As shown in [Figure II-2.2d-e](#), the polymerization profiles of all the three-compound PISs are much better than the blank control which is only composed of the co-initiators (Iod, 1.5%, w/w and EDB, 1.5%, w/w), thus demonstrating the huge effect of the presence of the carbazole/TPA-based chalcones. Furthermore, by comparing [Figure II-2.2b-c](#), it's clear that the polymerization efficiency of the combination of chalcone / Iod (1.5% / 1.5%, w/w) is better than that of the three-component systems, which may be due to the fact that EDB competes with the electron-donating group inside the structure of chalcones to reduce the polymerization efficiency of the three-component PISs. Nevertheless, in comparison with the effectiveness of the final monomer conversions (in the [Table II-2.1](#)) and the rates of the polymerization reaction (the slope of the curves), much better efficiencies were achieved when using the chalcone 4 and 10 based two-component PISs (e.g.; FCs are 92% and 90%, respectively).

In the [Figure II-2.2e](#), RT-FTIR monitoring of the polymerization process for the 10 different chalcones in thick molds was extended until 600 s due to the lower efficiency of the three-component systems in these thick sample conditions. Indeed, compared to the blank control which is capable to furnish a FC of 93%, all the three-component systems furnished a lower final monomer conversion except the system based on chalcone 7 which provided a final conversion on par with that of the reference system (FC = 92%) and a higher polymerization rate. In addition, according to the [Figure II-2.2a-c](#), it's obvious that the polymerization profiles of these two-compound PISs based on chalcone / Iod are much better than that of the three-component systems except for chalcones 1, 2 and 8, which further prove that EDB can inhibit the generation of free radicals and reduce the efficiency of the free radical polymerization of PEG-DA monomers when combined with Iod and chalcones. Remarkably, the polymerization efficiency is straightforwardly related to the absorption properties of the chalcone derivatives as chalcones 4 and 7 were the leaders in the efficiency trend and also exhibit

the higher extinction coefficients at 405 nm, outperforming the others (see [Table II-2.2](#)).

More interestingly, the chalcone 7 based three-component PIS (chalcone/Iod/amine) and two-component PIS (chalcone/Iod) were able to induce the polymerization of PEG-DA monomers automatically in several minutes upon daylight without light irradiation in thick molds showing a huge photosensitivity; while this phenomenon does not occur in the presence of chalcone 7/EDB based PIS or chalcone 7 based PI. In addition, all chalcones showed a yellow fluorescence during the photopolymerization process and the color of the polymers obtained after polymerization were clearly deepened or even changed to red or purple [14]. As chalcones 4, 7 and 10 demonstrated the highest efficiency for the thick molds and thin samples both in the combination with Iod or Iod/EDB, they were selected from the series of 10 chalcones for the following chemical mechanism investigation.

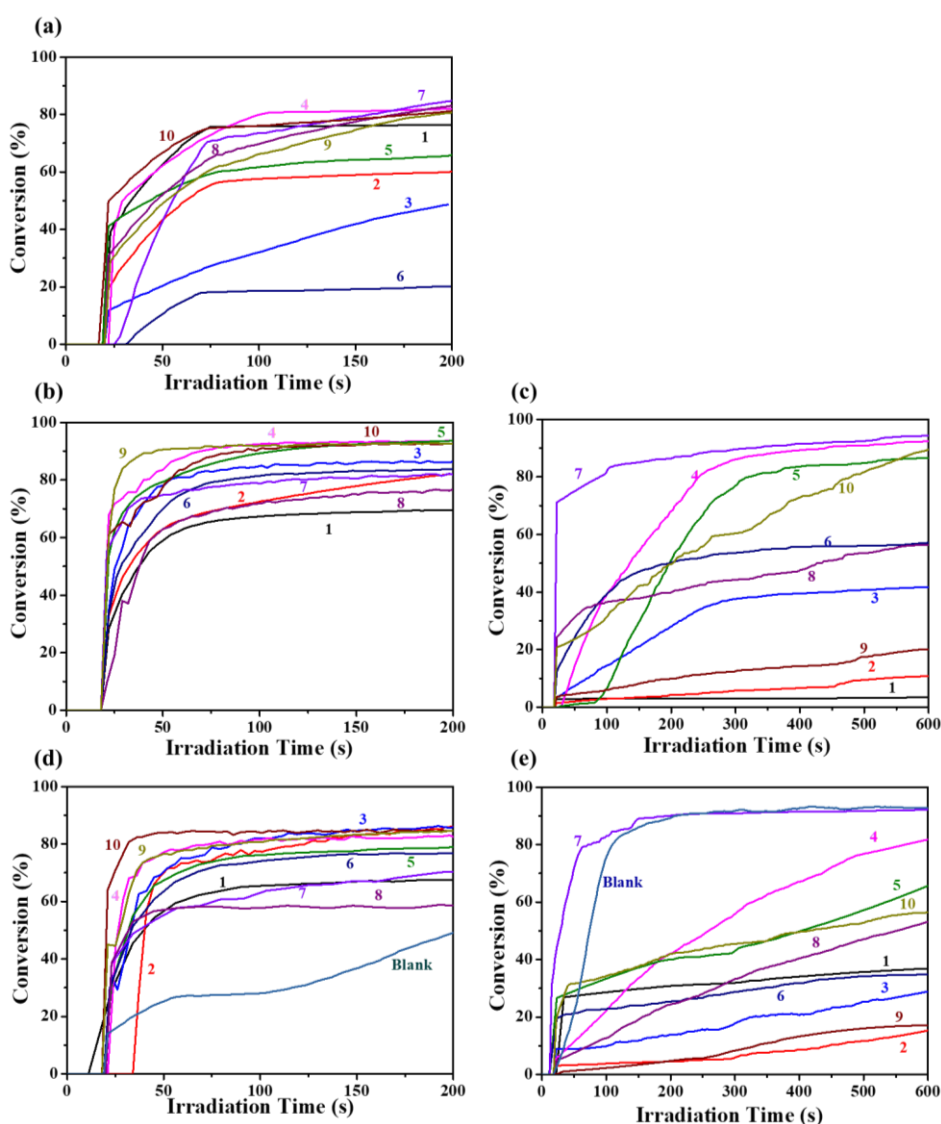


Figure II-2.2. Photopolymerization profiles of PEG-DA (acrylate function conversion vs irradiation time) upon exposure to a LED@405nm in laminate, initiated by chalcones 1-10 in the presence of (a) without any additive in thin films; (b) EDB in thin films; (c) Iod in thin films; (d) Iod in thick films; (e) Iod and EDB in thin films; (f) Iod and EDB in thick films, at the same weight ratio chalcones 1-10: Iod: EDB=1.5%:1.5 %:1.5%, w/w/w in 1g PEG, the irradiation starts for t = 20 s.

Final acrylate function conversions (FCs)				
chalcones	chalcone/Iod/EDB		chalcone/ Iod	
	Thin films (%)	Thick molds (%)	Thin films (%)	Thick molds (%)
1	68	37	70	3
2	86	15	82	10
3	86	29	87	42
4	82	82	94	92
5	79	66	94	87
6	77	52	84	57
7	71	92	82	94
8	58	53	77	56
9	85	17	93	20
10	85	77	93	90
Blank	50	93		

Table II-2.1. Summary of the final acrylate function conversion (FCs) obtained for the PEG-DA monomer while using the three-component PISs based on chalcones (1.5%, w/w)/Iod (1.5%, w/w)/amine (EDB, 1.5%, w/w) and using the two-component PISs based on chalcones (1.5%, w/w)/Iod (1.5%, w/w) both in thin films and in thick molds upon LED@405nm exposure in laminate.

3. Proposed Chemical Mechanisms.

3.1 UV-visible absorption properties of the chalcones in acetonitrile.

The ground state absorption spectra of the novel PIs (chalcones 1-10) in acetonitrile are shown in [Figure II-2.3](#), and the related parameters are presented in the [Table II-2.2](#). Except the four compounds chalcones 2, 3, 5 and 6 which exhibit high extinction coefficients around 360 nm, all the other compounds exhibit high extinction

coefficients (ϵ_{\max}) in the visible range (e.g.; 23 900 $\text{M}^{-1}\text{cm}^{-1}$ for chalcone 4, 18 740 $\text{M}^{-1}\text{cm}^{-1}$ for chalcone 7 and 9020 $\text{M}^{-1}\text{cm}^{-1}$ for chalcone 10). The maximum absorption of chalcones 4, 7 and 10 appeared around 408 nm, 405 nm and 430 nm, guaranteeing a good overlap with the emission spectrum of the LED@405 nm used in this work.

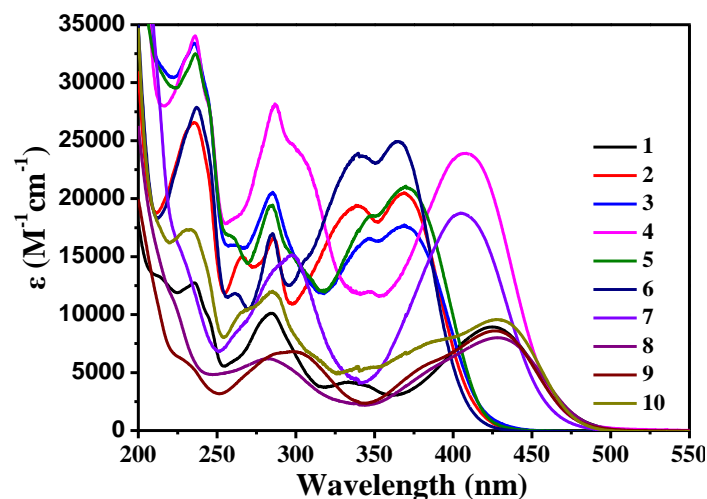


Figure II-2.3. The UV-visible absorption spectra of chalcones 1-10 in acetonitrile.

	λ_{\max} (nm)	ϵ_{\max} ($\text{M}^{-1}\text{cm}^{-1}$)	$\epsilon_{@405\text{nm}}$ ($\text{M}^{-1}\text{cm}^{-1}$)
chalcone 1	425	8930	7450
	285	10 120	
chalcone 2	369	20 520	4830
	266	15 000	
	235	26 560	
chalcone 3	369	17 740	5960
	285	20 550	
chalcone 4	408	23 900	23 850
	287	28 180	
chalcone 5	370	21 100	7020
	284	18 380	
chalcone 6	360	24 900	3530
	285	17 000	
	237	27 880	
chalcone 7	405	18 740	18 740
	300	15 180	
chalcone 8	430	7990	6760
	280	6210	
chalcone 9	428	8540	7200
	300	6820	
chalcone 10	430	10 500	9020
	285	12 030	

Table II-2.2. Light absorption properties of chalcones in acetonitrile in near UV/visible region: maximum absorption wavelengths λ_{\max} ; extinction coefficients at λ_{\max} (ϵ_{\max}) and extinction coefficients at the emission wavelength of the LED@405 nm ($\epsilon_{@405\text{nm}}$).

3.2 Steady state photolysis of chalcones.

The steady-state photolysis experiments of chalcones 4, 7 and 10 in the presence of an iodonium salt and an amine in acetonitrile have been carried out. Upon irradiation with a LED@405 nm, obvious and significant declines of the UV-visible absorption intensity were observed (Figure II-2.4a-c). Photolysis of chalcone 4 was so fast that it completely decomposed within 9 s, and then, the second is chalcone 7 that completely decomposed within 36 s, while for chalcone 10, the photolysis was relatively slower, with a complete decomposition after 180 s, owing to its lower extinction coefficients compared to that of chalcones 7 and 10 (see in Table II-2.2)

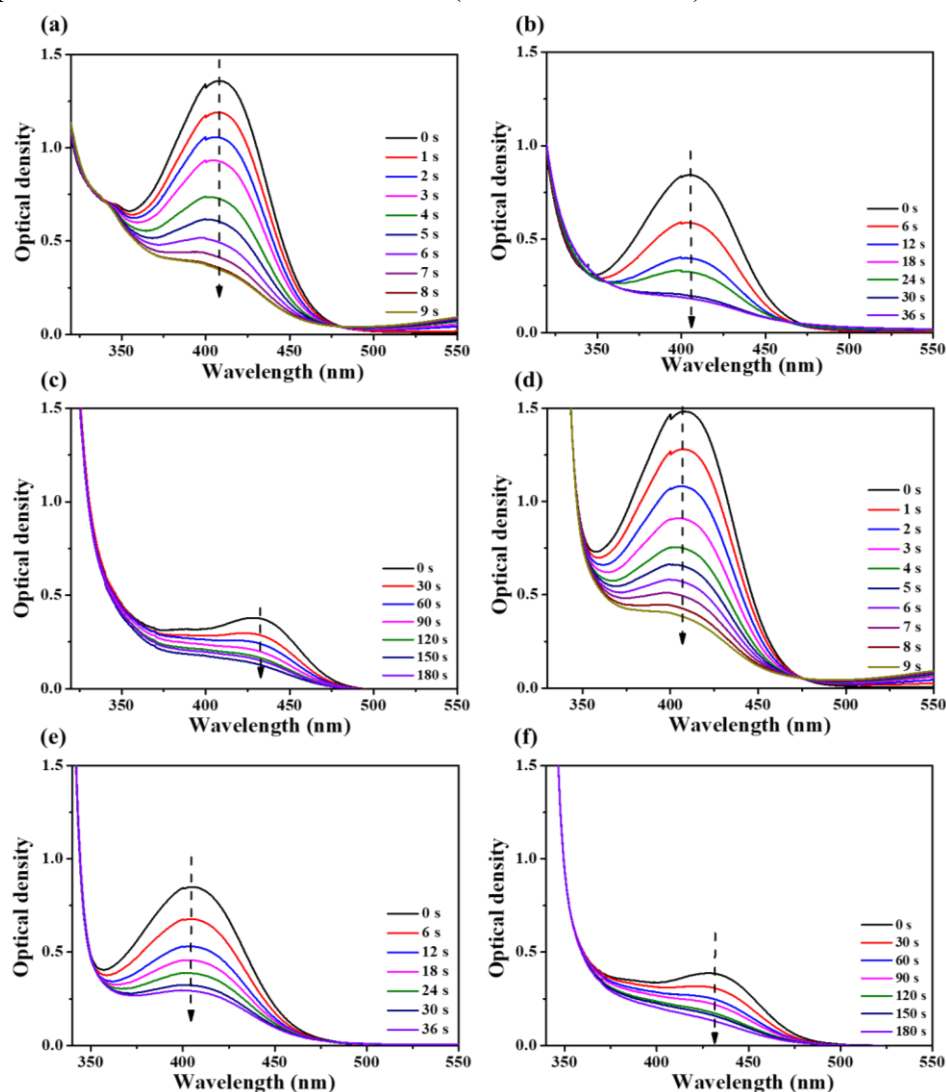


Figure II-2.4. Steady state photolysis of chalcones (5×10^{-5} M) upon exposure to a LED@405 nm under air in the solvent of acetonitrile: (a) chalcone 4/Iod/EDB; (b) chalcone 7/Iod/EDB; (c) chalcone 10/Iod/EDB; (d) chalcone 4/Iod; (e) chalcone 7/Iod; (f) chalcone 10/Iod.

To better understand the interaction of the iodonium salt or the amine with the chalcones in the different systems, steady state photolysis of chalcones combined with the iodonium salt or the amine independently was also studied. As shown in **Figure II-2.4d-f**, in the presence of Iod, similar to previously mentioned for the three-component PIS, intensity of the characteristic peaks of chalcones in the UV-visible absorption spectra significantly decreased and were completely photolyzed in a short time under light irradiation. However, for the chalcone/amine systems (**Annex II-2.1a-c**), only the absorption spectrum of chalcone 4 decreased upon light irradiation even though it's very slow, while for chalcones 7 and 10, the absorption spectra did not change for the same irradiation time, which may be due to the introduction of an electron donating group - a carbazole or a methoxyphenyl group into the electron-withdrawing group of chalcones reducing the reaction efficiency between chalcones and EDB [15].

In addition, upon the light irradiation, the absorption spectra of chalcone 4 itself decreased slowly which was similar to the chalcone 4/amine system, while for chalcones 7 and 10, like the chalcone/amine system, their absorption peaks did not change with the light irradiation (**Annex II-2.1d-f**). The above results indicate that an intramolecular charge transfer (ICT) can occur within the chalcone backbone and that chalcones can be combined with EDB to induce a reduction reaction (amine is electron donor), but all these reactions are poor and slow compared to the chalcone/Iod interaction.

As shown in the **Figure II-2.5**, a summary of the consumption of the chalcones vs. the irradiation time based on the abovementioned photolysis reactions (i.e. in different two and three-component systems) is provided. It is obvious that the highest consumption of chalcones 7 and 10 is achieved by the chalcones/Iod combinations (e.g. the consumption of chalcone 7 = 78% for chalcone 7/Iod, the consumption of chalcone

10 = 64% for chalcone 10/Iod), then, followed by that of the three-component PISs (chalcones/Iod/EDB) (e.g. 65% for chalcone7/ Iod/EDB and 55% for chalcone10/ Iod/EDB). However, for the same irradiation time, there were almost no consumption of chalcones 7 and 10 when using the two-component PISs based on chalcone 7/EDB and chalcone 10/ EDB or the PI based on chalcones 7 and 10 itself due to the weak interaction between chalcones and EDB as well as the weaker electron transfer within themselves. It is thus proposed that the two reactions r1 and r2 (shown in the [Scheme II-1.2, P72](#)) occurred for the chalcones 7 and 10/Iod based two-component PIS as well as for the chalcones 7 and 10/Iod/amine based three-component PIS during the photolysis process. According to the [Figure II-2.5a](#), the chalcone 4/Iod combination and the chalcone 4/Iod/EDB combination achieved the highest consumption of chalcone (~74%) together, while the chalcone 4/amine system led to the lowest consumption (~19%). Furthermore, the consumption of chalcone 4 itself (21%) is slightly higher than that of chalcone 4/amine system. EDB can be involved in (r3) but also in the regeneration of the chalcone through (r4). Chalcones can also be regenerated from chalcone-H[•] in the presence of iodonium salt (r5).

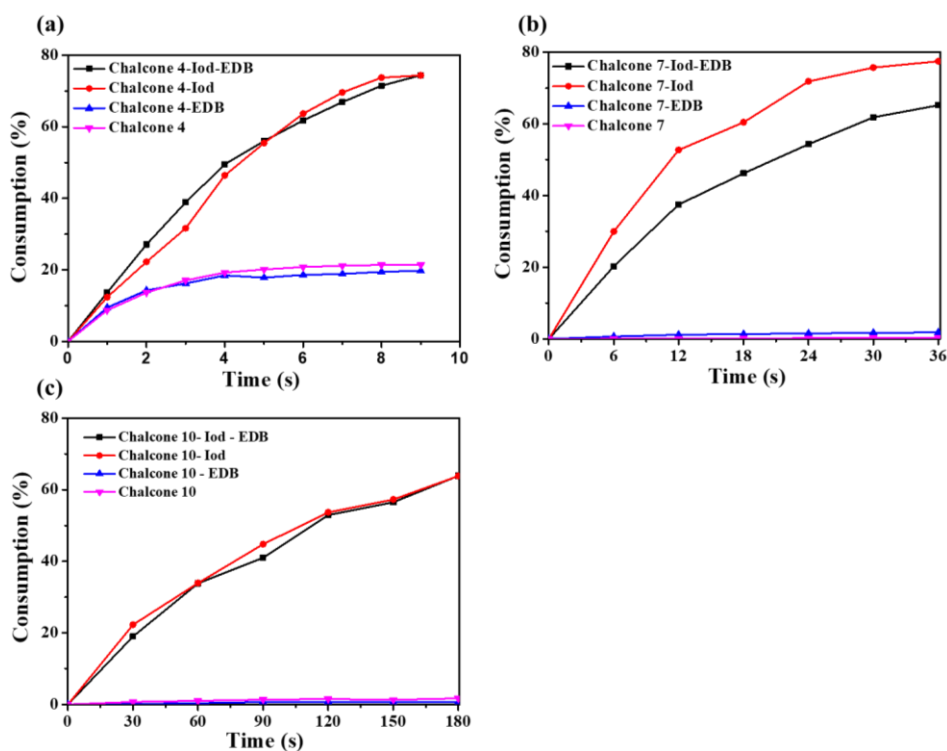


Figure II-2.5. Consumption of (a) chalcone 4; (b) chalcone 7; (c) chalcone 10 during

the photolysis process.

3.3 Fluorescence quenching experiments and cyclic voltammetry to study electron transfer reaction in chalcone based systems.

The first singlet excited state energy (E_{S1}) of chalcones 4, 7 and 10 can be determined by the crossing point between the UV-visible absorption and the fluorescence spectra in acetonitrile, the data are presented in the **Figure II-2.6** (e.g. $E_{S1} = 2.66$ V for chalcone 4, 2.60 V for chalcone 7 and 2.56 V for chalcone 10; **Table II-2.3**).

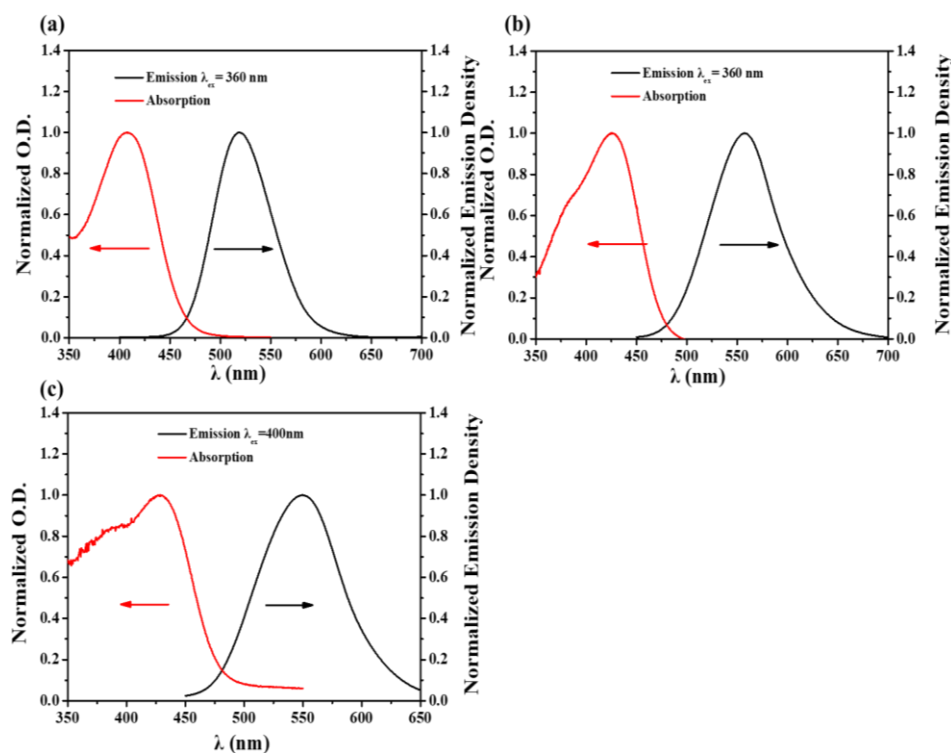


Figure II-2.6. Singlet state energy determination in acetonitrile of (a) chalcone 4; (b) chalcone 7; (c) chalcone 10.

Fluorescence quenching experiments for chalcones 4, 7 and 10 have been conducted in acetonitrile to seek the theoretical feasibility of an electron transfer reaction with the Iod [16]. As shown in **Figure II-2.7**, the upward curve of fluorescence quenching with the addition of Iod were observed for chalcones 4, 7 and 10 in acetonitrile, which seems more likely to be contributed by both static and dynamic quenching mechanisms simultaneously. Furthermore, favorable fluorescence quenching processes of the excited singlet states by Iod are shown by the high value of

the Stern–Volmer coefficients (K_{SV} , Table II-2.3) as well as the associated electron transfer quantum yield (ϕ_{et} , Table II-2.3) for the expected electron transfer reaction between the chalcones and Iod (r_2); ϕ_{et} were calculated applying the eq.6 or eq.7. Remarkably, very high electron transfer quantum yields (Φ_{et}) for chalcone 4 were calculated (Table II-2.3) in agreement with efficient r_2 and r_3 processes. Compared to chalcone 4, chalcone 7 and 10 showed lower electron transfer quantum yields (Φ_{et}), which can be probably attributed to a radiation-free excited state deactivation related to an aryl rings rotation [9, 17].

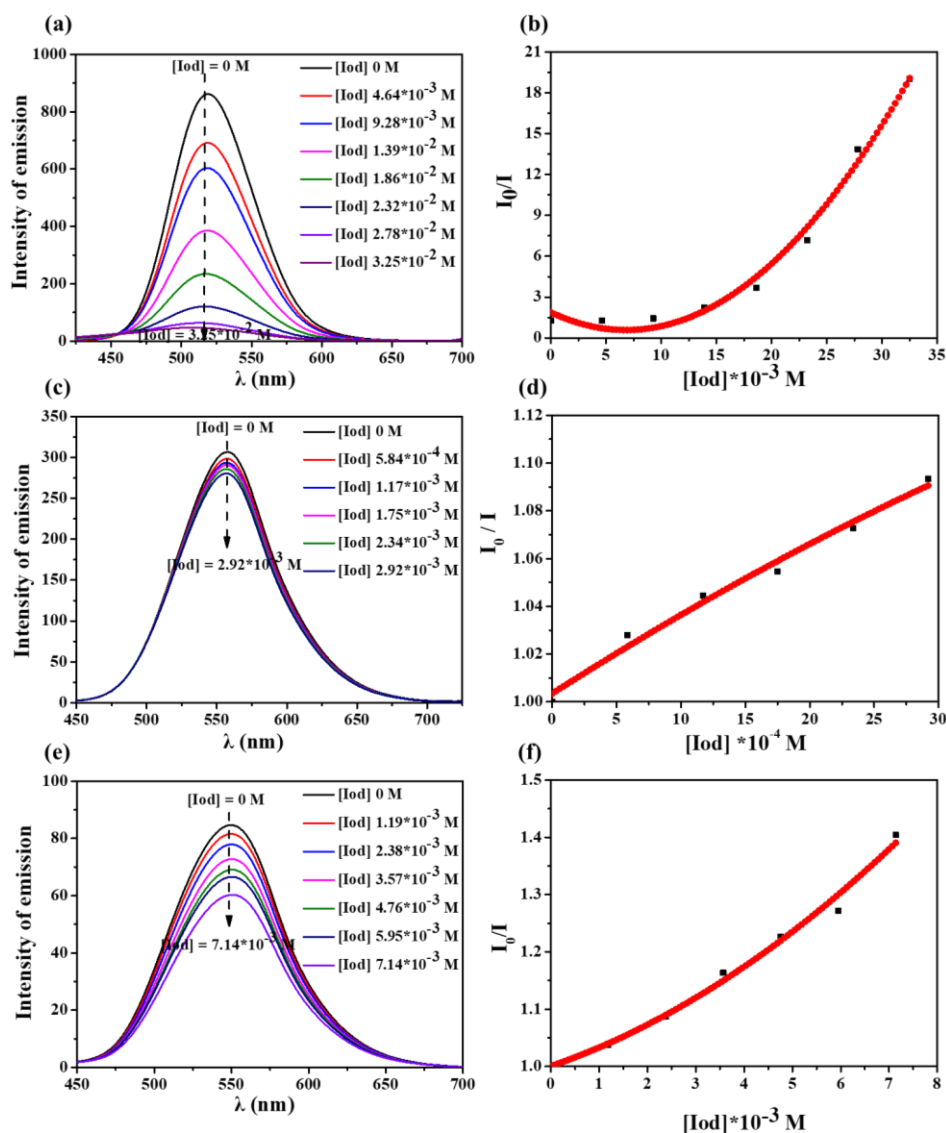


Figure II-2.7. (a) Fluorescence quenching of chalcone 4 by Iod; (b) Stern-Volmer treatment for the chalcone 4/Iod fluorescence quenching; (c) Fluorescence quenching of chalcone 7 by Iod; (d) Stern-Volmer treatment for the chalcone 7/Iod salt

fluorescence quenching. (e) Fluorescence quenching of chalcone 10 by Iod; (f) Stern-Volmer treatment for the chalcone 10/Iod salt fluorescence quenching.

	chalcone 4	chalcone 7	chalcone 10
$K_{SV}^{Iod} (M^{-1})$	240	29.9	54.8
Φ_{et}^{Iod}	0.88	0.48	0.63
$E_{S1} (V)$	2.66	2.60	2.56
$E_{T1} (V)$	2.12	2.05	2.05
$E_{ox} (V)$	0.73	0.99	0.83
$E_{red} (V)$	-0.68	-0.48	-0.06
ΔG_{S1}^{Iod}	-1.73	-1.41	-1.53
ΔG_{S1}^{EDB}	-0.98	-1.12	-1.5
ΔG_{T1}^{Iod}	-0.69	-0.86	-0.52
ΔG_{T1}^{EDB}	-0.44	-0.57	-0.99

Table II-2.3. Interaction rate constants (K_{sv}) of chalcone-Iod systems calculated by Stern-Volmer equation; electron transfer quantum yield (Φ_{et}^{Iod}) of chalcone/Iod interaction and singlet excited state energy (E_{S1}); oxidation potential (E_{ox}) and reduction potential (E_{red}) measured by cyclic voltammetry experiments as well as the parameters characterizing the chemical mechanisms associated with chalcones 4, 7 and 10 in acetonitrile.

For the mechanistic investigation, electrochemical reactions of chalcones 4, 7 and 10 were also examined by cyclic voltammetry. As shown in **Figure II-2.8**, a favorable electron transfer reaction occurs in chalcone/Iod with negative free energy changes: $\Delta G_{S1}^{Iod} = -1.73$ V, -1.41 V and -1.53 V for chalcones 4, 7 and 10, respectively (**Table II-2.3**). Electron transfer reactions also occurred in chalcone / EDB (e.g.; $\Delta G_{S1}^{EDB} = -0.98$ V, -1.12 V and -1.5 V for chalcones 4, 7 and 10 respectively, **Table II-2.3**). Furthermore, for chalcone 10, two oxidation peaks were observed in the positive potential range, which can be related to a further oxidation (not reversible) event at higher potentials [43]. The obtained LUMO/HOMO energy levels (Highest Occupied

Molecular Orbital HOMO and Lowest Unoccupied Molecular Orbital LUMO) are shown in [Annex II-2.2](#). The HOMO of chalcones 7 and 10 are located mainly over the TPA moiety. Concerning the LUMO, for chalcones 7 and 10, this orbital is centered over the enone and vinyl-substituted aryl groups. However, for chalcone 4, the HOMO and LUMO are mainly located over the enone and aryl substituted with dimethylamine moiety. Moreover, triplet state energy levels (E_{T1}) of chalcones were also simulated and the results are presented in [Annex II-2.2](#). By calculating the free energy change of triplet state ΔG^{T1} from equations 3 and 4, the reaction of triplet state of chalcones 4, 7 and 10 with iodonium salt and EDB are also favorable ($\Delta G_{T1}^{Iod} < 0$ and $\Delta G_{T1}^{EDB} < 0$ in [Table II-2.3](#)) always in agreement with [Scheme II-1.2](#) for the proposed mechanisms.

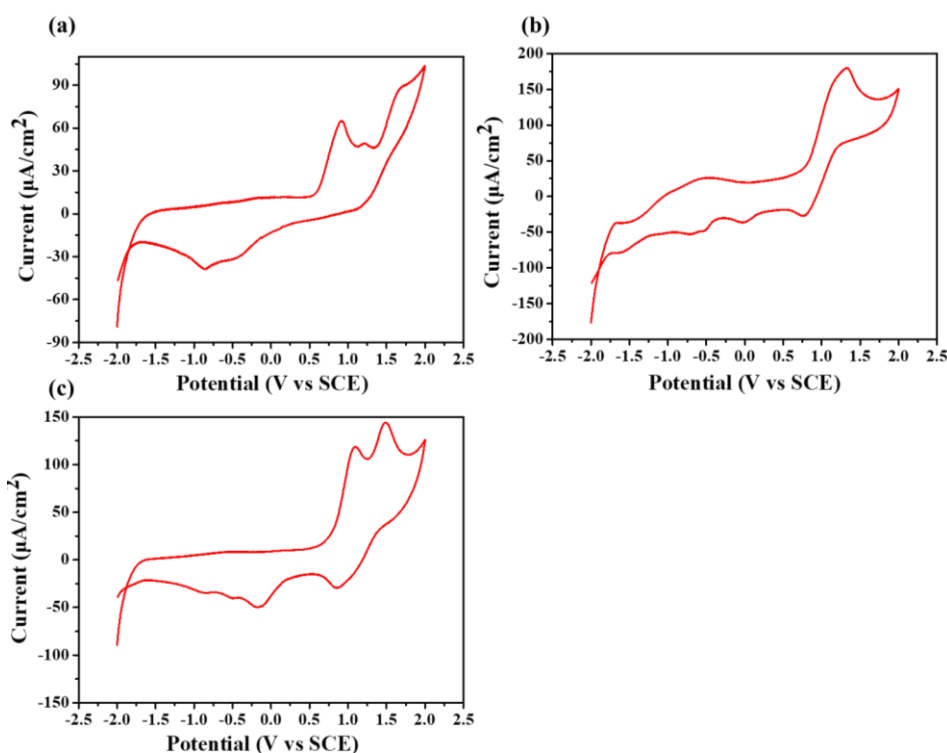


Figure II-2.8. Cyclic voltammograms of chalcones 4, 7 and 10 in acetonitrile solvent against saturated calomel electrode (SCE) under a nitrogen saturated atmosphere. (a) chalcone 4; (b) chalcone 7; (c) chalcone 10.

3.4 ESR experiments: free radicals generated in chalcone based systems.

To better understand the interactions that took place in the different PISs, ESR-spin trapping (ESR-ST) experiments were carried out on chalcones 4, chalcone 4/Iod, chalcone 4/amine and chalcone 4/Iod/EDB solutions under N_2 in the presence of *N*-

phenyl-*tert*-butyl nitron (PBN) as the spin trap agent. As shown in the **Figure II-2.9a-b**, in the presence of Iod and EDB, r2 and r3 occur: aryl radical and aminoalkyl radical adducts were clearly observed in ESR-ST [16, 18]. For the chalcone/Iod system (**Figure II-2.9c-d**), the PBN/aryl radical adduct is characterized by $a_N = 14.4$ G and $a_H = 2.2$ G [16], which is presently in full agreement with r2. While for the chalcone/EDB system (**Annex II-2.3a-b**), the hyperfine coupling constants for nitrogen and hydrogen were characterized by $a_N = 14.4$ G and $a_H = 2.1$ G that evidenced the generation of an aminoalkyl radical (r3) according to experimental data published elsewhere ($a_N = 14.1$ G and $a_H = 2.1$ G [18]). In addition, as shown in **Annex II-2.3c-d**, efficient intramolecular reactions occur in chalcones alone upon irradiation and radical adducts can also be observed (hyperfine coupling constants for nitrogen and hydrogen of $a_N = 14.4$ G and $a_H = 2.2$ G) in agreement with the photolysis of chalcones alone.

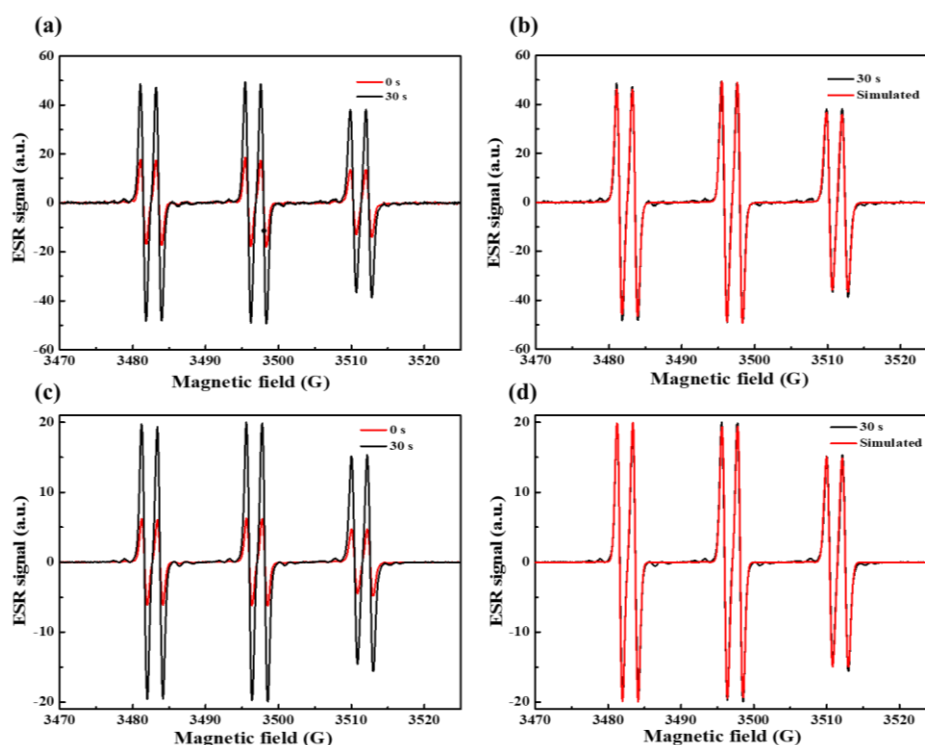


Figure II-2.9. ESR spectra obtained from ESR-spin trapping experiment using PBN = 2 mg/mL (as spin trap agent); Iod = 12.6 mg/mL; EDB = 12.6 mg/mL and chalcone 4 = 0.8 mg/mL in *tert*-butylbenzene under N_2 . (a) chalcone 4/Iod/EDB Irradiation time = 0 s (red) and = 30 s (black) spectra; (b) chalcone 4/Iod/EDB Irradiation time = 30 s experimental (black) and fitting (red) spectra; (c) chalcone 4/Iod Irradiation time = 0 s

(red) and = 30 s (black) spectra; (d) chalcone 4/Iod Irradiation time = 30 s experimental (black) and fitting (red) spectra.

4. 3D and 4D applications.

4.1 3D Printing experiments based on the two-component PISs.

Using a laser diode @405 nm, laser write experiments were successfully carried out under air with the two-component PIS based on chalcones/Iod (1.5%/1.5%, w/w), which is very reactive for the FRP of PEG-DA monomer. Remarkably, the high photosensitivity of chalcones 4, 7 and 10/Iod based PISs allowed the PEG-DA monomer to be effectively polymerized in 3D structures to obtain a stable 3D patterns (“C H E”) with a high spatial resolution ($\sim 50 \mu\text{m}$ corresponding to the size of the laser beam and the smallest objects observed) and for a very short irradiation time ($t \leq 2 \text{ min}$) (see [Figure II-2.10](#)).

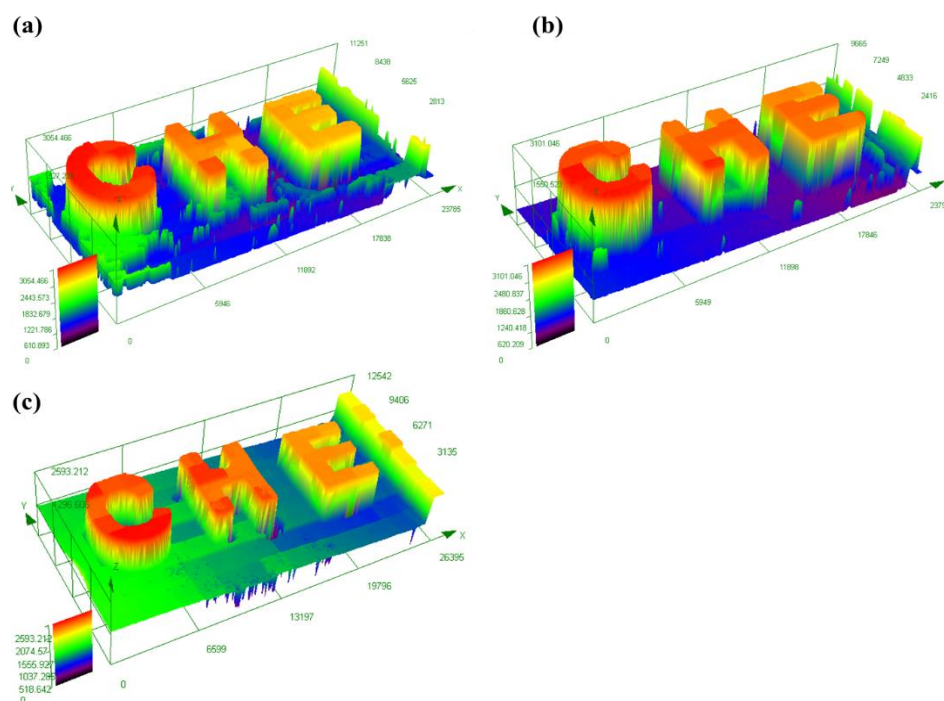


Figure II-2.10. Free radical photopolymerization experiments for laser write of 3D patterns initiated by chalcones based two-component PISs using PEG-DA monomer. Characterization by numerical optical microscopy of the morphology of the 3D overall appearance of 3D patterns with chalcones/Iod (1.5%/1.5%, w/w) in PEG-DA: (a) chalcone 4; (b) chalcone 7; (c) chalcone 10.

4.2 The swelling of PEG-polymer initiated by chalcone/Iod.

According to the [Figure II-2.11a](#), the swelling of the PEG-polymers obtained by photopolymerization using the two-component PIS based on chalcones/Iod (1.5%/1.5%, w/w) were investigated by immersing them into deionized water for 24 h. The highest swelling ratio was obtained with chalcone 10 approaching 80%, then, followed by the products based on the chalcone 7 and chalcone 4, the swelling ratios of them were about 60%, which is due to the higher extinction coefficients at the emission wavelength of the LED@405 nm (e.g.; 23 850 M⁻¹cm⁻¹ for chalcone 4, 18 740 M⁻¹cm⁻¹ for chalcone 7 and 9020 M⁻¹cm⁻¹ for chalcone 10), resulting in a higher degree of polymerization of chalcones 4 and 7. As shown in [Figure II-2.11b](#), the 3D patterns are also characterized by swelling properties. As a result of this, volumes of the different patterns increased by about 2-3 times (see [Table II-2.5](#)) compared to that of their initial volumes. Furthermore, the different patterns could return to their primary appearance after heating during 3h at 50°C, enabling to remove the water contained in the PEG-polymers, indicating that the swelling of these 3D patterns and polymers is reversible.

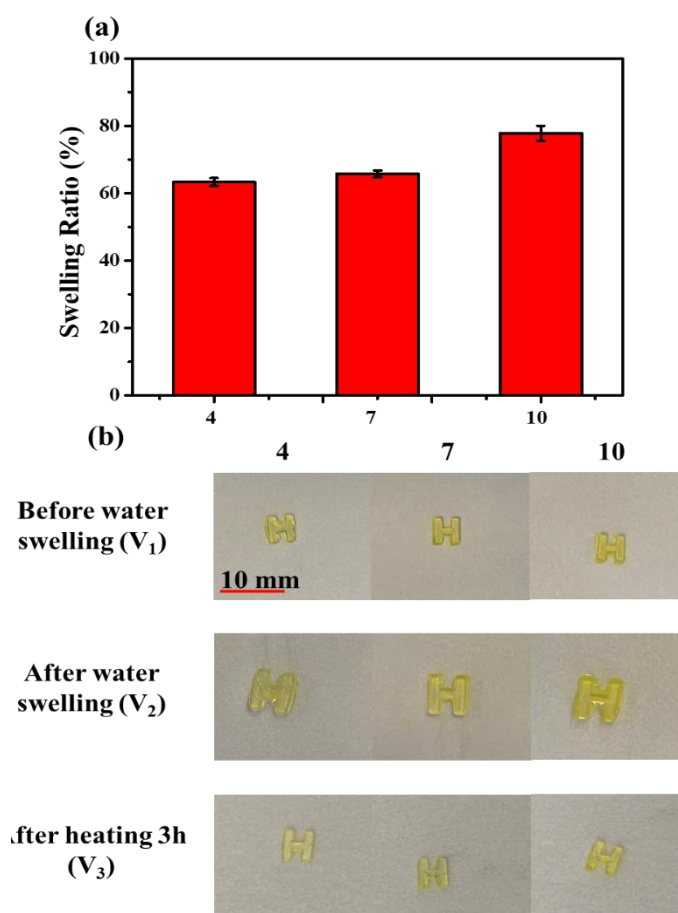


Figure II-2.11. (a) the swelling ratio of PEG-polymer prepared using chalcones as photoinitiators; (b) the photos of the “H” 3D patterns based on PEG-polymers (obtained

by laser write experiments using the chalcone/Iod two-component system) before water swelling, after water swelling for 24h and after heating for 3h to remove water.

	chalcone 4	chalcone 7	chalcone 10
V_1 (mm ³)	12	12	12
V_2 (mm ³)	40.5	44.1	55.6
V_3 (mm ³)	12	12	12
R (%)	237.5	267.5	363.3

Table II-2.5. The volumes of the “H” 3D pattern in the cycle: without water (V_1), water swelling (V_2), water removal (V_3) as well as the increase ratio of volume after swelling (R).

4.3 Reversible deformation: the form memory of 4D behavior of PEG-polymer via swelling and dehydration induced actuation.

Owing to the low solubility of typical PIs in water, rather few aqueous 3D printing systems have been developed in literatures [19-20]. Nevertheless, the newly proposed two-compound PIS in combination with PEG-diacrylate is suitable for 3D bioprinting with potential biocompatibility of aqueous systems. Apart from that, 4D printing products were manufactured using the proposed PIS through the swelling and dehydration induced actuation of the 3D printed hydrogels with spatial resolution characteristics. As the mechanical properties of PEG-diacrylate were dependent on the time of light exposure, different irradiation times were investigated to choose the best one. Specifically, a cross shaped object with spatially resolved properties was designed as shown in [Figure II-2.12a-b](#). After that, by placing the cross in a water filled beaker, we observed that it started to deform as swollen with water, resulting in a fully curled cross (namely, the degree change was approaching 180°) after swelling in water for 40s ([Figure II-2.12c](#)). Subsequently, the cross was removed from water and heated at 100°C to induce evaporation. Correspondingly, the curled cross flattened and recovered to its original shape for 100s as the contained water removed ([Figure II-2.12d](#)). Then, by continuing to heat for 10 min as the cross completely dehydrated, it inverted curled as shown in [Figure II-2.12e](#). Furthermore, we removed the cross from 100°C to room temperature for 10 min, and the curled one could gradually flatten out or even return to its original shape (see [Figure II-2.12f](#)). When we swelled the cross in the water again

for 30 s, it could still deform completely again as shown in [Figure II-2.12g](#). After heating at 100°C for 100s, the curled cross restored to its original shape (see [Figure II-2.12h](#)). After continuous heating to complete dehydration, the cross reversed curl again ([Figure II-2.12i](#)). These results demonstrated that the hydrogels initiated by the chalcone 7/Iod based novel PIS have a reversible deformation effect due to the thermal response and hydrophilic response, that is, the hydrogels have form memory ability [21-22].

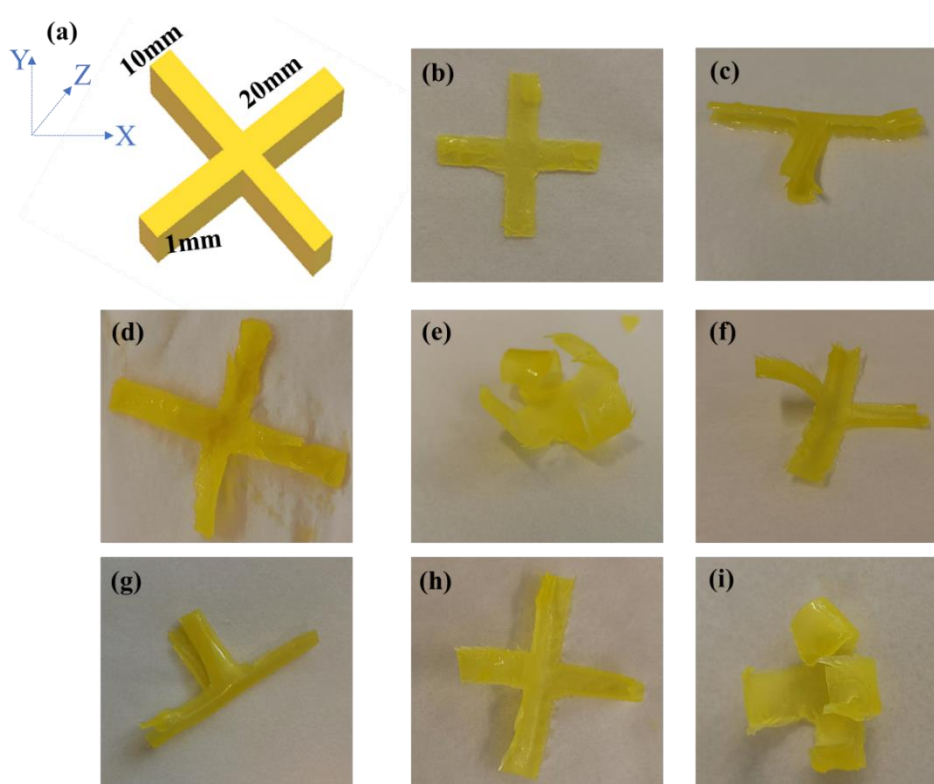
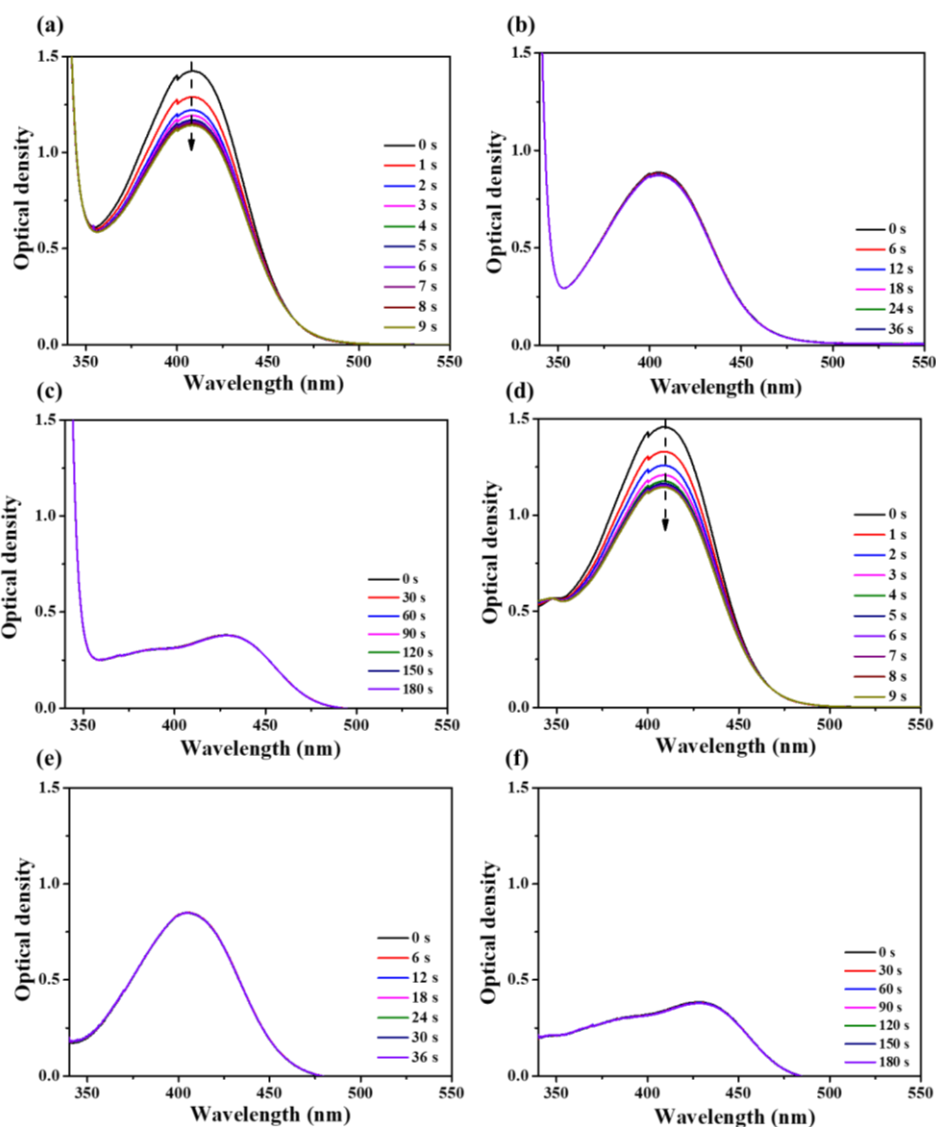


Figure II-2.12. Swelling and dehydration induced actuation of PEG-polymers obtained using chalcone 7/Iod initiating system @405 nm. (a) the designed geometrical form of the cross; (b) cross of PEG-polymer after photopolymerization; (c) shape of the cross after water swelling for 1 min; (d) shape of the cross after 100 seconds of dehydration (heating at 100°C); (e) shape of the cross after 10 min of dehydration (heating at 100°C); (f) cross after stay at room temperature for 10 min; (g) shape of the cross after water swelling again for 1 min; (h) shape of the cross after 100 seconds of dehydration (heating at 100°C); (i) shape of the cross after 10 min of dehydration (heating at 100°C).

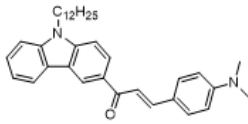
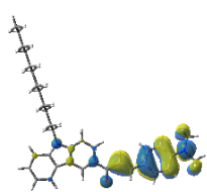
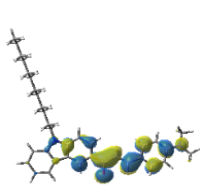
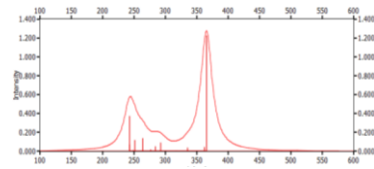
5. Conclusion.

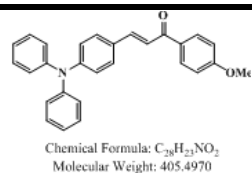
In summary, a series of novel carbazole/TPA-based chalcones was synthesized and characterized. Remarkably, all chalcones presented in this work have never been reported in literature except chalcone 7 which was developed as the starting materials for the synthesis of novel pyrazolines used for optical materials [45]. All chalcones displayed a strong absorption in the visible range due to the introduction of the carbazole or the TPA chromophores, and these chalcones showed good efficiency for the free radical polymerization of acrylates under irradiation with a LED@405nm. Remarkably, chalcones 4, 7 and 10 proved to be excellent PIs to boost efficient kinetics for the polymerization of PEG-diacrylate while using iodonium salt as the electron-acceptor. Photoinitiation ability and the photochemical mechanisms of the new PISs have been studied by RT-FTIR spectroscopy, fluorescence spectroscopy as well as ESR experiments. Finally, excellent 3D patterns with high resolution have been obtained by laser write experiments with the newly proposed three-component PISs. Apart from that, the shapes of 3D patterns can be reversibly modified by mean of a thermal response and a hydrophilic response of PEG for a 4D activation. Considering that the present work has clearly demonstrated the huge influence of the substitution pattern on the photoreactivity, future developments will consist in designing new carbazole and TPA-based chalcones to further improve their reactivity under the irradiation of longer-wavelength light.

Annex

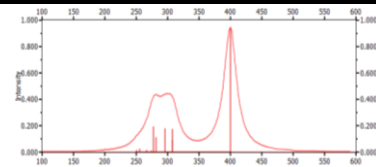


Annex II-2.1 Steady state photolysis of chalcones (5×10^{-5} M) upon exposure to LED@405nm under air in the solvent of acetonitrile: (a) chalcone 4/EDB; (b) chalcone 7/EDB; (c) chalcone 10/EDB; (e) chalcone 4; (f) chalcone 7; (g) chalcone 10.

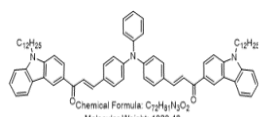
Chalcone	HOMO	LUMO	Calculated UV spectra	E_T (kcal/mol)
 Chemical Formula: $C_{25}H_{44}N_2O$ Molecular Weight: 508,75 chalcone 4			 $\lambda_{max} = 366 \text{ nm}$ $F = 1.228$	48.84



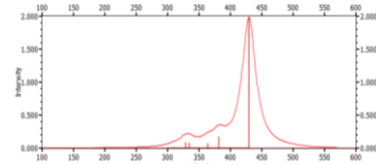
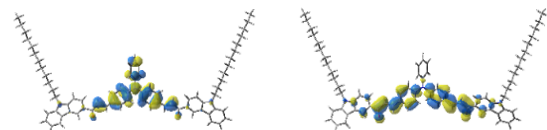
chalcone 7



47.08

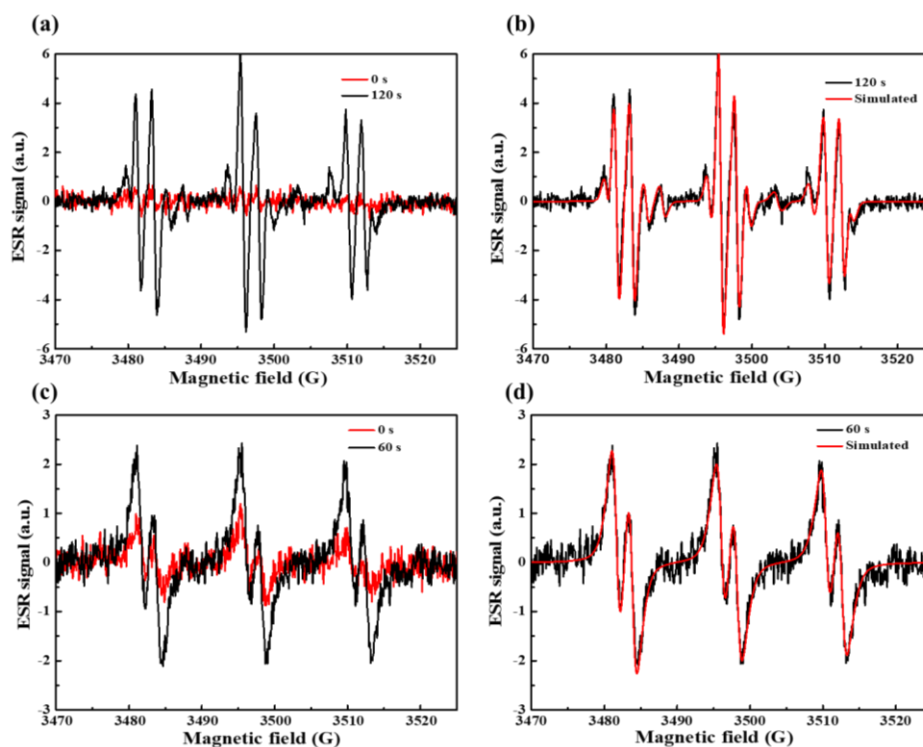


chalcone 10



47.33

Annex II-2.2. Contour plots of HOMOs and LUMOs for chalcones 4, 5, 7 and 10; structures optimized at the B3LYP/6-31G* level of theory.



Annex II-2.3. ESR spectra obtained from ESR-spin trapping experiment using PBN = 2 mg/mL (as spin trap agent); Iod = 12.6 mg/mL; EDB = 12.6 mg/mL and chalcone 4 = 0.8 mg/mL in *tert*-butylbenzene under N_2 . (a) chalcone 4/EDB Irradiation time = 0 s (red) and = 120 s (black) spectra; (b) chalcone 4/EDB Irradiation time = 120 s experimental (black) and fitting (red) spectra; (c) chalcone 4 alone Irradiation time = 0 s (red) and = 60 s (black) spectra; (d) chalcone 4 alone Irradiation time = 60 s experimental (black) and fitting (red) spectra.

References:

1. Corakci, B.; Hacıoglu, S. O.; Toppare, L.; Bulut, U. Long wavelength photosensitizers in photoinitiated cationic polymerization: The effect of quinoxaline derivatives on photopolymerization. *Polymer* **2013**, *54*(13), 3182-3187.
2. Gupta, I.; Kesavan, P. E. Carbazole substituted bodipys. *Frontiers in Chemistry* **2019**, *7*, 841-872.
3. Dumur, F. Carbazole-based polymers as hosts for solution-processed organic light-emitting diodes: Simplicity, efficacy. *Organic Electronics* **2015**, *25*, 345-361.
4. Dumur, F.; Beouch, L.; Peralta, S.; Wantz, G.; Goubard, F.; Gigmes, D. Solution-processed blue phosphorescent OLEDs with carbazole-based polymeric host materials. *Organic Electronics* **2015**, *25*, 21-30.
5. Al Mousawi, A.; Dumur, F.; Toufaily, J.; Hamieh, T.; Graff, B.; Gigmes, D.; Fouassier, J.P.; Lalevée, J. Carbazole scaffold based photoinitiator/photoredox catalysts: toward new high performance photoinitiating systems and application in led projector 3d printing resins. *Macromolecules* **2017**, *50*(7), 2747-2758.
6. Al Mousawi, A.; Arar, A.; Ibrahim-Ouali, M.; Duval, S.; Dumur, F.; Garra, P.; Lalevée, J. Carbazole-based compounds as photoinitiators for free radical and cationic polymerization upon near visible light illumination. *Photochemical & Photobiological Sciences* **2018**, *17*(5), 578-585.
7. Anandkumar, D.; Ganesan, S.; Rajakumar, P.; Maruthamuthu, P. Synthesis, photophysical and electrochemical properties and DSSC applications of triphenylamine chalcone dendrimers *via* click chemistry. *New Journal of Chemistry* **2017**, *41*(19), 11238-11249.
8. Planells, M.; Abate, A.; Hollman, D. J.; Stranks, S. D.; Bharti, V.; Gaur, J.; Robertson, N. Diacetylene bridged triphenylamines as hole transport materials for solid state dye sensitized solar cells. *Journal of Materials Chemistry A* **2013**, *1*(23), 6949-6960.
9. Da Costa, R. G.; Farias, F. R.; Maqueira, L.; Castanho, C.; Carneiro, L. S.; Almeida, J.; Limberger, J. Synthesis, photophysical and electrochemical properties of novel D- π -D and D- π -A triphenylamino-chalcones and β -arylchalcones. *Journal of the Brazilian Chemical Society* **2019**, *30*(1), 81-89.
10. Dadashi-Silab, S.; Doran, S.; Yagci, Y. Photoinduced electron transfer reactions for macromolecular syntheses. *Chemical Reviews* **2016**, *116*(17), 10212-10275.
11. Chen, G.; Wang, H. Y.; Liu, Y.; Xu, X. P.; Ji, S. J. The synthesis and characterisation of novel pyrazoline derivatives containing triphenylamine. *Dyes and Pigments* **2010**, *85*(3), 194-200.
12. Rammohan, A.; Reddy, J. S.; Sravya, G.; Rao, C. N.; Zyryanov, G. V. Chalcone synthesis, properties and medicinal applications: a review. *Environmental*

Chemistry Letters **2020**, *18*(2), 433-458.

13. Gaonkar, S. L.; Vignesh, U. N. Synthesis and pharmacological properties of chalcones: a review. *Research on Chemical Intermediates* **2017**, *43*(11), 6043-6077.
14. Lv, C.; Xia, H.; Shi, Q.; Wang, G.; Wang, Y. S.; Chen, Q. D.; Sun, H. B. Sensitively humidity-driven actuator based on photopolymerizable PEG-DA films. *Advanced Materials Interfaces* **2017**, *4*(9), 1601002-1601010.
15. Liang, Z. Q.; Wang, X. M.; Dai, G. L.; Ye, C. Q.; Zhou, Y. Y.; Tao, X. T. The solvatochromism and aggregation-induced enhanced emission based on triphenylamine-propenone. *New Journal of Chemistry* **2015**, *39*(11), 8874-8880.
16. Abdallah, M.; Magaldi, D.; Hijazi, A.; Graff, B.; Dumur, F.; Fouassier, J. P.; Lalevee, J. Development of new high-performance visible light photoinitiators based on carbazole scaffold and their applications in 3d printing and photocomposite synthesis. *Journal of Polymer Science Part A: Polymer Chemistry* **2019**, *57*(20), 2081-2092.
17. Son, K. I.; Kang, S. Y.; Noh, D. Y. Electrochemical and fluorescent properties of ferrocenyl chalcone with N-ethyl carbazole group. *Bulletin of the Korean Chemical Society* **2009**, *30*(2), 513-516.
18. Lalevée, J.; Blanchard, N.; Tehfe, M. A.; Peter, M.; Morlet-Savary, F.; Gigmes, D.; Fouassier, J. P. Efficient dual radical/cationic photoinitiator under visible light: a new concept. *Polymer Chemistry* **2011**, *2*(9), 1986-1991.
19. Pawar, A. A.; Halivni, S.; Waiskopf, N.; Ben-Shahar, Y.; Soreni-Harari, M.; Bergbreiter, S.; Magdassi, S. Rapid three-dimensional printing in water using semiconductor-metal hybrid nanoparticles as photoinitiators. *Nano Letters* **2017**, *17*(7), 4497-4501.
20. Niu, J.; Lunn, D. J.; Pusuluri, A.; Yoo, J. I.; O'Malley, M. A.; Mitragotri, S.; Hawker, C. J. Engineering live cell surfaces with functional polymers via cytocompatible controlled radical polymerization. *Nature Chemistry* **2017**, *9*(6), 537-545.
21. Champeau, M.; Heinze, D. A.; Viana, T. N.; de Souza, E. R.; Chinellato, A. C.; Titotto, S. 4D printing of hydrogels: a review. *Advanced Functional Materials* **2020**, *30*(31), 1910606-1910628.
22. Liu, Y.; Li, Y.; Yang, G.; Zheng, X.; Zhou, S. Multi-stimulus-responsive shape-memory polymer nanocomposite network cross-linked by cellulose nanocrystals. *ACS applied materials & interfaces* **2015**, *7*(7), 4118-4126.

Part III. Preparation of Composites Containing AgNPs Using Newly Developed Dyes-Based Photoinitiator and Their 3D/4D Applications

1. Introduction.

In recent years, due to the adjustable optical properties of the metal nanoparticles (MNP) such as silver, gold or platinum nanoparticles, the potential applications of these nano-objects in advanced materials such as photovoltaic technology [1], electronics [2] and optical detection systems [3], solar concentrators/reflectors or filters [4-5] etc, have attracted a great attention. In order to adapt the size and the shape of the nanoparticles to these new applications, extensive researches have been made concerning the optimization of the synthesis as well as the processing of the metal nanoparticles, in order to generate nano- or micro-layers on various substrates [6-7]. An appropriate synthetic method is the key to control the morphologies and the sizes of MNP and their subsequent physical and optical properties.

Many MNP synthetic routes e.g. chemical methods, radiation methods, and solvothermal methods, etc, have been reported in the literature, which mainly relied on the precipitation of nanoparticles from the precursor solution upon reduction by the appropriate reducers [8-9]. Notably, most of the procedures suffer from disadvantages. For example, several synthetic methods require sophisticated fabrication equipment, inducing expensive cost or producing particles lacking of mechanical strength, etc. [10]. To avoid these drawbacks, composite materials based on nanoparticles and polymer matrices have recently attracted attention due to their synergistic effects [11-12]. Photopolymerization technology can provide a useful method to generate polymers suitable for various applications ranging from imaging, radiation curing, and optics technologies to (bio)medicine, microelectronics, and materials science, as its mild reaction conditions and controllability in time and space [13-14]. The coordinated control of the kinetics of the two simultaneous processes of in-situ photoreduction and

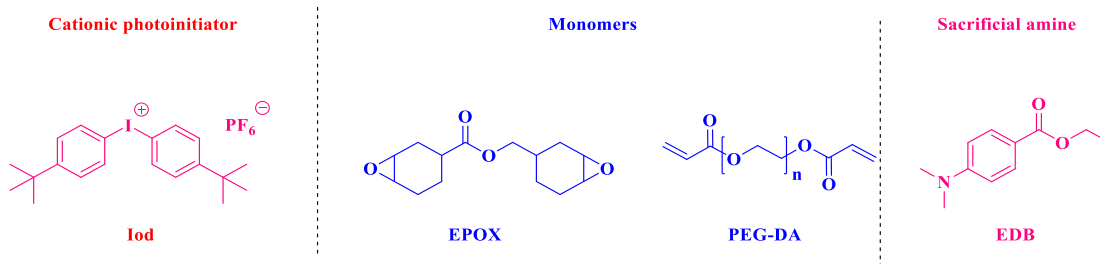
photopolymerization can adjust the morphology of silver nanoparticles (AgNPs) and the properties of the nanocomposite to meet the needs of various applications. The key point of the above process is a suitable photoinitiating system (PIS), which generate highly reactive specie through a series of redox reactions under the suitable light irradiation to reduce silver cations into AgNPs. In parallel, these active substances initiate the photopolymerization of the monomers to form the polymer network [15].

Concerning the enhancement of the light absorption properties, elongation of the π -conjugated spacer can red-shift the position of this band while improving the molar extinction coefficient, offering an efficient tool to finely tune the absorption of the chalcone-based dyes. Benefiting from these different advantages, in this part, we improved the absorption properties (including red-shift absorption wavelength and high molar extinction coefficient) of the chalcone derivatives by adjusting the chemical skeleton to prepare photoinitiators (PIs) that is more suitable for low-density visible light sources.

2. Materials and Methods.

2.1 Materials.

The polyethylene glycol diacrylate (PEG-DA, $M_w = 600$ g/mol) was obtained from Sartomer-Europe, while the cationic photopolymerization benchmark monomer 3,4-epoxycyclohexylmethyl 3,4-epoxycyclohexanecarboxylate (EPOX) was purchased from Allnex. Bis-(4-tert-butylphenyl) iodonium hexafluorophosphate (Iod) used as the co-initiator and ethyl 4-dimethylaminobenzoate (amine, EDB) was used as the electron/hydrogen donor. The two molecules were purchased from Lambson Ltd. The radical capture agent (phenyl-N-tert-butyl nitron, PBN) was purchased from Sigma-Aldrich (St. Louis, MO, USA). Their corresponding chemical structures are presented in **Scheme III-1**. The solvents (e.g. acetonitrile, dimethyl sulfoxide and tert-butylbenzene) used in this study were all of analytical grade and purchased from Sigma-Aldrich (St. Louis, MO, USA).



Scheme III-1. Chemical structures of additives and monomers used in this study.

2.2 Free radical photopolymerization (FRP) and cationic photopolymerization (CP) initiated by dye/Iod/amine based-PISs.

The photoinitiation abilities of combinations of the different dyes with Iod/amine for FRP and CP processes were investigated using real-time FTIR spectroscopy (JASCO FTIR 4100, RT-FTIR). In detail, the content of each component was optimized by comparing their solubility in the resin and photopolymerization efficiency, which were finally kept at 0.1%/1.5%/1.5% (w/w/w, calculated from the weight of the resins that used), respectively. All these dyes and additives are well dispersed into the resins (PEG-DA/EPOX). Then RT-FTIR was used to continuously monitor the conversion of epoxy or acrylate functional groups under visible light irradiation (LED@405 nm, $I_0 = 110 \text{ mW/cm}^2$; LED@470 nm, $I_0 = 70 \text{ mW/cm}^2$). During this process, the FRP of PEG-DA (thickness $\sim 0.1 \text{ mm} / 2 \text{ mm}$) was carried out in the laminated conditions to reduce the O_2 inhibition effect, while the CP of EPOX (thickness $\sim 0.1 \text{ mm} / 2 \text{ mm}$) was directly conducted in the air. The followed characteristic peak of EPOX is located around 790 cm^{-1} (thickness $\sim 0.1 \text{ mm}$) or 3700 cm^{-1} (thickness $\sim 2 \text{ mm}$), while for PEG-DA, the characteristic peak is around 1620 cm^{-1} (thickness of about $\sim 0.1 \text{ mm}$) or 6160 cm^{-1} (thickness $\sim 2 \text{ mm}$) [14]. Moreover, IPN polymers were fabricated *via* the FRP of PEG-DA and the CP of EPOX. Briefly, the proposed three-component PISs was used to initiate the photopolymerization reactions under visible light irradiation, in which the original single monomer (PEG-DA or EPOX, 100%, w/w) was replaced by blend of the monomers (i.e. PEG-DA: EPOX, 30%:70%, 50%:50%, 70%:30%, w/w) in different proportions [16].

2.3 Involved chemical mechanism.

2.3.1 UV-vis absorption properties of dyes and their steady-state photolysis process with Iod/amine.

UV-vis absorption properties of these proposed dyes were studied in acetonitrile at the concentration of 1×10^{-5} M by a JASCO V730 spectrophotometer. After that, steady-state photolysis of dyes with or without Iod/amine were also studied in acetonitrile, in which their concentrations were kept at 1×10^{-5} M and 0.01 M, respectively [17].

2.3.2 Fluorescence experiments of the dyes.

A JASCO FP-6200 spectrofluorimeter was used to determine the fluorescence spectra of the dyes and their fluorescence quenching with Iod/amine, which was conducted in acetonitrile at the concentration of about 1×10^{-5} M. The excitation wavelength was about 300 nm [17].

2.3.3 Electron spin resonance (ESR) spin trapping (ESR-ST) experiments and the redox potentials of dyes.

Radicals generated in N_2 saturated *tert*-butylbenzene solutions containing the dyes and Iod/EDB (0.1 %/1.5 %, w/w) upon irradiation with sunlight were captured by PBN (0.25%, w/w) and analyzed with an X-band spectrometer (Bruker EMX-plus) at room temperature. The obtained ESR spectra were then simulated and analyzed by using the WINSIM software [18].

Redox potentials (E_{ox} and E_{red}) of chalcone-based dyes were determined by cyclic voltammetry that used tetrabutylammonium hexafluorophosphate as the supporting electrolyte in acetonitrile. Free energy changes (ΔG_{S1}^{Iod} or ΔG_{S1}^{EDB}) were calculated to prove the possibility of the electron transfer reactions between the dyes and the additives (Iod/amine) and support the photopolymerization processes observed experimentally. Redox potentials (E_{ox} and E_{red}) of the proposed dyes were determined by cyclic voltammetry in acetonitrile, while E^* corresponding to the excited state energy level of the dyes was determined from the crossing point of their UV-visible and fluorescence spectra, respectively.

2.4 Preparation of the silver nanoparticles (AgNPs).

2.4.1 Preparation of AgNPs in DMF.

Silver nanoparticles were fabricated in DMF solution, which contained 0.5 wt%-Dye/Iod/amine-based PIS (0.1%/1.5%/1.5%, w/w/w) and 5 wt% AgNO₃, upon irradiation with LED@405 nm [19].

2.4.2 Preparation of AgNPs within polymers through in-situ photopolymerization processes.

The dyes/Iod/amine (0.1%/1.5%/1.5%, w/w/w)-based three-component PISs was entirely dissolved in the mixed monomer (PEG-DA-EPOX). After that, 5 wt% AgNO₃ was added. The resulting formulation was swirled at room temperature for 1 h before being ultrasonically mixed for 5 min to ensure the salt to be well-distributed into the formulation. Finally, the conversion profiles of the mixed monomers were followed by RT-FTIR spectroscopy, which not only enabled to determine the influence of the silver cations on the photopolymerization efficiency, but also enabled to prepare IPNs with uniformly distributed silver nanoparticles [19].

2.5. Characterization of polymers.

2.5.1 TEM and SEM of AgNPs.

Firstly, the microscopic morphology of AgNPs formed in DMF as the solvent after 120 min of irradiation under a LED@405 nm was examined by transmission electron microscope (TEM, FEI Quanta 250 FEG). Meanwhile, for AgNPs fabricated during the photopolymerization of PEG-polymers/IPNs, a scanning electron microscopy (SEM, FEI Quanta 250 FEG) was utilized to observe their morphologies [20, 21].

2.5.2 Dynamic time sweep rheology.

Photopolymerization processes of all the formulations were further detected through dynamic time-scanning rheology. In detail, 40 μL of resin was dropped on a glass slide and then a Haake-Mars Rotational Rheometer at a constant frequency of 1 Hz at 25 °C was used for the measurement [21].

2.5.3 Tensile strength of polymers.

Firstly, various samples (length 4 cm, width 2 mm and height 2.5 mm) were prepared by using molds under the irradiation of visible light LED@405nm, and then the tensile strength of the prepared single networks and interpenetrating polymer networks were carried out by a Dynamometer Instron with a 100 N loading at a displacement rate of 0.1 mm/min [17].

2.6. Applications in 3D and 4D printing.

2.6.1 Direct laser write experiments to prepare the single and IPN polymers with/without AgNPs.

Direct laser write experiments were performed by using PEG-DA and/or EPOX as the monomers through a computer programmed laser diode at 405 nm (Thorlabs). Photosensitive formulations containing dyes/Iod/amine-based PIS with/without AgNO₃ were prepared in solvent-free conditions. Writing processes were all carried out under air at room temperature and the obtained 3D patterns were analyzed using a numerical optical microscope (DSX-HRSU from Olympus Corporation) [20].

2.6.2 Swelling experiments of the obtained polymers.

Single-network and interpenetrated polymer networks obtained from direct laser write were immersed into deionized water for 24 h at room temperature to study their swelling properties. Furthermore, the wet weight (W_t) and volume (V_2) of the polymers after reaching the swelling equilibrium were measured and compared with their initial wet weights (W_0) and volumes (V_1). After that, the absorbed water was removed by heating at 40 °C, and their weights and volumes were also compared with their initial values [21-22].

2.6.3 Shape-memory effects of single and IPN polymers with/without AgNPs (4D behavior).

Swelling and dehydration were conducted to study the reversible temporary deformation effects of the 3D single networks and the interpenetrating polymer networks. In detail, the obtained 3D polymers were firstly immersed into deionized water at room temperature to observe their deformation processes; after that, the

deformed polymers were dehydrated in an oven to observe their morphological change processes (recovery or even reverse deformation processes). Finally, the samples were placed at room temperature to restore their original appearances [23, 24].

2.7 Antibacterial effect of IPN containing/without AgNPs.

As AgNPs are well-known to exhibit a broad range of antibacterial activities, in this work, gram-positive bacteria *Staphylococcus aureus* (CIP 4.83, Pasteur institute collection) and gram-negative bacteria *Pseudomonas aeruginosa* (strain PAO) were selected as bacterial models to investigate the antibacterial effects of the fabricated IPNs containing AgNPs.

Bacterial strains were stored at -80 °C in 15% glycerol. Strains were cultivated in LB medium (Lennox L: 1% Bacto-Tryptone, 0.5% Bacto-Yeast Extract, 1% NaCl, NaOH [3×10^{-3} M]) at 37 °C. Before the contact with IPNs, an overnight culture was employed to initiate a fresh culture until $OD_{580nm} = 1$ (approximately 10^9 bacteria/mL). 100 μ L were used to inoculate either a new LB liquid medium, a LB agar Petri dish, or the PBS buffer (no growth, but adhesion possible). The antibacterial effect was observed by eyes and counting the colony-forming unit (CFU/ mL) after one night of growth in contact with the IPN. To dislodge adherent bacterial cells, IPNs were removed from the medium, gently washed three times with PBS, then strongly vortexed in PBS for 10 min in order to detach adhered bacterial cells. CFU was assessed once again by dispersing appropriate dilutions. Controls with no IPN and controls with IPN but no AgNPs were systematically performed in parallel.

Reference:

1. Schejrn, A.; Ott, M.; Dabert, M.; Vidal, L.; Balan, L. Photo-induced design of reflective metallized gold@polymer coatings with tuned architecture. *Materials & Design* **2018**, *160*, 74-83.
2. Yue, G.; Su, S.; Li, N.; Shuai, M.; Lai, X.; Astruc, D.; Zhao, P. Gold nanoparticles as sensors in the colorimetric and fluorescence detection of chemical warfare agents. *Coordination Chemistry Reviews* **2016**, *311*, 75-84.
3. Zhang, M. R.; Chen, X. Q.; Pan, G. B. Electrosynthesis of gold nanoparticles/porous GaN electrode for non-enzymatic hydrogen peroxide detection. *Sensors and*

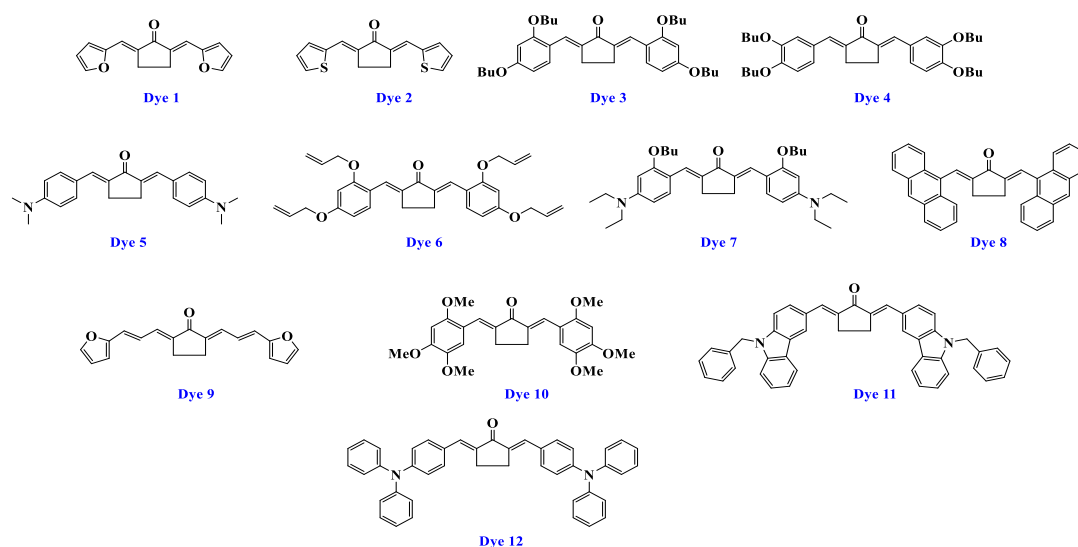
Actuators B: Chemical **2017**, *240*, 142-147.

4. Shenashen, M.; El-Safty, S.; Elshehy, E. Synthesis, morphological control, and properties of silver nanoparticles in potential applications. *Particle & Particle Systems Characterization* **2014**, *31*(3), 293-316.
5. Fahr, S.; Rockstuhl, C., Lederer, F. Metallic nanoparticles as intermediate reflectors in tandem solar cells. *Applied Physics Letters* **2009**, *95*(12), 121105-121108.
6. Chaikin, Y.; Kedem, O.; Raz, J.; Vaskevich, A. Rubinstein, stabilization of metal nanoparticle films on glass surfaces using ultrathin silica coating. *Analytical Chemistry* **2013**, *85*(21), 10022-10027.
7. Irvani, S.; Korbekandi, H.; Mirmohammadi, S. V.; Zolfagharil. B. Synthesis of silver nanoparticles: chemical, physical and biological methods. *Research in Pharmaceutical Sciences* **2014**, *9*(6), 385-406.
8. Tyagi, H.; Kushwaka, A.; Kumar, A.; Aslam, M. Magnetic behavior of surface nanostructured 50 nm nickel thin films. *Nanoscale Research Letters* **2010**, *5*(10), 1596-1602.
9. Malassis, L.; Dreyfus, R.; Murphy, R. J.; Hough, L.A.; Donnio, B.; Murray, C.B. One-step green synthesis of gold and silver nanoparticles with ascorbic acid and their versatile surface post-functionalization. *RSC Advance* **2016**, *6*(39), 33092-33100.
10. Zhu, S. Q.; Zhang, T.; Guo, X. L.; Wang, Q. L.; Liu, X. F.; Zhang, X. Y. Gold nanoparticle thin films fabricated by electrophoretic deposition method for highly sensitive SERS application. *Nanoscale Research Letters* **2012**, *7*(1), 1-7.
11. Zaier, M.; Vidal, L.; Hajjar-Garreau, S.; Balan, L. Generating highly reflective and conductive metal layers through a light-assisted synthesis and assembling of silver nanoparticles in a polymer matrix. *Scientific Report* **2017**, *7*(1), 1-10.
12. Balan, L.; Schneider, R.; Lougnot, D. J. In situ fabrication of polyacrylate-silver nanocomposite through photoinduced tandem reactions involving eosin dye. *Polymer* **2010**, *51*(6), 1363-1369.
13. Bagheri, A.; Jin, J. Y. Photopolymerization in 3D printing. *ACS Applied Polymer Materials* **2019**, *1*(4), 593-611.
14. Zhang, J.; Hill, N.; Lalevée, J.; Fouassier, J. P.; Zhao, J.; Graff, B.; Schmidt, T. W.; Kable, S. H.; Stenzel, M. H.; Coote, M. L.; Xiao, P. Multihydroxy-anthraquinone derivatives as free radical and cationic photoinitiators of various photopolymerizations under green LED. *Macromolecular Rapid Communications* **2018**, *39*(19), e1800172- e1800179.
15. Alexandridis, P.; Tsianou, M. Block copolymer-directed metal nanoparticle morphogenesis and organization. *European Polymer Journal* **2011**, *47*(4), 569-583.

16. Zhang, J.; Wang, S. H.; Lalevée, J.; Morlet-Savary, F.; Lam, E. S. H.; Graff, B.; Liu, J.; Xing, F. Y.; Xiao, P. 1, 2-Diketones as photoinitiators of both cationic and free-radical photopolymerization under UV (392 nm) or Blue (455 nm) LEDs. *Journal of Polymer Science* **2020**, *58(6)*, 792-802.
17. Xiao, P.; Zhang, J.; Dumur, F.; Tehfe, M. A.; Morlet-Savary, F.; Graff, B.; Gigmes, D.; Fouassier, J. P.; Lalevée, J. Visible light sensitive photoinitiating systems: Recent progress in cationic and radical photopolymerization reactions under soft conditions. *Progress in Polymer Science* **2015**, *41*, 32-66.
18. Laachir, S.; Moussetad, M.; Adhiri, R.; Fahli, A. Isotropic spin trap EPR spectra simulation by fast fourier transform (FFT). *E-Journal of Chemistry* **2005**, *2(2)*, 165-170.
19. Aleksandra, S.; Murielle, O.; Marine, D.; Loïc, V.; Lavinia, B. Photo-induced design of reflective metallized gold@polymer coatings with tuned architecture. *Materials & Design* **2018**, *160*, 74-83.
20. Chen, H.; Zhang, Y. J.; Ni, T. Y.; Ding, P.; Zan, Y.; Cai, X.; Zhang, Y. W.; Liu, M.; Pei, R. J. Construction of a silk fibroin/polyethylene glycol double network hydrogel with co-culture of HUVECs and UCMSCs for a functional vascular network. *ACS Applied Bio Materials* **2021**, *4(1)*, 406-419.
21. Chen, H.; Vahdati, M.; Xiao, P.; Dumur, F.; Lalevée, J. Water-soluble visible light sensitive photoinitiating system based on charge transfer complexes for the 3D printing of hydrogels. *Polymers* **2021**, *13(18)*, 3195-3205.
22. Chen, H.; Noirbent, G.; Zhang, Y. J.; Sun, K.; Liu, S. H.; Brunel, D.; Gigmes, D.; Graffa, B.; Morlet-Savary, F.; Xiao, P.; Dumur, F.; Lalevée, J. Photopolymerization and 3D/4D applications using newly developed dyes: Search around the natural chalcone scaffold in photoinitiating systems. *Dyes and Pigments* **2021**, *188(109213)*, 1-13.
23. Zhao, W.; Wang, Z.; Zhang, J.; Wang, X.; Xu, Y.; Ding, N.; Peng, Z. Vat photopolymerization 3D printing of advanced soft sensors and actuators: From architecture to function. *Advanced Materials Technologies* **2021**, *6(8)*, 2001218-2001249.
24. Liu, Y.; Li, Y.; Yang, G.; Zheng, X. T.; Zhou, S. B. Multi-stimulus-responsive shape-memory polymer nanocomposite network cross-linked by cellulose nanocrystals. *ACS Applied Materials & Interfaces* **2015**, *7(7)*, 4118-4126.

Chapter 1. In Situ Generation of Ag Nanoparticles During Photopolymerization by Using Newly Developed Dyes-Based Three-Component Photoinitiating Systems and The Related 3D Printing Applications and Their Shape Change Behavior

Silver nanoparticles (AgNPs) play a crucial role in biology and medical research as their extensive and efficient antibacterial activity and high electrical and thermal conductivity. However, the generation of them with a certain morphology under mild conditions (under air, solvent-free, room temperature, etc.) is still a huge challenge. Herein, a simple one-step method is proposed to generate AgNPs in situ at room temperature under air by combining the photopolymerization process with the formation process of AgNPs within a few minutes. In detailed, twelve different dyes based on 2,5-diethylene-cyclopentan-1-one were firstly synthesized and used as high-performance Type II PIs (see [Scheme III-1.1](#)). When using in conjunction of Iod and EDB, they can effectively boost the FRP of PEG-DA and the CP of EPOX upon irradiation with LED@405nm. Furthermore, all the formulations containing/without AgNPs can be successfully used to perform the direct laser write experiment. However, even if all of the obtained 3D patterns exhibited reversible swelling performance and shape-memory effects caused by swelling and dehydration for the access to 4D printing, the presence of AgNPs will affect these properties.



Scheme III-1.1. Chemical structures of dyes 1-12.

1. UV-Visible Absorption Properties of the Different Chalcones in Acetonitrile.

Photophysical properties as well as the chemical mechanisms involved while using the twelve different dyes as PIs were investigated in detail. Markedly, five of the new proposed dyes were never synthesized prior this work (i.e. dyes 3, 4, 6, 7 and 11). It can be seen from Annex III-1.1 that all dyes exhibited a strong absorption peak in the visible light region ($\lambda > 390$ nm) as dissolved in acetonitrile. In addition, a weaker absorption or shoulder can also be observed in the ultraviolet range ($\lambda < 300$ nm) for dyes 3, 5, 7, 8, 9, 10, 11 and 12. Interestingly, absorption maxima ranging between 460 nm and 480 nm were detected for dyes 5, 7 and 12 exhibiting the most red-shifted absorptions. Conversely, absorption maxima lower than 460 nm were found for the other dyes. In the view of the fact that absorption maxima ranging between 460 nm and 480 nm were detected for dyes 5, 7 and 12 exhibiting the most red-shifted absorptions, while absorption maxima lower than 460 nm were found for the other dyes, LED @ 405 nm and 470 nm were using as light irradiation sources for this work in order to ensure a good overlap between the emission spectrum of the light source and the absorption spectra of the dyes. Except for dye 8 for which a molar extinction coefficient that lower than $5 \times 10^3 \text{ M}^{-1} \text{ cm}^{-1}$ was determined, the other dyes exhibited high molar extinction coefficients (ϵ_{max}) in the visible range that summarized in Table III-1.1 (e.g., $58\,500 \text{ M}^{-1} \text{ cm}^{-1}$, $13\,620 \text{ M}^{-1} \text{ cm}^{-1}$ and $52\,680 \text{ M}^{-1} \text{ cm}^{-1}$ for dye 7 at λ_{max} , $\lambda_{@405\text{nm}}$ and $\lambda_{@470\text{nm}}$, respectively) corresponding to π - π^* electronic transitions. In addition, the different substituents attached to the central part of 2,5-dimethylenecyclopentan-1-one strongly affected their UV-visible absorption spectra. Remarkably, the introduction of electron-donating groups caused a red-shift of the absorption spectra. Therefore, the electron donating ability of the peripheral groups can be arranged using the following order: dye 7 > dyes 5 and 12 > dyes 9 and 10 > dyes 11 and 8 > dyes 3, 4 and 6 > dyes 1 and 2.

Dyes	λ_{max} (nm)	ϵ_{max} ($\text{M}^{-1} \text{ cm}^{-1}$)	$\epsilon_{@405\text{nm}}$ ($\text{M}^{-1} \text{ cm}^{-1}$)	$\epsilon_{@470\text{nm}}$ ($\text{M}^{-1} \text{ cm}^{-1}$)
------	-----------------------------	---	--	--

1	396	41 980	37 050	270
2	392	40 840	33 590	110
3	400	41 770	41 610	2720
	274	69 250		
4	399	42 500	41 580	1280
5	460	57 400	23 700	53 446
	274	37 300		
6	397	38 150	36 700	1710
7	485	65 670	16 200	59 370
	278	22 680		
8	418	6970	6800	1600
	268	12 890		
9	428	61 130	50 310	16 540
	283	15 340		
10	427	42 062	32 270	14 380
	280	14 160		
11	421	36 350	30 560	10 160
	236	46 810		
12	460	47 620	25 300	44 400
	298	35 060		

Table III-1.1. Light absorption properties of dyes 1-12 in acetonitrile: maximum absorption wavelengths λ_{\max} ; extinction coefficients at λ_{\max} (ϵ_{\max}) and the emission wavelength of the LED@405 nm ($\epsilon_{@405\text{nm}}$) and 470 nm ($\epsilon_{@470\text{nm}}$).

2. Photopolymerization Kinetics.

2.1 Free radical polymerization (FRP) kinetics of PEG-DA.

Photoinitiation abilities of the different dye/Iod/amine (0.1%/1.5%/1.5%, w/w/w) based three-component PISs for the FRP of PEG-DA were studied under a LED@405 nm or 470 nm at ambient temperature. The different polymerization profiles can be found in [Figure III-1.1](#), and the final acrylate function conversions (FCs) are summarized in the [Table III-1.2](#). It can be seen that all the dyes-based PISs exhibited better photoinitiation efficiencies than the blank PIS (FC = 76%) simply consisting of the co-initiators (Iod/amine, 1.5%/1.5%, w/w) upon irradiation with the LED@405nm at the thickness about 0.1 mm (see [Figure III-1.1a](#) with much better polymerization rate in presence of dyes). It demonstrated that the presence of the dyes was crucial to boost

their polymerization performances. Remarkably, dyes 2, 3, 8 and 9-based PISs achieved more than 90% of double bond conversions for the monomer within 50 s, which were much higher and faster than that obtained with the other dyes-based PISs.

Under the same conditions, for thick samples for which the thickness was about 2 mm, surprisingly, only dye 5-based PIS showed better photopolymerization kinetics in comparison to the blank PIS (conversion: 92% of dye 5 vs 87% for the blank), while the conversions obtained with the other dyes-based PIS were lower than 70%, even after 200 s of irradiation. It can be ascribed to the fact that the darker color of the photopolymerizable resin and the faster surface polymerization speed, which inhibits the penetration of light and leads to an internal light filtering effect. Photoinitiation ability for the EDB/Iod blank is ascribed to the formation of a light active charge transfer complex only absorbing in the near UV range [1].

More interestingly, upon irradiation with the LED@470 nm, the blank control based on the Iod/amine PIS could not lead to the photocuring of both samples with the thicknesses of 0.1 mm and 2 mm, while better photopolymerization kinetics could be observed for all the dyes-based PISs. Furthermore, as shown in [Figure III-1.1c](#), for thin samples, the double bond conversions achieved with the different dyes-based PISs were lower than 90% under the irradiation of the LED@470 nm, which was lower than that achieved upon irradiation of the LED@405 nm. Conversely, for thick samples, the dye 5-based PIS could achieve the best effectiveness (see [Figure III-1.1d](#)) which can be assigned to its high molar extinction coefficients at the different wavelengths used for photoinitiation (e.g., 63 170 M⁻¹cm⁻¹, 27 360 M⁻¹cm⁻¹ and 58 880 M⁻¹cm⁻¹ for dye 5 at λ_{\max} , $\lambda_{@405\text{nm}}$ and $\lambda_{@470\text{nm}}$ respectively, see [Table III-1.1](#)).

In comparison with the initiation ability including the final double bond conversions of the monomer (see [Table III-1.2](#)) and the rates of polymerization (the initial slope of the curves, [Figure III-1.1](#)) obtained for all dyes-based PISs, the LED@405 nm is proved to be a more appropriate light source to initiate the FRP of PEG-DA than the LED@470 nm. Under these conditions, dyes 2, 3, 5, 8, and 9 were selected as the excellent candidates to boost the polymerization of PEG-DA for samples with thicknesses of 0.1 mm or 2 mm in laminate, perfectly matching with their high molar extinction coefficients at 405 nm.

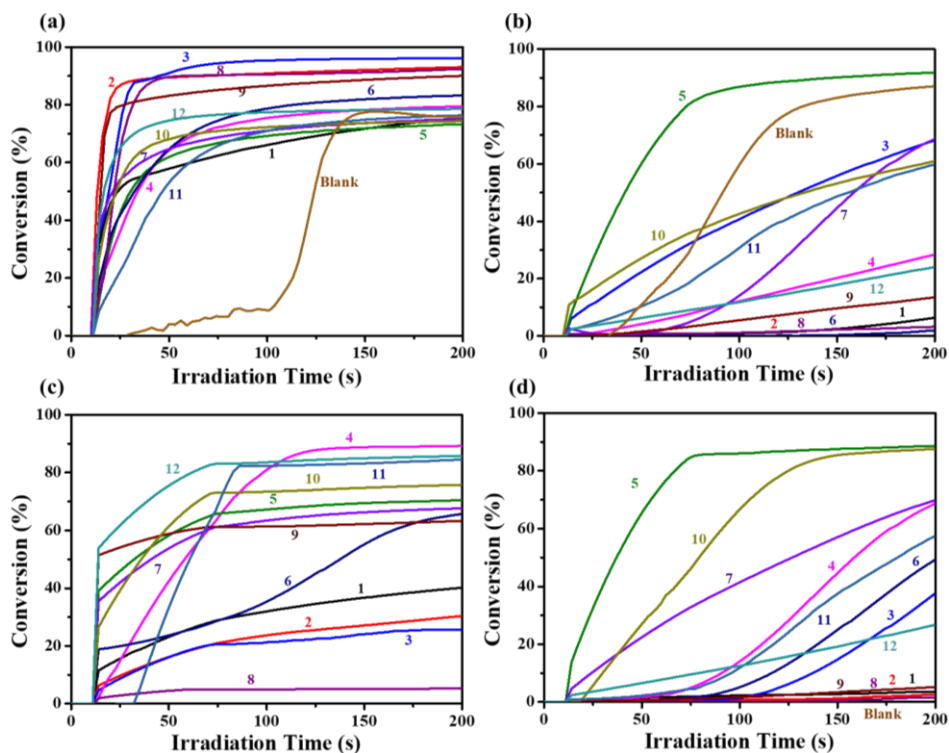


Figure III-1.1. Photopolymerization profiles of PEG-DA (conversion of C=C bonds vs irradiation time) initiated by dyes/Iod/amine (0.1%/1.5%/1.5%, w/w/w) in laminate with different conditions, (a) irradiation by LED@405 nm ($I_0 = 110 \text{ mW.cm}^{-2}$) with the thickness about 0.1 mm; (b) irradiation by LED@405 nm ($I_0 = 110 \text{ mW.cm}^{-2}$) with the thickness about 2 mm; (c) irradiation by LED@470 nm ($I_0 = 70 \text{ mW.cm}^{-2}$) with the thickness about 0.1 mm; (d) irradiation by LED@470 nm ($I_0 = 70 \text{ mW.cm}^{-2}$) with the thickness about 2 mm, the irradiation starts form $t = 10 \text{ s}$.

Final double bond conversions (FCs) initiated by dye/Iod/amine-based PIS

Dyes	LED@405 nm		LED@470 nm	
	Thickness ~ 0.1	Thickness ~ 2	Thickness ~ 0.1	Thickness ~ 2
	mm (%)	mm (%)	mm (%)	mm (%)
1	76	7	40	-
2	93	-	30	-
3	96	69	25	39
4	80	29	89	69
5	73	92	70	89
6	83	-	66	50
7	75	69	68	70

8	92	-	5	-
9	90	14	63	-
10	75	61	76	88
11	76	60	85	58
12	79	24	86	27
Blank	76	87	-	-

'-' means not deep curing after irradiation for 200s

Table III-1.2. The FCs for the PEG-DA monomer initiated by dye/Iod/amine-based PISs with the thickness about 0.1 mm or 2 mm under LED@405 nm or LED@470 nm. The blank corresponds to the Iod/amine PIS without dyes.

2.2 Cationic polymerization (CP) kinetics of EPOX.

Photoinitiation abilities of the proposed dyes-based PISs for the CP of the EPOX were also studied upon irradiation with the LED @405 nm under air. As shown in [Figure III-1.2](#), the photopolymerization rate (the initial slope of the curves) of all photosensitive formulations containing dyes-based PISs were much faster than that of the blank PIS (Iod/EDB without dye), while only the final conversion achieved with the dye 6-based PIS could outperform that obtained with the blank PIS (92% of dye 6 vs 77% of blank, as shown in [Table III-1.3](#)), confirming the crucial effect of the three-component PIS for the overall photopolymerization performance. In addition, the formulations in mold whose thickness is about 2 mm could not be cured in depth, while thin samples could be efficiently polymerized under the same conditions suggesting the presence of an inner filter effect. Efficiency of the PIS is clearly governed by the photochemical reactivity of the dyes with Iod and amine as well as the facility to generate cations ($\text{dye}^{\bullet+}$) (as shown in the chemical mechanisms depicted below).

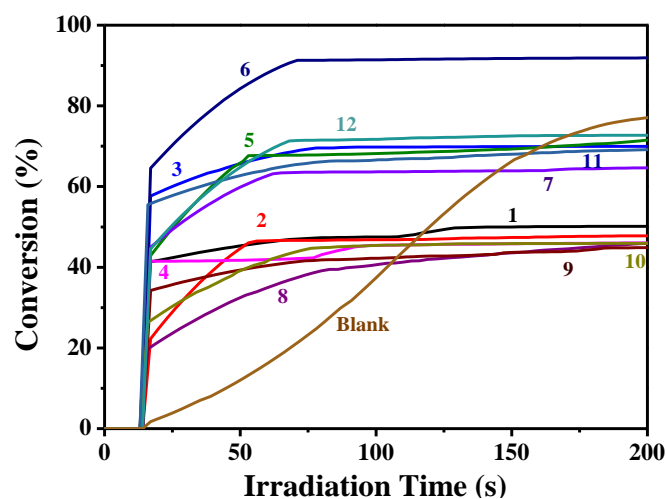


Figure III-1.2. Cationic polymerization profiles of EPOX (conversion of epoxy functions vs irradiation time) initiated by dyes/Iod/amine (0.1%/1.5%/1.5%, w/w/w)-based PIS in air under LED@405nm ($I_0 = 110 \text{ mW.cm}^{-2}$) with a thickness of 0.1 mm. The irradiation starts at $t = 10 \text{ s}$.

Final epoxy function conversions (FCs) initiated by dye/Iod/amine						
Dyes	1	2	3	4	5	6
FCs (%)	50	48	70	46	72	92
Dyes	7	8	9	10	11	12
FCs (%)	65	46	45	46	69	73

Table III-1.3. Summary of the FCs for the EPOX monomer dye/Iod/amine-based PISs with the thickness about 0.1 mm upon LED@405nm.

2.3 Free radical polymerization (FRP) initiated by Dyes 3 and 5-based two-component PISs or only dyes as the PIs.

The laser write experiments were mainly performed using dyes 3 and 5-based formulations (see below). Therefore, the photoinitiation ability of the two-component PIS of i) dye 3 or 5/Iod (0.1%/1.5%, w/w) and dye 3 or 5/EDB (0.1%/1.5%, w/w) and ii) dye 3 or 5 alone used as PI (0.1%, w/w) for PEG-DA were studied to emphasize the important effect of the dye/Iod/amine based three-component PIS on the overall performances. As depicted in the [Figure III-1.3](#) and [Annex III-1.2](#), deep curing cannot be observed either for thin samples or thick samples for formulations containing dyes 3 or 5 as PIs. Upon the addition of Iod, thick samples could also not be cured in depth, while thin samples could be polymerized. However, the final double bond conversions of the monomer were slightly lower than that achieved with the dyes 3 or 5/Iod/amine-based PISs (e.g. FCs ~90% of dye 3/Iod vs ~96% of dye3/Iod/amine). Furthermore, with the addition of amine, the initiation ability of the dye 3/amine combination for the thin sample was much lower than that achieved with the dye 3/Iod/amine-based three-component PIS (FC ~ 63% for dye 3/amine vs ~ 96% for the dye 3/Iod/amine system). Besides, thick samples could not be deeply cured with the dye 3/EDB two-component system. For the dye 5/EDB PIS, polymerization efficiencies determined for thin

samples and thick samples were slightly lower than that obtained with the three-component dye 5/Iod/EDB-based PIS under the same conditions. The above results proved that the coexistence of dyes, Iod and amine had a huge effect on improving the efficiency of FRP for PEG-DA.

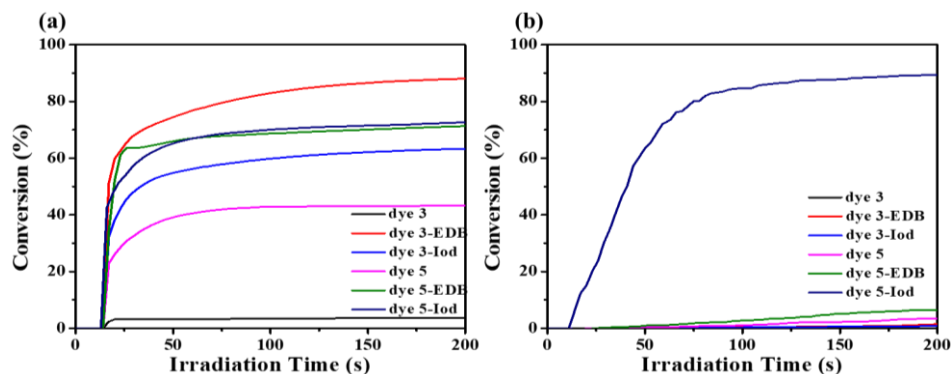


Figure III-1.3. FRP profiles of PEG-DA (conversion of C=C bonds vs irradiation time) under LED@405 nm ($I_0 = 110 \text{ mW.cm}^{-2}$) with the thickness (a) about 20 μm and (b) about 2 mm, initiated by 0.1% dye 3, 0.1% dye 3/1.5% Iod, 0.1% dye 3/1.5% EDB, 0.1% dye 5, 0.1% dye 5/1.5% Iod and 0.1% dye 5/1.5% EDB, w/w. The irradiation starts from $t = 10 \text{ s}$.

3. Proposed Chemical Mechanisms.

With their high reactivity, dyes 3 and 5 were chosen as representative derivatives to study the chemical mechanisms.

3.1 Steady state photolysis.

Steady-state photolysis experiments of the dyes, dyes/Iod, dyes/amine as well as the dyes/Iod/amine combination were carried out in acetonitrile upon irradiation with a LED@405 nm. As evidenced by the UV-visible absorption spectra in [Figure III-1.4](#), obvious photolysis and significant declines of the absorption intensity were observed within 2 min. In the case of dye 3-based PIS, three changes can be observed for dye 3 alone during the photolysis process, but only the main absorption peak near 400 nm decreased upon irradiation, and 15% consumption of dye 3 could be determined, which was closed to that achieved with the dye 3/EDB PIS for which only a decrease of the absorption peak at 400 nm could be observed. Furthermore, two changes can be detected for the dye 3/Iod-based PIS, which achieved 35% consumption for dye 3. The

main absorption peak near 400 nm decreased while the absorption peak around 350 nm increased with the light irradiation. The dye/Iod/amine-based PIS achieved the highest consumption of dyes (~ 42%) within 120 s and the main absorption peak near 400 nm also decreased.

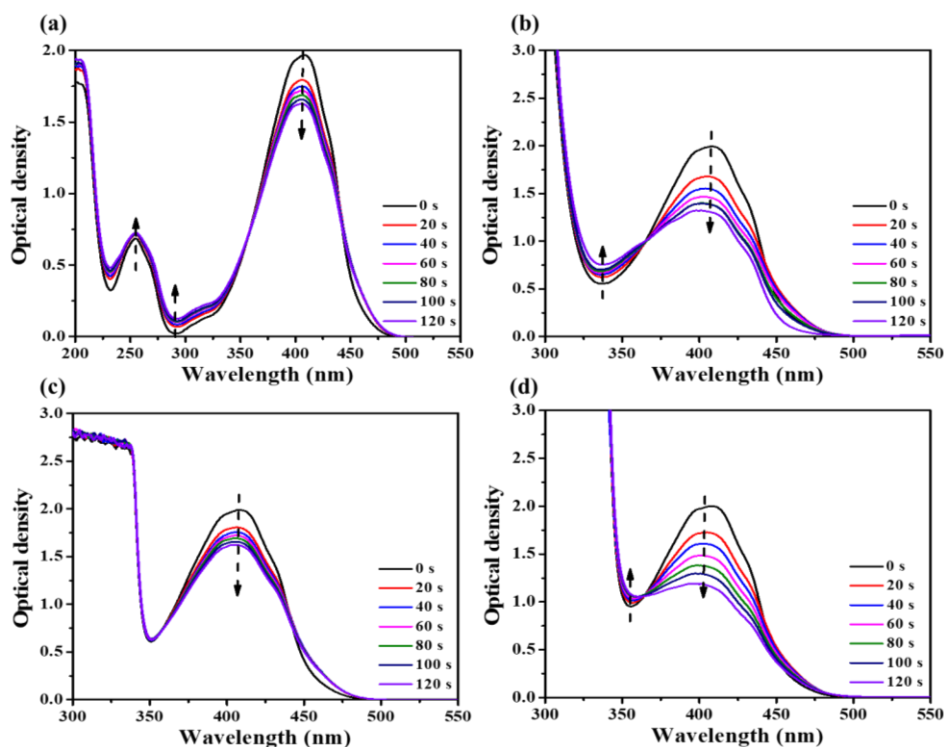


Figure III-1.4. Photolysis of (a) dye 3; (b) dye 3/Iod; (c) dye 3/amine and (d) dye 3/Iod/amine upon exposure to a LED@405nm under air in acetonitrile.

Remarkably, the photolysis process of the dye 5-based one/two or three-component PISs were different from that determined for the dye 3-based PISs, as shown in [Figure III-1.5](#). Consumptions of dye 5 in the different experiments are summarized in [Annex III-1.3](#). The dye 5/Iod- and dye 5/Iod/amine-based PIS exhibited a rapid photolysis so that the main absorption peak near 450 nm showed a blue-shift and disappeared within 25 s. Consumption of dye 5 reached approximately 80% with these two systems ([Annex III-1.3](#)). However, no obvious photolysis could be detected with the dye 5- and dye 5/amine-based PISs, which just realized 5% consumption of dyes after 25 s. Since the rate of the photolysis process depends on the ability of the dye to transfer an electron with Iod or the amine, the above photolysis results clearly evidenced that dye 5 can initiate faster electron transfer with Iod and amine than dye 3.

This difference of reactivity can be confidently assigned to the presence of the additional amino group contained in the chemical structure of dye 5.

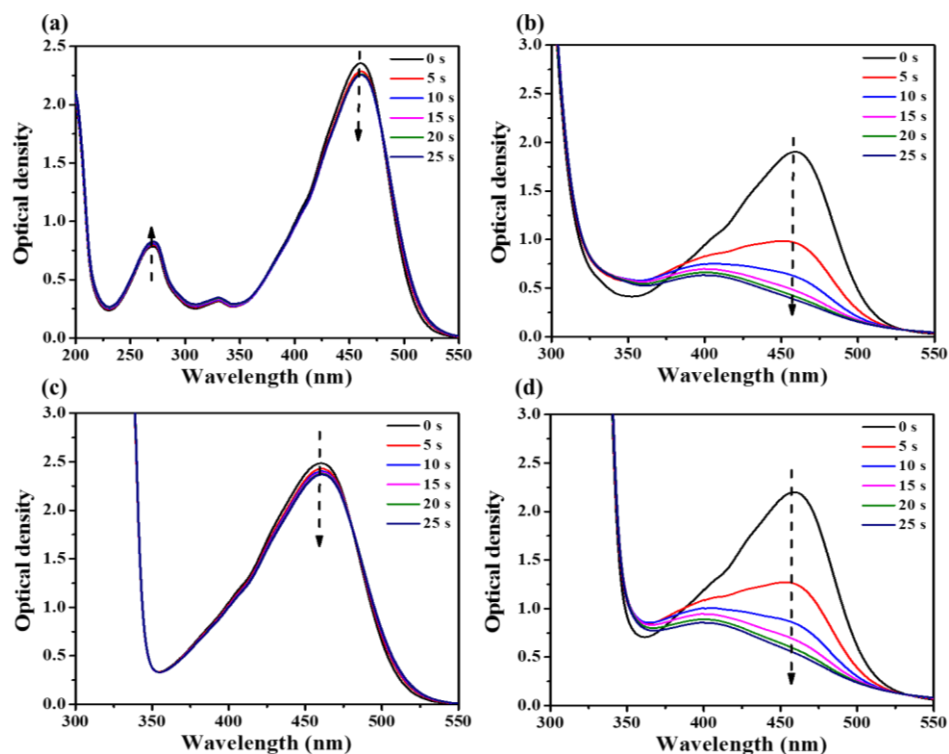


Figure III-1.5. Photolysis of (a) dye 5; (b) dye 5/Iod; (c) dye 5/amine and (d) dye 5/Iod/amine upon exposure to a LED@405nm under air in acetonitrile.

3.2 Fluorescence quenching experiments.

Emission and fluorescence quenching spectra of dyes 3 and 5 were recorded in acetonitrile and the different curves are presented in [Annex III-1.4](#). The addition of Iod or amine to dyes 3 or 5 resulted in a decrease of the emission intensity of dyes 3 and 5, demonstrating that Iod and EDB can act as efficient quenchers through the interactions of the dye with Iod or amine in the singlet excited state. It's noticeable that the fluorescence quenching process caused by the interaction of the dye with Iod is basically linear. In addition, the Stern-Volmer coefficient (K_{SV} , [Table III-1.4](#)) and the electron transfer quantum yield (Φ_{et} , [Table III-1.4](#)) related to the electron transfer reaction between the dye with Iod or amine can be determined by equation 6 or 7 [2-3].

The theoretical feasibility of the interactions between dye/Iod (or dye/amine) was also investigated by calculating the free energy changes of the electron transfer reactions (ΔG_{Iod} or ΔG_{EDB} , respectively). The first singlet excited state energy (E_{S1}) is

calculated from the crossing point between the standardized absorption and fluorescence spectra (e.g. $E_{S1} = 2.74$ V and 2.50 V for dye 3 and dye 5, respectively; see Table III-1.4). Figure III-1.6 showed the oxidation and reduction potentials of dyes 3 and 5 measured by cyclic voltammetry. It is obviously that two oxidation peaks are observed in the positive potential range of dye 5, which corresponds to irreversible further oxidation even at higher potentials. Reduction peaks could be also clearly observed. For dye 3, an oxidation peak and a reduction peak could be detected by cyclic voltammetry. According to the equations (1) or (2), ΔG_{Iod} or ΔG_{EDB} were determined from the oxidation potential E_{ox} (or from the reduction potential E_{red}), and the first singlet excited state energy (E_{S1}) that all of them were all less than 0 except the ΔG_{EDB} of dye 5 was 0. All these results revealed that the electron transfer reactions can be occurred between dyes/Iod and dyes/amine.

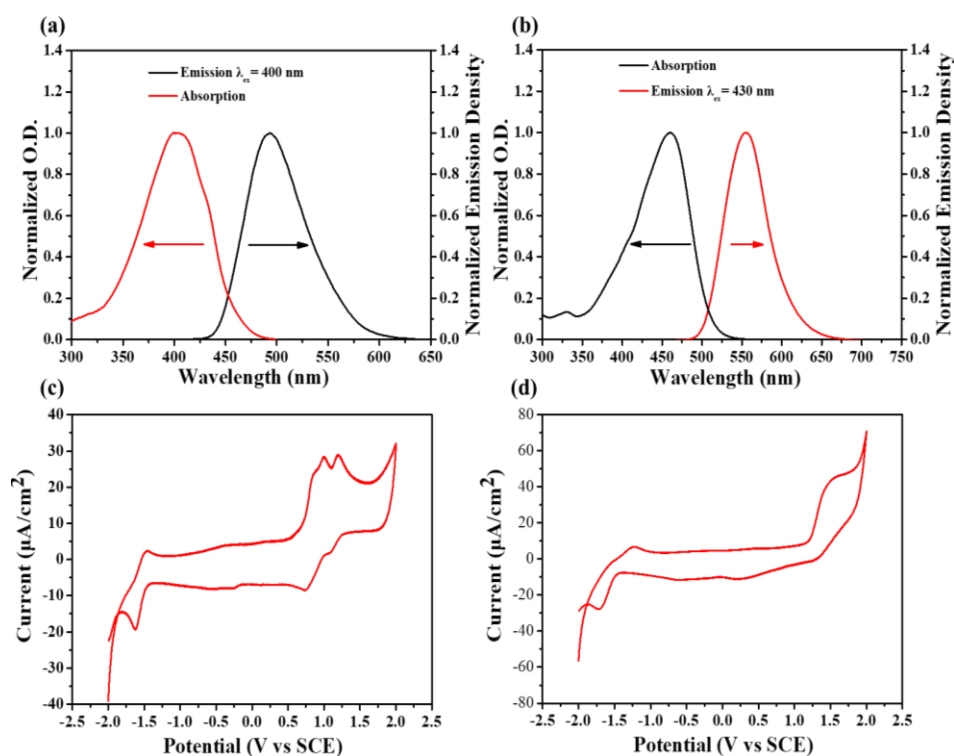
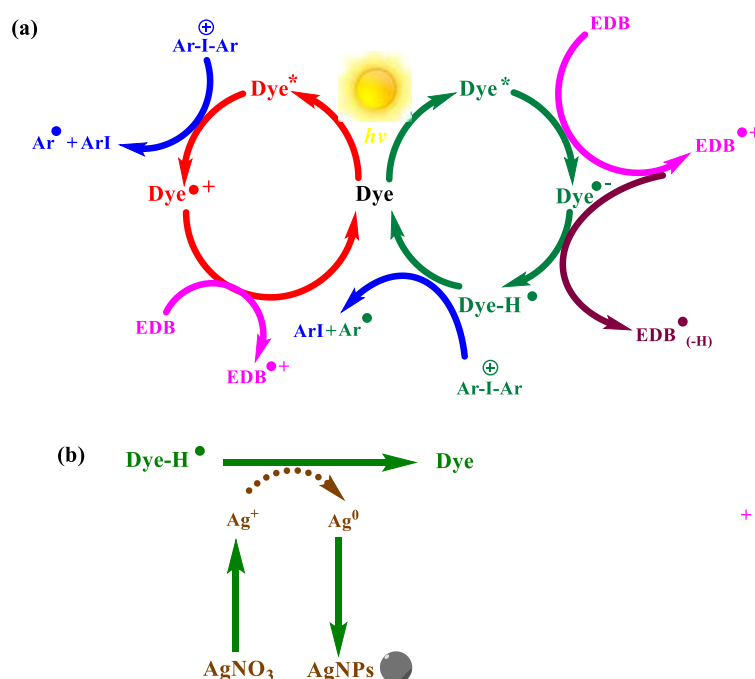


Figure III-1.6. Singlet state energy of (a) dye 3; (b) dye 5 determined in acetonitrile and the cyclic voltammograms of (c) dye 3 and (d) dye 5 in acetonitrile against saturated calomel electrode (SCE) for N_2 saturated solutions.

Dye 3	Dye 5
-------	-------

$K_{SV}^{Iod} (M^{-1})$	93	58
Φ_{et}^{Iod}	0.74	0.65
$K_{SV}^{amine} (M^{-1})$	11	10
Φ_{et}^{amine}	0.49	0.44
$E_{S1} (V)$	2.74	2.50
$E_{ox} (V)$	1.33	0.79
$E_{red} (V)$	-1.60	-1.50
ΔG_{S1}^{Iod}	-0.71	-1.01
ΔG_{S1}^{EDB}	-0.14	0

Table III-1.4. Parameters characterizing the fluorescence properties of dyes 3 and 5 in acetonitrile, redox potential (E_{ox}/E_{red}) as well as the free energy change of the singlet electrode (ΔG_{S1}).



Scheme III-1.2. (a) Proposed photoinitiation step mechanisms of dyes/Iod/amine initiating systems; (b) Photoinitiation mechanism of the generation of AgNPs.

3.3 ESR experiments.

ESR-spin trapping experiments were successfully performed under N_2 to detect

the generated radicals from the dye 5/ Iod and dye 5/amine solutions. As shown in the [Annex III-1.5](#), aryl radicals generated by the dye 5/ Iod combination could be trapped with PBN so that hyperfine coupling constants for nitrogen and hydrogen of $a_N = 14.4$ G and $a_H = 2.2$ G could be determined. These values were completely consistent with the literature [4] and also proved the occurrence of an interaction between dye and Iod as shown in the [Scheme III-1.2](#). Furthermore, the $a_N = 14.4$ G and $a_H = 2.2$ G detected from the dye 5/amine solution ([Annex III-1.5c-d](#) evidenced the generation of aminoalkyl radicals according to experimental data published elsewhere ($a_N = 14.4$ G and $a_H = 2.2$ G, [5]).

4. The Generations of AgNPs in DMF Solution and PEG-Polymers.

In this study, we proposed that through redox reactions between dyes and the additive (Iod/amine) a series of free radicals and cations could be generated upon irradiation with a LED@405nm (as shown in [Scheme III-1.2](#)), which demonstrated two roles: one was to induce the polymerization of PEG-DA monomers, and the other was to reduce the $AgNO_3$ into AgNPs *in situ*. The formation of AgNPs in DMF can be clearly evidenced by UV-visible absorption spectroscopy, which can also be demonstrated by the color change of the solutions. As shown in [Figure III-1.7a](#), two absorption peaks at 400 nm and 460 nm can be observed, with a decrease of the absorption peak at 460 nm during photolysis of dye 5, while the intensity of the absorption peak at 400 nm increased due to the generation of AgNPs upon irradiation for 90 min. Additionally, color of the solution changed from light brown to dark brown. Even, one side of the cuvette wall adopted a silver color, resulting from the coating by silver nanoparticles (see in [Figure III-1.7b](#)).

Furthermore, the AgNPs generated in PEG-polymers were characterized through the changes of the color of the PEG-monomer polymerized upon irradiation with LED@405 nm (see in [Figure III-1.7d](#)), which was monitored by RT-FTIR. The color also changed from light brown to dark brown, while the same changes can also be observed when coating thin films from 4 passes to 20 passes (the thickness of one pass is about 50 μm). However, although the polymerization efficiency of the formulation containing AgNPs shown in [Figure III-1.7c](#) is lower than that obtained for the

formulation without AgNPs, its final acrylate function conversion was still about 80% after irradiation for 300 s.

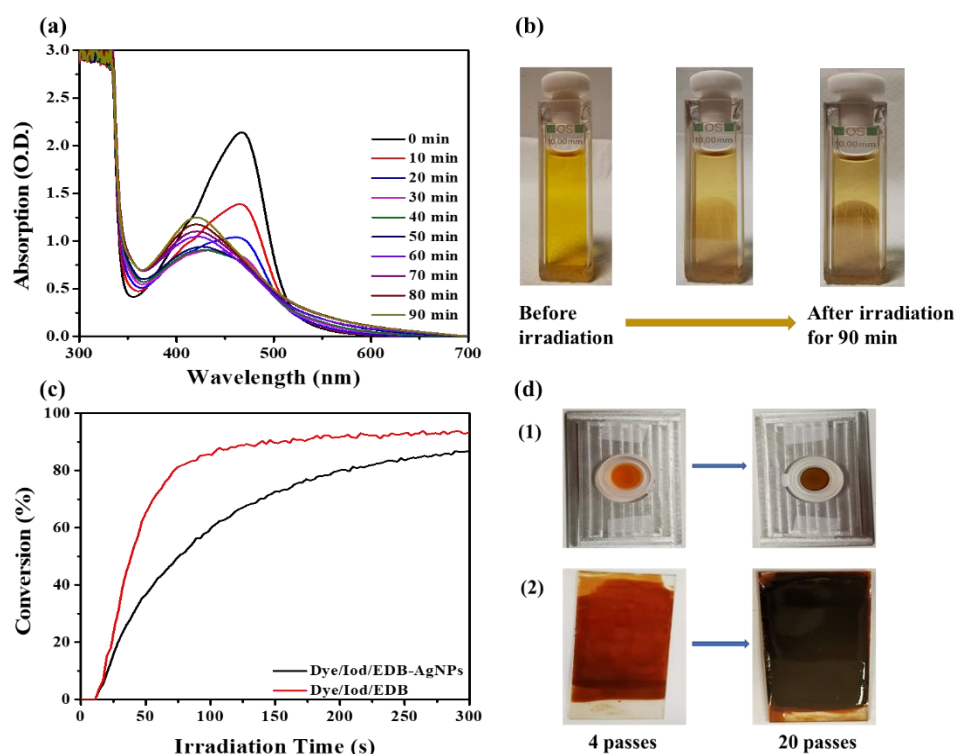


Figure III-1.7. (a) In-situ preparation of AgNPs with dye 5/Iod/EDB (0.05 wt%) and AgNO₃ (4 wt%) in DMF followed by UV-visible absorption spectroscopy in air atmosphere; (b) the color of solution turned to dark brown after 90 min light irradiation; (c) photopolymerization profiles of PEG-DA (conversion rate of C=C bonds vs irradiation time) containing AgNPs initiated by dye 5/Iod/amine upon exposure to a LED@405 nm in laminate. The irradiation starts at t = 10 s; (d) The color changes of PEG-polymers containing AgNO₃.

The size and the shape of the AgNPs generated in DMF and in PEG-polymers detected using TEM are depicted in Annex III-1.6. The AgNPs in DMF were irregularly spherical with a size of about 2~4 nm, whereas the AgNPs generated in PEG-polymer were in a regular spherical shape with the size varied from 20~40 nm, which were much larger than that obtained in DMF due to the aggregation of the particles in PEG-polymer.

5. The Influence of AgNPs on the Physical Properties of PEG-Polymers.

5.1 3D direct laser write experiments.

Since dyes 2, 3, 5, 8 and 9 were selected as excellent candidates for the FRP for PEG-DA upon irradiation with a LED@405 nm, direct laser write experiments were carried out under these conditions. However, only dyes 3 and 5-based formulations could be successfully written and furnished stable 3D letter patterns (“CZH”) with good spatial resolutions (limited by the size of the laser beam ~50 μm). Morphologies of the 3D structures were observed using a numerical optical microscope (Figure III-1.8). Interestingly, all direct laser write experiments could be finished within 3 min. However, a shorter irradiation time was required for the dye 5-based systems to get the 3D patterns than that used for the dye 3-based system. In addition, the color of the formulations become darker with the addition of silver cations, after laser write, the obtained polymers turned into yellowish-brown as the generation of AgNPs. Due to the photo-inhibition effect, it takes longer time to write a stable 3D pattern, whose morphology is rougher than that without AgNPs.

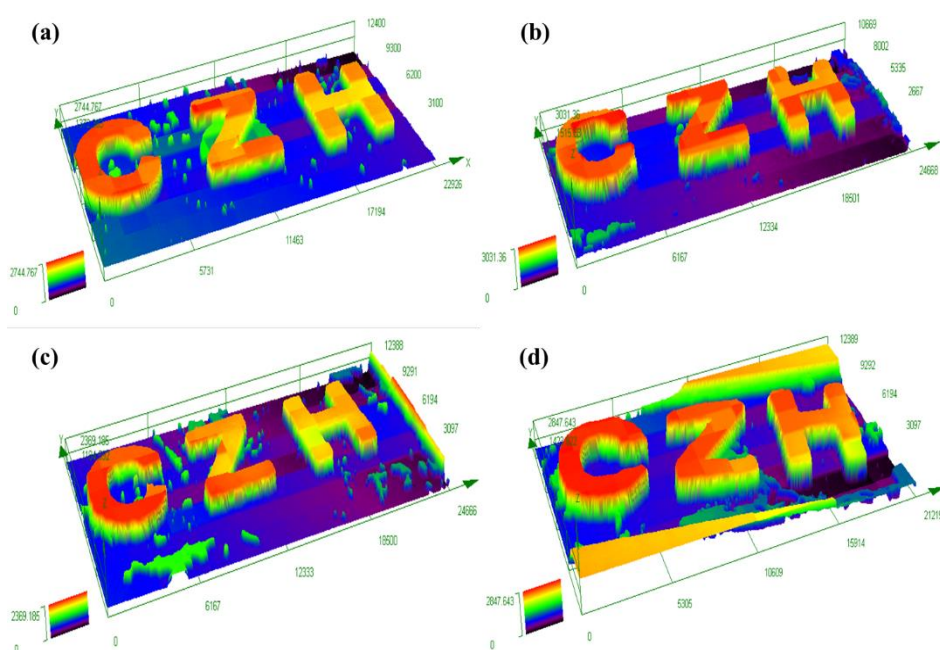


Figure III-1.8. Free radical photopolymerization of PEG-DA through direct laser write experiments initiated by dyes-based PIS with a laser diode @405nm. Characterization of the 3D patterns by numerical optical microscopy: (left) top surface morphology and (right) 3-D overall appearance: (a) containing dye 3-based PIS; (b) containing dye 5-based PIS; (c) containing dye 3-based PIS and AgNPs; (d) containing dye 5-based PIS and AgNPs.

5.2 Water swelling of PEG-polymers containing/without AgNPs.

By comparing the weight and volume changes of water swelled PEG-polymers

containing/without AgNPs prepared with three-component PIS based on dyes 3 or 5/Iod/amine (0.1%/1.5%/1.5%, w/w/w), the effect of the presence of AgNPs for the swelling process is studied. As displayed in **Figure III-1.9**, after the polymers swelled in water to reach the swelling equilibrium, the swelling rate of them without AgNPs were about 70%-90%, and their volumes increased about 170%-190% (see **Annex III-1.7**). However, the swelling ratio of the AgNPs-containing polymers were only about 60% and the ratio of their volume increased were about 150%-160%, which were smaller than that achieved by the polymers without AgNPs. This may be owing to the generated AgNPs and residual salts occupied some pores inside the polymers [6-8]. Subsequently, the polymers that reached the swelling equilibrium could return to their original weight and volume after dehydrated at 50 °C for 1 h, (as shown in **Figure III-1.9b**), while the morphologies were a little deformed, indicating that the swelling behavior of these polymers was reversible [9-10].

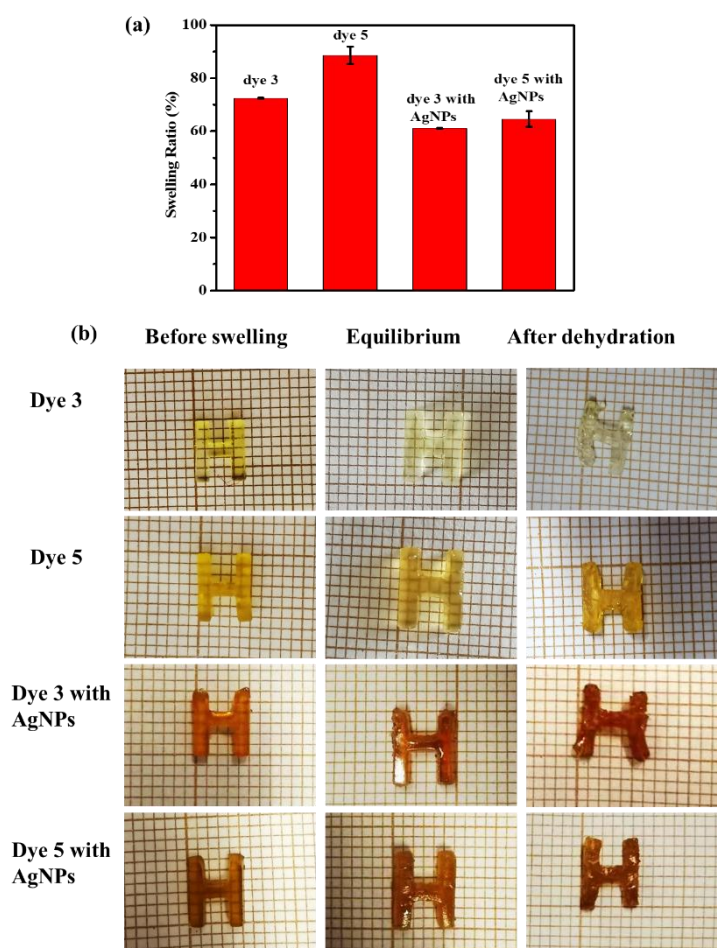


Figure III-1.9. (a) the swelling ratio of PEG-polymers containing/without AgNPs; (b) the photos of PEG-polymers containing/without AgNPs during the reversible water swelling process.

5.3 The reversible shape-memory effect of PEG-polymer containing/without AgNPs.

The combination of the dye 5/Iod/amine based PIS and PEG-DA can be potentially used for 3D bioprinting as its high biocompatibility and hydrophilicity. According to a previous study [11], the reversible deformation effect of PEG-polymers was closely related to the irradiation time, so that the best irradiation time was selected to prepare a cross object with good spatial resolution characteristics and detect its 4D deformation upon swelling and dehydration. Subsequently, influence of the silver nanoparticles on the 4D deformation properties of PEG-polymers was also studied by comparing the shapes change performance of PEG-polymers containing/without AgNPs. As shown in [Figure III-1.10a/b-1](#), the color of the prepared cross containing AgNPs was darker than that without AgNPs. After being immersed in a water filled beaker, these two polymers all curled as swelling in water, while the degree of deformation of the polymer without AgNPs was greater than that of the polymer containing nanoparticles (the process is clearly shown in [Figure III-1.10a/b-2](#)). Hereafter, the two deformed polymers were removed from the beaker and placed in an oven at 80°C to dehydrate. Interestingly, the rolled cross gradually flattened during this process and returned to its original shape after 5 min (see in [Figure III-1.10a/b-3](#)). With the continue dehydrate, the restored polymers curled upside down since the contained water was completely removed, which were shown in [Figure III-1.10a/b-4](#). The above results prove that the deformation degree of the polymer containing AgNPs is smaller than that of the polymer without nanoparticles, which is consistent with their swelling performance. Finally, the reverse-curved polymers were moved from 80 °C into room temperature, which gradually flatten to return their primary morphology (see [Figure III-1.10a/b-5](#)). [Figure III-1.10a/b-6 to 8](#) exhibited the second shape-memory process of these two polymers, which demonstrated that the available polymers initiated by the proposed PIS can be used for 4D printing due to their reversible deformation effect through thermal-/water-responsiveness. More interestingly, the photoinhibition effect caused by the darkening of the resin with the presence of AgNPs reduces its photopolymerization efficiency, resulting in a lower crosslink density of the obtained PEG-polymer, which decrease its surface tension and surface wettability, thereby inhibiting its deformation effect [12-13].

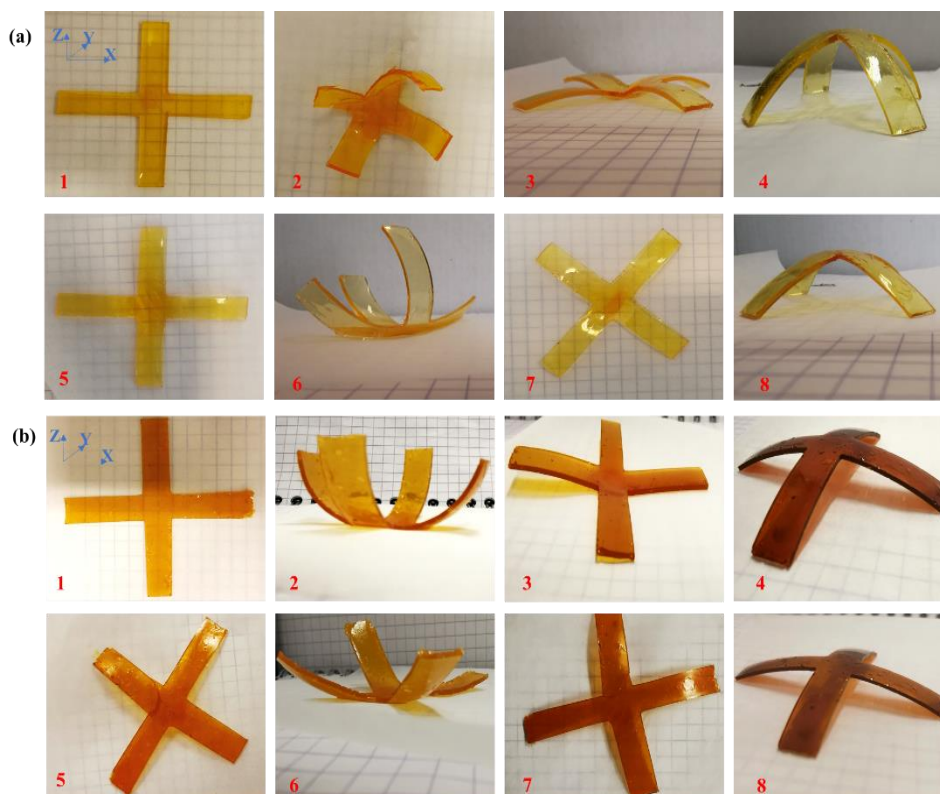


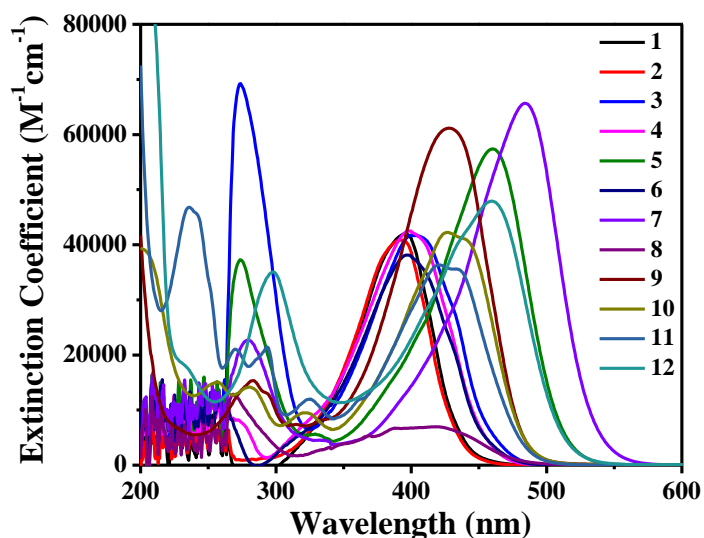
Figure III-1.10. The shepe-memory process of the prepared PEG-polymers and the PEG-polymers contained AgNPs : (1) Cross obtained under 1 min of light irradiation, (2) Deformed cross after swelling, (3) Cross restored to its original appearance after 2 min of dehydration ($T=80^{\circ}\text{C}$), (4) Reverse-curved cross after dehydration for 10 min, (5) Cross at room temperature for 10 min; (6) Deformed cross after swelling again, (7) Cross recovered to its original appearance after dehydrated again for 2 min ($T=80^{\circ}\text{C}$), (8) Reverse-curved cross after dehydrated again for 10 min again.

6. Conclusion.

In conclusion, twelve different dyes with 2,5-diethylene-cyclopentane-1-one as the main structure were synthesized and used as PIs with Iod and EDB. Under LED irradiation, the redox reactions could take place between dyes and Iod/EDB, which generated free radicals and cations to induce the polymerization reactions of PEG-DA and EPOX monomers. Furthermore, it could also reduce the AgNO_3 into AgNPs. Owing to the extended π -conjugation in the molecular structures of the different dyes examined in this work, a strong absorption appeared in the near UV or the visible range for all chromophores, which was in agreement with their excellent polymerization efficiencies for the free radical polymerization and the cationic polymerization. Remarkably, dyes 3 and 5 proved to be excellent PIs. The steady state photolysis,

fluorescence quenching, and ESR-ST experiments were successfully performed to characterize the involved photochemical mechanisms. Finally, the PEG-polymers with reversible deformation effect can also be observed and the generation of AgNPs could reduce their swelling and 4D deformation performance. In addition, the above-mentioned photocurable resins with the thermal- and water-response can be potentially used in emerging fields including biomedical engineering and smart response materials, etc.

Annex

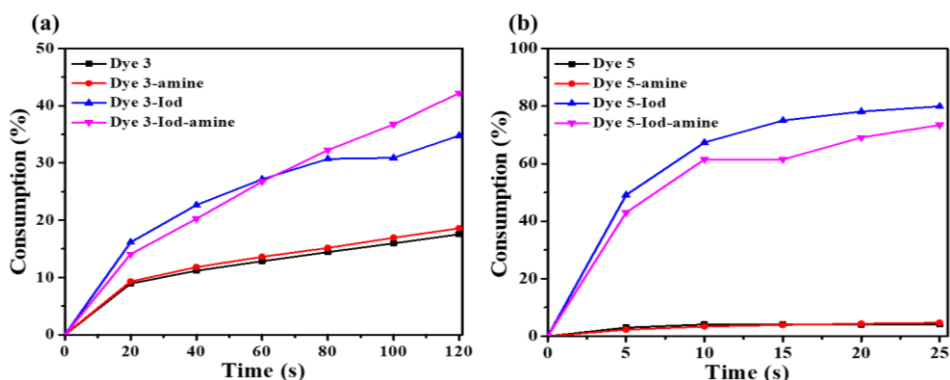


Annex III-1.1. The UV-vis absorption spectra of dye 1-12 in acetonitrile.

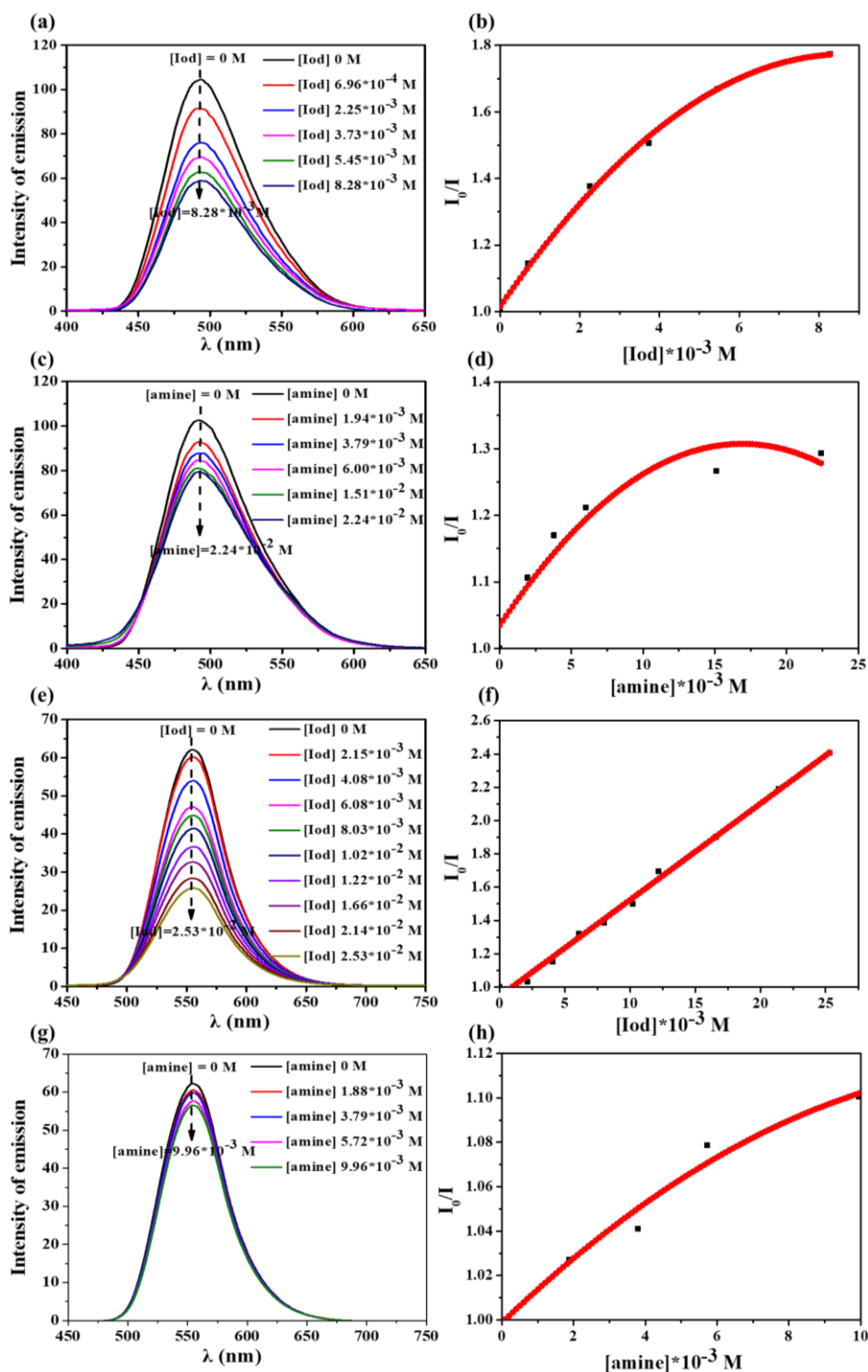
Final acrylate function conversions (FC) initiated by dyes 3 and 5-based PIS

Thickness	Dyes	3	3-Iod	3-EDB	5	5-Iod	5-EDB
~20 μm	FCs (%)	-	88	63	-	71	73
~2 mm	FCs (%)	-	-	-	-	-	89

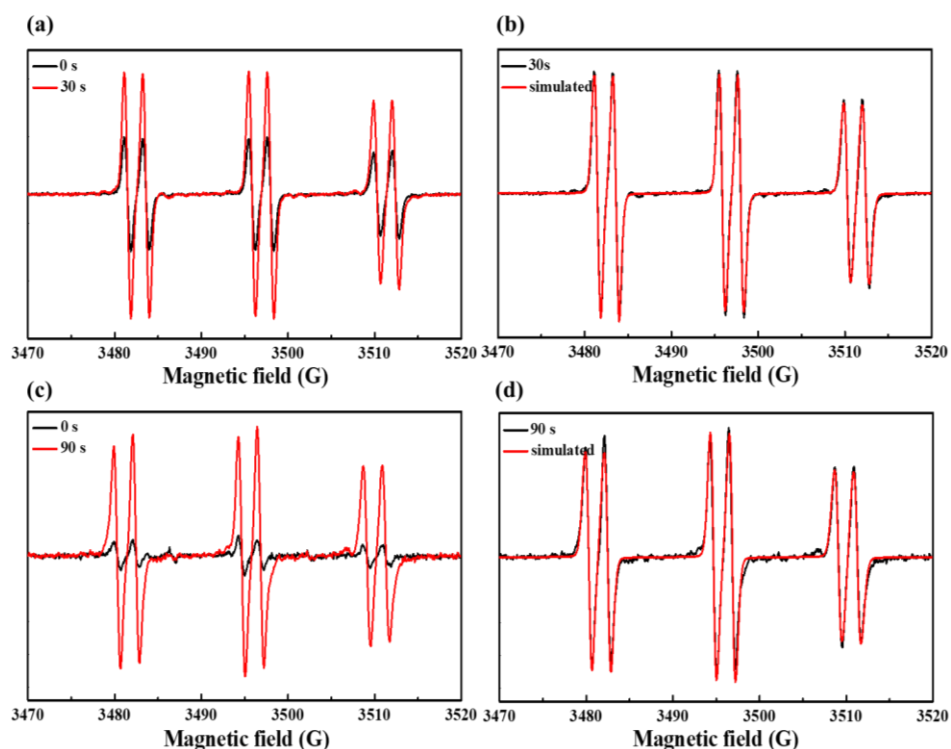
Annex III-1.2. Summary the FCs for the PEG-DA monomer upon irradiation with a LED@405 nm that initiated by 0.1% dye 3, 0.1% dye 3/1.5% Iod, 0.1% dye 3/1.5% EDB, 0.1% dye 5, 0.1% dye 5/1.5% Iod as well as 0.1% dye 5/1.5% EDB, w/w, in laminate.



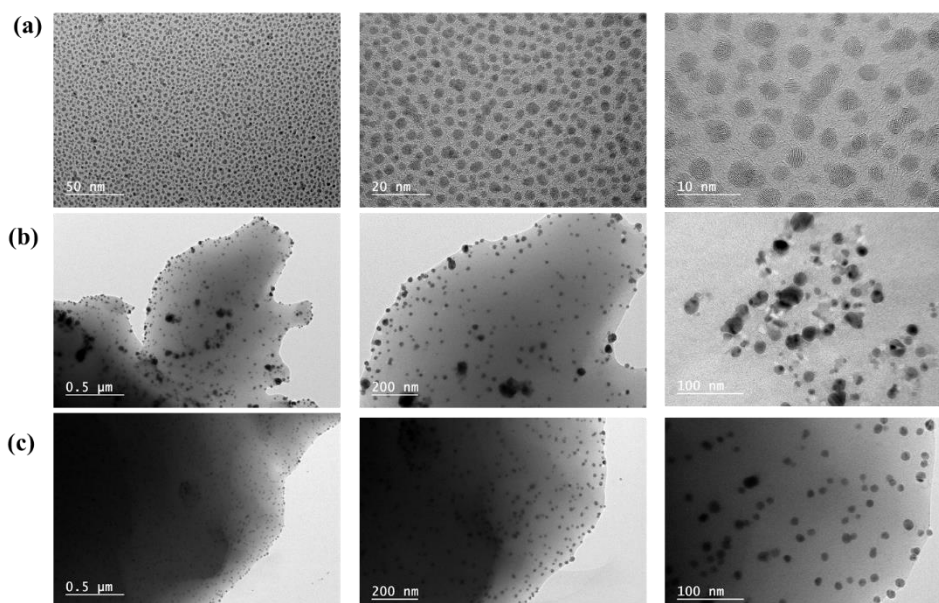
Annex III-1.3. The consumption of (a) dye 3 and (b) dye 5 during the photolysis process.



Annex III-1.4. (a) Fluorescence quenching of dye 3 by Iod; (b) Stern–Volmer treatment for the dye 3 / Iod fluorescence quenching; (c) Fluorescence quenching of dye 3 by EDB; (d) Stern–Volmer treatment for the dye 3 /EDB fluorescence quenching ; (e) Fluorescence quenching of dye 5 by Iod; (f) Stern–Volmer treatment for the dye 5 / Iod fluorescence quenching; (g) Fluorescence quenching of dye 5 by EDB; (h) Stern–Volmer treatment for the dye 5 /EDB fluorescence quenching.



Annex III-1.5. ESR spectra obtained from ESR-spin trapping experiment using PBN = 2 mg/mL (as spin trap agent); Iod = 12 mg/mL; EDB = 12 mg/mL and dye 5 = 0.8 mg/mL in acetonitrile under N₂. (a) dye 5/Iod; Irradiation time = 0 s (black) and = 30 s (red) spectra; (b) dye 5/Iod; Irradiation time = 30 s (black) and simulated (red) spectra; (c) dye 5/amine; Irradiation time = 0 s (black) and = 90 s (red) spectra; (d) dye 5/amine; Irradiation time = 90 s (black) and simulated (red) spectra.



Annex III-1.6. TEM images of (a) AgNPs prepared in DMF solution; (b) AgNPs prepared in PEG-polymer from FTIR experiment (thick film); (c) AgNPs prepared in

thin film (PEG-based polymer).

	Dye 3	Dye 5	Dye 3 with AgNPs	Dye 5 with AgNPs
V_1 (mm ³)	39.39	42.74	27.97	31.11
V_2 (mm ³)	69.32	81.23	40.27	49.60
V_3 (mm ³)	38.12	34.98	16.28	30.40
R (%)	176	190	144	160

Annex III-1.7. The summary of 3D pattern volumes and their increased ratio (R) during the reversible water swelling process.

References:

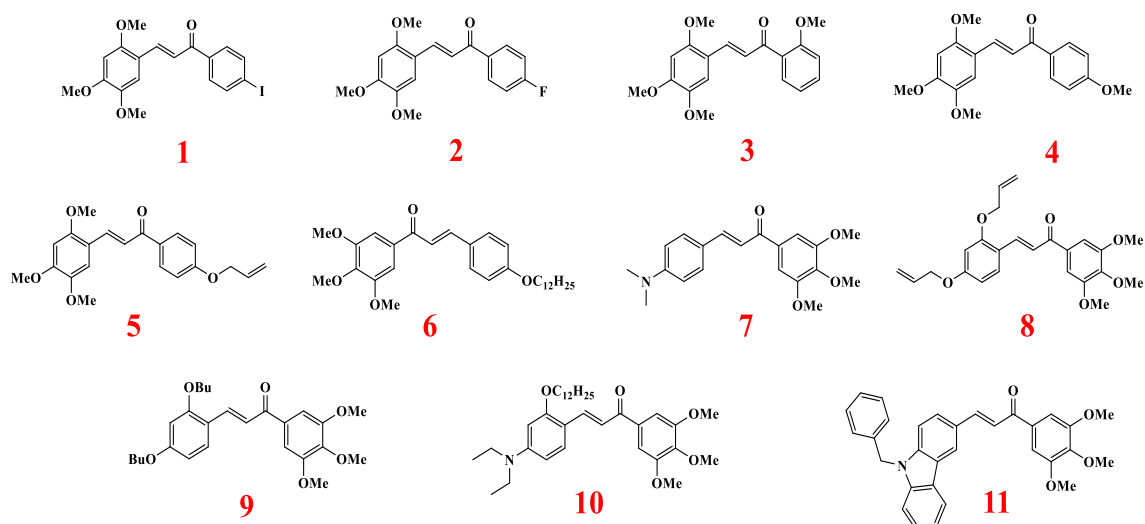
1. Garra, P.; Graff, B.; Morlet-Savary, F.; Dietlin, C.; Becht, J. M.; Fouassier, J. P.; Lalevée, J. Charge transfer complexes as pan-scaled photoinitiating systems: from 50 μm 3D printed polymers at 405 nm to extremely deep photopolymerization (31 cm). *Macromolecules* **2018**, *51*(1), 57-70.
2. Zeng, H. L.; Durocher, G. Analysis of fluorescence quenching in some antioxidants from non-linear Stern—Volmer plots. *Journal of Luminescence* **1995**, *63*(1-2), 75-84.
3. Langer, G.; Berer, T. Fluorescence quantum yield and excited state lifetime determination by phase sensitive photoacoustics: concept and theory. *Optics Letters* **2018**, *43*(20), 5074-5077.
4. Lalevée, J.; Tehfe, M. A.; Zein-Fakih, A.; Ball, B.; Telitel, S.; Morlet-Savary, F.; Graff, B.; Fouassier, J. P. N-vinylcarbazole: An additive for free radical promoted cationic polymerization upon visible light. *ACS Macro Letters* **2012**, *1*(7), 802-806.
5. Lalevée, J.; Gimes, D.; Bertin, D.; Graff, D.; Allonas, X.; Fouassier, J. P. Comparative reactivity of aminyl and aminoalkyl radicals. *Chemical Physics Letters* **2007**, *438*(4-6), 346-350.
6. Sahiner, N. In situ metal particle preparation in cross-linked poly(2-acrylamido-2-methyl-1-propanesulfonic acid) hydrogel networks. *Colloid and Polymer Science* **2006**, *285*(3), 283-292.
7. Schexnailder, P.; Schmidt, G. Nanocomposite polymer hydrogels. *Colloid and Polymer Science* **2009**, *287*(1), 1-11.
8. Arsuaga, J. M.; Sotto, A.; Rosario, del G.; Martínez, A.; Molina, S.; Teli, S. B.; Abajo, de J. Influence of the type, size, and distribution of metal oxide particles on the properties of nanocomposite ultrafiltration membranes. *Journal of Membrane Science* **2013**, *428*, 131-141.
9. Chen, H.; Zhang, Ni, T. Y.; Ding, P.; Zan, Y.; Cai, X.; Zhang, Y. W.; Liu, M.; Pei, R. J. Construction of a silk fibroin/polyethylene glycol double network hydrogel with co-culture of HUVECs and UCMSCs for a functional vascular network. *ACS Applied Bio Materials* **2021**, *4*(1), 406-419.
10. Zhang, Y. J.; Josien, L.; Salomon, J. P.; Simon-Masseron, A.; Lalevée, J. Photopolymerization of zeolite/polymer-based composites: toward 3D and 4D printing applications. *ACS Applied Bio Materials* **2021**, *3*(1), 400-409.
11. Chen, H.; Zhang, Y. J.; Bonfiglio, A.; Morlet-Savary, F.; Mauro, M.; Lalevée, J. Rhenium(I) N-heterocyclic carbene complexes in photoinitiating systems for polymerization upon visible light: development of photosensitive resins for 3D and 4D applications. *ACS Applied Bio Materials* **2021**, *3*(1), 464-473.

12. Liu, Y.; Li, Y.; Yang, G.; Zheng, X. T.; Zhou, S. B. Multi-stimulus-responsive shape-memory polymer nanocomposite network cross-linked by cellulose nanocrystals. *ACS Applied Materials Interfaces* **2015**, *7*(7), 4118-4126.
13. Liu, C. D.; Chun, S. B.; Mather, P. T. Chemically cross-linked polycyclooctene: synthesis, characterization, and shape memory behavior. *Macromolecules* **2002**, *35*(27), 9868-9874.

Chapter 2. Interpenetrating Polymer Network Hydrogels Using Natural Based Dyes Initiating Systems: Antibacterial Activity and 3D/4D Performance

Interpenetrating polymer networks (IPNs) are not just a mixture of two or more preformed polymers but refers to networks comprising two or more partially interwoven polymer networks that are not covalently bonded to each other [1-2]. Compared with a single polymer network, IPN hydrogels rely on the interweaving of multiple networks to form special cell-like structures, interpenetrated interface, and two-phase continuity, which greatly improve their physical and chemical properties or functions [3-4]. In addition, due to the continuity and synergy of the two phases, their properties are homogenized and the final polymers exhibit unique properties that are different from those of the two polymers considered separately, which greatly broadens their scope of applications [5-7].

In this work, the best candidates were selected from the firstly synthesized 11 dyes based on 1-aryl-3-(2,4,5-trimethoxyphenyl)prop-2-en-1-one or 3-aryl-1-(3,4,5-trimethoxyphenyl)prop (see [Scheme III-2.1](#)), and then combined with EDB and Iod as a three-component visible light PISs to initiate both FRP of PEG-DA and CP of EPOX and in situ reduction of silver cations into silver nanoparticles to prepare IPN with antibacterial activity for Gram-positive bacteria (e.g. *Staphylococcus aureus*) and Gram-negative bacteria (e.g. *Pseudomonas aeruginosa*). More interestingly, stable 3D patterns were successfully produced through direct laser write (DLW) technique, and they exhibited reversible swelling properties and shape memory effects caused by swelling and dehydration processes, thus enabling 4D printing.



Scheme III-2.1. Chemical structures of dyes 1-11.

1. Photoinitiation Ability of the Proposed Dyes-Based PISs Upon Visible Light.

1.1 Free radical polymerization (FRP) of PEG-DA.

At first, the visible light source, namely the LED@405 nm, was used to examine the photoinitiation ability of the dye/Iod/amine (0.1%/1.5%/1.5%, w/w/w)-based three-component PISs for the FRP of PEG-DA at room temperature. We monitored the photopolymerization kinetics of the different formulations with thicknesses of about 0.1 mm (thin films) and 2 mm (thick films) upon light irradiation for 200 s. Polymerization profiles are shown in [Figure III-2.1](#). For the thin films, compared to the blank control which is only composed of the two-component Iod/amine combination, all the newly proposed dyes-based three-component PIS showed better photoinitiation efficiencies (the increased final functional groups conversions and /or photopolymerization rates), which proved that the presence of the dyes was essential to improve the overall polymerization performance. In addition, under the same condition, for thick samples with the thickness of about 2 mm, except for the three-component PISs based on dyes 6, 8 and 9, all the other PISs showed better photoinitiation abilities than the blank control (conversion rate $\geq 90\%$ of the experimental group vs. 87% of the blank group, [Table III-2.1](#)).

More interestingly, under a LED@405nm irradiation, whether for thin films or thick films, the final conversions achieved by the PISs based on dyes 1, 2, 3, 4, 5, 9 and 11 were greater than 90%, which can be ascribed to their higher molar extinction coefficients as discussed below.

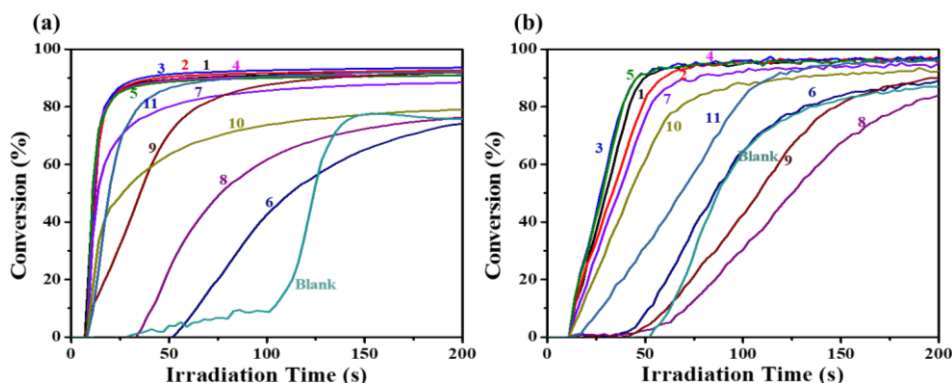


Figure III-2.1. Photopolymerization profiles of PEG-DA (conversion of C=C bonds vs irradiation time) initiated by dyes/Iod/amine (0.1%/1.5%/1.5%, w/w/w) in laminate upon irradiation with LED@405 nm ($I_0 = 110 \text{ mW}\cdot\text{cm}^{-2}$) with the thickness of about (a) 0.1 mm and (b) 2 mm, the irradiation starts at $t = 10 \text{ s}$.

1.2 Cationic polymerization (CP) of EPOX.

The photoinitiation abilities of the three-component PISs for the cationic photopolymerization of EPOX were studied. As shown in [Figure III-2.2](#), Iod/amine system cannot initiate the cationic photopolymerization of EPOX even after 200 s of light irradiation, while in the case of thin films initiated by the proposed dyes-based three-component PIS, deep curing was observed for all of the formulations ([Figure III-2.2a](#)). However, for thick films with a thickness of about 2 mm, only the three-component PISs based on dyes 1, 2, 3, 4 and 5 could lead to the curing of EPOX formulations ([Figure III-2.2b](#)). All these results highlighted the crucial role of the three-component systems for the overall photopolymerization efficiency.

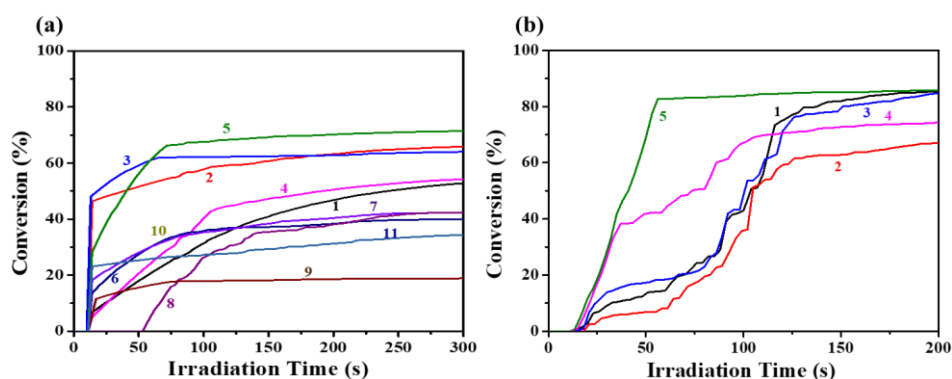


Figure III-2.2. Photopolymerization profiles of EPOX (conversion of epoxy functions vs irradiation time) initiated by dyes/Iod/amine (0.1%/1.5%/1.5%, w/w/w) under air upon irradiation with a LED@405nm ($I_0 = 110 \text{ mW}\cdot\text{cm}^{-2}$) with the thickness of about (a) $10 \mu\text{m}$ and (b) 2 mm, the irradiation starts at $t = 10 \text{ s}$.

Final function conversions (FCs) initiated by dye/Iod/amine				
Dyes	Thin films ~ 0.1 mm		Thick films ~ 2 mm	
	EPOX (%)	PEG-DA (%)	EPOX (%)	PEG-DA (%)
1	27	92	85	96
2	45	93	67	95
3	63	94	85	98
4	64	91	74	97
5	70	91	86	97
6	39	75	-	90
7	40	88	-	95
8	38	76	-	84
9	19	92	-	90
10	31	80	-	92
11	47	92	-	96
Iod/EDB (blank)	-	75.8	-	87

'-' means not deep curing after irradiation for 200s

Table III-2.1. Summary of the final function conversions for PEG-DA (acrylate) and EPOX (epoxy) monomers while using dyes/Iod/amine-based PISs with a thickness of about 10 μm and 2 mm upon irradiation with a LED@405nm. The blank corresponds to the Iod/amine initiating system without dyes.

1.3 The fabrication of IPN polymers through different ratios of PEG-DA and EPOX.

Based on the abovementioned results, dyes 1-5/Iod/amine based three-component PISs proved to be the best candidates as all of them could not only initiate the photopolymerization of PEG-DA, but also could promote the curing of EPOX. In addition, a variety of studies have shown that the interpenetrating polymer networks have their unique structures and properties compared with the single polymer networks, which broaden their applications [4]. In this work, we further studied the initiation ability of the newly proposed dyes-based PISs for PEG-DA/EPOX mixed monomers. Three ratios of resins based on mixed monomers were prepared (in detail, PEG-DA:

EPOX = 3:7, 5:5, 7:3). Their final function conversions (acrylate and epoxide) are summarized in [Table III-2.2](#). A 70/ 30 ratio of PEG-DA/EPOX monomers was determined as the best composition in terms of polymerization efficiencies for the two functionalities (acrylates and epoxides) [8] (see [Table III-2.2](#) for other ratios).

Final function conversions (FCs) initiated by dye/Iod/amine										
Dye	Thin films (PEG-DA:EPOX, %)					Thick films (PEG-DA:EPOX, %)				
	100:0	70:30	50:50	30:70	0:100	100:0	70:30	50:50	30:70	0:100
1	92	94/57	34/23	25/8	38	96	95/46	94/27	96/45	97
2	93	82/53	31/13	76/62	19	96	95/39	94/26	85/46	23
3	94	82/48	96/44	20/50	63	98	94/41	64/44	93/63	14
4	91	76/24	85/67	78/56	34	97	91/55	98/67	83/69	32
5	91	80/44	70/27	29/26	31	97	93/41	94/27	95/51	86

Table III-2.2. Summary of the final function conversions for PEG-DA and EPOX monomers while using dyes/Iod/amine-based PISs for different ratios of PEG-DA/EPOX mixed monomers with the thickness of about 0.1 mm and 2 mm upon irradiation with a LED@405nm.

2. The Involved Chemical Mechanisms.

2.1 UV-*vis* absorption properties of the proposed dyes.

Firstly, the UV-visible absorption properties of eleven dyes were examined in acetonitrile and their absorption spectra are shown in [Figure III-2.3](#). Except for dyes 6, 8 and 9 that only exhibited an absorption peak in the near UV region, all the other dyes showed two or three absorption peaks in the UV and visible region, in which the maximum absorption peaks appeared in the near visible region (≥ 390 nm). These absorption maxima perfectly overlapped with the emission wavelength of the visible light sources (LED@405 nm). Notably, their absorption wavelengths (λ_{\max}), the molar extinction coefficients at their maximum absorption wavelengths (ϵ_{\max}) and at the emission wavelength of the visible light source LED@405 nm ($\epsilon_{@405\text{nm}}$) are summarized in [Table III-2.3](#). More interestingly, the strongest absorption peaks of the

selected five dyes (1-5) all appeared between 380 ~ 400 nm. Meanwhile, all of them also showed higher molar extinction coefficients (ϵ_{\max}) at 405 nm (such as 20 140 $\text{M}^{-1}\text{cm}^{-1}$, 18 390 $\text{M}^{-1}\text{cm}^{-1}$, 9350 $\text{M}^{-1}\text{cm}^{-1}$, 12 540 $\text{M}^{-1}\text{cm}^{-1}$ and 12 130 $\text{M}^{-1}\text{cm}^{-1}$ for these five dyes, respectively), which was in agreement with their excellent photoinitiation abilities. Remarkably, the introduction of electron-donating groups caused a red-shift of the absorption spectra.

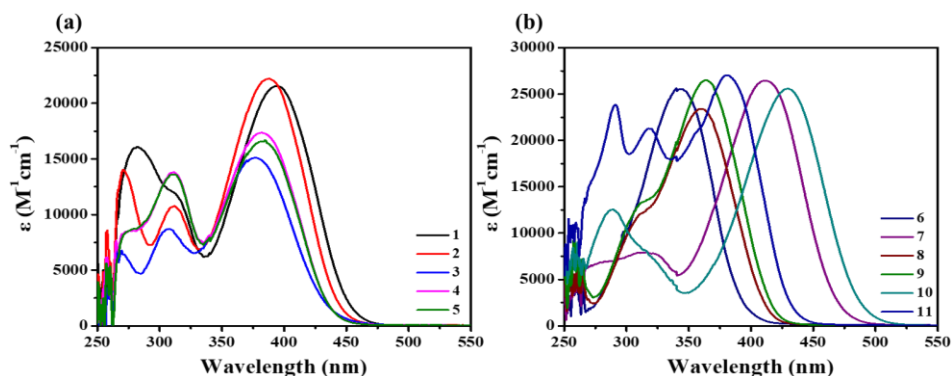


Figure III-2.3. Light absorption properties of (a) dyes 1 ~5 and (b) dyes 6 ~11 in acetonitrile.

DYES	λ_{\max} (nm)	ϵ_{\max} ($\text{M}^{-1}\text{cm}^{-1}$)	$\epsilon_{@405\text{nm}}$ ($\text{M}^{-1}\text{cm}^{-1}$)
1	395	21 560	20 140
	282	16 100	
2	388	22 200	18 390
	312	10 770	
	270	14 040	
3	378	15 090	9350
	307	8720	
4	382	17 360	12 540
	311	13 820	
5	385	16 660	12 130
	312	13 610	
6	340	25 620	970
	430	19 500	
7	411	26 440	26 010
	316	7990	
8	360	23 400	4290
	429	6760	
9	364	26 500	6760
	429	6760	
10	430	25 560	19 500
	289	12 570	

11	380	27 030	17 480
	317	21 270	
	291	23 850	

Table III-2.3. Light absorption properties of dyes 1-11 in acetonitrile: maximum absorption wavelengths λ_{\max} ; molar extinction coefficients at λ_{\max} (ϵ_{\max}) and the emission wavelength of the LED@405 nm ($\epsilon_{@405\text{nm}}$).

Based on the photoinitiation ability of the eleven different dyes based PIS, dyes 1-5 were selected as the best candidates for the following studies devoted to investigate their photochemical properties and the associated chemical mechanisms.

2.2 Steady-state photolysis.

Interactions between the proposed dyes and Iod or amines in acetonitrile were examined through the steady-state photolysis using a visible light LED@405 nm. As shown in [Figure III-2.4](#), [Annex III-2.1](#), [III-2.2](#) and [III-2.3](#), obvious photolyses were observed for all samples within 1 min of light irradiation. Furthermore, according to their photolyses, consumptions of the dyes were calculated to intuitively measure the efficiency of the reactions between dyes with Iod/amines. For dye 1 (as shown in [Figure III-2.4](#)), the three-component PIS achieved the maximum consumption of dyes, which was about 80% (see [Annex III-2.3](#)). Conversely, the two-component dye/Iod based PIS only achieved about 50% consumption; Finally, for the other two-component dye/amine PIS and the dyes alone, only 10% consumption could be achieved. Interestingly, for dyes 2 and 3 (see [Annex III-2.1](#)), the maximum consumption was achieved with the dye/Iod based two-component PIS, which could reach about 90%; the second one was the dyes/Iod/amine-based three-component PIS with about 40% of consumption; the dyes/amines and dyes alone based PIS both achieved the lowest consumption (~20%, see [Annex III-2.3](#)). The above results may be ascribed to the introduction of electron-donating groups into the structures of dyes 2 and 3. Indeed, the internal electron transfer in the molecule competes with the electron transfer between the dye and the amine, thereby slowing down the reactions between the dyes and Iod as well as the amine, which decrease the dyes consumption [9-10]. More interestingly, photolysis processes

of dyes 4 and 5- based systems were completed within 15 s (see [Annex III-2.2](#)), which was faster than that observed for the other three dyes; furthermore, dyes consumptions achieved by these four different systems were similar (about 40%, see [Annex III-2.3](#)). In addition, the absorption peak around 310 nm also showed a blue shift upon light irradiation for the dyes 4 and 5-based systems.

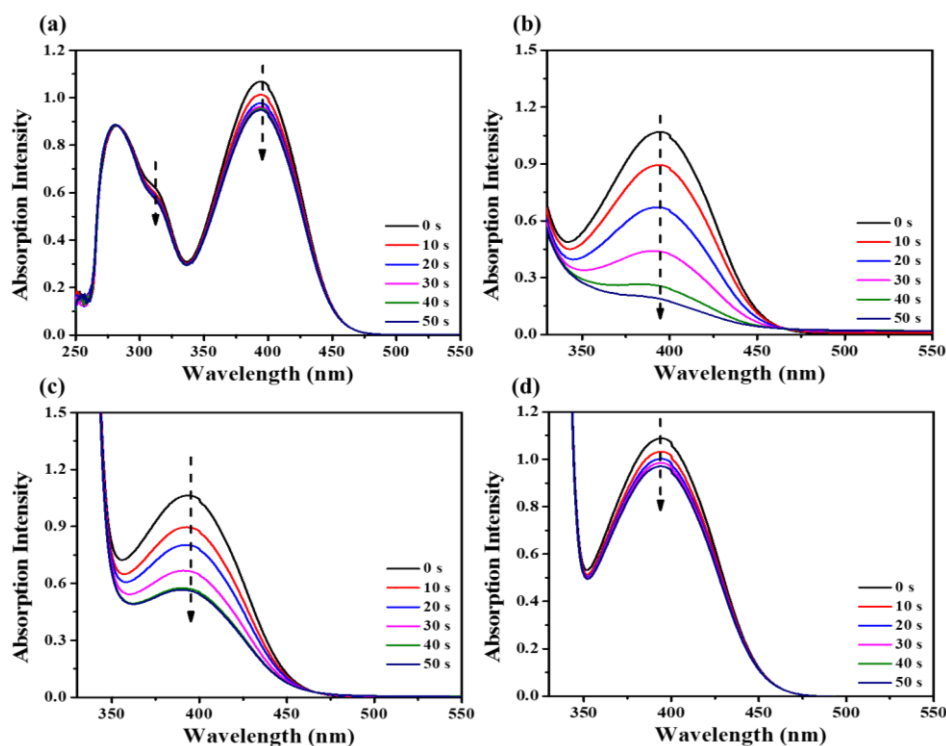


Figure III-2.4. Steady-state photolysis of (a) dye 1; (b) dye 1/Iod; (c) dye 1/amine and (d) dye 1/Iod/amine-based formulations upon exposure to LED@405nm under air in acetonitrile.

2.3 Fluorescence quenching experiments.

The electron transfer efficiency between dyes 1-5 and Iod/EDB was also studied through fluorescence quenching experiments. For dye 1 (see [Annex III-2.4](#)), a significant decrease of the emission intensity was observed with the addition of Iod. Furthermore, as shown in [Annex III-2.4c-f](#), the gradual addition of Iod/EDB could decrease the emission intensities of dyes 2 and 3 based formulations. More interestingly, the interaction between Iod and these two dyes was much stronger than that between dyes and amine. Remarkably, [Figure III-2.5](#) clearly presents the fluorescence quenching of dyes 4 and 5 in the presence of Iod/EDB, whose fluorescence emission intensity

greatly decreased, which proved that Iod and the amine can act as good quenchers during the interaction between the dyes with Iod/amine in the excited states. A linear fit can be observed from the fluorescence quenching process between dyes 4 and 5 with Iod, indicating that the process exclusively corresponded to the dynamic quenching mechanism, that is, only the dynamic interactions of the quencher (Iod) and the fluorophore (the fluorophore in the excited state of the dyes) [11]. While the fluorescence quenching process between dyes 4 and 5 with EDB is depicted as non-linear with upward curvature (shown in [Figure III-2.5](#)), resulting from the simultaneous contributions of static and dynamic quenching [12]. In addition, the Stern-Volmer coefficients (K_{SV} , slope of the curve, summarized in [Table III-2.4](#)) and the electron transfer quantum yields (Φ_{et} , summarized in [Table III-2.4](#)) of the electron transfer reaction between these dyes and Iod or amine were calculated by using their fluorescence quenching curve, and all of them are positively correlated with the efficiency of electron transfer. Remarkably, the parameters between dye 5 and Iod/EDB (summarized in [Table III-2.4](#)) were bigger than those between dye 4 and Iod/EDB, demonstrating that the electron transfer reactions between dye 5 and the quenchers were stronger, which was entirely compatible with the better photoinitiation ability of dye 5 based PISs.

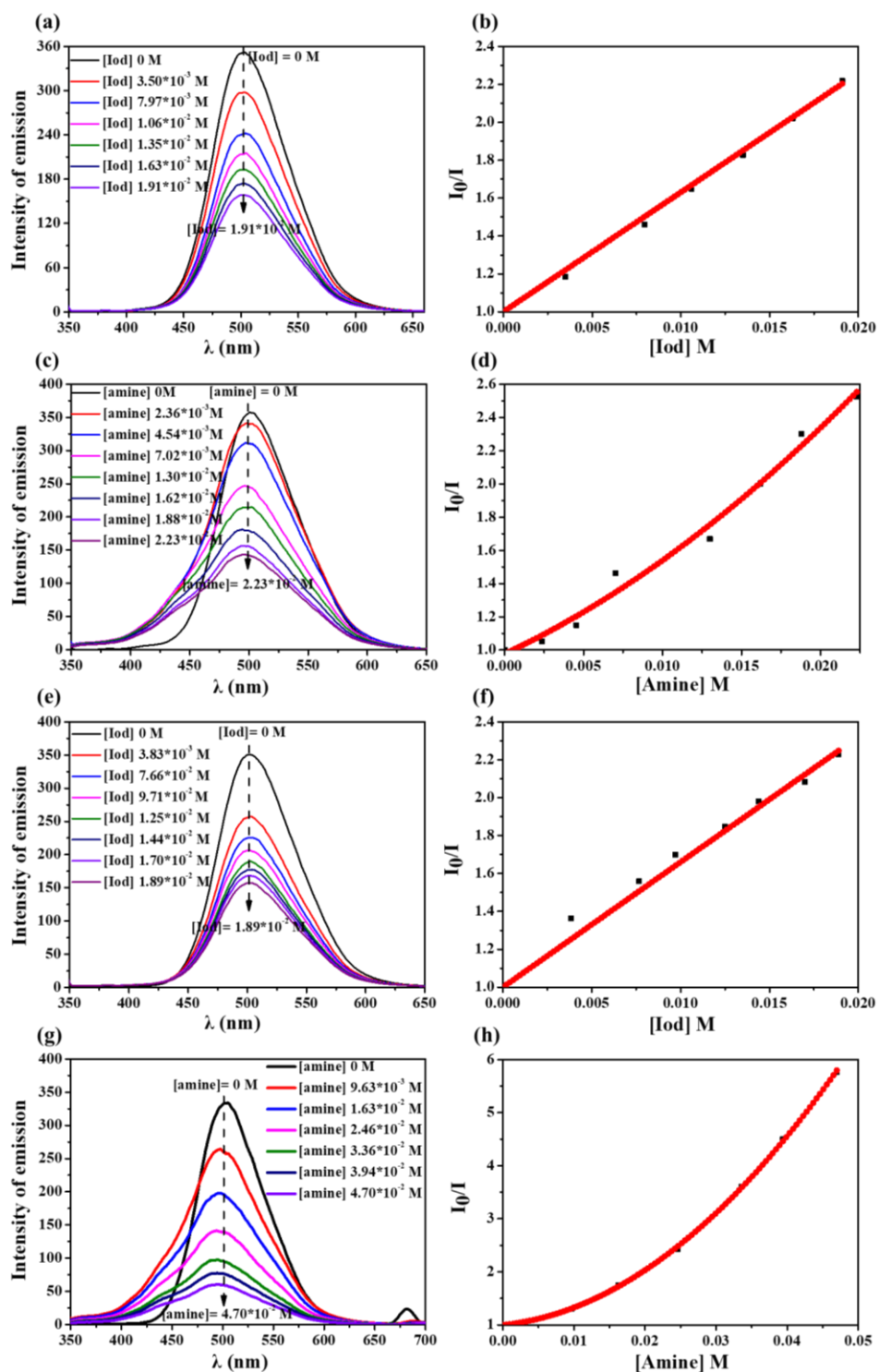


Figure III-2.5. (a) Fluorescence quenching of dye 4 by Iod; (b) Stern-Volmer treatment for the dye 4/Iod fluorescence quenching; (c) Fluorescence quenching of dye 4 by EDB; (d) Stern-Volmer treatment for the dye 4/EDB fluorescence quenching; (e) Fluorescence quenching of dye 5 by Iod; (f) Stern-Volmer treatment for the dye 5/Iod fluorescence quenching; (g) Fluorescence quenching of dye 5 by EDB; (h) Stern-

Volmer treatment for the dye 5/EDB fluorescence quenching.

2.4 Feasibility of the interactions between dyes and Iod/amines.

Based on the above results concerning their UV/visible absorption properties and fluorescence characteristics, their first singlet excited state energy (E_{S1} , see [Annex III-2.5](#) and [Table III-2.4](#)) can be obtained from the crossing point of their standardized visible light absorption and fluorescence spectra. Furthermore, the oxidation potential and reduction potential of these dyes were detected by cyclic voltammetry and determined through the position of their oxidation and reduction peaks (see [Table III-2.4](#)). As shown in [Figure III-2.6](#), a clear oxidation peak can be observed in their positive potential range, among which a weak oxidation peak can also be detected for dyes 1 and 2. However, in the negative potential range, an obvious reduction peak can also be observed for all dyes. In addition, dyes 2-5 also possessed a weak reduction peak. Finally, according to the above-mentioned parameters summarized in [Table III-2.4](#), the free energy change (ΔG_{Iod} or ΔG_{EDB}) of the electron transfer reactions between dye/Iod (or dye/amine) were calculated using equations (3), and all of them were less than 0, indicating the theoretical/practical feasibility of the interactions between the dyes and Iod/amines, which further proved that reactions (as shown in [Scheme III-1.2](#)) can occur to generate the corresponding free radicals and cations to initiate the polymerization of mixed monomers under visible light.

	Dye 1	Dye 2	Dye 3	Dye 4	Dye 5
$K_{sv}^{Iod} (M^{-1})$	30	29	51	36	66
Φ_{et}^{Iod}	0.48	0.48	0.61	0.53	0.67
$E_{S1} (V)$	2.7	2.76	2.80	2.81	2.82
$E_{ox} (V)$	1.13	1.17	1.1	1.1	1.08
$E_{red} (V)$	-1.49	-1.57	-1.62	-1.64	-1.69
ΔG_{S1}^{Iod}	-0.87	-0.89	-1	-1.01	-1.04

ΔG_{S1}^{EDB}	-0.21	-0.19	-0.18	-0.17	-0.13
-----------------------	-------	-------	-------	-------	-------

$$I_0/I = 1 + kq\tau\theta \text{ [additive]}$$

$$2 \Phi_{eT} = kq\tau\theta \text{ [additive]} / (1 + kq\tau\theta \text{ [additive]})$$

$$3 \Delta G = E_{ox} - E_{red} - E_{S1} + C$$

Table III-2.4. Summary of the relevant parameters of the fluorescence properties of dyes 1-5, namely the interaction constant (K_{sv}) and electron transfer quantum yield (Φ_{et}) of the dye-Iod; singlet excited state energy (E_{S1}) and oxidation/reduction potential (E_{ox}/E_{red}) of dyes 1-5 as well as the free energy change of the electron transfer reaction between dye and Iod/EDB (ΔG_{S1}).

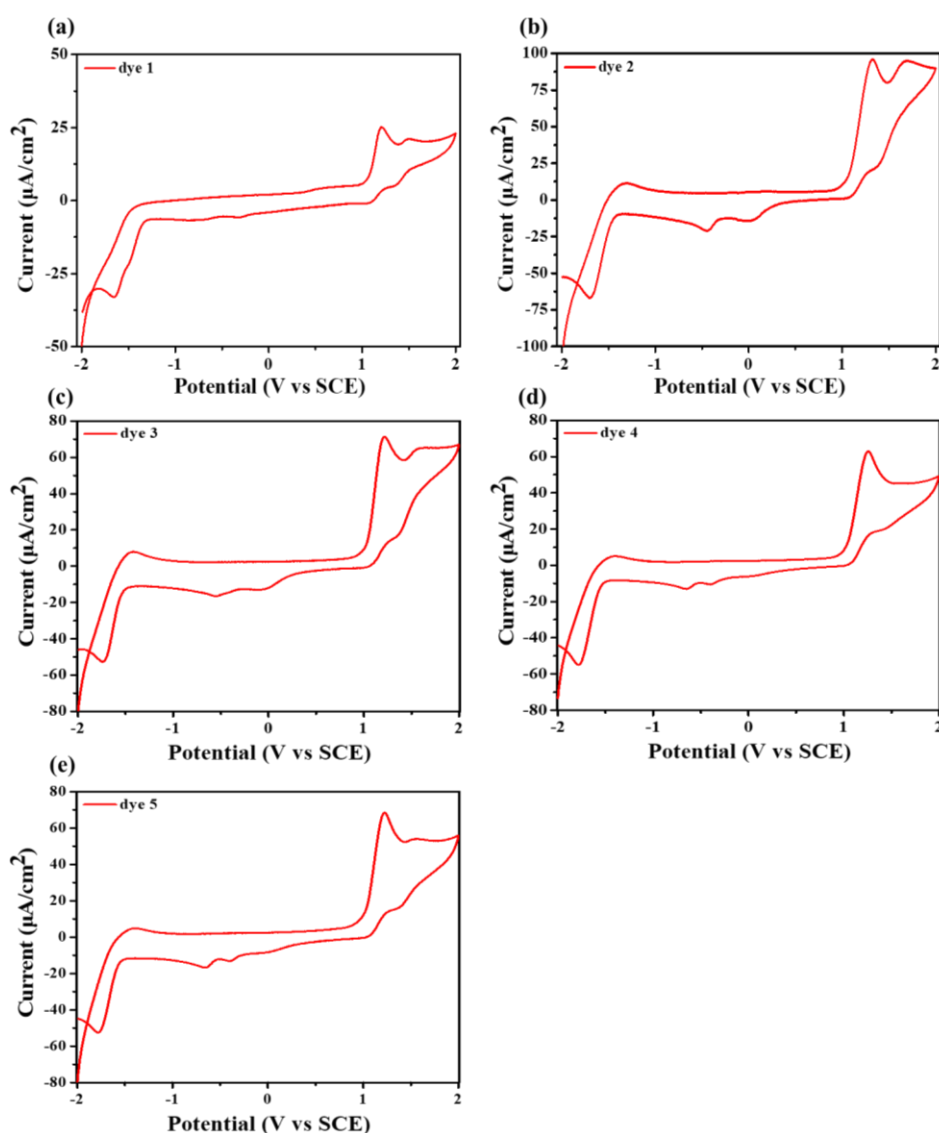


Figure III-2.6. Cyclic voltammograms of dyes 1-5 in acetonitrile

2.5 ESR-spin trapping experiments for dye 5 with Iod/EDB system.

It has been proved that the proposed redox electron transfer reaction can occur, as

demonstrated with the above results. Furthermore, the generated radicals were detected by ESR-spin trapping experiments upon irradiation with sunlight of dye 5-Iod and dye 5-amine solutions. As shown in [Annex III-2.6](#), aryl radicals were detected in the dye 5-Iod solutions, characterized by the hyperfine coupling constants of nitrogen and hydrogen: $a_N = 14.4$ G and $a_H = 2.1$ G, which were in full agreement with the values in the literature [13]. Meanwhile, under sunlight irradiation, aminoalkyl radicals ($a_N = 14.4$ G and $a_H = 2.5$ G, 90%, [13]) and a few of other free radicals such as PBNox have captured from the dye 5-amine system. All of them also proved that the series of electron transfer reactions proposed in [Scheme III-1.2](#) can occur during the photopolymerization process.

3. AgNPs Generated in DMF Solution and IPN-Polymers.

According to our previous studies, it has been proved that the redox reactions performed between some dyes-based PIs and additives Iod/amine under visible light irradiation can generate free radicals and cations, which can be used to initiate the photopolymerization reactions [14]. Meanwhile, they can also reduce the metal salts into metal nanoparticles. In this work, DMF solutions containing three-component PIS (dye/Iod/EDB) and silver nitrate were irradiated upon visible light and the absorption spectra were collected at different times. As shown in [Figure III-2.7a](#), the characteristic absorption peak of the dye at 390 nm gradually decreased upon visible light irradiation, indicating that the dye interacted with Iod/EDB. At the same time, a new absorption peak appeared at 430 nm and its absorbance gradually increased, which indicated that the Ag^+ were reduced into AgNPs [15-16]. In addition, the solution changed from light yellow to yellow-brown during the light irradiation process, and a yellow-brown silver nanoparticle coating was observed on the side of the cuvette (see [Figure III-2.7b](#)). Furthermore, nanoparticles produced in DMF solutions were measured using TEM and regular spheres with sizes at about 3-5 nm were determined (as shown in [Annex III-2.7](#)).

Subsequently, to prepare different IPNs containing AgNPs, visible light LED@405nm was used to initiate the photopolymerization of the formulation based on

PEG-DA/EPOX (70%/30%) containing AgNO₃ (5wt%) and dye/Iod/EDB (0.1wt%/1.5wt%/1.5wt%) (Table III-2.5). At the same time, the polymerization kinetics of the different formulations were followed by RT-FTIR. As shown in Figure III-2.7c-f, compared to the photopolymerization of mixed monomers without AgNO₃, for the thin samples with the thickness of about 10 μm, the presence of Ag⁺ promoted the cationic polymerization of EPOX and weaken the free radical polymerization efficiency of PEG-DA. In addition, for the polymerization of thick samples (thickness about 2 mm), the presence of Ag⁺ also improved the cationic polymerization efficiency of EPOX, while for the free radical polymerization of PEG-DA, even though there were no changes for their final conversions, their photopolymerization rates (from the maximum of the first derivative of the double bond conversions versus time curves during photopolymerization) decreased. Furthermore, the color of IPNs obtained after photopolymerization was obviously darkened and turned into dark brown. Remarkably, AgNPs obtained from the photopolymerization process of IPN-polymers were aggregated into irregular spherical shapes, as observed by SEM (Annex III-2.7). Particle sizes at the upper surface of the polymer networks were more than 100 nm, while the sizes of AgNPs at the bottom of the sample were just about 30~60 nm, which were significantly larger than those produced in DMF solutions (Annex III-2.7). As more nanoparticles are formed at the surface of the sample mainly due to the influence of the light penetrating ability, the particle sizes of AgNPs on the upper surface were larger than those at the bottom surface.

Final function conversions (FCs) initiated by dye/Iod/amine-based PISs				
Dye	Thin films		Thick films	
	EPOX (%)	PEG-DA (%)	EPOX (%)	PEG-DA (%)
1	36	35	85	95
2	33	66	76	97
3	75	44	73	99
4	52	26	96	98
5	84	94	90	96

Table III-2.5. Summary of the final function conversions of PEG-DA (acrylate

functions) and EPOX (epoxy functions) monomers using dye/Iod/amine-based PIS to 70% PEG-DA/30% EPOX mixed monomer (thickness of about 0.1mm and 2 mm) under LED@405nm irradiation.

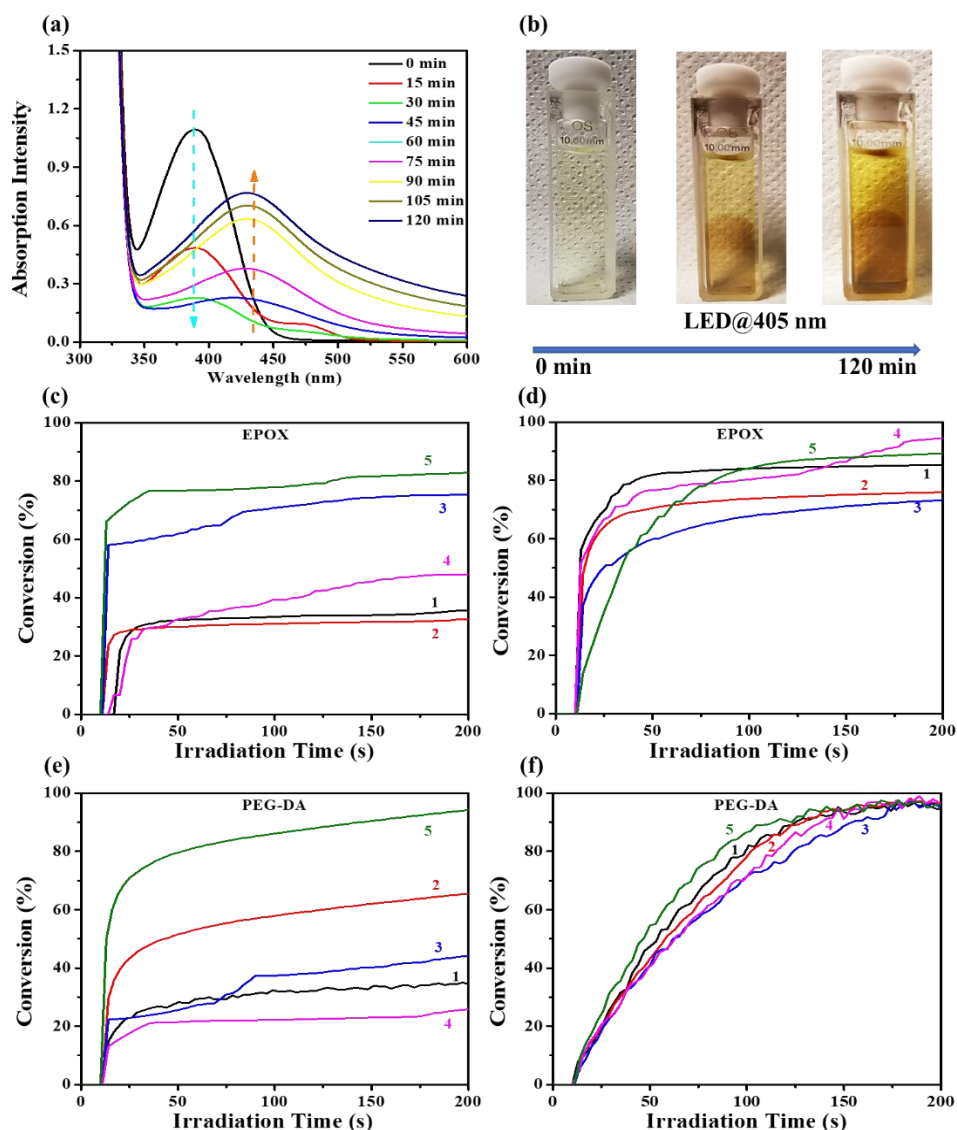


Figure III-2.7. (a) UV-visible absorption spectra of DMF solutions containing dye 5/Iod/EDB (0.001 wt%/0.015 wt%/0.015 wt%) and AgNO₃ (5 wt%) in air atmosphere during 120 min visible light irradiation process; (b) the changes of the color of solution after 120 min visible light irradiation; photopolymerization profiles of IPN (70%PEG-DA/30%EPOX) containing AgNO₃ initiated by dyes 1-5/Iod/amine upon exposure to a LED@405nm in laminate; (c) for EPOX of IPN with the thickness of about 0.1 mm; (d) for EPOX of IPN with the thickness of about 2 mm; (e) for PEG-DA of IPN with the thickness of about 0.1 mm; (f) for PEG-DA of IPN with the thickness of about 2

mm.

4. Characterization of IPN Polymers.

As discussed above, the dye 5-based three-component PIS achieved the highest efficiency, so that the dye 5/Iod/EDB was selected as the PIS to study the mechanical properties of IPNs. At first, a series of mixed solutions with different components (pure PEG-DA monomer, different ratio of PEG-DA/EPOX mixed monomers, mixed monomers containing AgNO_3 , pure EPOX monomers) were prepared. Then a time scanning rheometer was used to detect the photopolymerization rates of these formulations. Since the PEG material exhibited a volume shrinkage after it transformed from the liquid phase into the solid phase during the light irradiation process, the curves appeared disordered after photopolymerization [17-18]. As shown in [Figure III-2.8a](#), the pure PEG-DA monomer exhibited the highest polymerization rate, while for the mixed monomers, the curing rates gradually slowed down as the content of PEG-DA decreased. The addition of Ag^+ also significantly decreased the curing speed of mixed monomers. More interestingly, when the EPOX content is higher than 70%, no shrinkage was observed on the volume of the obtained polymers, which may be ascribed to the less effect on the volume shrinkage with the lower PEG-DA content. In addition, neither gelation point nor obvious phase inversion phenomenon was observed during the time-sweep for the polymerization of pure EPOX formulations, which simply became more viscous as the G'' increased with light irradiation (see [Annex III-2.8](#)). This is mainly due to the following reasons: firstly, the polymerization of pure EPOX was not efficient; secondly, the optical density of the light source for the rheometer used is less than that of RT-FTIR spectroscopy.

Subsequently, a series of IPN polymers with different components were produced using molds upon visible light irradiation, and their tensile properties were measured. The results are shown in [Figure III-2.8b](#). Since the pure PEG-polymer was brittle, the tensile property was very poor. For the IPN-polymers, enhanced their tensile property is found i.e. the mixed monomer composed of 70%PEG-DA/30%EPOX exhibited the best tensile performance (the elongation increased from 5% to 15% and the fracture

potential energy increased from 0.55 MPa to about 1.2 MPa compared to pure PEG-polymer). The addition of AgNO₃ to the precursor solution would reduce the tensile properties of the IPN-polymer. The above results also showed that 70% PEG-DA/30% EPOX was the best ratio, which not only exhibited excellent photopolymerization ability but also produced polymers with the best mechanical properties.

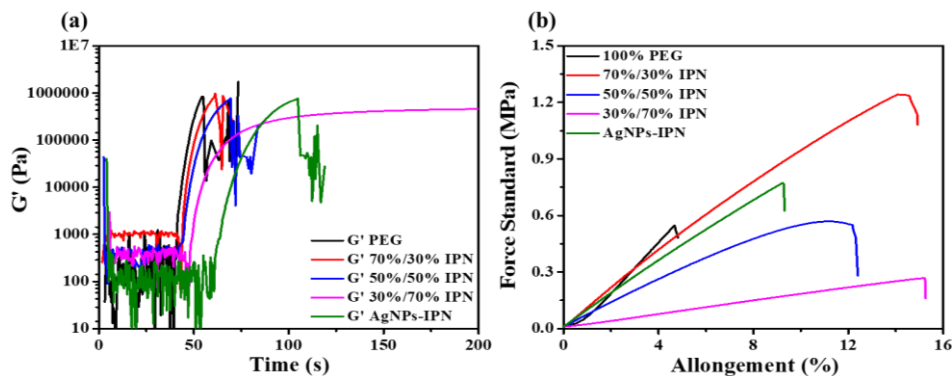


Figure III-2.8. (a) Storage modulus G' vs time during the photopolymerization process (irradiation starts at $t = 30$ s, volume is about 40 μ L) of the pure PEG-DA monomer, different ratio of PEG-DA/EPOX mixed monomers as well as the mixed monomers containing AgNO₃; (b) Tensile property of PEG-polymer, IPN-polymer as well as AgNPs contained IPN-polymers.

5. Applications in 3D and 4D Printing.

5.1 3D laser write experiments based on the dye 5-based three-component PIS.

Pure PEG-DA, pure EPOX, IPN, and AgNPs contained IPN with dye 5/Iod/EDB as PIS was prepared to perform direct laser write experiments under visible light irradiation. These four formulations were successfully written to obtain stable 3D cross patterns ("+") with excellent spatial resolution. Among them, the fastest writing speed was achieved for pure PEG-DA, and a complete 3D pattern could be obtained within 1 min. Conversely, longer irradiation times were required for IPNs and AgNPs containing IPNs to get the 3D patterns compared to that required for pure PEG-DA. The writing speed of EPOX was the slowest, taking around 5 min to complete the writing. Furthermore, the morphology of the obtained 3D patterns was observed with a digital optical microscope.

As shown in [Figure III-2.9](#), the morphology of the obtained pure PEG-DA-based 3D pattern was the best with the smooth surface and the uniform thickness at about 2.4 mm (see [Figure III-2.9a](#)). For the cross pattern from pure EPOX, its shape was

incomplete with defects at the lower end of the cross and uneven thickness (1.7-1.9 mm, see [Figure III-2.9b](#)). The shape of the IPN cross pattern was complete, but the surface was not smooth enough. There were partial collapses at the upper and lower ends, while the middle was relatively uniform with a thickness of about 2.2 mm (see [Figure III-2.9c](#)). AgNPs containing IPN cross pattern was darker than the other three polymer patterns, whose surface was not smooth and the thickness was about 2 mm, which was decreased compared to the IPN pattern (see [Figure III-2.9d](#)).

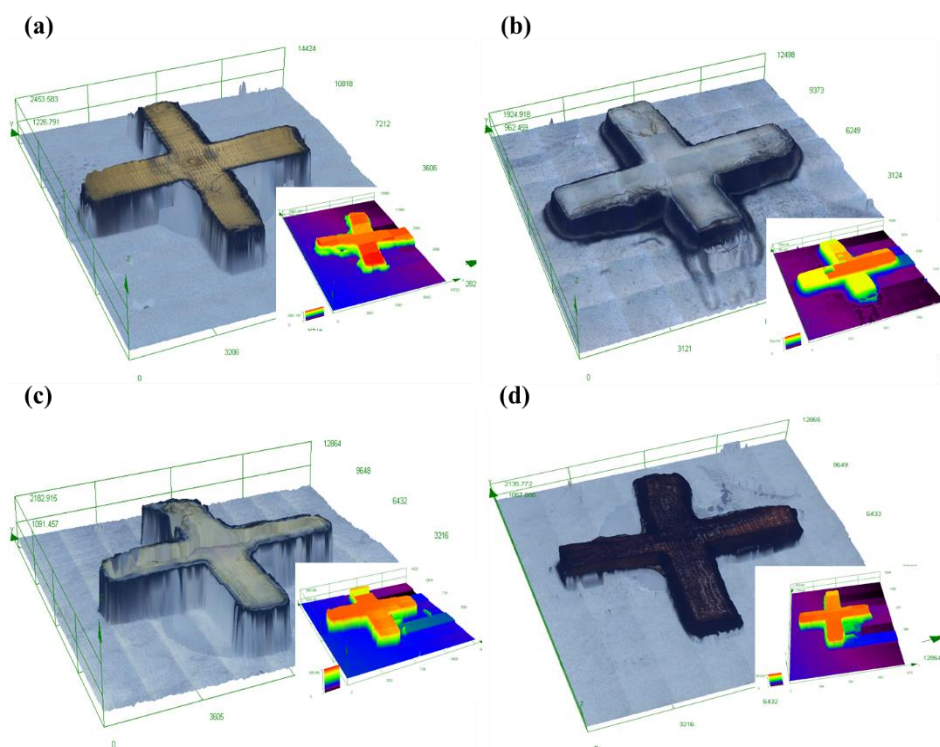


Figure III-2.9. Characterization of the 3D overall appearance of the 3D patterns produced by the laser writing experiment through a numerical optical microscope. (a) for PEG-polymer (b) for EPOX-polymer; (c) for IPN polymer (d) for AgNP containing IPN polymer.

5.2 Swelling of PEG-DA-, EPOX-, IPN- and AgNP containing IPN- polymers.

The hydrophilic properties of the four kinds of polymers obtained through laser writing experiments were studied by immersing them in deionized water to compare their weight and morphological changes. At first, the initial wet weight of the four polymers was compared with those after reaching the swelling equilibrium to calculate the swelling ratio, the result is shown in [Figure III-2.10](#). The pure PEG-DA polymer exhibited the best hydrophilicity, and the swelling rate was about 80%; while the volume and weight of pure EPOX polymer did not change as the EPOX was

hydrophobic. For the IPN polymer (70%PEG-DA/30% EPOX), as the existence of EPOX hydrophobic component reduced the hydrophilicity of IPN polymer, its swelling ratio decreased to 60%. Furthermore, the introduction of AgNPs into IPN also decreased their hydrophilic character, which achieved about 40% swelling ratio. Compared with their initial morphologies, the polymers became bigger after reaching the swelling equilibrium (see [Figure III-2.10b](#)) and the volumes also increased (see [Annex III-2.9](#)). The volume of pure PEG-DA, IPN and AgNPs containing IPN polymer increased about 199%, 166% and 138%, respectively, which exactly matched with their swelling rates. Subsequently, the absorbed water in the polymers could be removed by dehydration to restore their original weight and morphology. However, their color became lighter after the swelling process [19-20].

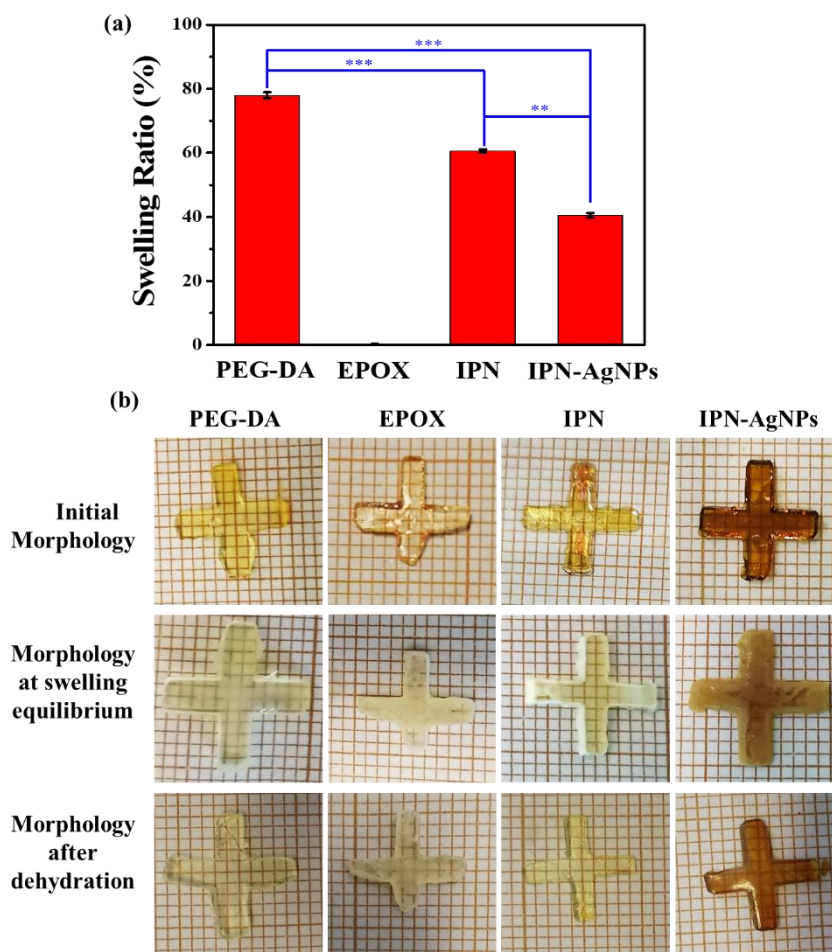


Figure III-2.10. (A) the swelling ratio of PEG-DA-, EPOX-, IPN- and AgNPs contained IPN- polymers initiated by dye 5/Iod/amine; (B) the photos of them during the swelling process: initial morphology, morphology at swelling equilibrium and morphology after dehydration.

5.3 The reversible deformation effect of PEG-DA-, IPN- and AgNP containing IPN- polymer.

Pure PEG-DA, IPN and AgNPs-IPN polymers were used to study their reversible deformation effects. The best light irradiation time was selected by comparing the influence of the irradiation time to prepare the 3D cross samples, and then their 4D deformation effects were studied through swelling and dehydration processes [21-22]. As shown in [Figure III-2.11a](#), the shortest time (~30 s) was taken to prepare the pure PEG-DA sample, which was yellow and transparent. It was completely deformed after being swelled in water for 1 min, and then dehydrated at 80 °C for 6 min to restore its original appearance. While for the second deformation process, even though it only took 15 s to swell again to achieve a complete deformation, it still dehydrated for 6 min to recover its initial appearance. When the dehydration of the PEG sample was continued, a reverse curling can be observed. For the IPN polymer shown in [Figure III-2.11b](#), the preparation time was also short, about 45 s and the polymer was yellow and opaque. Driven by swelling and dehydration, it also exhibited a reversible deformation effect, but due to its hydrophilic property which was lower than that of pure PEG polymer, its deformation process was faster and can be finished within 2 min, and no reverse curling effect was observed with continuous heating. After introducing AgNPs into IPN polymers (see [Figure III-2.11c](#)), it took a long time (3 min) to produce the samples which is brown-yellow. The reversible 4D deformation effect can also be observed through repeated swelling and dehydration processes, and the time required was shorter which may be due to its lowest polymerization efficiency which led in turn to a looser polymerization network and easier deformation. In addition, continued dehydration only deepened the color of the polymer. The above results indicated that the 4D deformation effect caused by the thermal response and hydrophilic responsiveness of the IPN polymer was better than that of the pure PEG polymer, but after the introduction of metal nanoparticles, although the sample preparation time was prolonged, the quality of the obtained polymer sample was reduced. However, effect of its 4D deformation was not greatly affected.

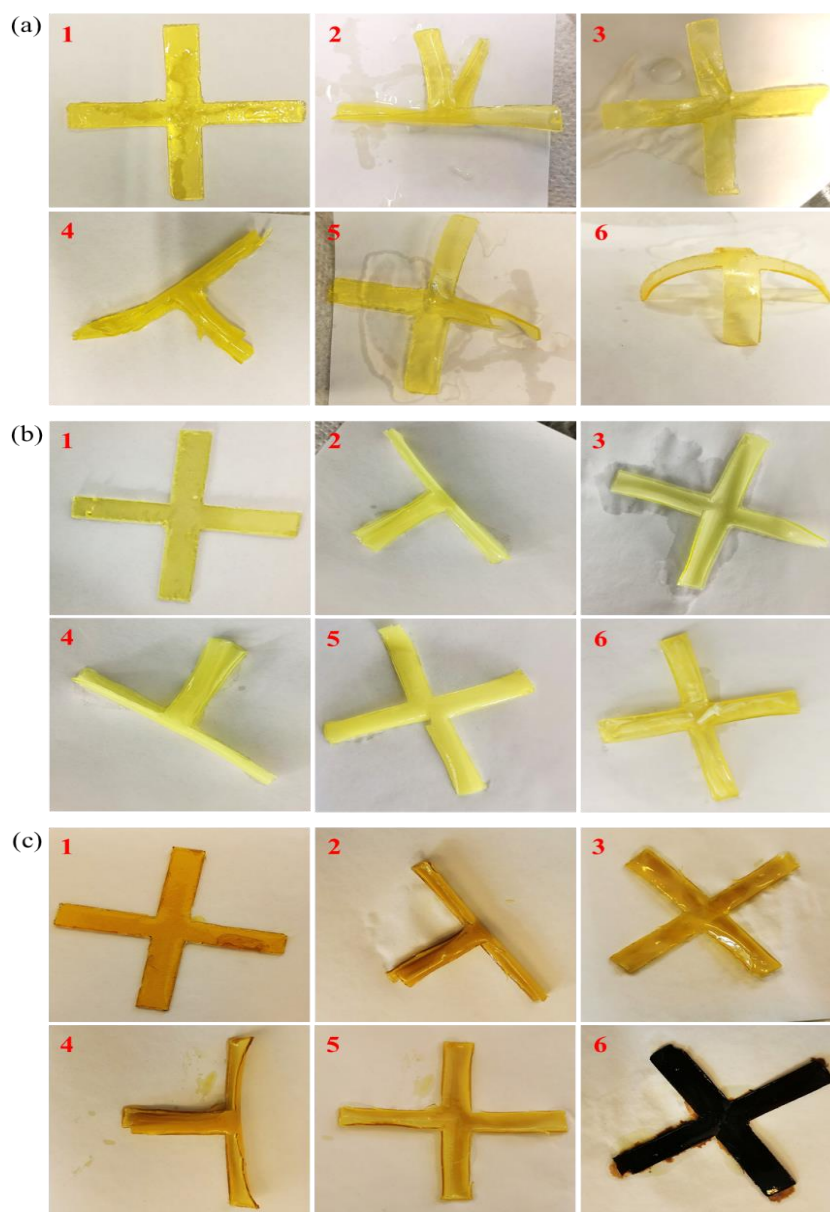


Figure III-2.11. Swelling and dehydration induced reversible deformation effect of (a) PEG-polymer, (b) IPN-polymer and (c) AgNPs contained IPN-polymer initiated by dye 5/Iod/amine upon irradiation with LED@405 nm: (1) photos of 3D cross polymers prepared with the visible light irradiation; (2) photos of 3D cross polymers after swelling in water; (3) photos of 3D cross polymers after dehydration (heating at 80 °C); (4) photos of 3D cross polymers after swelling again in water; (5) photos of 3D cross polymers after dehydration again (heating at 80 °C); (6) photos of 3D cross polymers after continuing dehydration (heating at 80 °C).

6. Antibacterial Effect of IPN Containing/Without AgNPs.

As plenty of studies have proved that AgNPs exhibit a broad range of antibacterial activities, which represent a new generation of antimicrobials [23-26]. Therefore, in this work, the Gram-positive bacteria *Staphylococcus aureus* and the Gram-negative bacteria *Pseudomonas aeruginosa* were selected to investigate the antibacterial effect of the manufactured AgNPs containing IPN polymer. At first, cultures of *S. aureus* and *P. aeruginosa* were performed in liquid LB and LB-agar in the presence of IPN alone, in presence of AgNPs containing IPN, and nothing (control). After stirring overnight at 37°C in agitation, the comparison by eyes of the Erlen flasks (see [Annex III-2.10](#)) revealed that no turbidity was visible in the culture of *S. aureus* when AgNPs-IPN and IPN were present, whereas a normal growth was detected in the control group that contained nothing (final OD at approximately 3). However, for the culture of *P. aeruginosa*, only the presence of AgNPs-IPN could observe the solution was not turbid, normal growth was found in the presence of IPN or nothing (final OD was about 4). It was shown that the presence of IPN-Ag could kill *S. aureus* and *P. aeruginosa*; moreover, the presence of IPN could restrict the growth of *S. aureus* but not the growth of *P. aeruginosa*. In the solid medium, a halo of growth inhibition was also observable around the AgNPs-IPN and the IPN in *S. aureus*, as well as the AgNPs-IPN in *P. aeruginosa* (see [Annex III-2.10c-d](#)). Secondly, to determine if the presence of the AgNPs-IPN has a bacteriostatic or bacteriolytic effect, 100 µL of each culture was spread on LB Petri dishes to collect CFU. The growth curves of them in [Figure III-2.12](#) demonstrated that the presence of the AgNPs-IPN has killed the *S. aureus* cells and the IPN without Ag also prevented a normal growth of *S. aureus* cells in comparison to the control, whereas, for *P. aeruginosa*, the effect is less drastic because the spreading of 100 µL from the AgNPs-IPN containing Erlen showed the formation of a bacterial layer covering the Petri dishes. As a result, the antibacterial effect on the Gram-negative strain appears to be only bacteriostatic. Finally, we also examined the capacity of both bacterial species to adhere to the polymer. Logically no adhesion was observed for *S. aureus* on the AgNPs-IPN in comparison to the 40 +/- 10 adherent cells

on the IPN. 20 ± 10 cells of *P. aeruginosa* were retrieved from the AgNPs-IPN, and $10^3 \pm 100$ cells were adherent to the IPN (see Annex III-2.11).

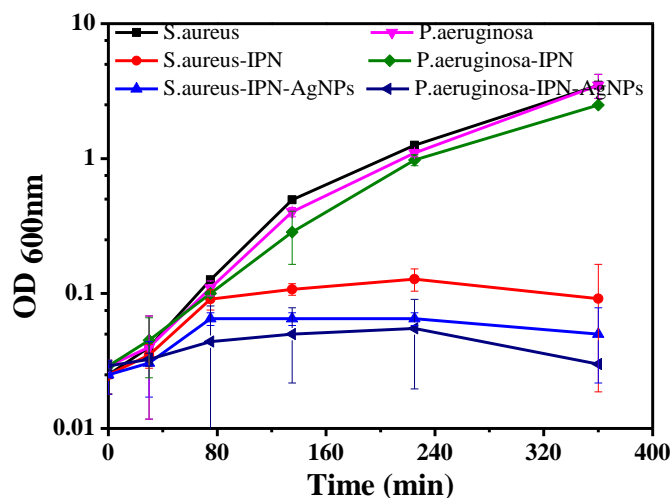


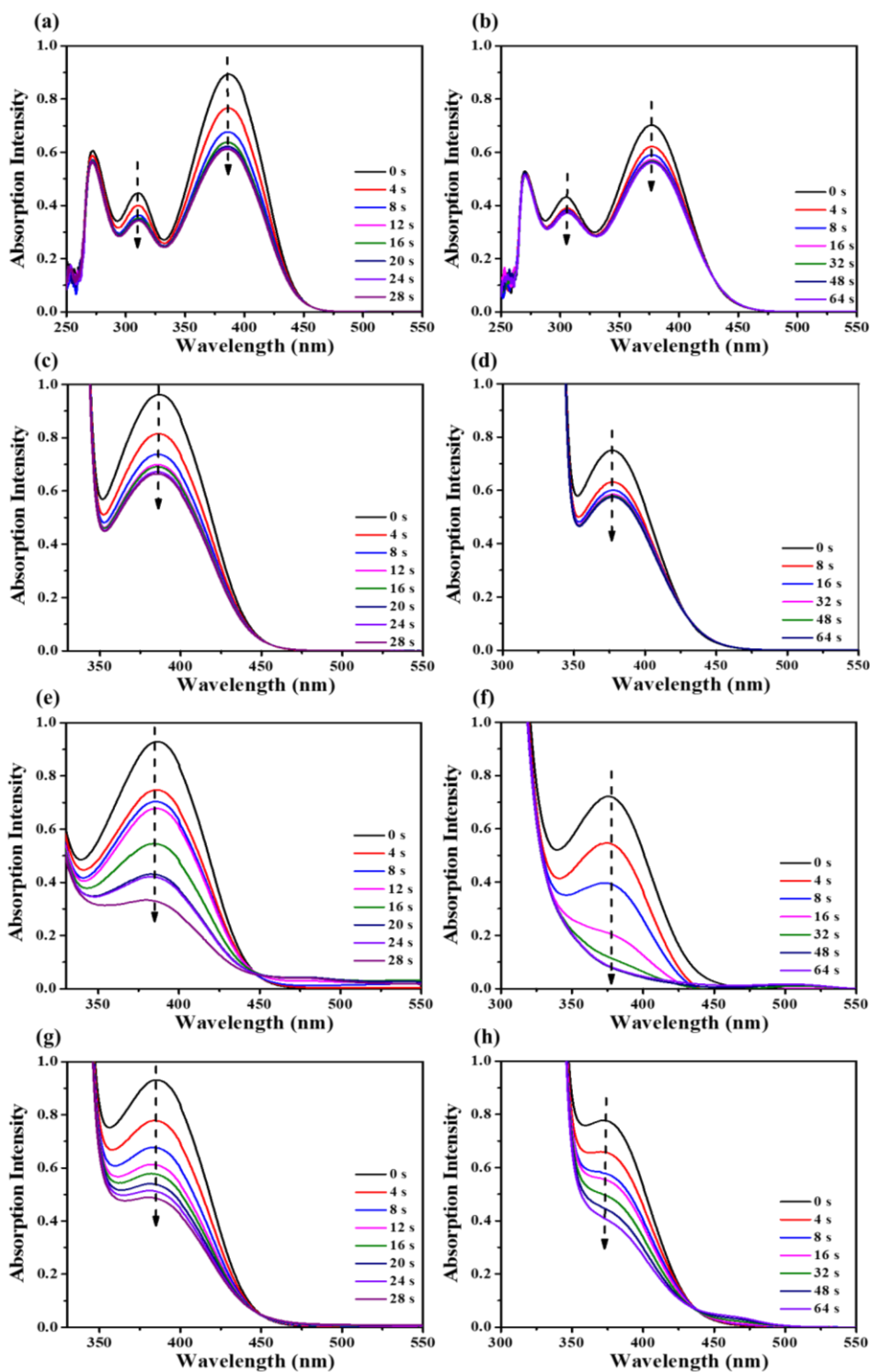
Figure III-2.12. The growth curves of *S. aureus* and *P. aeruginosa* in presence of IPN, AgNPs contained IPN pellet or nothing (control) during the overnight culture at 37°C.

7. Conclusions.

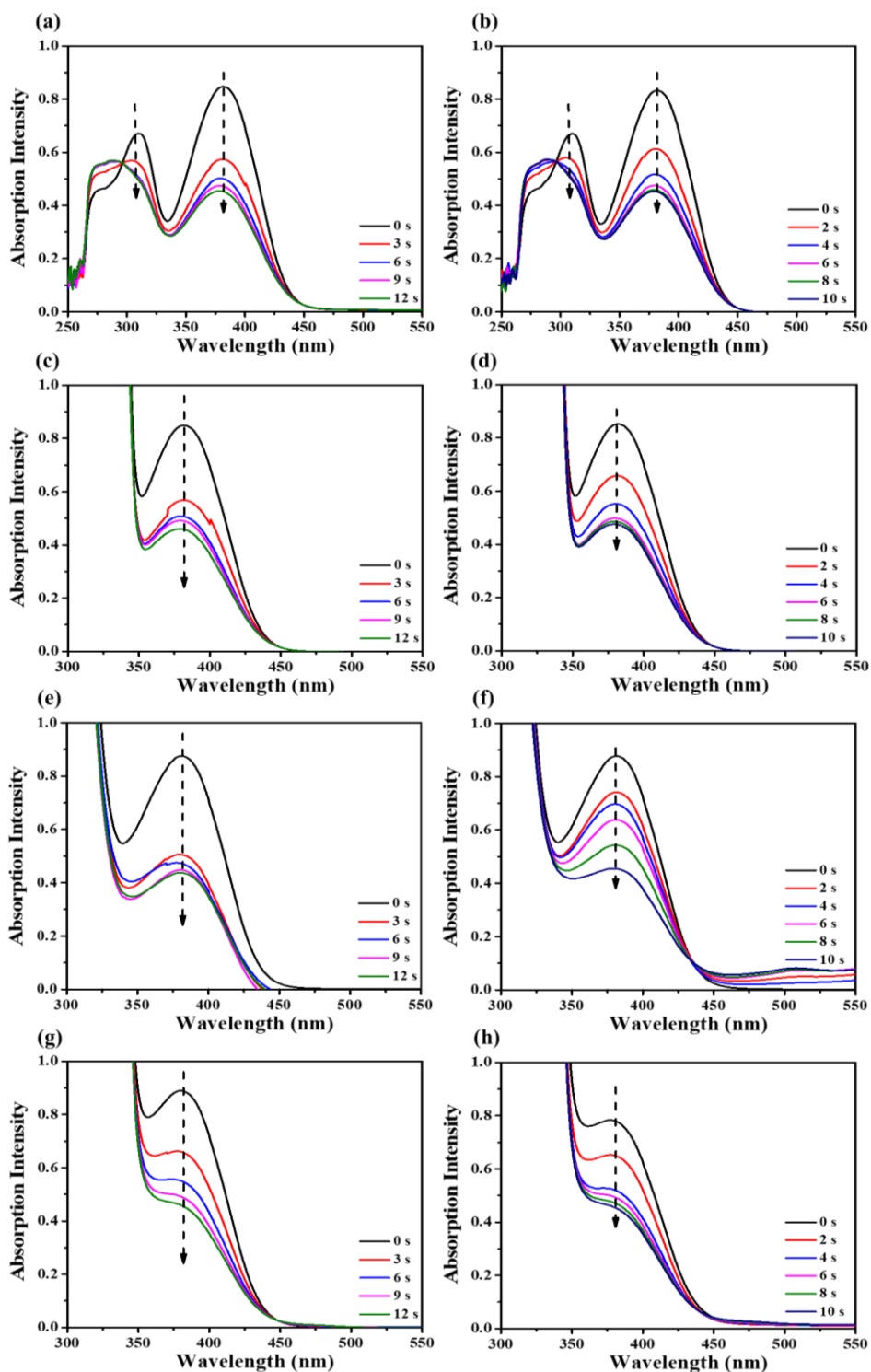
In this work, eleven different dyes based on the natural based chalcone scaffold were synthesized and combined with Iod and EDB as visible light PISs. Under LED@405nm irradiation, the redox reactions between the dyes and Iod/EDB generated free radicals and cations to initiate the polymerization of PEG-DA and EPOX monomers, in which dye 5 was selected as the best candidate for the preparation of IPN polymers. According to the photopolymerization efficiency and mechanical properties of different IPN polymers, the mixed monomer composed of 70%PEG-DA/30%EPOX proved to be the best ratio. The mechanical strength of the obtained IPN polymer was greatly improved, demonstrating that compared with a single network, the IPN exhibited a unique performance due to the combination of multiple monomers. Due to the hydrophilicity of PEG and the hydrophobicity of EPOX, the IPN polymer exhibited a reversible deformation effect that was different from that of pure PEG polymer. In addition, the three-component PIS based on the dye 5/Iod/EDB can not only induce the photopolymerization reaction, but also reduce the metal salt to AgNPs. However, the formation of AgNPs darkened the color of the polymer, meanwhile, it also exhibited some negative effects on the photopolymerization process, making the properties of the polymer inferior to IPN. Remarkably, the dye-based PISs combined free radical polymerization and cationic polymerization to prepare an IPN polymer that contains

the hydrophilicity and hydrophobicity of the two resins. In addition, the silver nanoparticles generated by *in situ* reductions during the photopolymerization process exhibited excellent antibacterial activity for *S. aureus* and *P. aeruginosa*, providing new ideas for the fields of biomedical engineering, intelligent response and antibacterial materials.

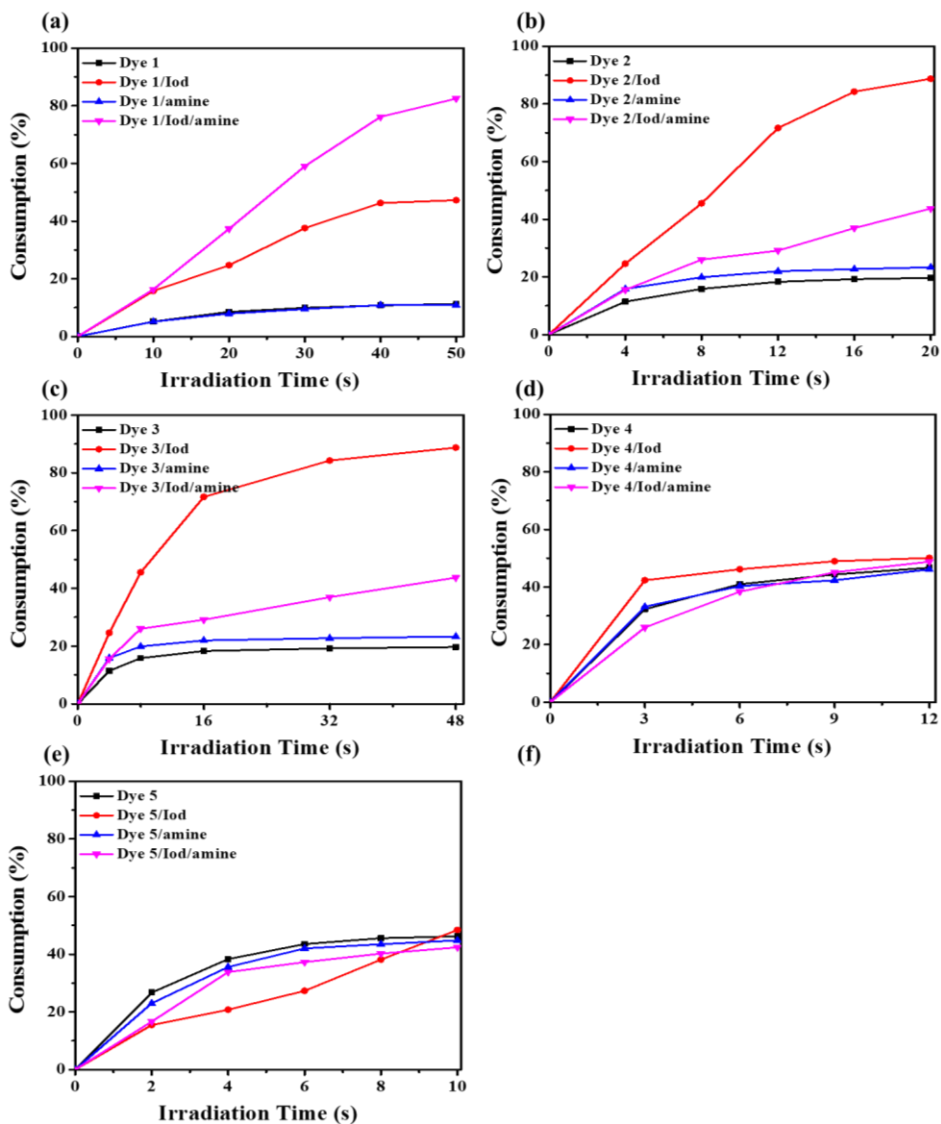
Annex



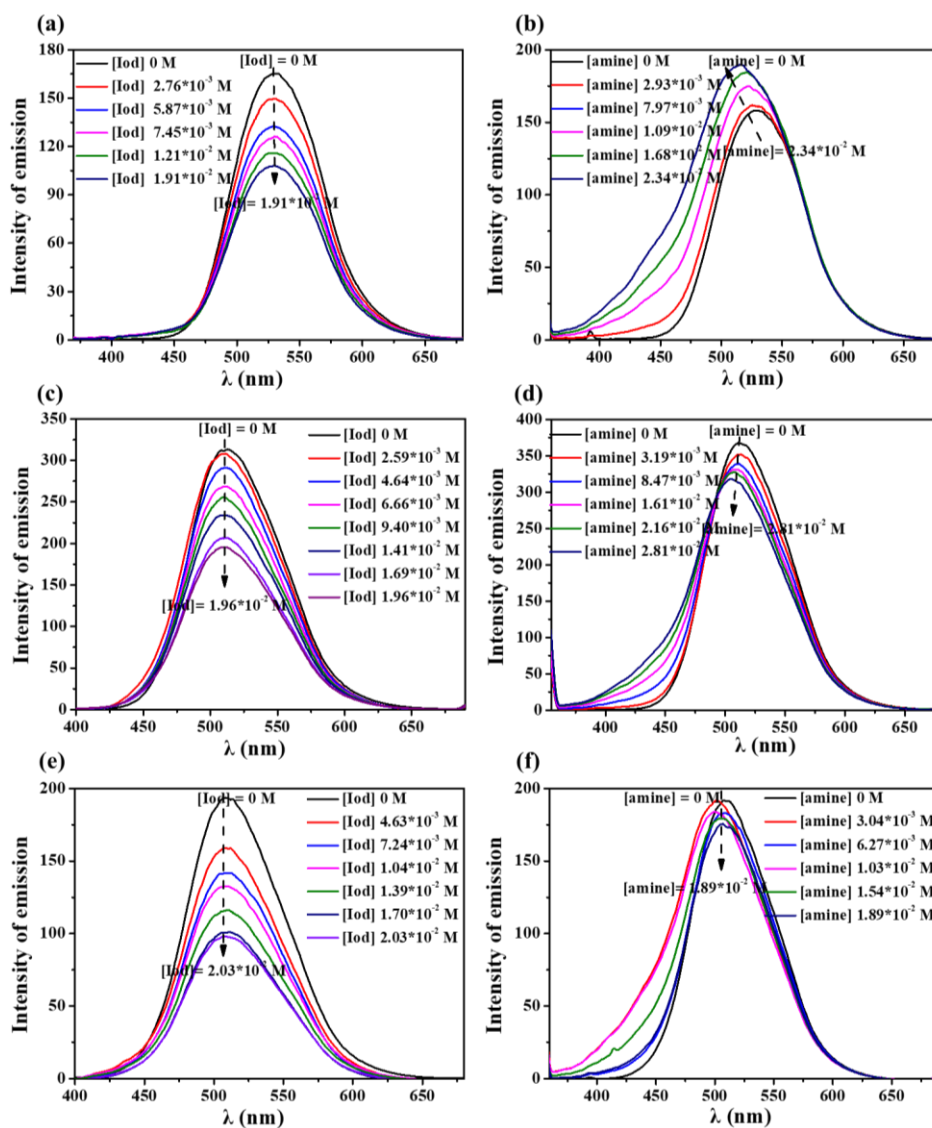
Annex III-2.1. Photolysis of (a) dye 2; (b) dye 3; (c) dye 2/amine and (d) dye 3/amine; (e) dye 2/Iod; (f) dye 3/Iod; (g) dye 2/Iod/amine and (h) dye 3/Iod/amine-based systems upon exposure to LED@405nm under air in acetonitrile.



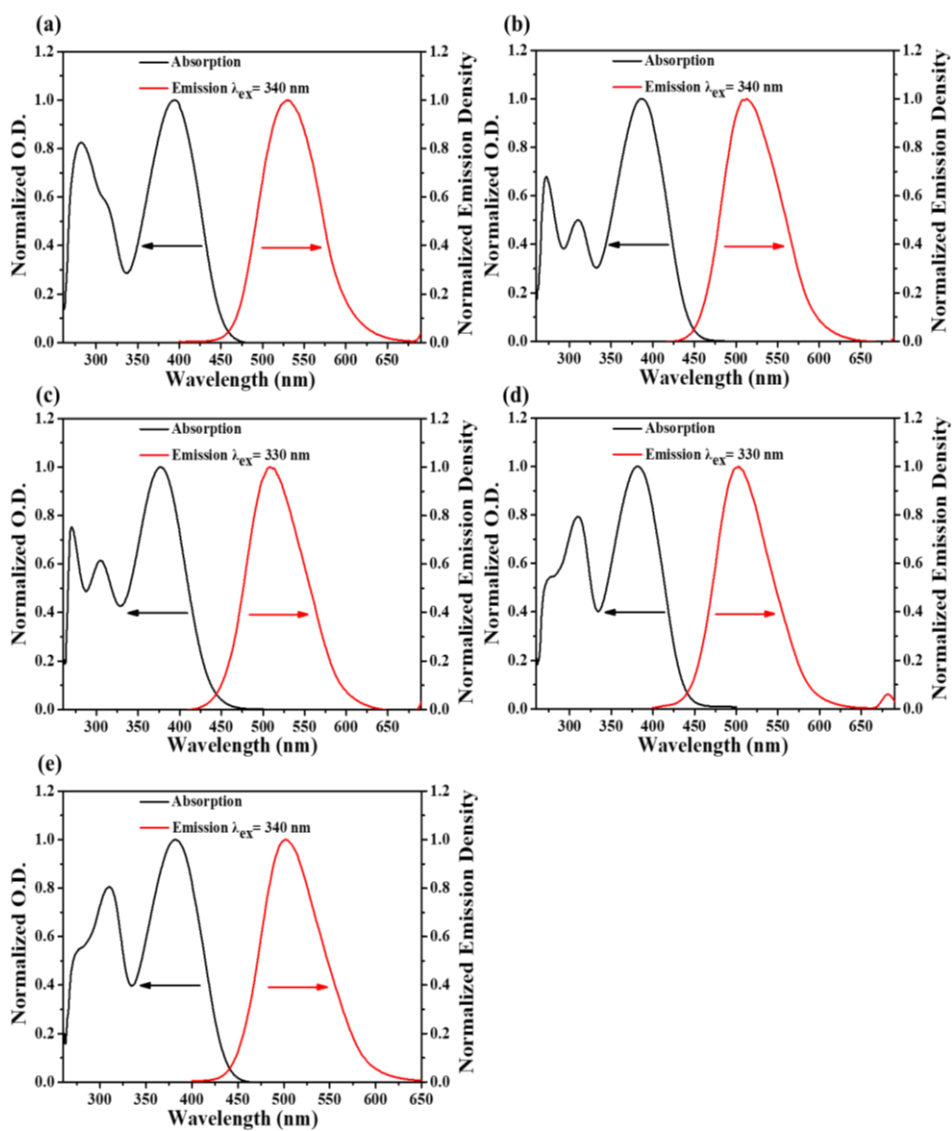
Annex III-2.2. Photolysis of (a) dye 4; (b) dye 5; (c) dye 4/amine; (d) dye 5/amine; (e) dye 4/Iod; (f) dye 5/Iod; (g) dye 4/Iod/amine and (h) dye 5/Iod/amine-based systems upon exposure to LED@405nm under air in acetonitrile.



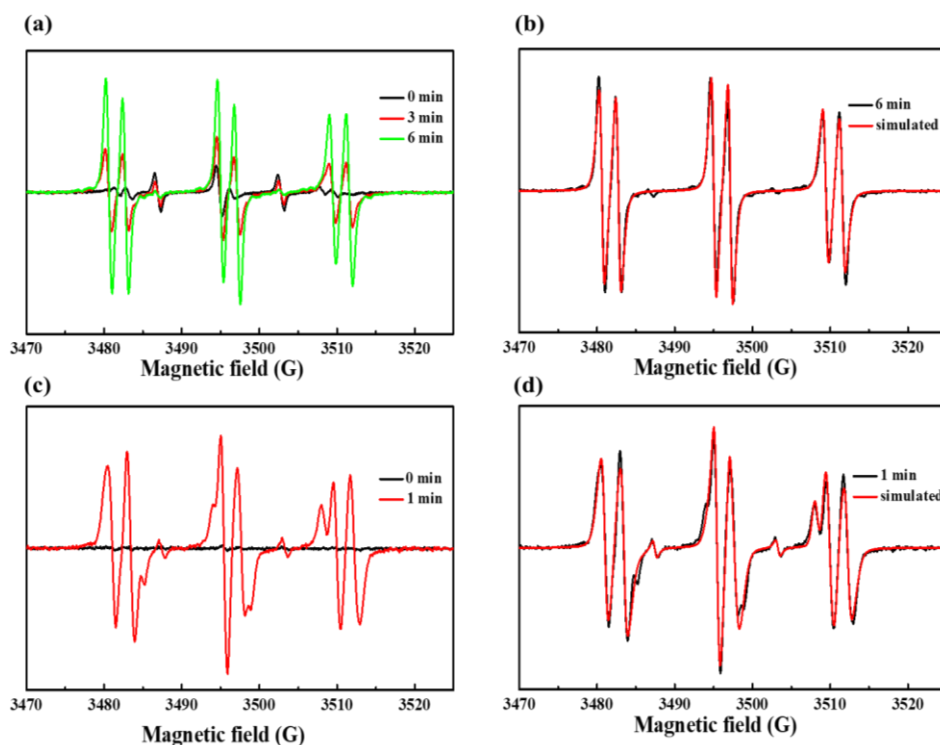
Annex III-2.3. The consumption of dyes for the (a) dye 1-; (b) dye 2-; (c) dye 3-; (d) dye 4- and (e) dye 5- based one/two/three-compound systems during the photolysis process.



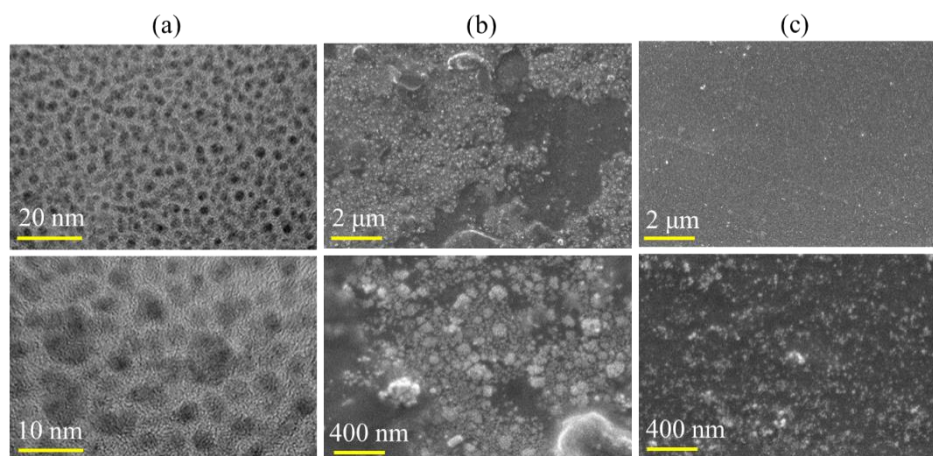
Annex III-2.4. Fluorescence quenching of (a) dye 1 by Iod (speedcure 938); (b) dye 1 by amine (speedcure EDB); (c) dye 2 by Iod (speedcure 938); (d) dye 2 by amine (speedcure EDB); (e) dye 3 by Iod (speedcure 938); (f) dye 3 by amine (speedcure EDB).



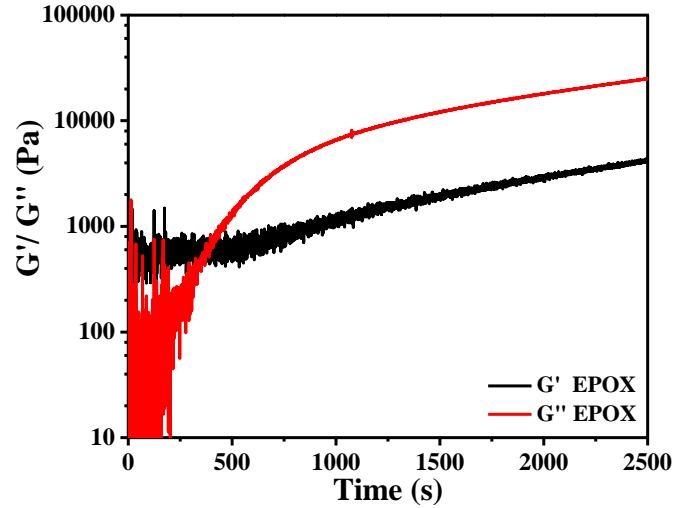
Annex III-2.5. Singlet state energy of (a) dye 1, (b) dye 2, (c) dye 3, (d) dye 4 and (e) dye 5 determined by the cross-point of standardized UV/visible absorption spectra and fluorescence emission spectrum.



Annex III-2.6. ESR spectra obtained by the ESR-spin trapping process of different formulations upon sunlight irradiation at different times. (a) from dye 5/Iod system with irradiation time = 0 min (black), 3 min (red) and 6 min (green); (b) from dye 5/Iod system with irradiation time = 6 min (black) and simulated (red) spectra; (c) from dye 5/EDB system with irradiation time = 0 min (black) and 1 min (red); (d) from dye 5/EDB system with irradiation time = 1 min (black) and simulated (red) spectra.



Annex III-2.7. (a) TEM images of AgNPs prepared in DMF solution; SEM images of AgNPs (b) on the upper surface and (c) on the down surface of obtained IPN-polymer from FTIR experiment.

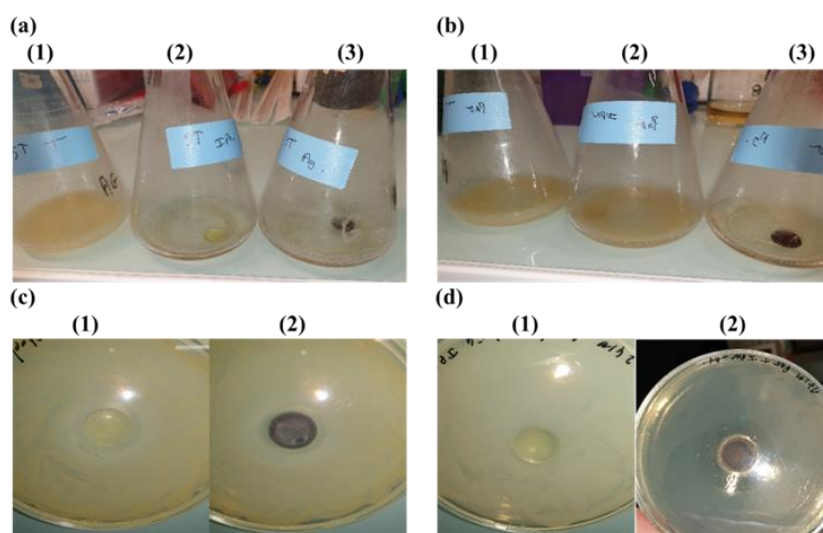


Annex III-2.8. Storage modulus (G') and loss modulus (G'') vs irradiation time during the photopolymerization process (irradiation starts at $t = 30$ s, volume is about $40 \mu\text{L}$) of the pure EPOX monomer.

	PEG-DA	EPOX	IPN	IPN-AgNPs
V_1 (mm^3)	51.0	47.5	47.0	44.3
V_2 (mm^3)	101.6	47.6	78.2	61.0
V_3 (mm^3)	54.3	47.5	46.8	45.6
R (%) ^b	199.2	0	166.4	137.7

^a $Sr = (m_2 - m_1) / m_1 * 100\%$ ^b $R = V_2 / V_1 * 100\%$

Annex III-2.9. Volumes of the obtained 3D patterns during swelling process: initial volume (V_1), volumes at swelling equilibrium (V_2), volume after dehydration (V_3) as well as the volume change ratio (R).



Annex III-2.10. (a) Effect of the growth of *S. aureus* in liquid LB with (1) nothing, (2) the presence of IPN pellet and (3) the presence of AgNPs contained IPN pellet; (b) Effect of the growth of *P. aeruginosa* in liquid LB with (1) nothing, (2) the presence of IPN pellet and (3) the presence of AgNPs contained IPN pellet; (c) Effect of the growth of *S. aureus* in LB-agar with (1) the presence of IPN pellet and (2) the presence of AgNPs contained IPN pellet; (d) Effect of the growth of *P. aeruginosa* in LB-agar with (1) the presence of IPN pellet and (2) the presence of AgNPs contained IPN pellet.

	Dilutions factors	ND	-1
The activity for <i>S. aureus</i> (Number of bacteria adhered on polymers)	Colony number on IPN	38	0
	Colony number on IPN-Ag	0	0
	Colony number on IPN	>1000	850
The activity for <i>P. aeruginosa</i> (Number of bacteria adhered on polymers)	Colony number on IPN-Ag	21	3

Annex III-2.11. The number of colony grown from cellular adhered to the surface of IPN pellet/ AgNPs contained IPN pellet cultured in liquid LB.

Reference:

1. Klemmner, D., Sperling, L. H., & Utracki, L. A. Interpenetrating polymer networks (No. CONF-910812-). American Chemical Society, Washington, DC (United States), **1994**.
2. Munsur, A. Z. A.; Goo, B. H.; Kim, Y.; Kwon, O. J.; Paek, S. Y.; Lee, S. Y.; Kim, H. J.; Kim, T. H. Nafion-based proton-exchange membranes built on cross-linked semi-interpenetrating polymer networks between poly (acrylic acid) and poly (vinyl alcohol). *ACS Applied Material Interfaces* **2021**, *13*(24), 28188-28200.
3. Alizadeh, N.; Bird, S. A.; Mendez, R. B.; Jajam, K. C.; Alexander, A. C.; Tippur, H. V.; Auad, M. L. Chapter 11: Synthesis and characterization of high performance interpenetrating polymer networks with polyurethane and poly (methyl methacrylate). In *Unsaturated Polyester Resins*, Elsevier, **2019**, 243-255.
4. Sundaram, B. M.; Mendez, R. B.; Auad, M. L.; Tippur, H. V. Quasi-static and dynamic mechanical behavior of transparent graft-interpenetrating polymer networks (Graft-IPNs). *Polymer Testing* **2018**, *70*, 348-362.
5. Sundararajan, S.; Samui, A. B.; Kulkarni, P. S. Interpenetrating phase change polymer networks based on crosslinked polyethylene glycol and poly (hydroxyethyl methacrylate). *Solar Energy Materials and Solar Cells* **2016**, *149*, 266-274.
6. Yu, F.; Yang, P. Y.; Yang, Z. Q.; Zhang, X. C.; Ma, J. Double-network hydrogel adsorbents for environmental applications. *Chemical Engineering Journal* **2021**, *131900*, 1-13.
7. Smith, G. N.; Brok, E.; Schmiele, M.; Mortensen, K.; Bouwman, W. G.; Duif, C. P.; Hassenkam, T.; Alm, M.; Thomsen, P.; Arleth, L. The microscopic distribution of hydrophilic polymers in interpenetrating polymer networks (IPNs) of medical grade silicone. *Polymer* **2021**, *224*, 123671-123680.
8. Lalevée, J.; Rahal, M.; Mokbel, H.; Graff, B.; Pertici, V.; Gimes, D.; Toufaily, J.; Hamieh, T.; Dumur, F. Naphthalimides based dyes as photoinitiators under visible light irradiation and their application: photocomposite synthesis, 3D printing and polymerization in water. *ChemPhotoChem*. **2021**, *5*(5), 476-490.
9. Chen, H.; Noirbent, G.; Zhang, Y. J.; Brunel, D.; Gimes, D.; Liu, S. H.; Sun, K.; Morlet-Savary, F.; Graff, B.; Xiao, P.; Dumur, F.; Lalevée, J. Novel D- π -A and A- π -D- π -A three-component photoinitiating systems based on carbazole/triphenylamino based chalcones and application in 3D and 4D printing. *Polymer Chemistry* **2020**, *11*(40), 6512-6528.
10. Liang, Z. Q.; Wang, X. M.; Dai, G. L.; Ye, C. Q.; Zhou, Y. Y.; Tao, X. T. The solvatochromism and aggregation-induced enhanced emission based on triphenylamine-propenone. *New Journal of Chemistry* **2015**, *39*(11), 8874-8880.
11. Campbell, K.; Andrew, Z.; Uwe, B.; Yonathan, S. T.; Bucknall, D. G. Fluorescence

- quenching of a poly (para-phenylene ethynyls) by C₆₀ fullerenes. *Journal of Photochemistry and Photobiology A: Chemistry*, **2012**, *249*, 41-46.
12. Blatt, E.; Chatelier, R. C.; Sawyer, W. H. Effects of quenching mechanism and type of quencher association on Stern-Volmer plots in compartmentalized systems. *Biophysical Journal* **1986**, *50*(2), 349-356.
 13. Caldwell, S. T.; Quin, C.; Edge, R.; Hartley, R. C. A dual sensor spin trap for use with EPR spectroscopy. *Organic Letters* **2007**, *9*(18), 3499-3502.
 14. Chen, H.; Noirbent, G.; Liu, S. H.; Zhang, Y. J.; Sun, K.; Morlet-Savary, F.; Gignes, D.; Xiao, P.; Dumur, F.; Lalevée, J. In situ generation of Ag nanoparticles during photopolymerization by using newly developed dyes-based three-component photoinitiating systems and the related 3D printing applications and their shape change behavior. *Journal of Polymer Science* **2021**, *59*(10), 843-859.
 15. Arsuaga, J. M.; Sotto, A.; Rosario, del G.; Martínez, A.; Molina, S.; Teli, S. B.; Abajo, de. J. Influence of the type, size, and distribution of metal oxide particles on the properties of nanocomposite ultrafiltration membranes. *Journal of Membrane Science* **2013**, *428*, 131-141.
 16. Caillosse, E.; Zaier, M.; Mezghani, M.; Hajjar-Garreau, S.; Vidal, L.; Lougnot, D.; Balan, L. Photo-induced self-assembly of silver nanoparticles for rapid generation of first and second surface mirrors. *ACS Applied Nano Materials* **2020**, *3*(7), 6531-6540.
 17. Kurdikar, D. L.; Peppas, N. A. The volume shrinkage, thermal and sorption behaviour of polydiacrylates. *Polymer* **1995**, *36*(11), 2249-2255.
 18. Löwenberg, C.; Balk, M.; Wischke, C.; Behl, M.; Lendlein, A. Shape-memory hydrogels: evolution of structural principles to enable shape switching of hydrophilic polymer networks. *Accounts of Chemical Research* **2017**, *50*(4), 723-732.
 19. Albers, P. T. M.; Ven, L. G. J. V. D.; Benthem, R. A. T. M. V.; Esteves, A. C. C.; Gijsbertus, D. W. Water swelling behavior of poly (ethylene glycol)-based polyurethane networks. *Macromolecules* **2020**, *53*(3), 862-874.
 20. Katono, H.; Maruyama, A.; Sanui, K.; Ogata, N.; Okano, T.; Sakurai, Y. Thermo-responsive swelling and drug release switching of interpenetrating polymer networks composed of poly (acrylamide-co-butyl methacrylate) and poly (acrylic acid). *Journal of Controlled Release* **1991**, *16*(1-2), 215-227.
 21. Wang, Y. R.; Li, J.; Li, X. J.; Pan, Y.; Zheng, Z. H.; Ding, X. B.; Peng, Y. X. Relation between temperature memory effect and multiple-shape memory behaviors based on polymer networks. *RSC Advances* **2014**, *4*, 20364-20370.
 22. Liu, G. Q.; Ding, X. B.; Cao, Y. P.; Zheng, Z. H.; Peng, Y. X. Shape memory of

- hydrogen-bonded polymer network/poly (ethylene glycol) complexes. *Macromolecules* **2004**, *37*(6), 2228-2232.
23. Li, W. R.; Xie, X. B.; Shi, Q. S.; Zeng, H. Y.; Ou-Yang, Y. S.; Chen, Y. B. Antibacterial activity and mechanism of silver nanoparticles on Escherichia coli. *Applied Microbiology and Biotechnology* **2010**, *85*(4), 1115-1122.
24. Li, W. R.; Xie, X. B.; Shi, Q. S.; Duan, S. S.; Ouyang, Y. S.; Chen, Y. B. Antibacterial effect of silver nanoparticles on Staphylococcus aureus. *Biomaterials* **2011**, *24*(1), 135-141.
25. Martínez-Castañón, G. A.; Martínez-Martínez, R. E.; Loyola-Rodriguez, J. P.; Patino-Marin, N.; Reyes-Macias, J. F.; Ruiz, F. Antibacterial effect of silver nanoparticles against streptococcus mutans. *Materials Letters* **2009**, *63*(29), 2603-2606.
26. Rai, M.; Yadav, A.; Gade, A. Silver nanoparticles as a new generation of antimicrobials. *Biotechnology Advances* **2009**, *27*(1), 76-83.

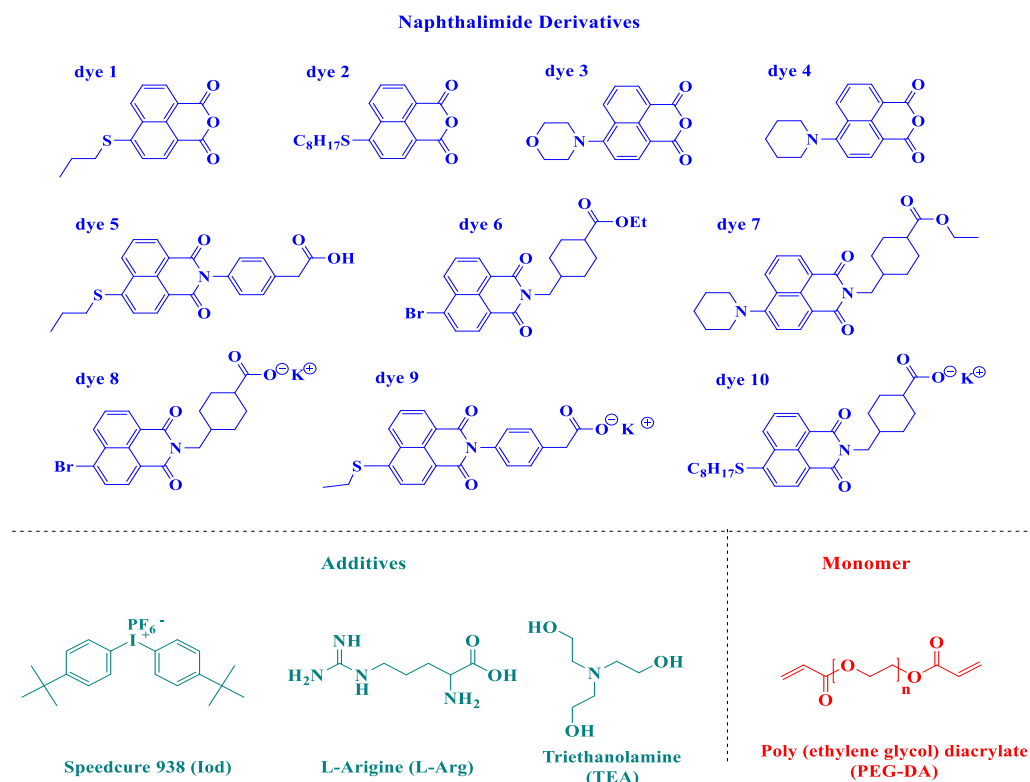
Part IV. Water-Soluble/Visible-Light-Sensitive Naphthalimide Derivative Based Photoinitiating Systems: 3D Printing of Antibacterial hydrogels

1. Introduction.

The combination of the photopolymerization process with 3D printing technology can provide an efficient tool to elaborate structures with a high precision of shape using hydrogels and enabling to achieve the fusion of structure and function. To realize the 3D printing of hydrogels, especially with cells, it is important to develop an efficient water-soluble PI/PIS which is one of the essential components in water-borne 3D formulations. Among the limited selection of commercially available water-soluble PIs, 2-hydroxy-4'-(2-hydroxyethyl)-2-methylpropiophenone (Irgacure 2959) is the most commonly used aqueous photoinitiator. Due to the limited solubility of this compound in water (~ 0.47 wt %), continuous stirring or moderate heating was required to fully dissolve them [1]. Noticeably, this photoinitiator has a low ability to initiate the polymerization to prepare the hydrogels when exposed to light sources at wavelengths longer than 385 nm [2-3]. In addition, biocompatible riboflavin (Vitamin B₂) has also been reported as a water-soluble PI [4]. However, it can only be utilized in expensive two-photon polymerization printers with extremely tiny build sizes [5]. Furthermore, it also required a co-initiator (e.g. triethanolamine), nitrogen purge (particularly sensitive to oxygen), and high power input (>244 mW) [6-8]. Several studies have also shown that the riboflavin-triethanolamine mixture exhibited a lower photosensitivity than that achieved from the commercially available water-soluble PI (e.g. I2959) [5]. Another highly efficient commercial water-soluble photoinitiator, TPO-Li, exhibits a significantly improved water solubility compared to that of I2959. In addition, the polymerization is very fast and the double bond conversions of more than 97% are achievable. However, this molecule is primarily sensitive to UV light, which is a severe limitation for the printing of hydrogels involving living cells [9]. Therefore, there is an unmet need for highly efficient water-compatible PIs with high absorbance in the visible region to enable fast 3D printing of hydrogels.

Recently, we have reported on six naphthalimide derivatives used as efficient visible-light-sensitive photoinitiators in the combination of Iod and amine for free

radical polymerization of acrylates and cationic polymerization of epoxy monomers [10]. However, only one naphthalimide sodium salt exhibited good water solubility, which can be used as a highly efficient water-soluble photoinitiator for the preparation of hydrogels. This encouraging result prompted us to explore further the possibility of specifically preparing novel water-soluble naphthalimide derivatives with various substituents. In this study, we designed and synthesized a series of naphthalimide derivatives modified with different functional groups, although half of the compounds (dyes 1, 2, 3, 4 and 10) were previously reported as efficient blue light-sensitive photoinitiators in the literature [10-15], their water solubility has not yet been investigated. Therefore, in this work, we initially evaluated the water solubility of these five compounds and found that their water solubility is small and difficult to apply to the polymerization of aqueous monomers. Based on these derivatives, we synthesized five novel compounds, namely dyes 5-9, in which only two naphthalimide potassium salts (dyes 8 and 9) exhibited excellent water solubility. These two compounds were combined with aqueous co-initiators to form two- and three-component photoinitiating systems (PIS), and their photopolymerization efficiencies were investigated by real-time Fourier transform infrared spectroscopy upon irradiation with a LED@405 nm. After that, the involved redox mechanisms were investigated by combining several experiments such as photolysis and fluorescence quenching. The best PIS was chosen to initiate the photopolymerization of poly(ethylene glycol) diacrylate (PEG-DA) aqueous solution of monomers while reducing the silver ions dispersed in the formulations into silver nanoparticles. Due to the aqueous solution of monomers used in this experiment, we evaluated the swelling properties of the produced hydrogels *via* rapid 3D printing method using a low-cost SLA-based 3D printer without any organic solvents through two routes. Finally, *Escherichia coli* was selected to explore the effect of the antibacterial activity of AgNPs contained PEG-hydrogels prepared with different concentrations of AgNO₃.



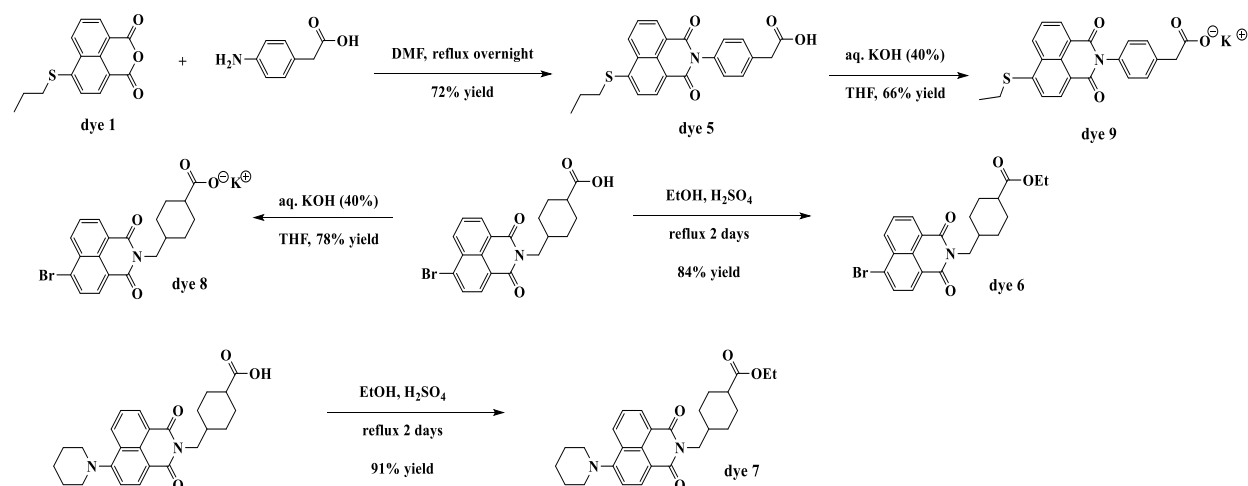
Scheme IV-1. Chemical structures of the naphthalimide derivatives used as PI, additives of Speedcure 938 (Iod), L-Arginine (L-Arg), Triethanolamine (TEA), and the functional benchmark monomer (PEG-DA) used in this work.

2. Materials and Methods.

2.1 Chemical compounds.

The functional benchmark monomer used in this work, namely, poly(ethylene glycol) diacrylate (PEG-DA: SR 610) was purchased from Sartomer-Europe (Arkema, Colombes). The water-soluble co-initiator triethanolamine and L-Arginine (TEA/ L-Arg, used as an electron donor), as well as *bis*-(4-tert-butylphenyl)iodonium hexafluorophosphate (Iod, used as an electron acceptor) were all purchased from Sigma-Aldrich (Saint-Quentin-Fallavier). Their molecular structures are shown in **Scheme IV-1**. The solvent (i.e. Dimethyl sulfoxide) was also purchased from Sigma-Aldrich and was of analytical grade. Naphthalimide derivatives were prepared as described in Supporting Information and their chemical structures are also shown in **Scheme IV-1** (dyes 1-10). It has to be noticed that compounds 1, 2, 3, 4 and 10 were previously reported in the literature [10-15]. Compound 5 was synthesized in one step, by condensation of 6-(propylthio)-1H,3H-benzo[de]isochromene-1,3-dione (dye 1) with 4-aminophenylacetic acid, furnishing 2-(4-(1,3-dioxo-6-(propylthio)-1H-benzo[de]isoquinolin-2(3H)-yl)phenyl)acetic acid (dye 5) in 72% yield. By use of an aq.

KOH solution, the anion of dye 5 could be prepared in 66% yield (dye 9). Dyes 8 and 6 were prepared from the same intermediate i.e. 4-((6-bromo-1,3-dioxo-1*H*-benzo[*de*]isoquinolin-2(3*H*)-yl)methyl)cyclohexane-1-carboxylic acid. By use of aqueous conditions, dye 8 could be obtained in 78% yield. Conversely, dye 6 was prepared in 84% yield by esterification of the corresponding acid. Finally, dye 7 was also obtained in 91% yield by esterification with ethanol using a catalytic amount of concentrated sulfuric acid (see Scheme IV-2).



Scheme IV-2. Synthetic routes to dyes 5-9.

2.2 Water solubility of proposed naphthalimide derivatives.

The previous researches of our group have shown that some naphthalimide derivatives can be dissolved in water [15]. Therefore, in this work, 10 different naphthalimide derivatives were specifically synthesized and used as visible light-sensitive photoinitiators. Water solubility of the ten dyes was investigated in deionized water and the best candidates were selected for the following studies.

2.3 Photopolymerization experiments.

Initiating ability of the one/two/three-component systems (dyes alone, dyes/Iod, dyes/TEA or L-Arg, dyes/Iod/TEA or L-Arg) comprising the selected water-soluble dyes was examined for an aqueous monomer (50% PEG-DA/50% water) and studied by real-time Fourier transform infrared spectroscopy (RT-FTIR, JASCO FTIR 4700, Lisses, France). Co-initiators TEA and L-Arg are hydrophilic substances that dissolve readily in an aqueous monomer, with the water solubility of TEA being greater than that of L-Arg. However, the Iod also cannot dissolve in water, but the presence of PEG-DA allows it to be well-dispersed in an aqueous monomer. A visible light LED@405nm whose intensity is about 110 mW/cm² was used to initiate the polymerization of

photosensitive formulations between two polypropylene (PP) films with a thickness of 0.1 mm or into molds (between two polypropylene films) with a thickness of 2 mm to reduce O₂ inhibition. The monitored peak is located around 1620 cm⁻¹ (thickness of about ~ 0.1 mm) or 6160 cm⁻¹ (thickness ~ 2 mm).

2.4 Involved chemical mechanisms.

2.4.1 UV-Vis absorption properties of the selected dyes and their photolysis process and fluorescence quenching process with Iod and amine.

A JASCO V730 spectrophotometer was used to study the UV-vis absorption properties of the proposed water-soluble dyes. Analyses were carried out in the water with a concentration of 5×10⁻³ wt%. As the iodonium salt is insoluble in water, photolysis of the dyes with Iod/amine and the dyes alone in DMSO was carried out using the JASCO V730 spectrophotometer, keeping the concentration of the water-soluble dyes at 5×10⁻³ wt%, while for the co-initiators (e.g. Iod and amine), concentrations were at about 1.5 wt%.

In addition, fluorescence spectra of the selected dyes were determined using a JASCO FP-6200 Spectrofluorimeter at a concentration of 5×10⁻³ wt% in water. Fluorescence quenching of the dyes with Iod or amine was carried out in DMSO.

2.4.2 Electron spin resonance (ESR) spin trapping experiments (ESR-ST) and the free energy changes of dyes with Iod/amine.

Radicals generated by the interactions between the proposed water-soluble dyes with Iod or amine under sunlight irradiation were trapped by PBN (0.25 wt%) in N₂ saturated DMSO solutions and then monitored using an X-band spectrometer (Bruker EMX-plus) at room temperature. Finally, the obtained ESR spectra were simulated and analyzed using WINSIM software.

Remarkably, the free energy changes (e.g. ΔG_{S1}^{Iod} or ΔG_{S1}^{EDB}) were calculated to detect the electron transfer reactions between the dyes and the additives (Iod/amine) and to support the experimentally observed photopolymerization processes. The redox potentials (E_{ox} and E_{red}) of the proposed dyes were determined by cyclic voltammetry in DMSO, and E^* , corresponding to the excited state energy level of the dyes, was determined by the intersection of their normalized UV-visible and fluorescence spectra.

2.5 Dynamic time sweep rheology and tensile strength of the manufactured hydrogel.

Photopolymerization processes of all formulations were further examined by dynamic time-scan rheology. Specifically, 40 μL of photosensitive resin was dropped on a glass slide and then measured at a constant frequency of 0.1 Hz at 25 °C using a Haake-Mars rotational rheometer with LED@405 nm.

Tensile strength of the fabricated hydrogels (width \sim 4 mm, length \sim 50 mm, height \sim 2.5 mm) was measured using an Instron dynamometer at a displacement rate of 10 mm/min at room temperature until rupture. From the subsequent stress/strain curves, the final tensile strength and modulus of elasticity could be calculated. At least, three measurements were made for each specimen and the average value is reported.

2.6 Preparation of silver nanoparticles (AgNPs).

2.6.1 Preparation of AgNPs in DMF/ water using the proposed water-soluble PIS.

DMF/water solutions containing 0.5 wt% three components PIS (dye/Iod/EDB) and 4 wt% AgNO_3 were irradiated with visible light and their absorption spectra were measured at different times using a JASCO V730 spectrophotometer to confirm whether AgNPs were produced under visible light irradiation.

2.6.2 Preparation of AgNPs in hydrogels.

Hydrogels containing AgNPs were prepared by adding different proportions of AgNO_3 (1 wt%, 2 wt%, 4 wt%, and 8 wt%) in an aqueous monomer (50% PEG-DA/50% water, w/w), in which the dyes/Iod/amine (0.1%/1.5%/1.5%, w/w/w)-based three-component PISs were completely dissolved. The resulting solutions were stirred at room temperature for 1 h to ensure that the salt was well distributed in the photosensitive formulations. RT-FTIR spectroscopy was then used to track the monomer conversion, which not only allowed to examine the impact of the presence of the Ag^+ on the initiation ability of the proposed water-soluble PIS, but also allowed hydrogels containing different ratios of uniformly distributed AgNPs to be prepared.

2.7 Applications in 3D and 4D.

2.7.1 Laser direct write experiments to prepare hydrogels.

Photosensitive formulations were prepared in aqueous monomer (50% PEG-DA/50% water, w/w), in which the proposed dye/Iod/amine-based PIS and/without metal salt (AgNO_3) were well distributed. Then, all direct laser write experiments were successfully performed under air at room temperature using a SLA-based 3D printer with a laser diode at 405 nm (Thorlabs). Finally, topography and precision of the

obtained 3D patterns were analyzed using a numerical optical microscope (DSX-HRSU from Olympus Corporation).

2.7.2 Swelling experiments of the obtained hydrogels.

Since the aqueous monomer contains 50% water, two approaches were used in this work to study the swelling properties of the resulting hydrogels. The first approach consisted in soaking the obtained hydrogels directly in deionized water at room temperature for 24 hours and then measuring their wet weight (Wt) and volume (V_1) after reaching swelling equilibrium. Then, the swollen hydrogels were heated in an oven at 40°C to remove the absorbed water, while their weight and volume were also measured. Another method consists in first heating the obtained hydrogels in an oven at 40°C to remove their internal moisture and then perform the subsequent swelling test according to the specific steps of the first method. The swelling ratio and volume change value of the obtained hydrogels were determined by comparing their wet weight (Wt) and volume (V_1) values after reaching the swelling equilibrium with their initial values.

2.8 Antibacterial activity of hydrogels with different content of AgNPs.

To demonstrate the effect of different contents of AgNPs in hydrogels on the antibacterial activity, *Escherichia coli* was selected as a bacterial model in this work. PEG-hydrogel without AgNPs was used as a reference to systematically investigate the antibacterial activity of the obtained PEG-hydrogels with different content of AgNPs (1 wt%, 2 wt%, 4 wt%, 8 wt%). The bacterial strains were stored in 15% glycerol at -80 °C. The strains were cultured in LB medium (Lennox L: 1% bacto -tryptone, 0.5% bacto-yeast extract, 1% NaCl, NaOH [3×10^{-3} M]) at 37 °C. Prior to contact with the PEG-hydrogels, an overnight culture was established to start a new culture until $OD_{580nm} = 1$ (approximately 10^9 bacteria/ mL). 100 μ L is used to inoculate the new LB agar dish. After overnight growth in contact with PEG-hydrogels, the antibacterial activity was directly observed [16-17].

3. Results and Discussion.

3.1 Water solubility of proposed naphthalimide-derivatives.

Since the previous work of our group has shown that some naphthalimide - derivatives have good water solubility [15], in this work, 10 different naphthalimide - derivatives were synthesized and used as photosensitive initiators. As can be seen in

Figure IV-1, dyes 1, 2, 4, 6, and 7 were completely insoluble in water. Conversely, dyes 3, 5, and 10 were slightly soluble in water and their aqueous solutions were pale yellow and cloudy. Remarkably, dyes 8 and 9 were soluble in water as their solutions were yellow, clear, and transparent.

To confirm the solubility of these two dyes in water, concentration of these dyes in water was gradually increased. **Annex IV-1** shows images of these two dyes in water at different concentrations from 0 to 10 wt% (more specifically 0.1 wt%, 1 wt%, 3 wt%, 5 wt%, 6 wt%, 7 wt%, 8 wt%, and 10 wt%). Color of the aqueous solution of dye 8 gradually deepened from colorless to yellow, and the solution remained clear and transparent until the concentration increased to 10%. For dye 9, the color of the aqueous solution also became darker as the concentration increased. However, the aqueous solution turned from clear to cloudy when the concentration increased from 6 to 7 wt%. It indicated that the solubility of dye 8 is higher than 10%, while 6 wt% may be close to the saturation concentration for dye 9 in water, which is much larger than that of the commercially available water-soluble PI (e.g. the solubility of I2959 is about 0.47 wt% [1]).

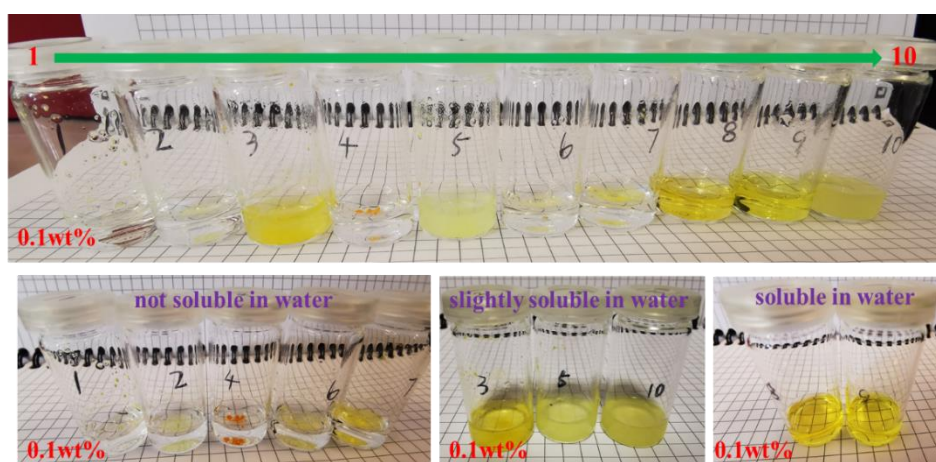


Figure IV-1. Images of 10 different dyes based on naphthalimide-derivatives in water at a concentration of 0.1 wt%.

3.2 Photopolymerization efficiency of the proposed water-soluble dyes based PIS.

Photoinitiation ability of dyes 8 and 9 in combination with additives (Iod, TEA/L-Arg) as photoinitiating systems was investigated under visible light LED@405nm irradiation in laminate. Polymerization profiles of the aqueous monomer PEG-DA (50 wt% PEG-DA/50 wt% water) are depicted in **Figure IV-2** (see also **Table IV-1**). No polymerization can be observed in the formulations containing only dyes 8 or 9. After

the addition of co-initiators or additives, initiation ability of the dye-based two-component PIS (Dye-Iod, Dye-TEA, and Dye-L-Arg) was improved so that a deep-curing could now occur at a thickness of about 2 mm. While for thin films of about 0.1 mm, except for dye 8 with the TEA/L-Arg based formulation, all other resins could also be polymerized to form hydrogels.

To further improve the efficiency of the free radical photopolymerization of waterborne monomer PEG-DA, a co-initiator Iod and an additive TEA/L-Arg were added and combined with the water-soluble dyes to form a three-component photoinitiating system (dye-Iod-TEA/dye-Iod-L-Arg). Although Iod is insoluble in water, they were fully dispersed in the resins in the presence of PEG-DA. As shown in **Figure IV-2**, dye 9-Iod-TEA based three-component PIS achieved the best polymerization efficiency including higher final acrylate functional conversion (about 97% for thick films and 71% for thin films) and higher polymerization rate (the slope of the polymerization curves). In addition, all of them can be deeply cured within 100 s of light exposure. Moreover, when compared to the blank control that was initiated by Iod/TEA (the involved photoinitiation mechanism is shown in Scheme 3b), the polymerization efficiency of the dyes-based three components PISs is higher, demonstrating the importance of the presence of dyes.

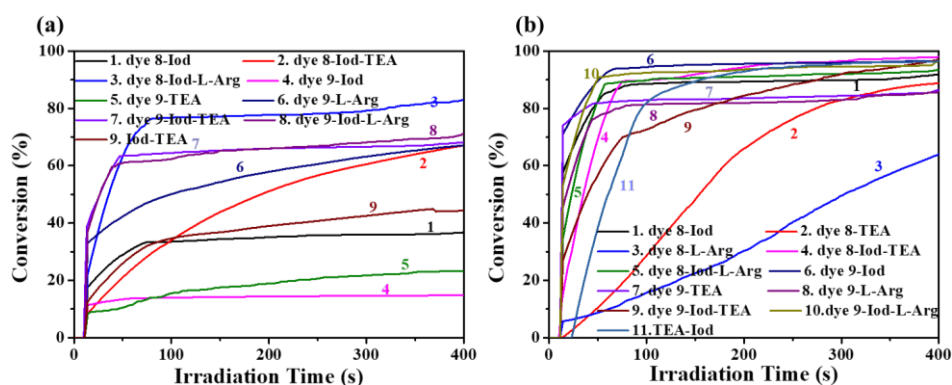


Figure IV-2. Photopolymerization kinetics (conversion of acrylate function vs. time) of the aqueous monomer PEG-DA (50 wt% PEG-DA/50 wt% water) initiated by dyes 8/9 based one/two/three-component PISs (dyes, dye-Iod, dye-TEA(or L-Arg), dye-Iod-TEA (or L-Arg)) in the laminate upon irradiation with a LED @ 405 nm with a thickness of (a) 0.1 mm and (b) 2 mm. The irradiation starts at $t = 10$ s.

Final Acrylate Function Conversions (FCs, 50% PEG-DA/50% water, w/w)

Dye 8

Dye 9

	Thin (%)	Thick (%)	Thin (%)	Thick (%)
Dye	-	-	-	-
Dye-Iod	37	92	15	96
Dye-TEA	-	89	23	87
Dye-L-Arg	-	64	67	86
Dye-Iod-TEA	67	98	67	97
Dye-Iod-L-Arg	83	94	71	97
Iod-TEA	45	96	45	96

“-” means no deep-curing can be observed

Table IV-1. Summary of the final acrylate function conversions of aqueous monomers (50 wt% PEG-DA/50 wt% water) initiated by dyes 8/9 based one/two/three-component photoinitiating systems (dyes, dye-Iod, dye-TEA/L-Arg, dye-Iod-TEA/L-Arg) and blank control (Iod/TEA) in laminate upon irradiation with a LED @ 405 nm having a thickness of about 0.1 and 2 mm.

3.3 Investigation of the involved chemical mechanisms.

Absorption property of the selected water-soluble dyes 8 and 9 was investigated in water and the corresponding spectra are presented in [Figure IV-3](#). It is evident that both dyes 8 and 9 have a relatively broad absorption range, from around 270-550 nm, which guarantees a good overlap with the emission spectrum of the LED@405 nm used in this work. In addition to the maximum absorption peak observed around 300 nm, dye 8 also has two absorption shoulders about 375 nm and 425 nm, respectively; while dye 9 showed two main absorption peaks around 400 nm and 325 nm, respectively. Furthermore, the extinction coefficients of these two dyes around 405 nm were summary in [Annex IV-2](#), e.g. $9150 \text{ M}^{-1} \text{ cm}^{-1}$ for dye 9 and $4280 \text{ M}^{-1} \text{ cm}^{-1}$ for dye 8.

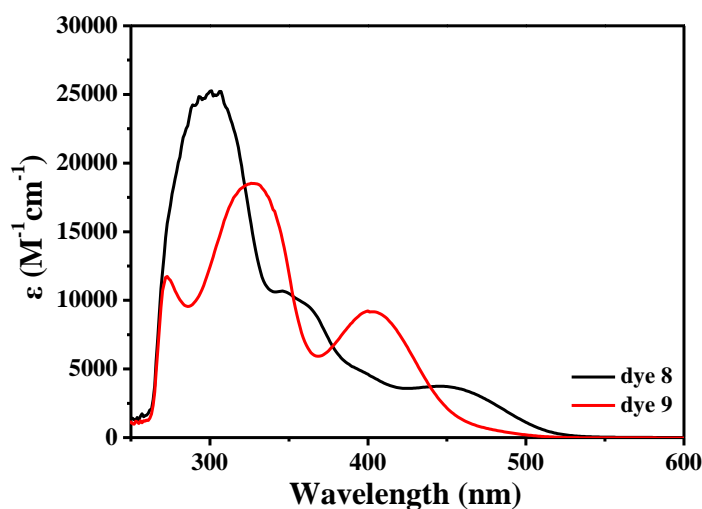


Figure IV-3. UV–Vis absorption spectra of dyes 8 and 9 (5×10^{-3} wt%) in water.

Since Iod is not soluble in water, photolysis of these two dyes was carried out with Iod/TEA in DMSO solvent. As shown in [Annex IV-3](#), absorption intensity of the characteristic peaks of the dye 8 based one-/two-/three-component photoinitiating systems (dye 8, dye 8-Iod, dye 8-TEA, dye 8-Iod-TEA) at 350 nm dropped with light irradiation, while the absorption intensity of the other peak near 450 nm increased steadily. This indicated that some new products were generated during the photolysis process. Moreover, although the combination of dye 8 with Iod and TEA reached the highest dye consumption during the whole photolysis process, the consumption value was still low (only about 26%).

Interestingly, there was no significant photolysis activity for dye 9 in the presence of Iod, and only the absorption intensity at 340 nm was reduced upon light irradiation at LED@405nm (see [Figure IV-4](#)). However, substantial changes were observed in the absorption spectra of dye 9 alone or dye 9 with Iod and amine, and their photolysis (irradiation time 10 min) was faster than that of dye 8 (irradiation time ≤ 60 min), due to its greater molar extinction coefficient at 405 nm (see [Annex IV-2](#)). Furthermore, throughout the photolysis process, the absorption intensity of two characteristic absorption peaks around 280 nm and 400 nm decreased with light irradiation, except for a new absorption peak at 340 nm, where the absorption intensity gradually increased.

Furthermore, -the obvious photolysis process of the two characteristic absorption peaks at around 280 nm and 400 nm could be clearly observed after the addition of amine to a solution of dye 9. In addition, two new absorption peaks appeared at 340 and 500 nm, and their absorption intensity gradually increased with continuous irradiation, accompanied by a red-shift phenomenon. [Annex IV-4](#) shows that the consumption of dye 9 reached by the three-component PIS (dye 9/Iod/amine) was slightly higher than that of the two-component PIS based on dye 9/amine combinations, which are both close to 80% and much higher than the values achieved with dye 9 alone (e.g. consumption of about 50%). Except for dye 9-Iod, the consumption of the other three groups (dye 9 alone, dye 9-TEA, dye 9-Iod-TEA) are significantly higher than that achieved by each group of dye 8, which is compatible with their photoinitiation ability shown in [Figure IV-2](#).

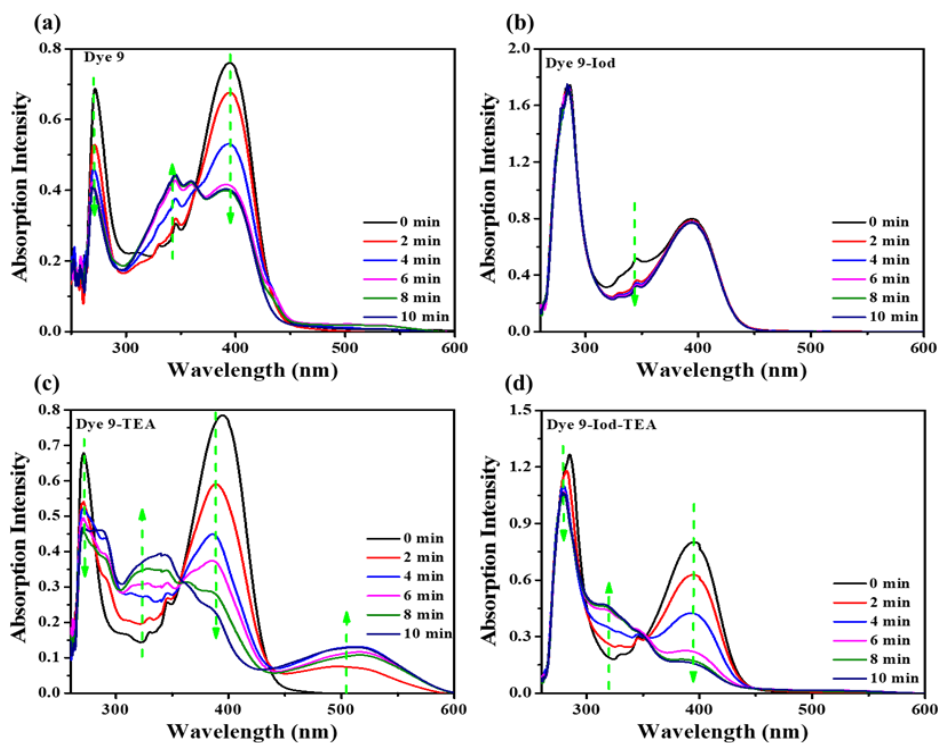


Figure IV-4. The photolysis of dyes 9 based one/two/three-component systems (a) dye 9, (b) dye 9-Iod, (c) dye 9-TEA, (d) dye 9-Iod-TEA) in DMSO under LED@405nm.

To demonstrate the feasibility of the interactions between dye 9 and Iod/amine, fluorescence quenching of dye 9 was also performed in DMSO. The emission peak of dye 9 appeared around 500 nm, and its intensity steadily dropped after the addition of Iod/amine. Remarkably, the fluorescence quenching process between dye 9 and Iod was depicted as non-linear curvature (as shown in [Figure IV-5](#)), which seems more likely to be contributed by both static and dynamic quenching mechanisms simultaneously, while a linear fit can be observed from the fluorescence quenching process between dye 9 with amine; this indicates that the process exclusively corresponded to the dynamic quenching mechanism, that is, only the dynamic interactions of the quencher (amine) and the fluorophore (the fluorophore in the excited state of the dyes, [18]). These results demonstrated that both Iod and amine could be used as effective quenchers for dye 9.

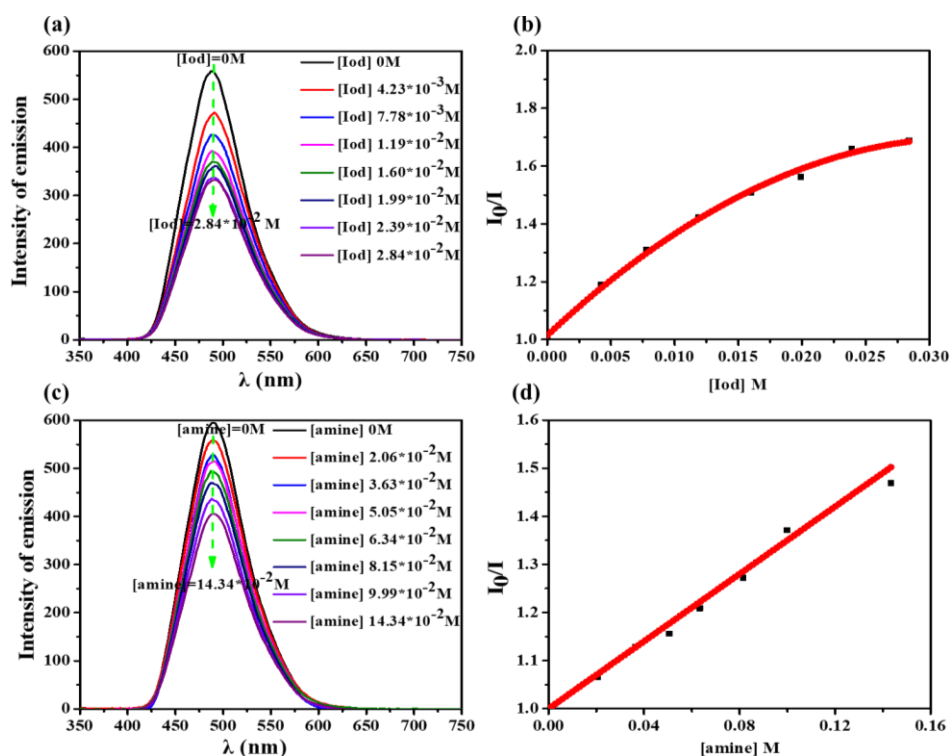


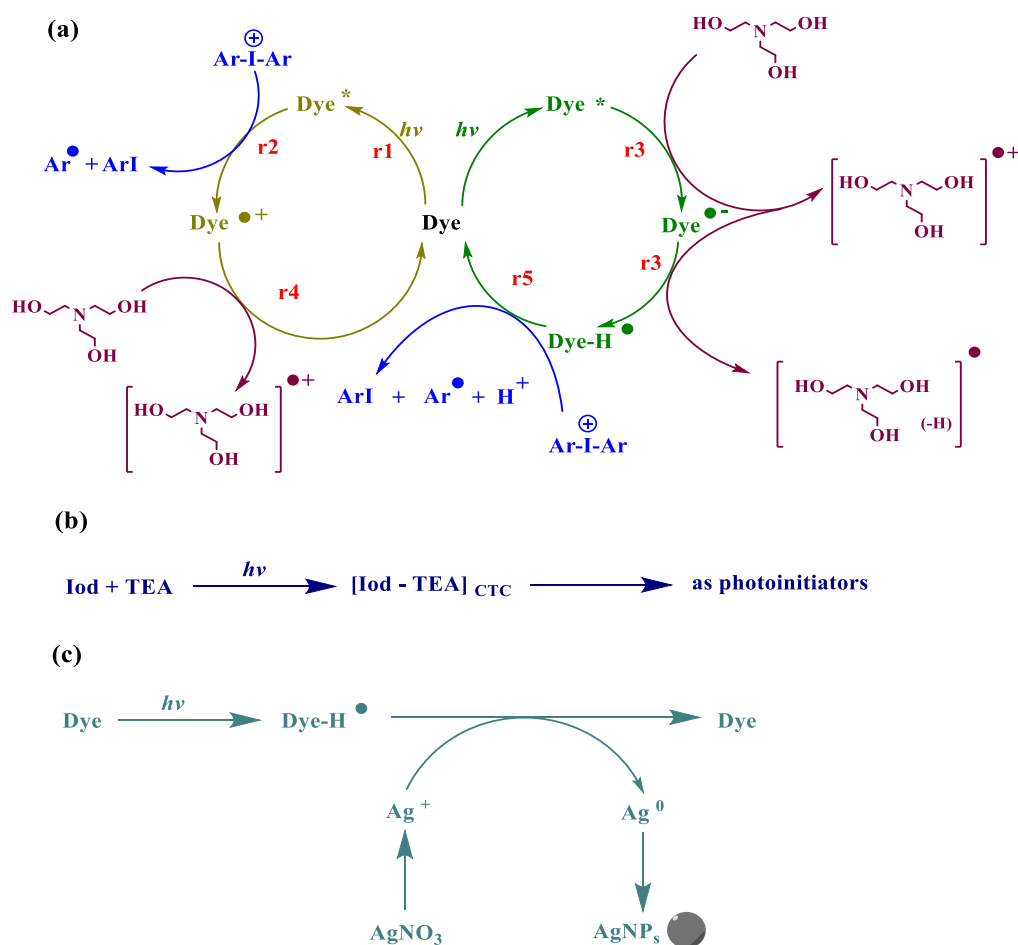
Figure IV-5. (a) Fluorescence spectrum of the fluorescence quenching process between dye 9 with Iod; (b) Stern-Volmer treatment for the fluorescence quenching of dye 9/Iod; (c) Fluorescence spectrum of the fluorescence quenching process between dye 9 with amine; (d) Stern-Volmer treatment for the fluorescence quenching of dye 9/amine.

	Dye 8	Dye 9
E_{S1} (V)	3.31	2.72
E_{ox} (V)	-	0.10
E_{red} (V)	-0.43	-0.51
ΔG_{S1}^{Iod}	-	-1.92
ΔG_{S1}^{TEA}	-1.88	-1.22

Table IV-2. Parameters of dye 8 and 9 in DMSO: singlet excited state energy (E_{S1}); reduction potential (E_{red}) and oxidation potential (E_{ox}) measured by Cyclic Voltammetry experiments as well as free energy changes of the electron transfer processes.

To further understand the interactions existing between dye and Iod/amine, the free energy changes of the electron transfer processes ($\Delta G_{Iod} / \Delta G_{EDB}$) described in [Scheme IV-3](#) were also examined. First, the energy of the first excited singlet state (E_{S1})

was estimated from the intersection of the normalized absorption spectrum with the normalized fluorescence spectrum (see [Table IV-2](#) and [Annex IV-5](#)). Oxidation and reduction potentials of dyes 8 and 9 in DMSO were then evaluated using cyclic voltammetry (see [Annex IV-6](#)). Finally, according to the above parameters, the free energy changes of the electron transfer reactions between the dye and the Iod/amine are all negative according to the following equation, indicating that the electron transfer process between the dye and the two additives Iod/amine may occur, proving the practicality of the involved mechanisms outlined in [Scheme IV-3](#).



Scheme IV-3. (a) Proposed photoinitiation step mechanisms of dyes/Iod/amine based water-soluble initiating systems (r1-r5); (b) the involved mechanism of Iod/TEA based initiating systems as the blank control; (c) the involved photoinitiation mechanism of the generation of AgNPs.

In ESR-spin trapping research in DMSO solutions containing dye 9-Iod or dye 9-amine protected by N_2 , *N*-phenyl-*tert*-butyl nitron (PBN) was used as a spin trap agent.

Since DMSO is a more polar solvent, both a_N and a_H values were increased compared to those obtained in *tert*-butylbenzene [19]. As illustrated in Figure IV-6, PBN/aminoalkyl radical adducts were detected in the dye 9-TEA system (r3 in Scheme IV-3), which exhibited hyperfine nitrogen and hydrogen coupling constants of 15.0 G and 2.8 G. Regarding the dye 9-Iod formulation, according to experimental results published elsewhere [20], the hyperfine coupling constant determined by simulated spectra (Figure IV-6) revealed the formation of aryl radicals ($a_N = 14.8$ G and $a_H = 2.6$ G, r2 in Scheme IV-3).

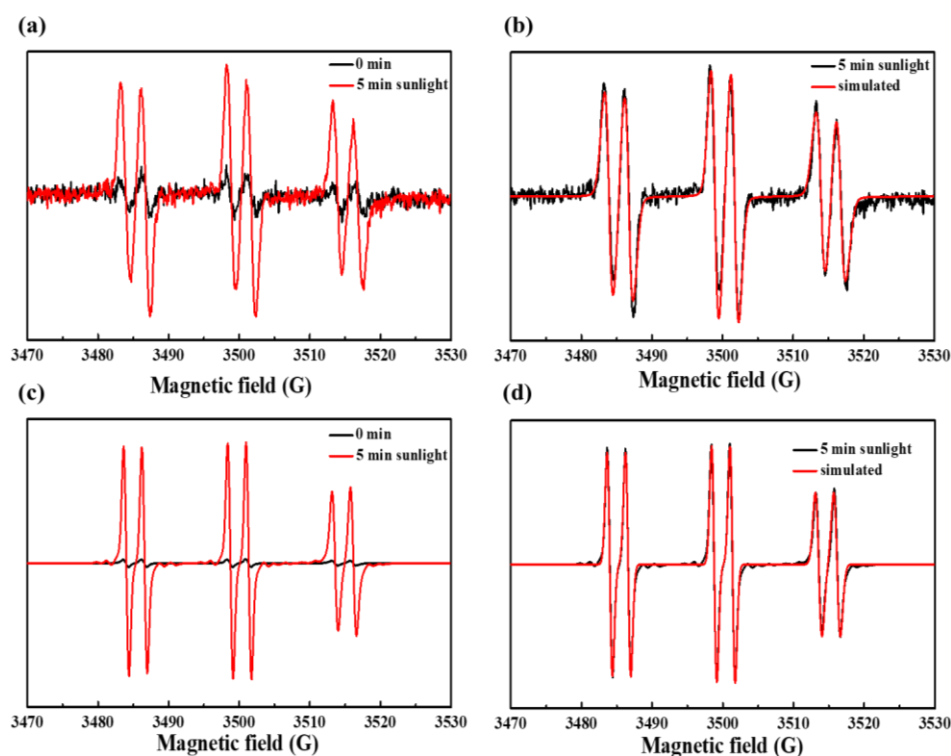


Figure IV-6. ESR spectra of (a) dye 9-TEA with irradiation time = 0 min (black), 5 min under sunlight; (b) dye 9-TEA system with irradiation time = 5 min (black) and simulated (red) spectra; (c) dye 9-Iod system with irradiation time = 0 min (black) and 5 min (red); (d) dye 9-Iod system with irradiation time = 5 min (black) and simulated (red) spectra.

3.4 Preparation of silver nanoparticles (AgNPs).

In this study, the proposed water-soluble dyes and additives (Iod/amine) were irradiated at LED@405 nm to generate a series of radicals and cations *via* a series of redox reactions (as shown in Scheme IV-3), mainly initiating the polymerization of PEG-DA monomers, as well as contributing to the *in-situ* reduction of $AgNO_3$ to AgNPs. As shown in Figure IV-7a, absorbance of the characteristic peak of silver

nanoparticles at 420 nm [21] in DMF solution increased with the sustained light irradiation, indicating that the proposed photoinitiating system (i.e. dye 9/Iod/TEA) could reduce Ag^+ to AgNPs (as shown in [Scheme IV-3c](#), [22-23]) [19]. During the irradiation process, color of the solution changed from light yellow to dark yellow, and a coating of silver nanoparticles was visible on one side of the cuvette after 100 min of light irradiation (see [Figure IV-7b](#)). Nothing was observed by TEM before the light exposure, while after 100 min of light irradiation, the generated silver nanoparticles were uniformly distributed in the DMF solution in the form of round spheres with a size of about 7 nm, accompanied by a small number of nanoparticles aggregated in the form of larger spheres with a size of about 20 nm (see [Annex IV-7a](#)). Due to the polarity of the water and the effect of sunlight, a large number of particles with a size of about 10-20 nm can be observed in the aqueous solution prior to exposure to LED@405nm, (see [Figure IV-7c](#) and [Annex IV-7b](#)); however, after irradiated for 30 min, the color of the solution deepened, and the particles increased and agglomerated in irregular shapes (see [Figure IV-7c](#) and [Annex IV-7c](#)).

Furthermore, we used RT-FTIR to investigate the influence of the presence of different concentrations of silver ions on the photopolymerization efficiency of PEG-DA aqueous monomer. [Figure IV-7d](#) shows that the inclusion of a tiny amount of silver ions ($\leq 1\%$) had no significant effect on the polymerization of PEG hydrogels, which may be deep-cured within 100 s with a final acrylate functional conversion of about 99%. When the concentration of silver ions was raised to 8%, polymerization efficiency of PEGDA monomers decreased noticeably, and the final functional conversions dropped to 55%, owing to the competition between the polymerization of PEGDA monomers and the reduction of Ag^+ to AgNPs. Furthermore, the solution darkened with increasing silver ion concentration, impeding the light penetration. The upper surface of the produced PEG hydrogel was covered with silver nanoparticles, whereas the silver nanoparticles on the bottom surface were less and aggregated into clusters due to the influence of light penetration (see [Annex IV-7d-e](#)).

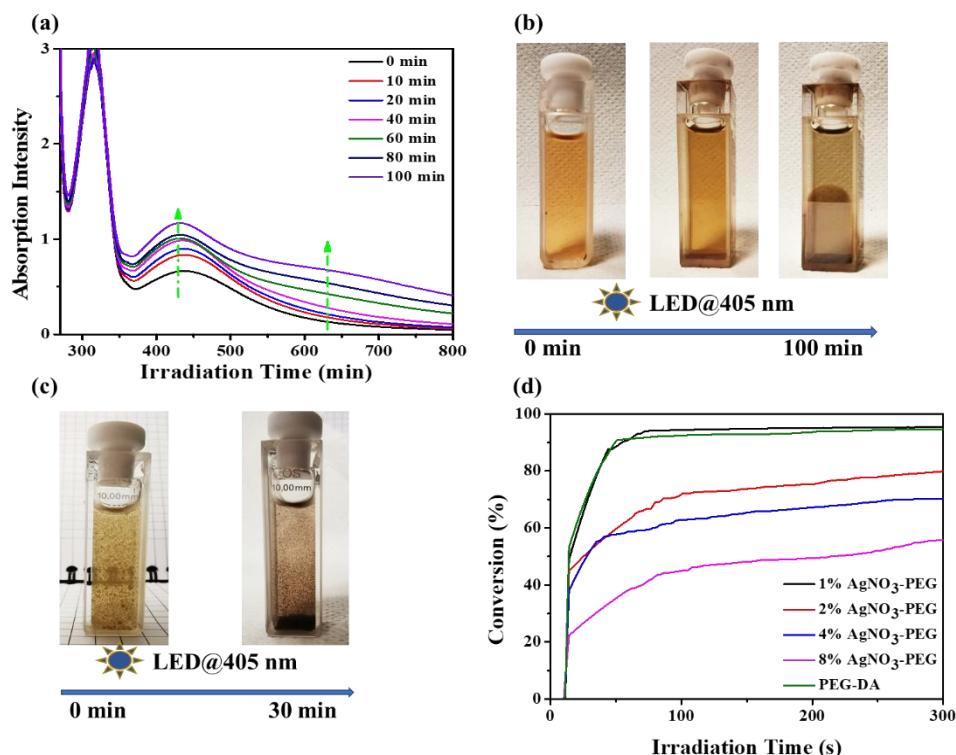


Figure IV-7. (a) In-situ photochemical preparation of AgNPs with 0.1 wt% dye8-1.5 wt% TEA-1.5 wt% Iod (0.1 wt%) and AgNO₃ (4 wt%) in DMF followed by UV-Vis absorption spectroscopy in air atmosphere; (b) The color changes of DMF containing 0.1 wt% dye8-1.5 wt% TEA-1.5 wt% Iod (0.1 wt%) and AgNO₃ (4 wt%) after 100 min light irradiation; (c) The color changes of water containing 0.1 wt% dye8-1.5 wt% TEA-1.5 wt% Iod (0.1 wt%) and AgNO₃ (4 wt%) after 30 min light irradiation; (d) Photopolymerization kinetics using dye 9 with the additive (1.5 wt% TEA or L-Arg and 1.5 wt% Iod) and different concentrations of AgNO₃ in the monomer of PEGDA (50 wt%)-water(50 wt%) upon LED@405 nm irradiation. Thickness is about 2 mm and the irradiation starts from $t = 10$ s.

3.5 Mechanical properties of obtained hydrogels.

Photoinitiation ability of the water-soluble dyes-based PIS was further explored by measuring the change in storage (G') modulus during the formation of hydrogels *via* photopolymerization using a Haake-Mars rotational photorheometer with time-scan experiments. The irradiation starts at $t = 20$ s and the results are presented in **Figure IV-8a**. In comparison to the commercially available water-soluble UV photoinitiator I2959, the water-soluble photoinitiating system not only exhibited higher water solubility but also was appropriate for visible light and demonstrated better photopolymerization efficiency (slope of the curve, the larger the slope the higher the polymerization

efficiency). Within 100 s, all three-component PIS based on dyes 8 and 9 were able to complete the phase transition and reached the maximum storage modulus (G'). PIS based on dye 9 demonstrated a much higher polymerization efficiency than that of dye 8 based PIS. Effect of varying the silver ion concentrations on the polymerization efficiency under visible light was further investigated. Addition of 1wt%, 2 wt%, and 4 wt% silver ions had no effect on the ultimate storage modulus (G') of the fabricated hydrogels; however, the polymerization efficiency of the photosensitive formulations reduced dramatically with increasing silver ion concentration.

Furthermore, as shown in [Figure IV-8b](#), the PEG hydrogels produced with I2959 reached a 10% elongation strain, equivalent to tensile fracture energy of roughly 0.9 MPa. Under visible light irradiation, the elongation and the corresponding fracture potential of the PEG hydrogels prepared with the PIS based on water-soluble dyes were lower than those prepared with I2959, with the exception of the dye 9-Iod- TEA based PIS, which the elongation of the hydrogels prepared reached 13%. FTIR results showed that there was no significant difference in the photopolymerization efficiency of the water-soluble PIS consisting of L-Arg or TEA as amines paired with Iod and dye. However, TEA was eventually chosen as the electron donor (amine) due to its better stability and water solubility than L-arg. Subsequently, the tensile properties of dye-Iod-TEA and dye-Iod-L-Arg-initiated hydrogels were studied, and the results demonstrated that the hydrogels prepared from dye-Iod-TEA displayed longer elongation strain and higher fracture potentials, proving that TEA is more suitable to be used as an electron donor. Furthermore, the stretching properties of the dye 9-based hydrogels were much better than those of dye-8, which corresponded to the superior photoinitiation ability of the dye-9-based PIS. More crucially, with the addition of silver ions, the dye-Iod-TEA based PIS initiated free-radical photopolymerization and also reduced the silver cations to silver nanoparticles. These two processes competed with each other, resulting in a considerable drop in the polymerization efficiency of the photosensitized formulations and a steady weakening of the tensile properties of the produced hydrogels with increasing silver ion concentration.

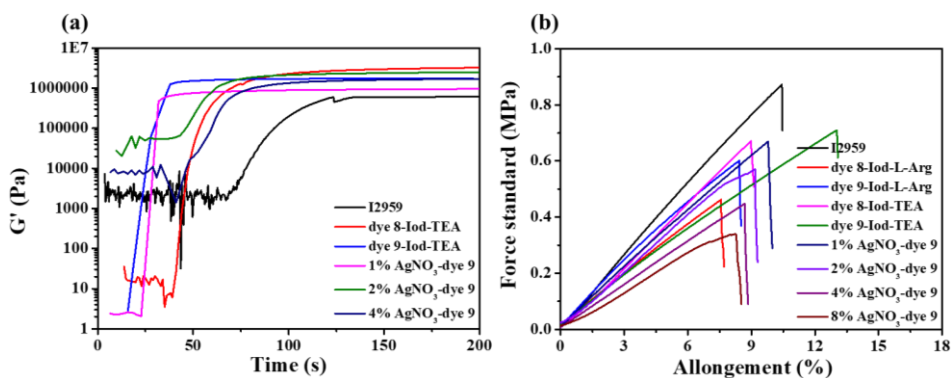


Figure IV-8. (a) The storage (G') modulus of hydrogels during the photopolymerization process initiated with 0.5 wt% I2959 and dyes-based three-component PIS with/without AgNO_3 ; (b) Tensile property of hydrogels obtained with 0.5 wt% I2959 and dyes-based three-component PIS with/without AgNO_3 .

3.6 Applications in 3D and 4D printing.

Since dyes 8 and 9 /Iod/TEA-based PISs displayed excellent photopolymerization efficiencies under visible light irradiation, direct laser write experiments were directly carried out to fabricate the PEG-hydrogels. The sensitive formulations were effectively written to generate stable 3D hydrogels, as illustrated in Figure IV-9. In comparison to the dye 8/Iod/amine-based PIS, the dye 9/Iod/amine-based formulation needed a reduced irradiation time (~ 1 min) to achieve a 3D pattern. In addition, incorporation of AgNO_3 to the formulation required a longer irradiation time (~ 5 min) to obtain 3D patterns (see Figure IV-9), demonstrating that the presence of AgNO_3 significantly reduced the polymerization efficiency of PEGDA, which was in full agreement with the results obtained for free radical polymerization.

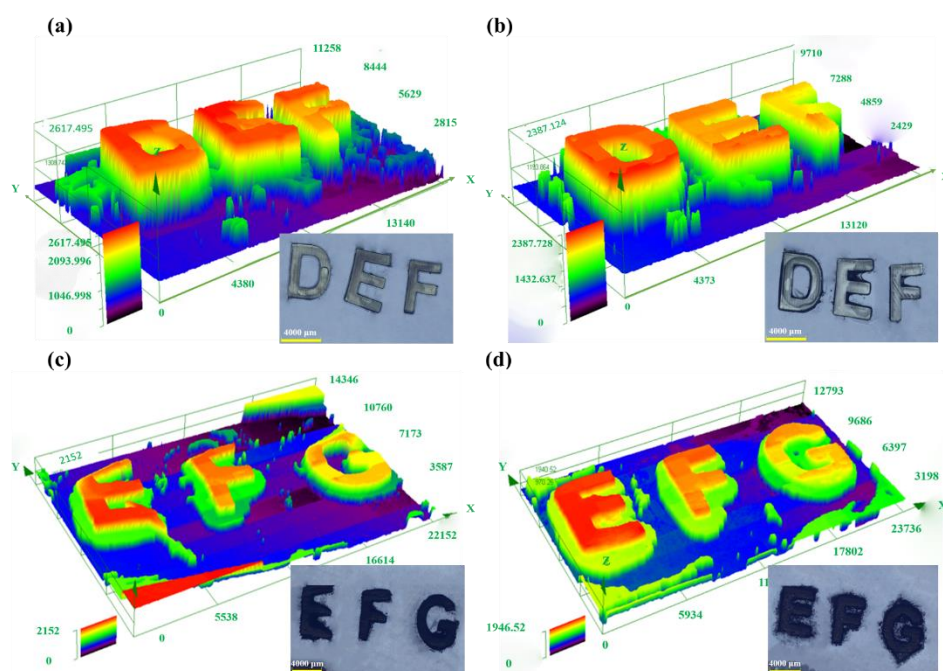


Figure IV-9. 3D morphologies of the 3D patterns obtained through the direct laser write experiment initiated with proposed water-soluble dyes-based PIS in PEG-DA aqueous monomer characterized by numerical optical microscope: (a) initiated by dye 8-Iod-TEA; (b) initiated by dye 9-Iod-TEA; (c) initiated by dye 8-Iod-TEA with 4 wt% AgNO₃; (d) initiated by dye 9-Iod-TEA with 4 wt% AgNO₃.

Since the water content of the monomer used was about 50 wt%, the swelling properties of the obtained four kinds of PEG-hydrogels were investigated using two methods: direct immersion in water until swelling equilibrium was reached as well as dehydration to remove the internal water before immersion in water. The swelling ratio of each group of hydrogels was calculated by comparing their initial wet weight to the wet weight after attaining the swelling equilibrium, and the result was shown in **Figure IV-10**. PEG hydrogels initiated by dye 8-based PIS exhibited an improved hydrophilicity during swelling in water after dehydration, with the swelling ratio increasing from 35% achieved from the direct swelling process to 55%. However, the immediate swelling process of the PEG hydrogel prepared with the dye 9 based PIS resulted in greater hydrophilicity, with a swelling ratio of about 70%, which is much higher than that of post-dehydration swelling (~57%). Furthermore, introduction of AgNPs into PEG hydrogels also reduced their hydrophilicity (e.g. the swelling ratio of PEG hydrogels prepared by dye 9/Iod/amine decreased from 70% to 35%). **Annex IV-8** and **Annex IV-9** clearly show that the morphology and the volume of the PEG-hydrogel also changed significantly during these two swelling processes.

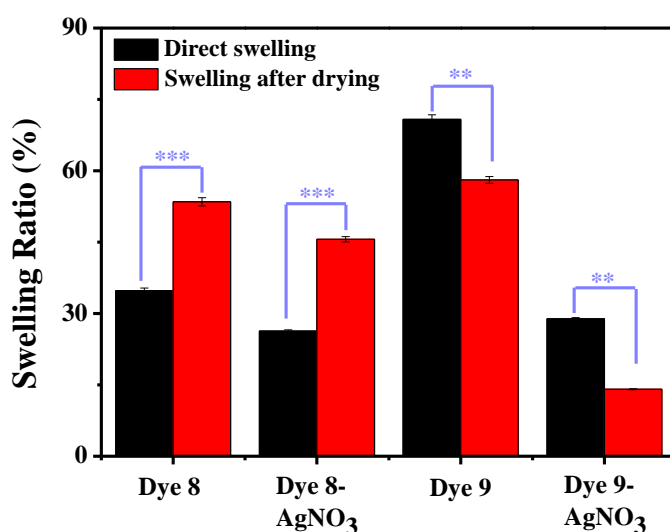


Figure IV-10. Swelling ratio of PEG hydrogels and AgNPs contained PEG hydrogels

initiated with water-soluble dyes 8 and 9 based PIS obtained by two swelling routes.

3.7 Antibacterial activity of hydrogels with different content of AgNPs.

Numerous studies have demonstrated that AgNPs have broad antibacterial activities and represent an interesting generation of antibacterial agents [24-26]. Therefore, in this work, *Escherichia coli* was selected to study the antibacterial effect of the prepared AgNPs-containing PEG hydrogels. Initially, the culture of *E. coli* was carried out in solid LB-agar, pure PEG hydrogel was used as the control group, and hydrogels with different contents were used as the experimental group. A halo of growth inhibition was clearly observed only around the hydrogels of the experimental group (see **Figure IV-11a**). Second, in order to determine the effect of different contents of AgNPs-PEG hydrogels on the antibacterial effect, we calculated the area of the antibacterial ring of each group, as shown in **Figure IV-11b**, with the increase of AgNPs content, its antibacterial activity also increased. Considering the polymerization efficiency of the hydrogels with different contents of silver nanoparticles and the mechanical properties of the prepared hydrogels, AgNPs-containing PEG-hydrogels prepared with 4% AgNO_3 were finally selected as the best combination for the preparation of antibacterial material.

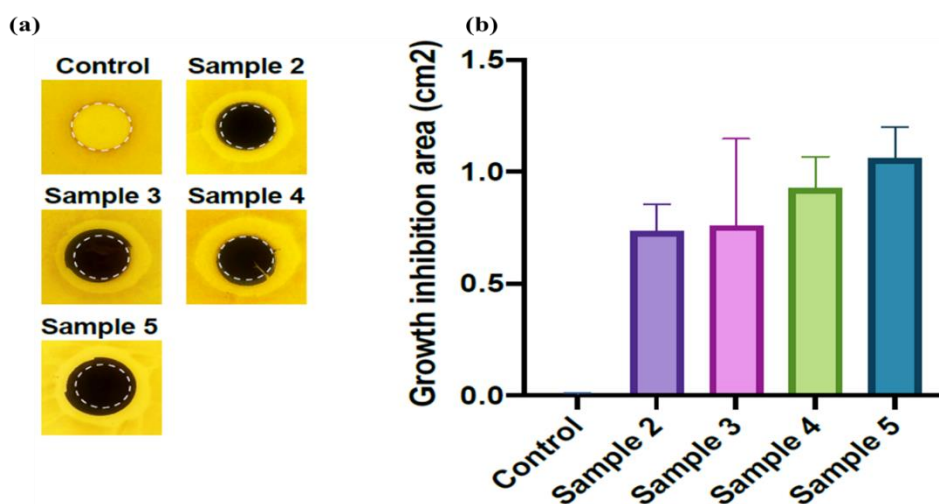
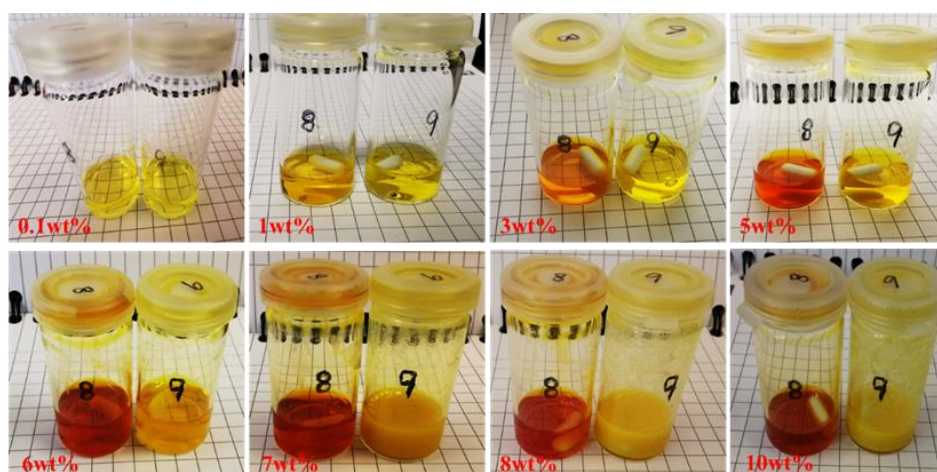


Figure IV-11. (a) Pictures of *Escherichia coli* in presence of PEG, AgNPs contained PEG pellet during the overnight culture at 37°C; (b) the areas of halo of growth inhibition appeared around different content of AgNPs contained PEG pellet. (PEG hydrogel-control; 1% AgNPs contained PEG hydrogel -sample 2; 2% AgNPs contained PEG hydrogel - sample 3; 4% AgNPs contained PEG hydrogel - sample 4; 8% AgNPs contained PEG hydrogel - sample 5).

4. Conclusion.

In this research, a series of new naphthalimide derivatives that can be used for the 3D printing of hydrogels was prepared to address the challenge of developing highly efficient water-soluble PIs in the UV-visible region. The prepared two naphthalimide potassium salts (dyes 8 and 9) not only showed water solubility far beyond that of the commercially available PI (I2959), but also achieved extremely high polymerization efficiency when used in combination with a co-initiator (Iod/amine) under visible light irradiation. We fabricated hydrogel scaffolds with high resolution using an SLA-based 3D printer, and they exhibited better mechanical properties than the hydrogels prepared from the PI I2959. The advantage of the proposed dyes-based aqueous PIS is the high photoinitiation efficiency for aqueous monomer PEG-DA while reducing Ag^+ to AgNPs to prepare the antibacterial hydrogels, where the optimal antibacterial concentration of silver nitrate used was 4 wt%. In conclusion, our developed aqueous PIs showed better performance than the existing commercial aqueous PI I2959, thus offering various new possibilities for a wide range of applications.

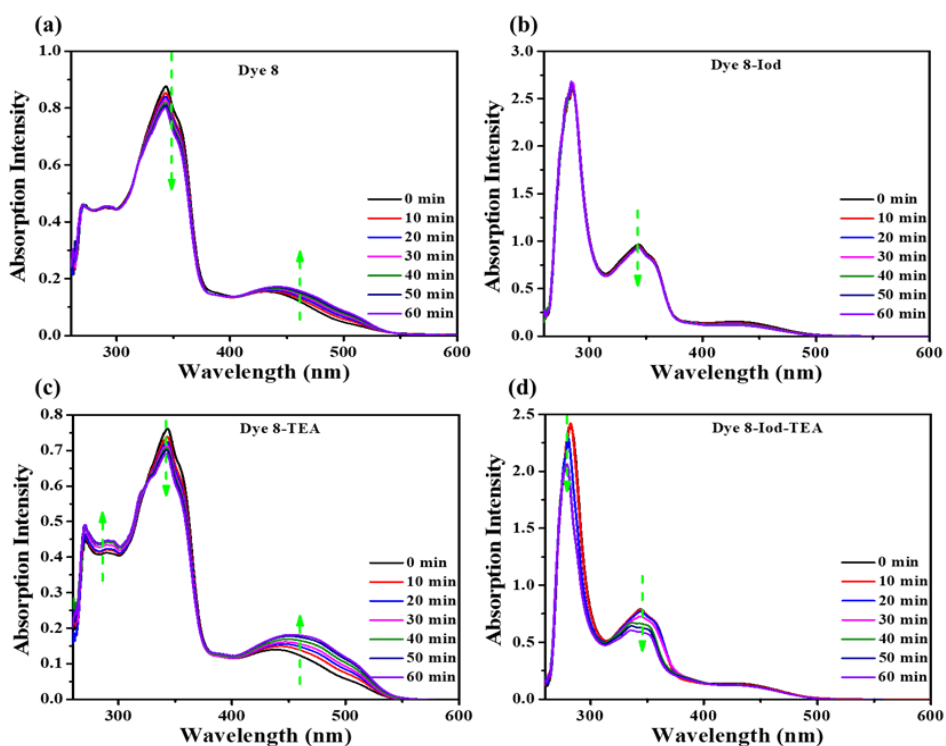
Annex



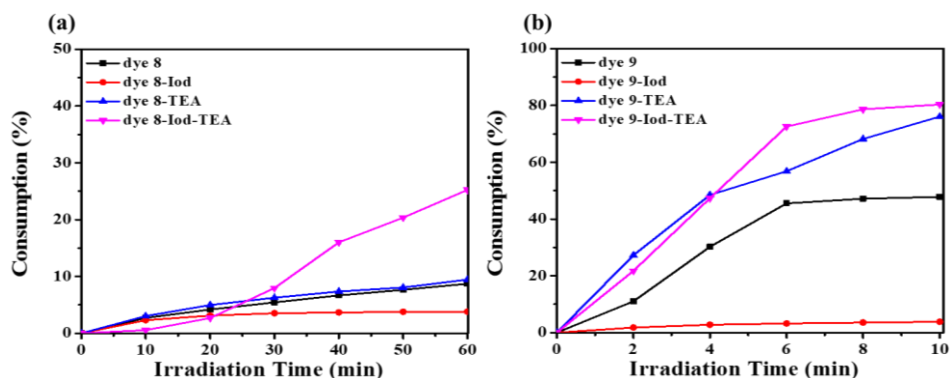
Annex IV-1. Pictures of dyes 8 and 9 in water with different concentrations of 0.1 wt%, 1 wt%, 0.1 wt%, 3 wt%, 5 wt%, 6 wt%, 7 wt%, 8 wt% and 10 wt%.

Dyes	λ_{\max} (nm)	ϵ_{\max} ($M^{-1} cm^{-1}$)	$\epsilon_{@405nm}$ ($M^{-1} cm^{-1}$)
8	300	25 260	4280
9	325	18 530	9150
	400	9230	

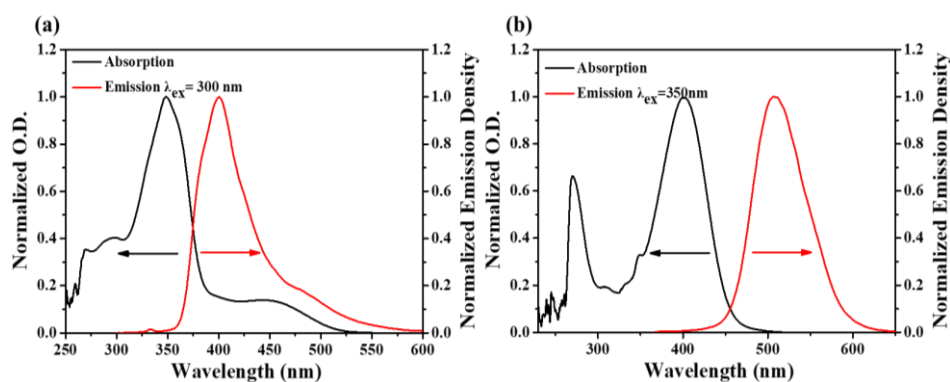
Annex IV-2. Summary of light absorption properties of dyes 8 and 9 in water: maximum absorption wavelengths λ_{\max} ; molar extinction coefficients at λ_{\max} (ϵ_{\max}) and the emission wavelength of the LED@405 nm ($\epsilon_{@405nm}$).



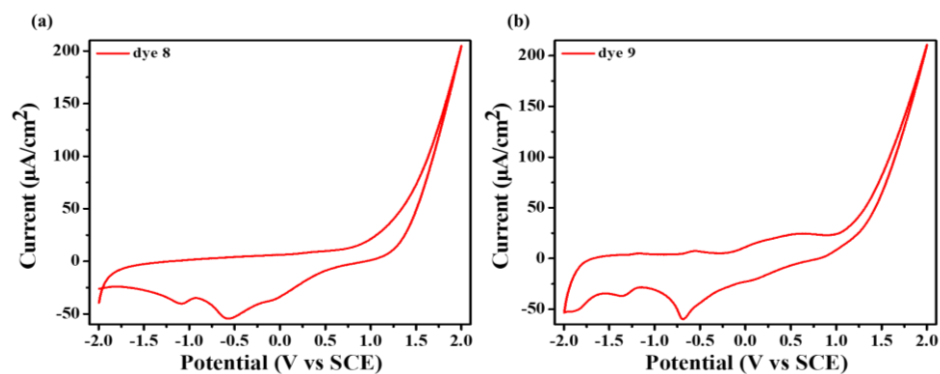
Annex IV-3. The photolysis of dyes 8 based one/two/three-component systems (a) dye 8, (b) dye 8-Iod, (c) dye 8-TEA, (d) dye 8-Iod-TEA) in DMSO under LED@405nm.



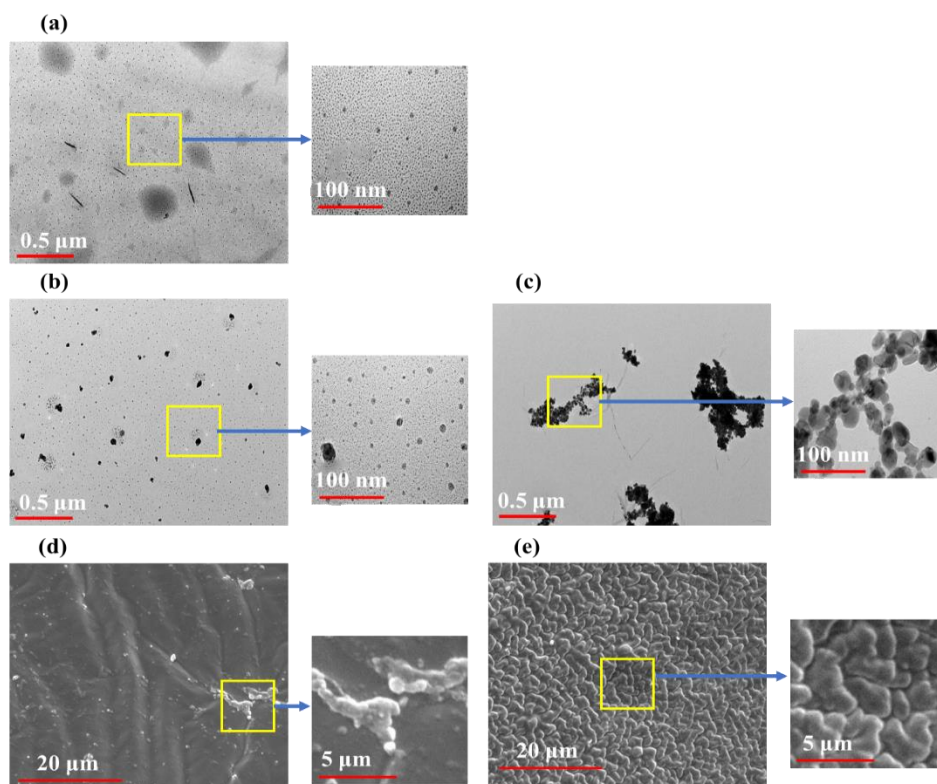
Annex IV-4. The consumption of (a) dye 8 and (b) dye 9 during the photolysis process.



Annex IV-5. Singlet state energy of (a) dye 8 and (b) dye 9 determined in water.



Annex IV-6. Cyclic voltammetry of (a) dye 8 and (b) dye 9 determined in DMSO.

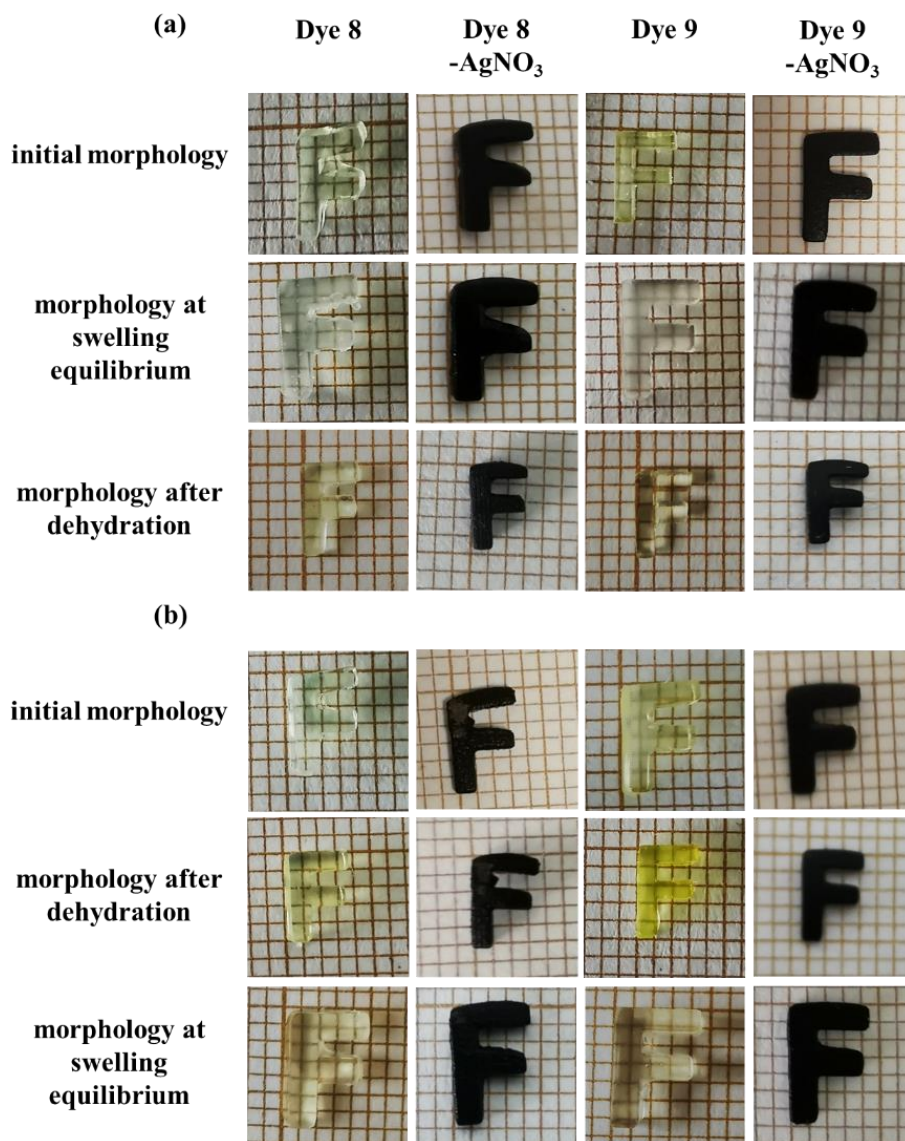


Annex IV-7. TEM images of (a) AgNPs prepared in DMF solution after irradiation for 100 min; (b) AgNPs prepared in water before open the light; (c) AgNPs prepared in water after irradiation for 30 min; (d) AgNPs on the down surface of obtained PEG-hydrogels from FTIR experiment; (e) AgNPs on the upper surface of obtained PEG-hydrogels from FTIR experiment.

	Dye 8	Dye 9	Dye 8-AgNO ₃	Dye 9-AgNO ₃	
Route 1	Original volume (V_0, mm^3)	28.86	30.06	14.70	16.88
	Volume at Swelling Equilibrium (V_1, mm^3)	41.69	55.55	19.86	23.91
	Volume after Dehydration (V_2, mm^3)	18.80	17.22	8.98	8.51
	R (%)	144	185	135	141
	Route 2	Original volume (V_0, mm^3)	26.52	31.50	15.75
Volume after Dehydration (V_1', mm^3)		21.45	18.34	10.85	10.66
Volume at Swelling Equilibrium (V_2', mm^3)		43.22	53.86	23.81	21.43
R (%)		163	173	151	125

Annex IV-8. Volumes of the obtained 3D patterns during two swelling routes: initial

volume (V_0), volumes at swelling equilibrium (V_1/V_2'), volume after dehydration (V_3/V_1') as well as the volume change ratio (R/R').



Annex IV-9. Photos of PEG hydrogels and AgNPs contained PEG hydrogels during the swelling process: (a) route 1 - initial morphology, morphology at swelling equilibrium and morphology after dehydration; (b) route 2 - initial morphology, morphology after dehydration, and morphology at swelling equilibrium.

References:

1. Williams, C. G.; Malik, A. N.; Kim, T. K.; Manson, P. N.; Elisseeff, J. H. Variable cytocompatibility of six cell lines with photoinitiators used for polymerizing hydrogels and cell encapsulation. *Biomaterials* **2005**, *26*(11), 1211-1218.
2. Fairbanks, B. D.; Schwartz, M. P.; Bowman, C. N.; Anseth, K. S. Photoinitiated polymerization of PEG-diacrylate with lithium phenyl-2, 4, 6-trimethylbenzoylphosphinate: polymerization rate and cytocompatibility. *Biomaterials* **2009**, *30*(35), 6702-6707.
3. Lin, H.; Zhang, D.; Alexander, P. G.; Yang, G.; Tan, J.; Cheng, A. W. M.; Tuan, R. S. Application of visible light-based projection stereolithography for live cell-scaffold fabrication with designed architecture. *Biomaterials* **2013**, *34*(2), 331-339.
4. Tomal, W.; Ortyl, J. Water-soluble photoinitiators in biomedical applications. *Polymers* **2020**, *12*(5), 1073-1103.
5. Nguyen, A. K.; Gittard, S. D.; Koroleva, A.; Schlie, S.; Gaidukeviciute, A.; Chichkov, B. N.; Narayan, R. J. Two-photon polymerization of polyethylene glycol diacrylate scaffolds with riboflavin and triethanolamine used as a water-soluble photoinitiator. *Regenerative Medicine* **2013**, *8*(6), 725-738.
6. Kim, S. H.; Chu, C. C. Visible light induced dextran-methacrylate hydrogel formation using -riboflavin vitamin B₂ as a photoinitiator and L-arginine as a co-initiator. *Fibers and Polymers* **2009**, *10*(1), 14-20.
7. Kim, S. H.; Chu, C. C. Fabrication of a biodegradable polysaccharide hydrogel with riboflavin, vitamin B₂, as a photo-initiator and L-arginine as coinitiator upon UV irradiation. *Journal of Biomedical Materials Research Part B: Applied Biomaterials* **2009**, *91*(1), 390-400.
8. Zhang, T.; Yeow, J.; Boyer, C. A cocktail of vitamins for aqueous RAFT polymerization in an open-to-air microtiter plate. *Polymer Chemistry* **2019**, *10*(34), 4643-4654.
9. Benedikt, S.; Wang, J.; Markovic, M.; Moszner, N.; Dietliker, K.; Ovsianikov, A.; Liska, R. Highly efficient water-soluble visible light photoinitiators. *Journal of Polymer Science Part A: Polymer Chemistry* **2016**, *54*(4), 473-479.
10. Rahal, M.; Mokbel, H.; Graff, B.; Pertici, V.; Gignes, D.; Toufaily, J.; Hamieh, T.; Dumur, F.; Lalevée, J. Naphthalimide-based dyes as photoinitiators under visible light irradiation and their applications: Photo-composite synthesis, 3D printing and polymerization in water. *ChemPhotoChem* **2021**, *5*(5), 476-490.
11. Ott, I.; Xu, Y.; Liu, J.; Kokoschka, M.; Harlos, M.; Sheldrick, W. S.; Qian, X. Sulfur-substituted naphthalimides as photoactivatable anticancer agents: DNA interaction, fluorescence imaging, and phototoxic effects in cultured tumor cells. *Bioorganic & medicinal chemistry* **2008**, *16*(15), 7107-7116.
12. Xiao, P.; Dumur, F.; Zhang, J.; Graff, B.; Morlet-Savary, F.; Fouassier, J. P.; Lalevée, J. Naphthalic anhydride derivatives: Structural effects on their initiating

- abilities in radical and/or cationic photopolymerizations under visible light. *Journal of Polymer Science Part A: Polymer Chemistry* **2015**, *53*(24), 2860-2866.
13. Li, C.; Wang, Y.; Huang, S.; Zhang, X.; Kang, X.; Sun, Y.; Liu, Y. A photostable fluorescent probe for long-time imagining of lysosome in cell and nematode. *Talanta* **2018**, *188*, 316-324.
 14. Ong, J. X.; Ang, W. H. Development of a pre-assembled through-bond energy transfer (TBET) fluorescent probe for ratiometric sensing of anticancer platinum (II) complexes. *Chemistry - An Asian Journal* **2020**, *15*(9), 1449-1455.
 15. Scherzer, T. Photopolymerization of acrylates without photoinitiators with short-wavelength UV radiation: A study with real-time Fourier transform infrared spectroscopy. *Journal of Polymer Science Part A: Polymer Chemistry* **2004**, *42*(4), 894-901.
 16. Bundjaja, V.; Santoso, S.P.; Angkawijaya, A.E.; Yuliana, M.; Soetaredjo, F.E.; Ismadji, S.; Ayucitra, A.; Gunarto, C.; Ju, Y.H.; Ho, M.H. Fabrication of cellulose carbamate hydrogel-dressing with rarasaponin surfactant for enhancing adsorption of silver nanoparticles and antibacterial activity. *Materials Science and Engineering: C* **2021**, *118*, 111542-111583.
 17. Chen, H.; Regard, C.; Salmi, H.; Morlet-Savary, F.; Giacoletto, N.; Nechab, M.; Lalevée, J. Interpenetrating polymer network hydrogels using natural based dyes initiating systems: Antibacterial activity and 3D/4D performance. *European Polymer Journal* **2022**, *166*, 111042-111058.
 18. Blatt, E.; Chatelier, R. C.; Sawyer, W. H. Effects of quenching mechanism and type of quencher association on Stern-Volmer plots in compartmentalized systems. *Biophysical Journal* **1986**, *50*(2), 349-356.
 19. Qi, Y.; Li, H.; Fouassier, J. P.; Lalevée, J.; Sheridan, J. T. Comparison of a new photosensitizer with Erythrosin B for use in a photopolymer. In *Holography: Advances and Modern Trends IV. International Society for Optics and Photonics*. **2015**, *9508*, 142-156.
 20. Tehfe, M. A.; Dumur, F.; Graff, B.; Morlet-Savary, F.; Fouassier, J. P.; Gigmès, D.; Lalevée, J. New push-pull dyes derived from michler's ketone for polymerization reactions upon visible lights. *Macromolecules* **2013**, *46*(10), 3761-3770.
 21. Du, L.; Xu, Q.; Huang, M.; Xian, L.; Feng, J. X. Synthesis of small silver nanoparticles under light radiation by fungus *Penicillium oxalicum* and its application for the catalytic reduction of methylene blue. *Materials Chemistry Physics* **2015**, *160*, 40-47.
 22. Yagci, Y.; Sangermano, M.; Rizza, G. A visible light photochemical route to silver-epoxy nanocomposites by simultaneous polymerization-reduction approach. *Polymer* **2008**, *49*(24), 5195-5198.
 23. Mutlu, S.; Metin, E.; Yuksel, S.A.; Bayrak, U.; Nuhoglu, C.; Arsu, N. In-situ photochemical synthesis and dielectric properties of nanocomposite thin films containing Au, Ag and MnO nanoparticles. *European Polymer Journal* **2021**, *144*, 110238-110251.

24. López-Heras, M.; Theodorou, L. G.; Leo, B. F.; Ryan, M. P.; Porter, A. E. Towards understanding the antibacterial activity of Ag nanoparticles: electron microscopy in the analysis of the materials-biology interface in the lung. *Environmental Science: Nano* **2015**, *2*(4), 312-326.
25. Nigussie, G. Y.; Tesfamariam, G. M.; Tegege, B. M.; Weldemichel, Y. A.; Gebreab, T. W.; Gebrehiwot, D. G.; Gebremichel, G. E. Antibacterial activity of Ag-doped TiO₂ and Ag-doped ZnO nanoparticles. *International Journal of Photoenergy* **2018**, *2018*, 1-7.
26. Sotiriou, G. A.; Teleki, A.; Camenzind, A.; Krumeich, F.; Meyer, A.; Panke, S.; Pratsinis, S. E. Nanosilver on nanostructured silica: Antibacterial activity and Ag surface area. *Chemical Engineering Journal* **2011**, *170*(2-3), 547-554.

Part V. Conclusions and Perspectives

1. Conclusions.

3D printing via Vat photopolymerization combines the advantages of photopolymerization technology with the benefits of 3D printing technology, which has been widely employed in medical, aerospace, construction areas, among others. Continuous research and development of 3D printing via photopolymerization technology is required to address the expanding requirements of people in daily life and manufacturing. The central theme of this thesis is the creation of PIs that are more suited to mild circumstances and their application in 3D/4D printing. In the first part, we provide a brief overview of photopolymerization and 3D printing technologies, and then focus on the recent development and application of 3D printing via photopolymerization technology (primarily on the development of new PIs/PISs and composite materials suitable for 3D printing). Following that, a series of studies were conducted to solve the scarcity of efficient PISs under mild conditions, and numerous three-component PISs were produced. RT-FTIR, steady-state photolysis, fluorescence methods, and ESR spin trapping studies were used to evaluate the relevant chemical mechanisms, light absorption, and photoinitiation abilities. This work also looks at their prospective uses, such as 3D/4D printing optical composites and antimicrobial materials.

The second part involves the design and synthesis of two series of dyes with chalcone as the core structure, both of which exhibit excellent absorption properties in the near UV/visible region and can be used with co-initiators [bis-(4-tert-butylphenyl) iodonium hexafluorophosphate (Iod) and ethyl 4-dimethylaminobenzoate (amine, EDB)] to initiate FRP via redox reactions. This part highlights not only the strong effect of substitution patterns but also the groups forming different chalcone (anthracene, ferrocene, alkoxy-substituted aromatic rings). Furthermore, by extending the elongation of the π -conjugate spacer and red-shifting the location of its absorption band while raising the molar extinction coefficient, it provides a more effective tool for

improving its photoinitiation capabilities. In the third part, a simple one-step approach for generating nano complexes, that is polymers containing silver nanoparticles (AgNPs), *in-situ* under air at room temperature is proposed, coordinating the photopolymerization process with the *in-situ* photoreduction process of AgNPs. This part continues to prepare two dye series by expanding the π -conjugated structure, which, when paired with co-initiator Iod/EDB, can successfully promote the FRP of PEG-DA and the CP of EPOX under LED@405nm irradiation. It can even be used to prepare AgNPs -containing IPN polymers with antibacterial activity against Gram-positive and Gram-negative bacteria like Staphylococcus aureus and Pseudomonas aeruginosa. The fourth part produced ten distinct naphthalimide derivatives, along with the two most soluble naphthalimide salts, whose water solubility exceeds that of the benchmark water-soluble PI-Irgacure 2959 (I2959) by 12 to 20 folds. As a three-component PIS, these novel PIs may be employed as extremely effective water-soluble initiators with water-soluble co-initiators, such as L-arginine (L-Arg)/triethanolamine (TEA) as electron donor and iodonium salt (Iod) as electron acceptor, to prepare antimicrobial nano complexes hydrogels containing AgNPs. These PIS are appealing when exposed to visible light (LED@405 nm) irradiation in response to the growing demand for radiation curable aqueous products.

In addition to the five efforts covered in this thesis, I also worked on other projects throughout my Ph.D., mainly focusing on visible light-sensitive Type II PISs and water-soluble PIs. Nine publications published as first author in international peer-reviewed journals enriched all of my efforts during my Ph.D. The findings of this thesis were also presented at the International Congress - 6th European Symposium on Photopolymer Science and 17th Science Day, which was co-hosted by the French polymer research group GFP Grand-Est East and the Grand-Est Federation of Materials and Nanosciences (GFP-Grand Est/FRMNGE).

2. Perspectives.

When compared to other 3D printing techniques, photopolymerization provides distinct benefits in terms of printing speed, geometric precision, and material

possibilities. The layer-by-layer printing process allows for the polymerization of formulations into 3D objects in seconds, but there are still numerous challenges to solve, such as printing with live cells and printing high-resolution components at huge sizes. Until far, 3D printing via photopolymerization has mainly been employed to fabricate small-scale items. Microprojection stereolithography has shown to be a viable way for printing fine features with generally acceptable print areas, encompassing a larger range of applications. Printing high-resolution components at high speeds and in huge sizes, on the other hand, remains a high difficulty. As a result, the development of high-resolution, fast-speed, and high-throughput photopolymer printing technology is a long-term research topic that necessitates considerable efforts.

Composite materials have numerous features that may strengthen or overcome the shortcomings of a single material, fully exploit the advantages of each material, and provide materials with new properties, and thus offer a wide range of applications in 3D printing via photopolymerization. Several businesses have investigated and commercialized the printing of complicated ceramic components. Nonetheless, several emergent uses of 3D printing via photopolymerization are still in their infancy, such as the printing of instantly useable soft tissue engineering constructs. On the one hand, this is owing to the immaturity of multi-material printing capabilities of photopolymerization, as most human organs are heterogeneous and require high multi-material printing skills. Besides, additional research into the curing mechanism of multifunctional biomedical hydrogels is needed, and it remains difficult to build tissue structures fast and precisely. The study of the impacts of printing parameters, as well as the creation and optimization of multi-material printers, will definitely pave the way for the technology's acceptance.

Furthermore, the personalizability of 3D printing via photopolymerization opens up new avenues for its application in the biomedical area. Currently, this technology is solely employed to create medical gadgets, instructional models, and so forth. Although there are examples of its effective application in tissue engineering in the literature, the printing and widespread application of complex parenchymal organs containing live

cells still confront significant obstacles. Based on a review of the literatures, the key issues currently under consideration include the following: 1) the issue of toxicity, which must be addressed by establishing safe systems containing non-cytotoxic prepolymers as well as natural and biocompatible PIs/PISs; 2) due to the safety concerns connected with UV irradiation, it is advised that visible light be used to trigger the photoreaction, which must be addressed by the creation of visible light sensitive PIs/PISs. Unfortunately, there are relatively few visible light-sensitive PIs/PISs that are biodegradable and have high cytocompatibility; 3) printing involving living cells is generally performed in an aqueous environment, which needs to be addressed by developing aqueous PIs/PISs. Furthermore, additive manufacturing offers a tremendous opportunity or photopolymerizable biomaterials that is currently underutilized. Manufacturing using 3D printing has a significant benefit since biomedical equipment may be 3D adjusted for specific purposes and have specialized capabilities.

Finally, the fabrication of functionalized smart materials using 3D printing via photopolymerization has progressively gained broad interest and is predicted to grow fast in the next years. This will necessitate the creation of polymers with adequate physical characteristics, as well as responsive and 3D printable structures such as conductivity, light, water, heat, and so on, in order to introduce functionalization, such as sensors. As a result, smart materials made by 3D printing and photopolymerization can make major contributions to medical devices, aerospace, and other fields.